NASA-CR-144887
19800006814

NASA Contractor Report 144887

ANALYSES AND TESTS OF THE B-1 AIRCRAFT STRUCTURAL MODE CONTROL SYSTEM

John H. Wykes, Thomas R. Byar, Cary J. MacMiller,
and David C. Greek

Contract NAS4-2519
January 1980

NASA

William M. Adams Jr.
Mailstop 152A
Langley Research Center
Hampton, VA 23665

CR-144,887
Wykes, J. H.
Analyses and tests of the B-1 aircraft structural
mode control system.
NASA

[redacted]

NASA Contractor Report 144887

ANALYSES AND TESTS OF THE B-1 AIRCRAFT STRUCTURAL MODE CONTROL SYSTEM

John H. Wykes, Thomas R. Byar, Cary J. MacMiller,
and David C. Greek
Rockwell International
El Segundo, California

Prepared for
Dryden Flight Research Center
under Contract NAS4-2519

National Aeronautics and
Space Administration

1980

TABLE OF CONTENTS

TABLE OF CONTENTS - (Continued)

LIST OF ILLUSTRATIONS

LIST OF ILLUSTRATIONS - (Continued)

LIST OF ILLUSTRATIONS - (Continued)

LIST OF ILLUSTRATIONS (Continued)

LIST OF ILLUSTRATIONS (Continued)

LIST OF ILLUSTRATIONS - Continued

LIST OF ILLUSTRATIONS - (Continued)

LIST OF ILLUSTRATIONS - (Concluded)

LIST OF TABLES

ANALYSES AND TESTS OF THE B-1 AIRCRAFT STRUCTURAL MODE CONTROL SYSTEM

John H. Wykes, Thomas R. Byar, Cary J. MacMiller,
and David C. Greek
Rockwell International,
North American Aircraft Division

SUMMARY

An 18-month program was conducted to compile and document for publication information pertaining to analyses and flight tests of the B-1 Structural Mode Control System (SMCS). This is the second phase of a continuing effort; results from the first phase study are documented in reference 1. This report covers the following topics:

(1) Flexible aircraft equations of motion

(2) Description of flexible aircraft analyses model

(3) Comparison of analyses and flight-test performance results of the SMCS

(4) A summary of the study of the forward SMCS sensor package relocation

(5) Truncated analytical models used in simulation effort

(6) An analysis of the SMCS vane interference effects

(7) Impact of SMCS on selected loads

(8) Flight-test results of the SMCS vane effects on inlet/engine characteristics

(9) Summary of SMCS flight-test results

INTRODUCTION

The B-1 aircraft is one of the first vehicles to include a control configured vehicle (CCV) concept in the early design phases. The aircraft has a requirement to provide a specified level of ride quality for the crew. This requirement has been met on the B-1 through the use of an automatic control system (SMCS) whose main external feature is a set of vanes (near the crew station) which are canted down 30 degrees from the horizontal. (See figure 1.)

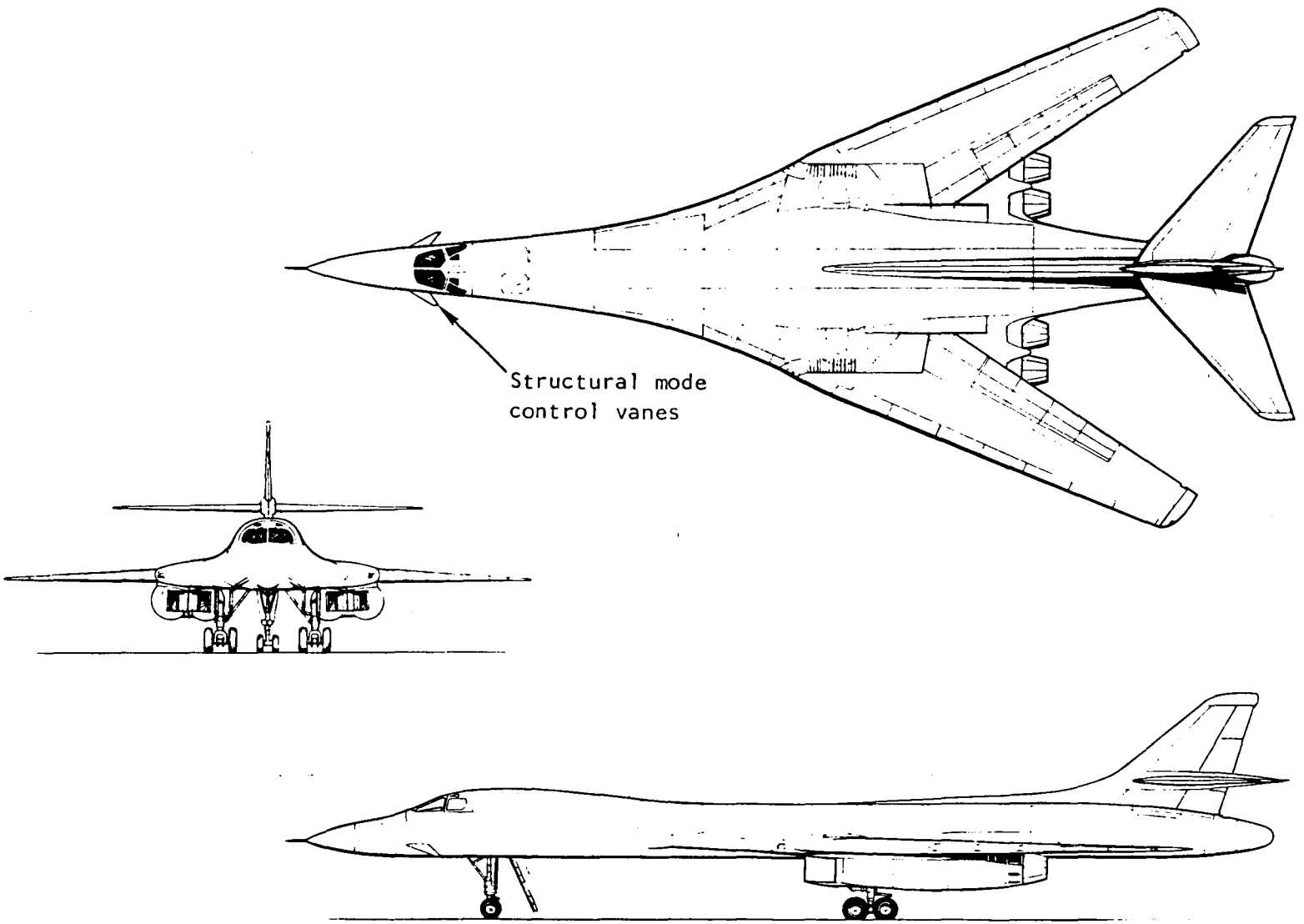

Figure 1. - B-1 aircraft with wings swept aft.

A substantial savings in weight was achieved with this approach as compared to direct material stiffening. The details of system requirements had to be determined from a production (long-life) point of view, which has not been done before for a system of this type. Extensive wind tunnel tests of the vane characteristics were conducted. Analytical models of the flexible aircraft and control systems were developed to analyze requirements and to investigate stability and performance. Component parts were tested to the requirements in the laboratory. Flight tests of the SMCS have been conducted, and comparisons with analytical predictions have been made. Because of all of this, it has been recognized that the B-1 offers an excellent opportunity for much needed further evaluation of such a system as the SMCS to insure the optimum use of these systems for future applications.

The overall objective of this research area is to compile and document information about the conceptual design, development, and flight tests of the B-1 SMCS and its impact on ride quality. Since the B-1 is the first aircraft to have a system such as the SMCS designed for production and long-service use, it is expected that the reports prepared will add to the technology base for design of future large military or civil aircraft. The specific overall objectives are to:

(1) Investigate the improvements in total dynamic response of a flexible aircraft and the potential benefits to ride qualities, handling qualities, crew efficiency, and reduced dynamic loads on the primary structures

(2) Evaluate the effectiveness and performance of the SMCS, which uses small aerodynamic surfaces at the vehicle nose to provide damping to the structural modes

The major effort of the phase 1 study (ref. 1) was to compile, edit, and prepare for publication as a NASA contractor report the existing information on the B-1 SMCS conceptual design and development. The major effort of the present phase II study is to report on the analyses and flight tests of the SMCS; existing information has been augmented by some additional limited analyses and flight-test data reductions.

FLEXIBLE AIRCRAFT EQUATIONS OF MOTION

The equations of motion of the flexible B-1 form the foundation of much that is to follow and so it is appropriate to discuss them first. The treatment of these equations is such that they are not developed herein from first principles. There are many textbooks that do this task; references 2 and 3 are typical of these. The equations, however, are presented in sufficient detail to be readily related to the textbook treatments. The equations of

motion of this section of the report were developed to serve the purposes of ride quality, terrain-following, and handling qualities evaluations; the equations of motion related to the loads analyses are discussed in a subsequent section. An attempt was made to include the main aircraft characteristics important to these several types of studies; however, as specific studies were conducted, minor modifications were often made. It is not intended to catalog all of these iterations; where important to the studies reported herein, they will be discussed.

The discussions touch upon the key features of these equations along with explanations of the form of the data where it is felt that this would be helpful. The authors have elected to stay away from matrix notation in these initial discussions in order to show as much information about the dynamic modeling as possible. The appendix contains a list of symbols used in defining the equations of motion of this section.

The equations of the motion in tables I, II, and III are written in a body axes system (figures 2 and 3) where the X-axis passes through the center of gravity and is parallel to the vehicle fuselage reference axis (FRL). To help those who are more familiar with stability axes notation, it should be observed that all of the aerodynamic coefficients but two appear the same in either the stability axes system or the body axes system. The two that are different are the normal force coefficient, C_N (body axes), versus lift coefficient, C_L (stability axes), and the chord force coefficient, C_C (body axes), and drag coefficient, C_D (stability axes). For small angles of attack, C_N nearly equals C_L and C_C nearly equals C_D.

All accelerations and velocities are defined positive as indicated in figure 2. One exception is noted relative to the definition of the vertical load factor. As a concession to stability and control and flight test convention, a positive load factor, n_z, is associated with a positive C_N. In contrast, the definition of Z-axis acceleration (consistent with the positive definitions of figure 2) is associated with a positive C_Z in figure 3 ($C_Z = -C_N$).

Ride quality analyses have been conducted on the simulator using time-domain equations while frequency-domain analyses have been conducted using digital computing equipment. The equations in the time domain are presented in table I and the frequency domain in tables II and III.

The structural flexibility of the air vehicle is defined in terms of free vibration modes of the structure (often referred to as normal modes). Figure 4 defines the sign conventions used in association with these normal

TABLE I. - GENERAL FLEXIBLE VEHICLE EQUATIONS OF MOTION, TIME DOMAIN
[Total Vehicle, Body Axes, Units: ft, lb, rad, sec]

FORCE EQUATIONS, RIGID-BODY MODES

$$\dot{V}_o = +\frac{T}{m} + V_o\dot{\alpha}\alpha + V_o\dot{\beta}\beta - V_o q\alpha + V_o r\beta - \left(\frac{q_o S_w}{m}\right)\left[C_{C_{(\alpha)}} + C_{C_{\delta_H}}\delta_H + C_{C_{\delta_{cv}}}\delta_{cv} + C_{C_{\delta_R}}\delta_R\right] - g\sin\Theta$$

$$\dot{\alpha} = +q - P\beta - \left(\frac{\dot{V}_o}{V_o}\right)\alpha - \left(\frac{T}{mV_o}\right)\sin\delta_T + \left(\frac{g}{V_o}\right)\cos\Theta\cos\Phi - \left(\frac{q_o S_w}{mV_o}\right)\left\{C_{N_{(\alpha)}} + C_{N_{\dot{\alpha}}}\left(\frac{\bar{c}_w}{2V_o}\right)\dot{\alpha} + C_{N_q}\left(\frac{\bar{c}_w}{2V_o}\right)q\right.$$
$$\left. + C_{N_{\dot{q}}}\left(\frac{\bar{c}_w}{2V_o}\right)^2\dot{q} + \sum_{i=1}^{n}\left[C_{N_{\eta_i}}\eta_i + C_{N_{\dot{\eta}_i}}\left(\frac{\dot{\eta}_i}{V_o}\right)\right] + C_{N_{\delta_H}}\delta_H + C_{N_{\dot{\delta}_H}}\dot{\delta}_H + C_{N_{\delta_{cv}}}\delta_{cv} + C_{N_{\dot{\delta}_{cv}}}\dot{\delta}_{cv} + C_{N_{\delta_R}}\delta_R + C_{N_{\dot{\delta}_R}}\dot{\delta}_R\right\}$$
$$- \left(\frac{m_H l_H}{mV_o}\right)\ddot{\delta}_H - \left(\frac{m_{cv} l_{cv}}{mV_o}\right)(\cos r)\ddot{\delta}_{cv} - \left(\frac{m_R l_R}{mV_o}\right)\ddot{\delta}_R - \left(\frac{q_o S_w}{mV_o}\right)\left[\left(C_{N_{w_g}}\right)^{TF} w_g\right]$$

$$\dot{\beta} = -r + P\alpha - \left(\frac{\dot{V}_o}{V_o}\right)\beta + \left(\frac{g}{V_o}\right)\cos\Theta\sin\Phi + \left(\frac{q_o S_w}{mV_o}\right)\left\{C_{Y_{\beta_{(\alpha)}}}\beta + C_{Y_{\dot{\beta}}}\left(\frac{b_w}{2V_o}\right)\dot{\beta} + C_{Y_r}\left(\frac{b_w}{2V_o}\right)r + C_{Y_{\dot{r}}}\left(\frac{b_w}{2V_o}\right)^2\dot{r}\right.$$
$$+ C_{Y_p}\left(\frac{b_w}{2V_o}\right)P + C_{Y_{\dot{p}}}\left(\frac{b_w}{2V_o}\right)^2\dot{P} + \sum_{\substack{i=1\\ \text{ANTISYMMETRIC}}}^{m}\left[C_{Y_{\eta_i}}\eta_i + C_{Y_{\dot{\eta}_i}}\left(\frac{\dot{\eta}_i}{V_o}\right)\right] + \sum_{\substack{i=1\\ \text{SYMMETRIC}}}^{n}\left(C_{Y_{\beta\eta_i}}\eta_i\right)\beta + C_{Y_{\delta_r}}\delta_r + C_{Y_{\dot{\delta}_r}}\dot{\delta}_r$$
$$\left. + C_{Y_{\delta'_H}}\delta'_H + C_{Y_{\dot{\delta}'_H}}\dot{\delta}'_H + C_{Y_{\delta_{cv}}}\delta_{cv} + C_{Y_{\dot{\delta}_{cv}}}\dot{\delta}_{cv} + C_{Y_{\delta_R}}\delta_R + C_{Y_{\dot{\delta}_R}}\dot{\delta}_R\right\} + \left(\frac{m_r l_r}{mV_o}\right)\ddot{\delta}_r + \left(\frac{m_{cv} l_{cv}}{mV_o}\right)(\sin r)\ddot{\delta}_{cv} + \left(\frac{m_R l_R}{mV_o}\right)\ddot{\delta}_R$$
$$+ \left(\frac{q_o S_w}{mV_o}\right)\left[\left(C_{Y_{w_g}}\right)^{TF} w_g\right]$$

TABLE I. - Continued

STRUCTURAL MODE EQUATIONS

Symmetric modes, i = 1 to n

$$\ddot{\eta}_i = -g_{s_i}\omega_i\dot{\eta}_i - \omega_i^2\eta_i + \left(\frac{q_o S_w}{M_i}\right)\Bigg\{C_{\eta_{i(\alpha)}} + C_{\eta_{i\dot{\alpha}}}\left(\frac{\bar{c}_w}{2V_o}\right)\dot{\alpha} + C_{\eta_{iq}}\left(\frac{\bar{c}_w}{2V_o}\right)q + C_{\eta_{i\dot{q}}}\left(\frac{\bar{c}_w}{2V_o}\right)^2\dot{q} + \sum_{j=1}^{n}\left[C_{\eta_i\eta_j}\eta_j + C_{\eta_i\dot{\eta}_j}\left(\frac{\dot{\eta}_j}{V_o}\right)\right]$$

$$+ C_{\eta_{i\delta_H}}\delta_H + C_{\eta_{i\dot{\delta}_H}}\dot{\delta}_H + C_{\eta_{i\delta_{cv}}}\delta_{cv} + C_{\eta_{i\dot{\delta}_{cv}}}\dot{\delta}_{cv} + C_{\eta_{i\delta_k}}\delta_k + C_{\eta_{i\dot{\delta}_k}}\dot{\delta}_k\Bigg\} - \left(\frac{\phi_i^H m_H l_H - \phi_i^{H'} I_{H_H}}{M_i}\right)\ddot{\delta}_H - \left(\frac{\phi_i^{cv} m_{cv} l_{cv} - \phi_i^{cv'} I_{cv_H}}{M_i}\right)(\cos\Gamma)\ddot{\delta}_c$$

$$- \left(\frac{\phi_i^k m_k l_k - \phi_i^{k'} I_{k_H}}{M_i}\right)\ddot{\delta}_k + \left(\phi_i^{\prime_{ENG.}}\frac{I_R\omega_R}{M_i}\right)r + \left(\frac{q_o S_w}{M_i}\right)\left[\left(C_{\eta_{i_{W_g}}}\right)^{TF} W_g\right]$$

Antisymmetric modes, i = 1 to m

$$\ddot{\eta}_i = -g_{s_i}\omega_i\dot{\eta}_i - \omega_i^2\eta_i + \left(\frac{q_o S_w}{M_i}\right)\Bigg\{C_{\eta_{i\beta_{(\alpha)}}}\beta + C_{\eta_{i\dot{\beta}}}\left(\frac{b_w}{2V_o}\right)\dot{\beta} + C_{\eta_{ir_{(\alpha)}}}\left(\frac{b_w}{2V_o}\right)r + C_{\eta_{i\dot{r}}}\left(\frac{b_w}{2V_o}\right)^2\dot{r} + C_{\eta_{iP_{(\alpha)}}}\left(\frac{b_w}{2V_o}\right)P$$

$$+ C_{\eta_{i\dot{P}}}\left(\frac{b_w}{2V_o}\right)^2\dot{P} + \sum_{j=1}^{m}\left[C_{\eta_i\eta_j}\eta_j + C_{\eta_i\dot{\eta}_j}\left(\frac{\dot{\eta}_j}{V_o}\right)\right] + \sum_{j=1}^{n}\left(C_{\eta_{i\beta}\eta_j}\eta_j\right)\beta + C_{\eta_{i\delta_r}}\delta_r + C_{\eta_{i\dot{\delta}_r}}\dot{\delta}_r + C_{\eta_{i\delta_H'}}\delta_H' + C_{\eta_{i\dot{\delta}_H'}}\dot{\delta}_H'$$

$$+ C_{\eta_{i\delta_{cv}}}\delta_{cv} + C_{\eta_{i\dot{\delta}_{cv}}}\dot{\delta}_{cv} + C_{\eta_{i\delta_k}}\delta_k + C_{\eta_{i\dot{\delta}_k}}\dot{\delta}_k\Bigg\} + \left(\frac{\phi_i^r m_r l_r - \phi_i^{r'} I_{r_H}}{M_i}\right)\ddot{\delta}_r + \left(\frac{\phi_i^H m_H l_H - \phi_i^{H'} I_{H_H}}{M_i}\right)\ddot{\delta}_H' + \Bigg\{\left(\frac{\phi_i^{cv} m_{cv} l_{cv} - \phi_i^{cv'} I_{cv_H}}{M_i}\right)$$

$$- \left(\frac{\phi_i^{cv^T} l_{cv}^T m_{cv} l_{cv}}{M_i}\right)\Bigg\}(\sin\Gamma)\ddot{\delta}_{cv} + \left(\frac{\phi_i^k m_k l_k - \phi_i^{k'} I_{k_H}}{M_i}\right)\ddot{\delta}_k + \left(\phi_i^{\prime_{ENG.}}\frac{I_R\omega_R}{M_i}\right)q + \left(\frac{q_o S_w}{M_i}\right)\left[\left(C_{\eta_{i_{V_g}}}\right)^{TF} V_g\right]$$

TABLE I. - Continued

MOMENT EQUATIONS, RIGID-BODY MODES

$$\dot{q} = +\left(\frac{I_{xz}}{I_y}\right)(r^2-p^2)+\left(\frac{I_z-I_x}{I_y}\right)pr-\left(\frac{I_R\omega_R}{I_y}\right)r+\left(\frac{\rho_o S_w \bar{c}_w}{I_y}\right)\Bigg\{C_{m_{(\alpha)}}+C_{m_{\dot{\alpha}}}\left(\frac{\bar{c}_w}{2V_o}\right)\dot{\alpha}+C_{m_q}\left(\frac{\bar{c}_w}{2V_o}\right)q+C_{m_{\dot{q}}}\left(\frac{\bar{c}_w}{2V_o}\right)^2\dot{q}$$
$$+\sum_{i=1}^{n}\left[C_{m_{\eta_i}}\eta_i+C_{m_{\dot{\eta}_i}}\left(\frac{\dot{\eta}_i}{V_o}\right)\right]+C_{m_{\delta_H}}\delta_H+C_{m_{\dot{\delta}_H}}\dot{\delta}_H+C_{m_{\delta_{cv}}}\delta_{cv}+C_{m_{\dot{\delta}_{cv}}}\dot{\delta}_{cv}+C_{m_{\delta_R}}\delta_R+C_{m_{\dot{\delta}_R}}\dot{\delta}_R\Bigg\}+\frac{l_T T}{I_y}$$
$$-\left(\frac{\bar{l}_H m_H l_H+I_{H_H}}{I_y}\right)\ddot{\delta}_H-\left(\frac{\bar{l}_{cv}m_{cv}l_{cv}+I_{cv_H}}{I_y}\right)(\cos r)\ddot{\delta}_{cv}-\left(\frac{\bar{l}_R m_R l_R+I_{R_H}}{I_y}\right)\ddot{\delta}_R+\left(\frac{\rho_o S_w \bar{c}_w}{I_y}\right)\left[\left(C_{m_{w_g}}\right)^{TF}w_g\right]$$

$$\dot{p} = +\left(\frac{I_{xz}}{I_x}\right)(\dot{r}+pq)-\left(\frac{I_z-I_y}{I_x}\right)qr+\left(\frac{\rho_o S_w b_w}{I_x}\right)\Bigg\{C_{l_{\beta_{(\alpha)}}}\beta+C_{l_{\dot{\beta}}}\left(\frac{b_w}{2V_o}\right)\dot{\beta}+C_{l_{r_{(\alpha)}}}\left(\frac{b_w}{2V_o}\right)r+C_{l_{\dot{r}}}\left(\frac{b_w}{2V_o}\right)^2\dot{r}+C_{l_p}\left(\frac{b_w}{2V_o}\right)p$$
$$+C_{l_{\dot{p}}}\left(\frac{b_w}{2V_o}\right)^2\dot{p}+\sum_{\substack{i=1\\ \text{ANTISYMMETRIC}}}^{m}\left[C_{l_{\eta_i}}\eta_i+C_{l_{\dot{\eta}_i}}\left(\frac{\dot{\eta}_i}{V_o}\right)\right]+\sum_{\substack{i=1\\ \text{SYMMETRIC}}}^{n}\left(C_{l_{\beta_{\eta_i}}}\eta_i\right)\beta+C_{l_{\delta_r}}\delta_r+C_{l_{\dot{\delta}_r}}\dot{\delta}_r+C_{l_{\delta_H'}}\delta_H'+C_{l_{\dot{\delta}_H'}}\dot{\delta}_H'+C_{l_{\delta_{cv}}}\delta_{cv}+C_{l_{\dot{\delta}_{cv}}}\dot{\delta}_{cv}$$
$$+C_{l_{\delta_R}}\delta_R+C_{l_{\dot{\delta}_R}}\dot{\delta}_R\Bigg\}+\left(\frac{l_r^T m_r l_r}{I_x}\right)\ddot{\delta}_r+\left(\frac{l_H^T m_H l_H}{I_x}\right)\ddot{\delta}_H'-\left(\frac{l_{cv}^T m_{cv} l_{cv}}{I_x}\right)\ddot{\delta}_{cv}+\left(\frac{l_R^T m_R l_R}{I_x}\right)\ddot{\delta}_R+\left(\frac{\rho_o S_w b_w}{I_x}\right)\left[\left(C_{l_{V_g}}\right)^{TF}V_g\right]$$

$$\dot{r} = +\left(\frac{I_{xz}}{I_z}\right)(\dot{p}-qr)-\left(\frac{I_y-I_x}{I_z}\right)pq+\left(\frac{I_R\omega_R}{I_z}\right)q+\left(\frac{\rho_o S_w b_w}{I_z}\right)\Bigg\{C_{n_{\beta_{(\alpha)}}}\beta+C_{n_{\dot{\beta}}}\left(\frac{b_w}{2V_o}\right)\dot{\beta}+C_{n_r}\left(\frac{b_w}{2V_o}\right)r+C_{n_{\dot{r}}}\left(\frac{b_w}{2V_o}\right)^2\dot{r}$$
$$+C_{n_{p_{(\alpha)}}}\left(\frac{b_w}{2V_o}\right)p+C_{n_{\dot{p}}}\left(\frac{b_w}{2V_o}\right)^2\dot{p}+\sum_{\substack{i=1\\ \text{ANTISYMMETRIC}}}^{m}\left[C_{n_{\eta_i}}\eta_i+C_{n_{\dot{\eta}_i}}\left(\frac{\dot{\eta}_i}{V_o}\right)\right]+\sum_{\substack{i=1\\ \text{SYMMETRIC}}}^{n}\left(C_{n_{\beta_{\eta_i}}}\eta_i\right)\beta+C_{n_{\delta_r}}\delta_r+C_{n_{\dot{\delta}_r}}\dot{\delta}_r+C_{n_{\delta_H'}}\delta_H'+C_{n_{\dot{\delta}_H'}}\dot{\delta}_H'$$
$$+C_{n_{\delta_{cv}}}\delta_{cv}+C_{n_{\dot{\delta}_{cv}}}\dot{\delta}_{cv}+C_{n_{\delta_R}}\delta_R+C_{n_{\dot{\delta}_R}}\dot{\delta}_R\Bigg\}-\left(\frac{\bar{l}_r m_r l_r+I_{r_H}}{I_z}\right)\ddot{\delta}_r-\left(\frac{\bar{l}_{cv}m_{cv}l_{cv}+I_{cv_H}}{I_z}\right)(\sin r)\ddot{\delta}_{cv}-\left(\frac{\bar{l}_R m_R l_R+I_{R_H}}{I_z}\right)\ddot{\delta}_R+\left(\frac{\rho_o S_w b_w}{I_z}\right)\left[\left(C_{n_{V_g}}\right)^{TF}V_g\right]$$

TABLE I. - Continued

LOAD-FACTOR EQUATIONS (ACCELEROMETER READINGS)

$$n_z = \left(\frac{V_o}{g}\right)\left(q - \dot{\alpha} - p\beta - \left(\frac{\dot{V}_o}{V_o}\right)\alpha\right) + \left(\frac{l_x}{g}\right)\left(\dot{q} - rp\right) - \left(\frac{l_y}{g}\right)\left(\dot{p} + qr\right) + \left(\frac{l_z}{g}\right)\left(p^2 + q^2\right) - \sum_{i=1}^{n}\left(\frac{\phi_i}{g}\right)^{x,y}\ddot{\eta}_i + (\cos\Theta\cos\Phi - 1)$$

[FROM 1g TRIM AT ANY STATION X,Y,Z]

n_z IS + IN THE SAME DIRECTION AS + C_N

$$n_y = \left(\frac{V_o}{g}\right)\left(\dot{\beta} + r - p\alpha + \left(\frac{\dot{V}_o}{V_o}\right)\beta\right) + \left(\frac{l_x}{g}\right)\left(\dot{r} + pq\right) - \left(\frac{l_y}{g}\right)\left(r^2 + p^2\right) - \left(\frac{l_z}{g}\right)\left(\dot{p} - qr\right) + \sum_{i=1}^{m}\left(\frac{\phi_i}{g}\right)^{x,y,z}\ddot{\eta}_i - \cos\Theta\sin\Phi$$

[AT ANY STATION X,Y,Z]

n_y IS + IN THE SAME DIRECTION AS + C_y

ROTARY-RATE EQUATIONS (RATE GYRO READINGS)

$$\underset{\left[\begin{smallmatrix}\text{AT ANY}\\ \text{STATION X,Y}\end{smallmatrix}\right]}{q} = q - \sum_{i=1}^{n}\phi_i'^{x,y}\dot{\eta}_i \quad \text{(SYMMETRIC MODES)}$$

$$\underset{\left[\begin{smallmatrix}\text{AT ANY}\\ \text{STATION X,Y,Z}\end{smallmatrix}\right]}{p} = p + \sum_{i=1}^{m}\phi_i'^{x,y,z}\dot{\eta}_i \quad \text{(ANTISYMMETRIC MODES)}$$

$$\underset{\left[\begin{smallmatrix}\text{AT ANY}\\ \text{STATION X,Y,Z}\end{smallmatrix}\right]}{r} = r + \sum_{i=1}^{m}\phi'^{x,y,z}\dot{\eta}_i \quad \text{(ANTISYMMETRIC MODES)}$$

TABLE I. - Concluded

EULER ANGLES

$$\dot{\Theta} = q\cos\Phi - r\sin\Phi \qquad \dot{\Phi} = P + \dot{\psi}\sin\Theta \qquad \dot{\psi} = \frac{r\cos\Phi + q\sin\Phi}{\cos\Theta}$$

EARTH-AXES VELOCITIES

$$V_{x_e} = V_x\cos\Theta\cos\psi + V_y(\sin\Phi\sin\Theta\cos\psi - \cos\Phi\sin\psi) + V_z(\cos\Phi\sin\Theta\cos\psi + \sin\Phi\sin\psi)$$

$$V_{y_e} = V_x\cos\Theta\sin\psi + V_y(\cos\Phi\cos\psi + \sin\Phi\sin\Theta\sin\psi) + V_z(\cos\Phi\sin\Theta\sin\psi - \sin\Phi\cos\psi)$$

$$V_{z_e} = -V_x\sin\Theta + V_y\sin\Phi\cos\Theta + V_z\cos\Phi\cos\Theta$$

A convenient equivalent expression for V_{z_e} is in terms of altitude rate of change and α and β.

$$\dot{h} = V_a(\sin\Theta\cos\alpha\cos\beta - \cos\Theta\sin\Phi\sin\beta - \cos\Theta\cos\Phi\cos\beta\sin\alpha)$$

TABLE II. - EQUATIONS OF MOTION FOR LONGITUDINAL RIGID-BODY AND SYMMETRIC STRUCTURAL MODES, FREQUENCY DOMAIN

[Total Vehicle, Body Axes, Units: ft, lb, rad, sec]

NORMAL-FORCE EQUATION, RIGID-BODY MODE

$$+i\left(\frac{\omega}{K_\alpha}\right)\alpha - \frac{q}{K_\alpha} + \left[C_{N_\alpha} + i\omega C_{N_{\dot\alpha}}\left(\frac{\bar c_w}{2V_o}\right)\right]\alpha + \left[C_{N_q}\left(\frac{\bar c_w}{2V_o}\right) + i\omega C_{N_{\dot q}}\left(\frac{\bar c_w}{2V_o}\right)^2\right]q + \left[\left(C_{N_{\delta_H}}\right)_R + i\left(C_{N_{\delta_H}}\right)_I\right]\delta_H$$

$$+ \left[\left(C_{N_{\delta_{cv}}}\right)_R + i\left(C_{N_{\delta_{cv}}}\right)_I\right]\delta_{cv} + \left[\left(C_{N_{\delta_k}}\right)_R + i\left(C_{N_{\delta_k}}\right)_I\right]\delta_k + \sum_{i=1}^{n}\left[C_{N_{\eta_i}} + i\left(\frac{\omega}{V_o}\right)C_{N_{\dot\eta_i}}\right]\eta_i - \omega^2\left(\frac{m_H l_H}{g_o S_w}\right)\delta_H$$

$$- \omega^2\left(\frac{m_{cv} l_{cv}}{g_o S_w}\right)(\cos r)\delta_{cv} - \omega^2\left(\frac{m_k l_k}{g_o S_w}\right)\delta_k = -\left[\left(C_{N_{w_g}}\right)_R + i\left(C_{N_{w_g}}\right)_I\right]w_g$$

PITCHING-MOMENT EQUATION, RIGID-BODY MODES

$$-i\left(\frac{\omega}{K_q}\right)q + \left[C_{m_\alpha} + i\omega C_{m_{\dot\alpha}}\left(\frac{\bar c_w}{2V_o}\right)\right]\alpha + \left[C_{m_q}\left(\frac{\bar c_w}{2V_o}\right) + i\omega C_{m_{\dot q}}\left(\frac{\bar c_w}{2V_o}\right)^2\right]q + \left[\left(C_{m_{\delta_H}}\right)_R + i\left(C_{m_{\delta_H}}\right)_I\right]\delta_H$$

$$+ \left[\left(C_{m_{\delta_{cv}}}\right)_R + i\left(C_{m_{\delta_{cv}}}\right)_I\right]\delta_{cv} + \left[\left(C_{m_{\delta_k}}\right)_R + i\left(C_{m_{\delta_k}}\right)_I\right]\delta_k + \sum_{i=1}^{n}\left[C_{m_{\eta_i}} + i\left(\frac{\omega}{V_o}\right)C_{m_{\dot\eta_i}}\right]\eta_i + \omega^2\left(\frac{\bar l_H m_H l_H + I_{H_H}}{g_o S_w \bar c_w}\right)\delta_H$$

$$+ \omega^2\left(\frac{\bar l_{cv} m_{cv} l_{cv} + I_{cv_H}}{g_o S_w \bar c_w}\right)(\cos r)\delta_{cv} + \omega^2\left(\frac{\bar l_k m_k l_k + I_{k_H}}{g_o S_w \bar c_w}\right)\delta_k = -\left[\left(C_{m_{w_g}}\right)_R + i\left(C_{m_{w_g}}\right)_I\right]w_g$$

TABLE II. - Concluded

SYMMETRIC STRUCTURAL MODE EQUATION, i = 1 to n

$$+\left(\frac{\omega^2}{K\eta_i}\right)\eta_i - i\omega\left(\frac{g_{s_i}\omega_i^2}{\omega K\eta_i}\right)\eta_i - \left(\frac{\omega_i^2}{K\eta_i}\right)\eta_i + \left[C_{\eta_{i\alpha}} + i\omega C_{\eta_{i\dot{\alpha}}}\left(\frac{\bar{c}_w}{2V_o}\right)\right]\alpha + \left[C_{\eta_{iq}}\left(\frac{\bar{c}_w}{2V_o}\right) + i\omega C_{\eta_{i\dot{q}}}\left(\frac{\bar{c}_w}{2V_o}\right)^2\right]q + \left[\left(C_{\eta_{i\delta_{H_R}}}\right) + i\left(C_{\eta_{i\delta_{H_I}}}\right)\right]\delta_H$$

$$+\left[\left(C_{\eta_{i\delta_{cv}}}\right)_R + i\left(C_{\eta_{i\delta_{cv}}}\right)_I\right]\delta_{cv} + \left[\left(C_{\eta_{i\delta_k}}\right) + i\left(C_{\eta_{i\delta_k}}\right)\right]\delta_k + \sum_{j=1}^{n}\left[C_{\eta_i\eta_j} + i\left(\frac{\omega}{V_o}\right)C_{\eta_i\dot{\eta}_j}\right]\eta_j + \omega^2\left(\frac{\phi_i^H m_H l_H - \phi_i^{H'} I_{H_H}}{q_o S_w}\right)\delta_H$$

$$+\omega^2\left(\frac{\phi_i^{cv} m_{cv} l_{cv} - \phi_i^{cv'} I_{cv_H}}{q_o S_w}\right)(\cos\Gamma)\delta_{cv} + \omega^2\left(\frac{\phi_i^k m_k l_k - \phi_i^{k'} I_{k_H}}{q_o S_w}\right)\delta_k = -\left[\left(C_{\eta_{iw_g}}\right)_R + i\left(C_{\eta_{iw_g}}\right)_I\right]w_g$$

NORMAL LOAD FACTOR (INCREMENT FROM 1 g TRIM) (no lateral perturbations

$$n_{z_{\left[\text{AT ANY STATION } x,y,z\right]}} = \left(\frac{V_o}{g}\right)(q - i\omega\alpha) + i\omega\left(\frac{l_x}{g}\right)q + \left(\frac{l_z}{g}\right)q^2 + \sum_{i=1}^{n}\omega^2\left(\frac{\phi_i^{x,y}}{g}\right)\eta_i$$

Note: The variables are complex in form but have been written as α, q, η_i, δ_k, and w_g as a space-saving notation.
$[(\ )_{()_R} + i\ (\ )_{()_I}]$ represents real and imaginary parts of unsteady aerodynamics coefficient form.
These equations represent perturbations from a 1 g trimmed flight condition.

TABLE III. - EQUATIONS OF MOTION FOR LATERAL-DIRECTIONAL, RIGID-BODY, AND ANTISYMMETRIC STRUCTURAL MODES, FREQUENCY DOMAIN

[Total Vehicle, Body Axes, Units: ft, lb, rad, sec]

SIDE-FORCE EQUATION, RIGID-BODY MODE

$$-i\left(\frac{\omega}{K_\beta}\right)\beta-\left(\frac{r}{K_\beta}\right)+\left(\frac{P}{\alpha}\right)\alpha_o-i\left(\frac{W}{q_o S_w}\right)\cos\Theta_o\left(\frac{P}{\omega}\right)+\left[C_{Y_\beta}+i\omega C_{Y_{\dot\beta}}\left(\frac{b_w}{2V_o}\right)\right]\beta+\left[C_{Y_r}\left(\frac{b_w}{2V_o}\right)+i\omega C_{Y_{\dot r}}\left(\frac{b_w}{2V_o}\right)^2\right]r+\left[C_{Y_p}\left(\frac{b_w}{2V_o}\right)+i\omega C_{Y_{\dot p}}\left(\frac{b_w}{2V_o}\right)^2\right]P$$

$$+\left[\left(C_{Y_{\delta_r}}\right)_R+i\left(C_{Y_{\delta_r}}\right)_I\right]\delta_r+\left[\left(C_{Y_{\delta'_H}}\right)_R+i\left(C_{Y_{\delta'_H}}\right)_I\right]\delta'_H+\left[\left(C_{Y_{\delta_{cv}}}\right)_R+i\left(C_{Y_{\delta_{cv}}}\right)_I\right]\delta_{cv}+\left[\left(C_{Y_{\delta_k}}\right)_R+i\left(C_{Y_{\delta_k}}\right)_I\right]\delta_k+\sum_{i=1}^{m}\left[C_{Y_{\eta_i}}+i\left(\frac{\omega}{V_o}\right)C_{Y_{\dot\eta_i}}\right]\eta_i$$

$$-\omega^2\left(\frac{m_r l_r}{q_o S_w}\right)\delta_r-\omega^2\left(\frac{m_{cv} l_{cv}}{q_o S_w}\right)(\sin\Gamma)\delta_{cv}-\omega^2\left(\frac{m_k l_k}{q_o S_w}\right)\delta_k=-\left[\left(C_{Y_{V_g}}\right)_R+i\left(C_{Y_{V_g}}\right)_I\right]V_g$$

YAWING-MOMENT EQUATION, RIGID-BODY MODE

$$-i\left(\frac{\omega}{K_r}\right)r+i\left(\frac{\omega I_{xz}}{K_r I_z}\right)P+\left[C_{n_\beta}+i\omega C_{n_{\dot\beta}}\left(\frac{b_w}{2V_o}\right)\right]\beta+\left[C_{n_r}\left(\frac{b_w}{2V_o}\right)+i\omega C_{n_{\dot r}}\left(\frac{b_w}{2V_o}\right)^2\right]r+\left[C_{n_p}\left(\frac{b_w}{2V_o}\right)+i\omega C_{n_{\dot p}}\left(\frac{b_w}{2V_o}\right)^2\right]P$$

$$+\left[\left(C_{n_{\delta_r}}\right)_R+i\left(C_{n_{\delta_r}}\right)_I\right]\delta_r+\left[\left(C_{n_{\delta'_H}}\right)_R+i\left(C_{n_{\delta'_H}}\right)_I\right]\delta'_H+\left[\left(C_{n_{\delta_{cv}}}\right)_R+i\left(C_{n_{\delta_{cv}}}\right)_I\right]\delta_{cv}+\left[\left(C_{n_{\delta_k}}\right)_R+i\left(C_{n_{\delta_k}}\right)_I\right]\delta_k$$

$$+\sum_{i=1}^{m}\left[C_{n_{\eta_i}}+i\left(\frac{\omega}{V_o}\right)C_{n_{\dot\eta_i}}\right]\eta_i+\omega^2\left(\frac{\bar l_r m_r l_r+I_{r_H}}{q_o S_w b_w}\right)\delta_r+\omega^2\left(\frac{\bar l_{cv} m_{cv} l_{cv}+I_{cv_H}}{q_o S_w b_w}\right)(\sin\Gamma)\delta_{cv}+\omega^2\left(\frac{\bar l_k m_k l_k+I_{k_H}}{q_o S_w b_w}\right)\delta_k$$

$$=-\left[\left(C_{n_{V_g}}\right)_R+i\left(C_{n_{V_g}}\right)_I\right]V_g$$

TABLE III. - Continued

ROLLING-MOMENT EQUATION, RIGID-BODY MODE

$$-i\left(\frac{\omega}{K_P}\right)P + i\left(\frac{\omega I_{xz}}{K_P I_x}\right)r + \left[C_{l_\beta} + i\omega C_{l_{\dot\beta}}\left(\frac{b_w}{2V_0}\right)\right]\beta + \left[C_{l_r}\left(\frac{b_w}{2V_0}\right) + i\omega C_{l_{\dot r}}\left(\frac{b_w}{2V_0}\right)^2\right]r + \left[C_{l_P}\left(\frac{b_w}{2V_0}\right) + i\omega C_{l_{\dot P}}\left(\frac{b_w}{2V_0}\right)^2\right]P + \left[\left(C_{l_{\delta_r}}\right)_R + i\left(C_{l_{\delta_r}}\right)_I\right]\delta_r$$

$$+ \left[\left(C_{l_{\delta_H'}}\right)_R + i\left(C_{l_{\delta_H'}}\right)_I\right]\delta_H' + \left[\left(C_{l_{\delta_{cv}}}\right)_R + i\left(C_{l_{\delta_{cv}}}\right)_I\right]\delta_{cv} + \left[\left(C_{l_{\delta_k}}\right)_R + i\left(C_{l_{\delta_k}}\right)_I\right]\delta_k + \sum_{i=1}^{m}\left[C_{l_{\eta_i}} + i\left(\frac{\omega}{V_0}\right)C_{l_{\dot\eta_i}}\right]\eta_i - \omega^2\left(\frac{\bar l_r m_r l_r}{\rho_0 S_w b_w}\right)\delta_r$$

$$- \omega^2\left(\frac{l_H^T m_H l_H}{\rho_0 S_w b_w}\right)\delta_H' + \omega^2\left(\frac{l_{cv}^T m_{cv} l_{cv}}{\rho_0 S_w b_w}\right)\delta_{cv} - \omega^2\left(\frac{l_k^T m_k l_k}{\rho_0 S_w b_w}\right)\delta_k = -\left[\left(C_{l_{v_g}}\right)_R + i\left(C_{l_{v_g}}\right)_I\right]V_g$$

ANTISYMMETRIC STRUCTURAL MODE EQUATION, i = 1 to m

$$+\left(\frac{\omega^2}{K_{\eta_i}}\right)\eta_i - i\omega\left(\frac{g_{s_i}\omega_i^2}{\omega K_{\eta_i}}\right)\eta_i - \left(\frac{\omega_i^2}{K_{\eta_i}}\right)\eta_i + \left[C_{\eta_{i_\beta}} + i\omega C_{\eta_{i_{\dot\beta}}}\left(\frac{b_w}{2V_0}\right)\right]\beta + \left[C_{\eta_{i_r}}\left(\frac{b_w}{2V_0}\right) + i\omega C_{\eta_{i_{\dot r}}}\left(\frac{b_w}{2V_0}\right)^2\right]r + \left[C_{\eta_{i_P}}\left(\frac{b_w}{2V_0}\right) + i\omega C_{\eta_{i_{\dot P}}}\left(\frac{b_w}{2V_0}\right)^2\right]P$$

$$+ \left[\left(C_{\eta_{i_{\delta_r}}}\right)_R + i\left(C_{\eta_{i_{\delta_r}}}\right)_I\right]\delta_r + \left[\left(C_{\eta_{i_{\delta_H'}}}\right)_R + i\left(C_{\eta_{i_{\delta_H'}}}\right)_I\right]\delta_H' + \left[\left(C_{\eta_{i_{\delta_{cv}}}}\right)_R + i\left(C_{\eta_{i_{\delta_{cv}}}}\right)_I\right]\delta_{cv} + \left[\left(C_{\eta_{i_{\delta_k}}}\right)_R + i\left(C_{\eta_{i_{\delta_k}}}\right)_I\right]\delta_k + \sum_{j=1}^{m}\left[C_{\eta_{i_j}} + i\left(\frac{\omega}{V_0}\right)C_{\eta_{i_{\dot\eta_j}}}\right]\eta_i$$

$$- \omega^2\left(\frac{\Phi_i^r m_r l_r - \Phi_i^{r'} I_{r_H}}{\rho_0 S_w}\right)\delta_r - \omega^2\left(\frac{\Phi_i^H m_H l_H - \Phi_i^{H'} I_{H_H}}{\rho_0 S_w}\right)\delta_H' - \omega^2\left\{\left(\frac{\Phi_i^{cv} m_{cv} l_{cv} - \Phi_i^{cv'} I_{cv_H}}{\rho_0 S_w}\right) - \left(\frac{\Phi_i^{cvT} l_{cv}^T m_{cv} l_{cv}}{\rho_0 S_w}\right)\right\}(\sin\Gamma)\,\delta_{cv}$$

$$- \omega^2\left(\frac{\Phi_i^k m_k l_k - \Phi_i^{k'} I_{k_H}}{\rho_0 S_w}\right)\delta_k = -\left[\left(C_{\eta_{i_{v_g}}}\right)_R + i\left(C_{\eta_{i_{v_g}}}\right)_I\right]V_g$$

TABLE III. - Concluded

LATERAL LOAD FACTOR

$$n_{y_{\left[\begin{smallmatrix}\text{AT ANY}\\ \text{STATION } x,y,z\end{smallmatrix}\right]}} = \left(\frac{V_o}{g}\right)\left(i\omega\beta + r - p\alpha_o\right) + i\cos\Theta_o\left(\frac{p}{\omega}\right) + i\omega\left(\frac{l_x}{g}\right)r - \left(\frac{l_y}{g}\right)\left(r^2+p^2\right) - i\omega\left(\frac{l_z}{g}\right)p - \sum_{i=1}^{m}\left(\frac{\phi_i^{x,y,z}}{g}\right)\omega^2\eta_i$$

Note: The variables are complex in form but have been written as β, r, p, η_i, δ_k, and Vg as a space-saving notation. $[(\,)_R + i\,(\,)_I]$ represents real and imaginary parts of unsteady aerodynamics in coefficient form. These equations represent perturbations from 1 g trimmed flight conditions.

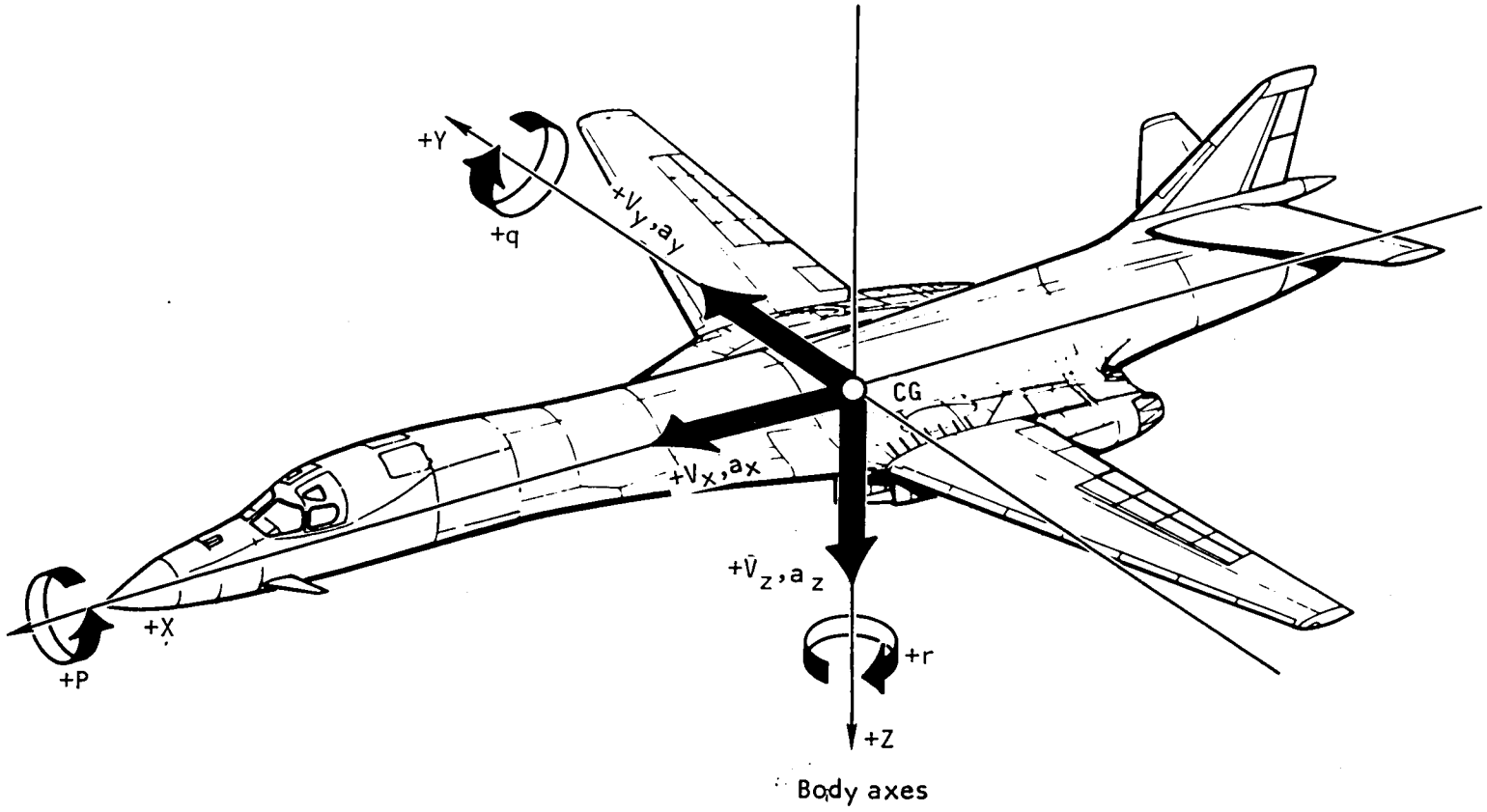

Figure 2. - Sign convention for rotational and linear rates and accelerations.

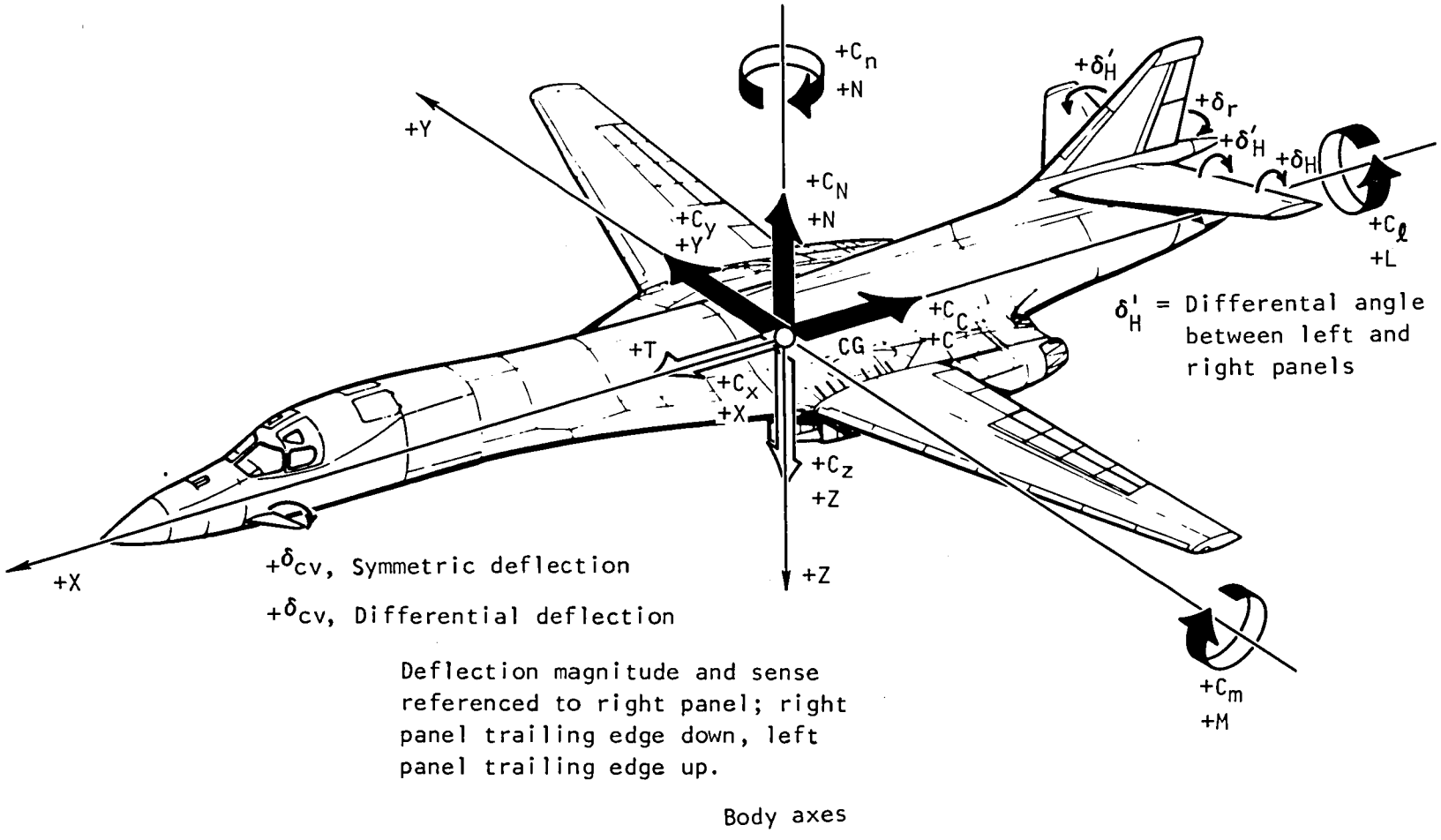

Figure 3. - Sign convention for coefficients and control surface deflections.

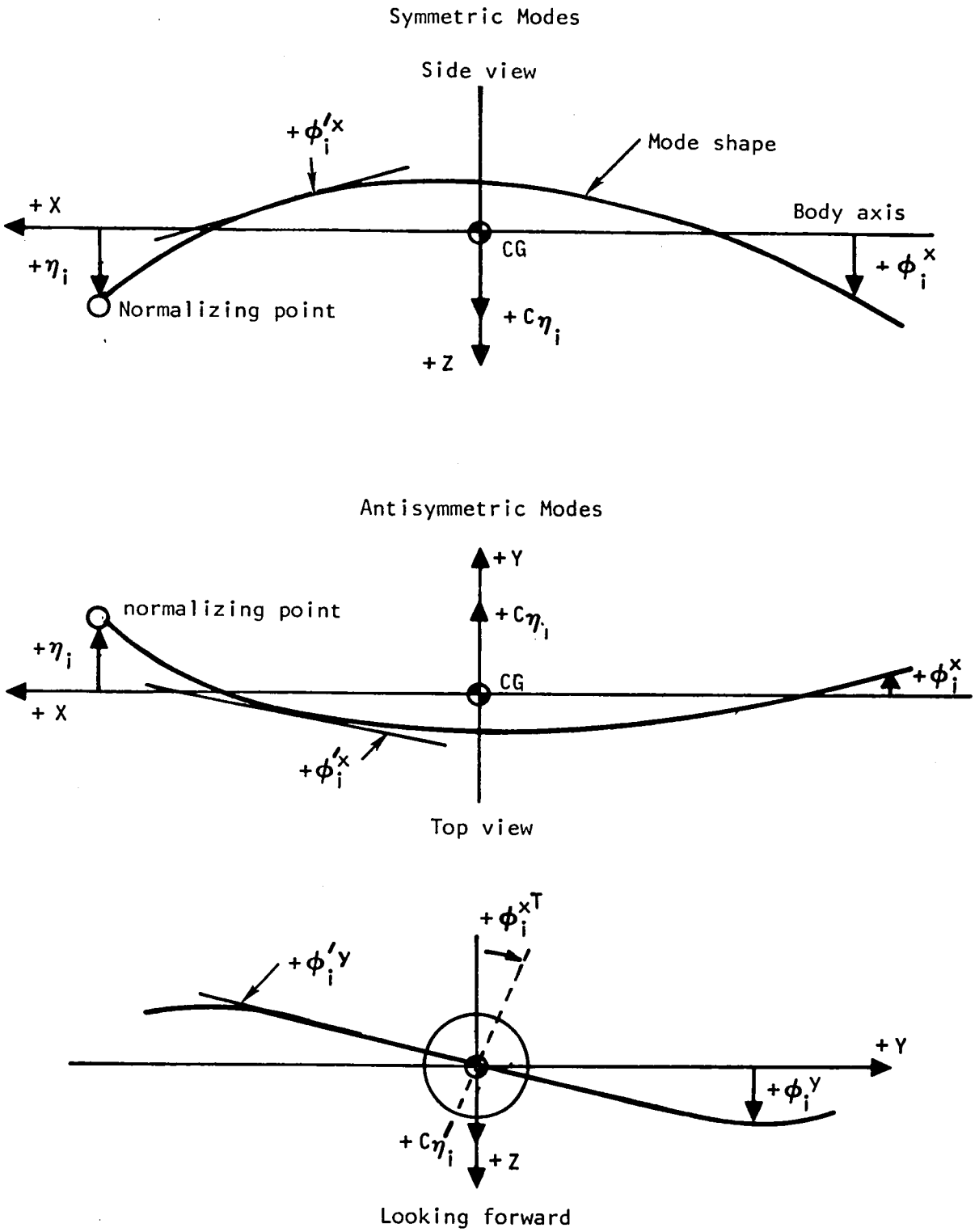

Figure 4. - Structural mode deflections, slopes, and generalized forces sign convention.

modes. There are a number of advantages to using the modal approach in contrast to the direct-influence coefficient approach for such studies as referred to herein.

(1) It can describe the static as well as dynamic characteristics of the flexible vehicle in a consistent manner within the same format.

(2) Both inertia and aerodynamic loadings are accounted for in the modal generalized force data for both the static and dynamic cases.

(3) The modal data are amenable to a number of simplification schemes.

(4) The approach integrates best with control system design requirements in the handling and ride qualities design areas.

Consider first, the most extensively detailed equations of motion in the time domain as described in table I. These equations need be used in this detailed form shown only when large-scale maneuvering is studied as in the terrain-following problem. More simplified equations will serve other analyses purposes.

These equations were developed assuming that the angles of attack, α, and sideslip angles, β, (figure 5), would be small (less than 10 degrees), but the vehicle orientation in space as defined by the Euler angles Ψ, Θ, and Φ (figure 6) would be unrestricted (except for $\Theta = 90$ degrees).

Aerodynamic data indicated are preliminary estimates of those required. These data are shown in derivative form except where it is anticipated nonlinear characteristics with α, β, or control deflection occur. As an example, the normal force curve was expected to be nonlinear with α so the normal force coefficient is expressed as $C_N(\alpha)$ instead of the more familiar linear form C_{N_α}.

The control surfaces explicitly shown are those anticipated being required by either the Stability and Control Augmentation System (SCAS) or SMCS. Other control-surface inputs are shown in general form as functions of δ_k for the k^{th} surface.

Because of the requirement to control structural motion at the frequencies of the lower free-vibration modes, it is necessary to consider unsteady aerodynamic effects of the control motion as well as the inertia reaction forces of these surfaces. In the normal force-equation format of table I, the unsteady aerodynamics are shown by the notion $C_{N_{\delta_k}}\delta_k + C_{N_{\dot{\delta}_k}}\dot{\delta}_k$ for the k^{th}

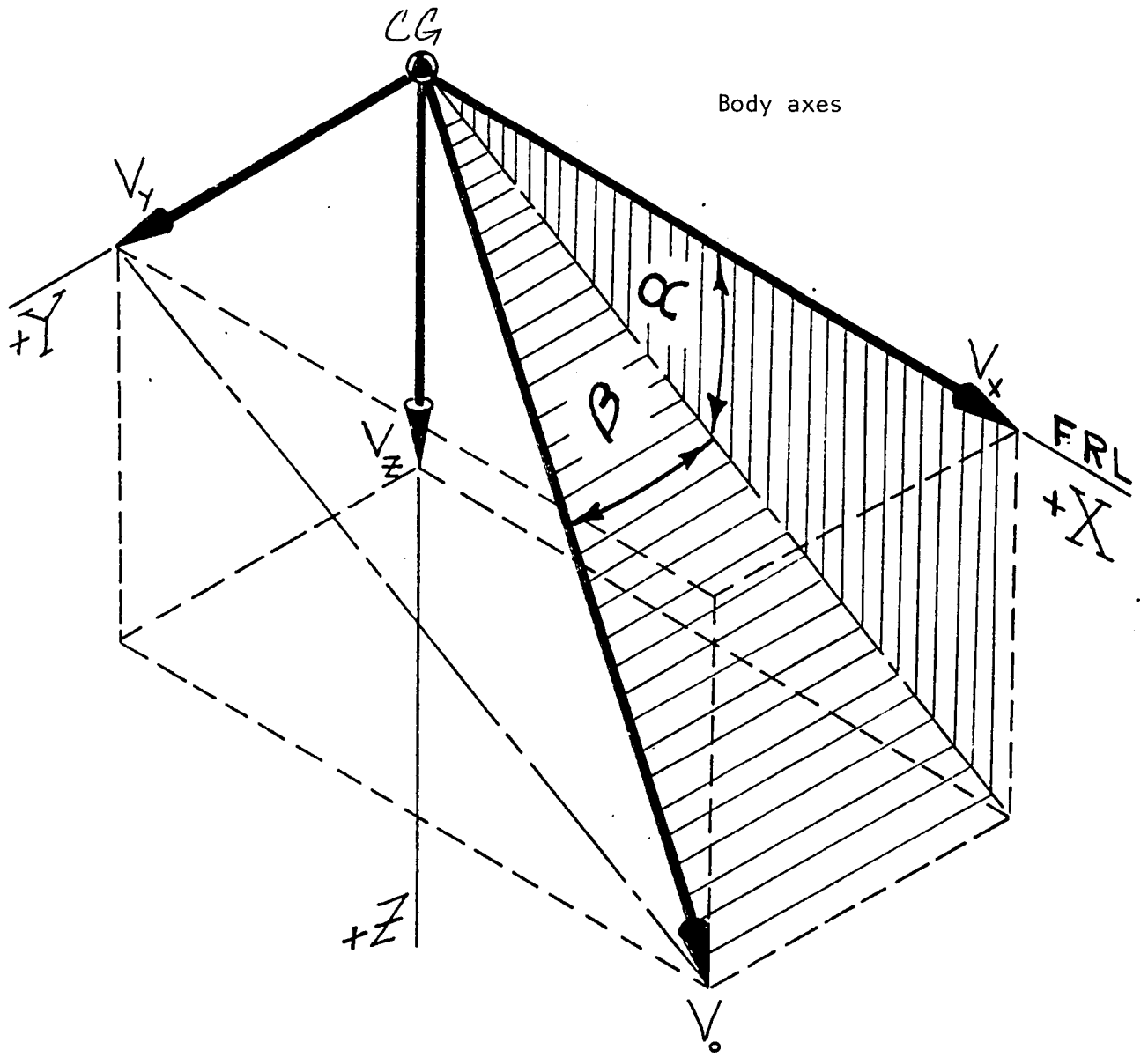

$$V_x = V_o \cos\beta \cos\alpha$$
$$V_y = V_o \sin\beta$$
$$V_z = V_o \cos\beta \sin\alpha$$

$$\alpha = \sin^{-1} \frac{V_z}{V_o \cos\beta} \qquad \beta = \sin^{-1} \frac{V_y}{V_o}$$

Figure 5. - Angle-of-attack (α) and sideslip (β) definitions.

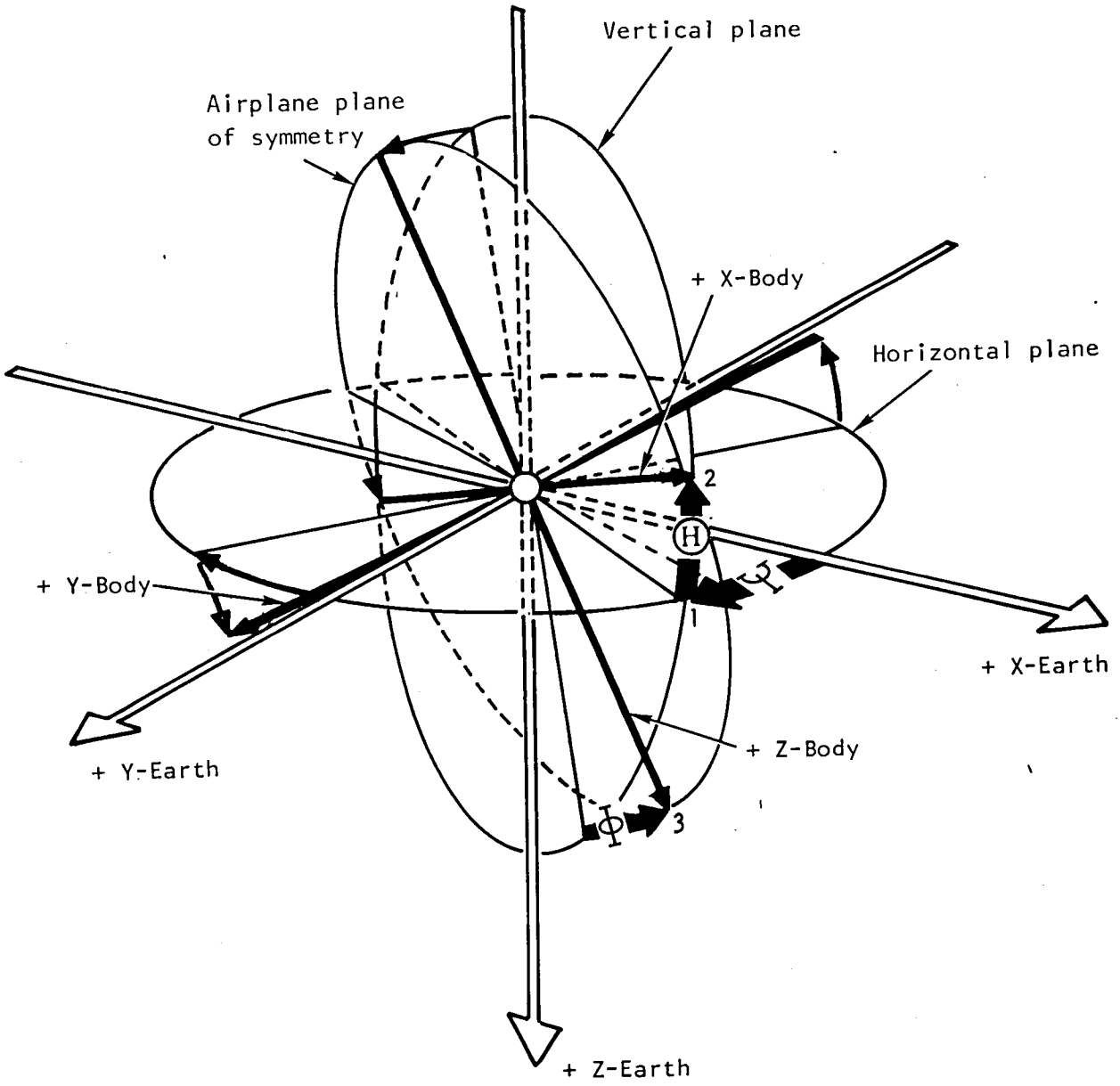

Rotation sequence indicated by numbers at arrow heads

Figure 6. Euler angle definitions and rotation sequence.

control surface. The control-surface inertia reaction force in this equation has the form $(m_k \ell_k) \ddot{\delta}_k$. Similar aerodynamic and inertia reaction-force terms may be recognized in the moment and structural mode equations.

Terms in table I involving $\dot{q}$, $\dot{\beta}$, $\dot{r}$, and $\dot{p}$ are generally of small consequence but have been included to be consistent with the frequency-domain equations of tables II and III where unsteady aerodynamics must be considered. The desirability of this consistency will become apparent as these equations are discussed in subsequent paragraphs.

The B-1 engine gyroscopic moments, $I_R \omega_R r$ and $I_R \omega_R q$, shown in the equations have not proved to be significant in handling qualities or terrain-following studies. It had been anticipated that they might have been significant in large-scale maneuvering. They have, however, been left in the equations of table I.

The equations of table I include the ability to change speed. It is assumed that if significant changes in Mach numbers are to be realized, these changes will be reflected in the appropriate use of Mach carpet data for the aerodynamics required. Velocity changes will show up directly in V_o, while combined altitude-velocity changes will appear indirectly in q_o, $(1/2\ \rho V_o^2)$.

The gust representation shown in table I is in the aerodynamic transfer-function form. The gust excitation, w_g and v_g, would come from random signal generation sources, shaped and scaled to reflect the desired gust power spectral density and intensity.

The longitudinal and lateral-directional rigid-body motions are coupled during large-scale maneuvers through the inertia terms and engine gyroscopic effects. The symmetric and antisymmetric structural mode motions are coupled by terms representing the dihedral effect due to symmetric wing bending. For small motions about a trim condition, the rigid-body mode equations can be decoupled through elimination of the inertia and gyroscopic coupling. The structural mode equations can be decoupled by using trimmed airplane static symmetric structural response parameters at fixed values to determine the effective dihedral due to symmetric wing bending.

The load factor and rotation rates of the large-scale maneuvering flexible air vehicle (as read by accelerometers and gyros mounted on the fuselage structure) are presented in table I.

Euler angle equations and earth axis velocities are given in table I and can be used in terrain-following studies to determine the vehicle attitude and location with respect to the earth's surface.

The frequency-domain equations of motion for the flexible airplane are given in table II for the longitudinal-symmetric case and table III for the lateral-directional-antisymmetric case. These equations are uncoupled and represent motion perturbations from wing-level 1 g trimmed flight. Comparison of these frequency-domain equations with the uncoupled time-domain equations will help in identifying equivalent terms.

As shown, the vehicle response aerodynamics (that is derivatives associated with response parameters such as α, $\dot{\alpha}$, q, $\dot{q}$) are quasisteady while the control surfaces and the gust are shown as functions of the forcing frequency in the form $[(\ )_R + i\ (\ )_I]$. This format has been convenient and sufficiently accurate for preliminary ride qualities and structural-mode control analyses. Digital programs are available at Rockwell; however, that will also accept vehicle response aerodynamics from unsteady aerodynamic theories as a function of frequency, permitting more refined ride quality and SMCS stability analyses.

The equation describing the normal load-factor response at any location in the flexible aircraft is presented in table II. The similar equation for the lateral load factor is given in table III. These responses are used in ride quality analyses.

FLEXIBLE AIRCRAFT ANALYSES MODEL

This section describes how the data were obtained to implement the flexible aircraft equations of motion used for ride quality analyses. It will not be the purpose of this presentation to provide a complete set of data used in all analyses discussed; but it will be the intent to provide understanding of the data used.

DYNAMIC ANALYSIS SYSTEM

As a basis of understanding the contents of this section better, as well as topics of other sections, the chart of figure 7 is presented. Shown is the complete dynamic analysis system supporting the development of flexible vehicle dynamic analysis models for control system development and ride quality analyses at Rockwell International's North American Aircraft Division, El Segundo. The path through this system as employed in developing the SMCS is as follows. (No supersonic analyses were conducted during SMCS development so the Mach-box program capability was not used.)

Starting at the top of the chart, it is seen that the process begins with a definition of the vehicle geometry, basic wind tunnel correlated aerodynamics, structural stiffness, and mass characteristics being provided to

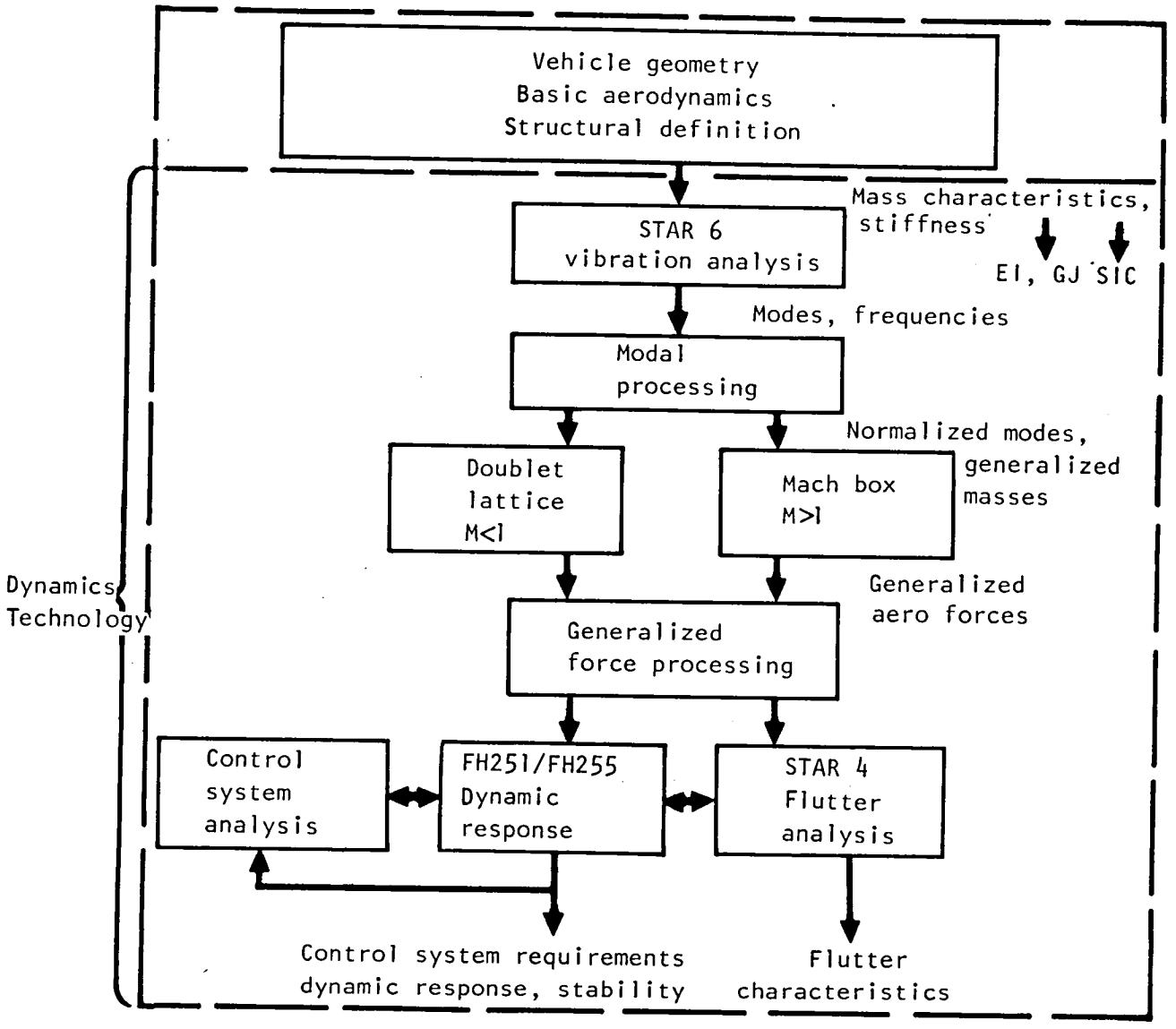

Figure 7. - Dynamic analysis system.

the Dynamics Technology Group. As indicated, the stiffness can be used in the EI-GJ format or in the form of structural influence coefficients (SIC). The mass and stiffness data enter the STAR 6 program, and vibration analyses of the whole vehicle are accomplished. The output of the program, then, is whole vehicle vibration mode shapes and frequencies.

These mode-shape data are next manipulated to produce normalized modes. For the B-1 ride quality analyses, both the symmetric and antisymmetric modes were normalized to a point on the nose of the vehicle. Generalized mass data consistent with the normalized modes are produced. Finally, modal deflection data are developed through interpolation programs along selected streamwise strips for input into the aerodynamic programs.

For the ride quality related studies reported herein, the Doublet Lattice Program has been used to provide theoretical aerodynamic generalized forces as required. These generalized aerodynamic forces are in dimensional form. Programs have been developed which process the data from dimensional form to the coefficient form required by the dynamic analyses programs. These dynamic analyses programs employ the frequency-domain equations of motion discussed earlier.

The FH-251 program provides dynamic response results for the longitudinal-symmetric case, while the FH-255 program provides dynamic response results for the lateral-directional-antisymmetric case. Both of these programs can accept either frequency-dependent or quasisteady data. Active controls can be included. Frequency responses due to gust or control forces may be obtained. When gust inputs are employed, ride quality parameters are output and control-system deflections and rate responses are obtained in power spectral density form. Stability analyses are performed using the characteristic determinant frequency evaluation technique of reference 4.

FREE-FREE VIBRATION MODAL DATA

The flexible aspects of the aircraft have been treated in the modal format as opposed to the direct-influence-coefficient approach. Ninety percent of the ride quality analyses performed have been accomplished using free-free vibration modes which were obtained using an EI-GJ description of the vehicle stiffness; more recent modal data have been obtained using structural influence coefficients. The details of the EI-GJ approach are discussed here.

Figure 8 shows the typical distribution of mass points on the elastic axes assumed. This is an early model; figure 9 shows a refinement of the fuselage elastic axis made at a later date. Each analysis included a flexible

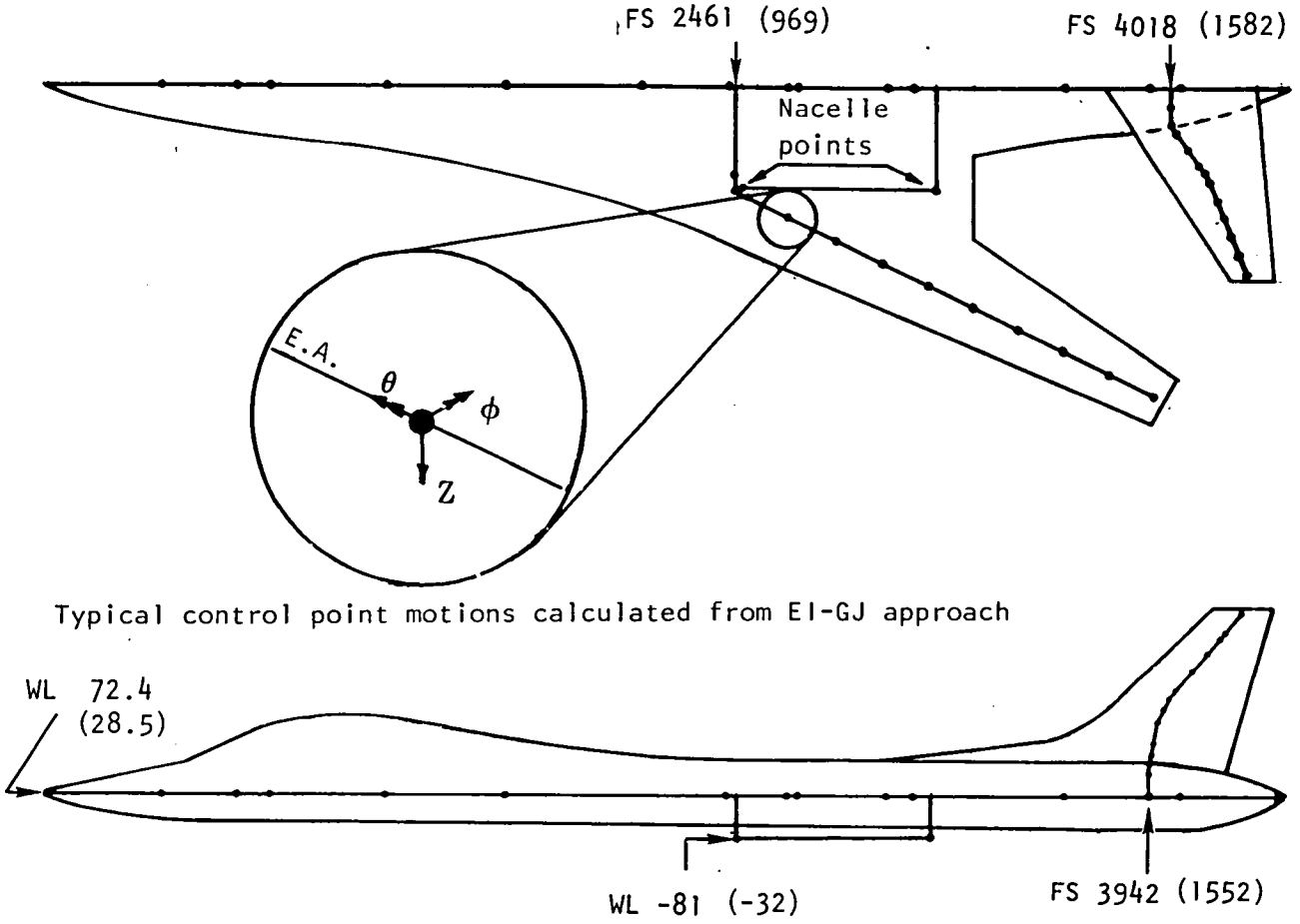

Figure 8. - Typical elastic axes and mass point locations.

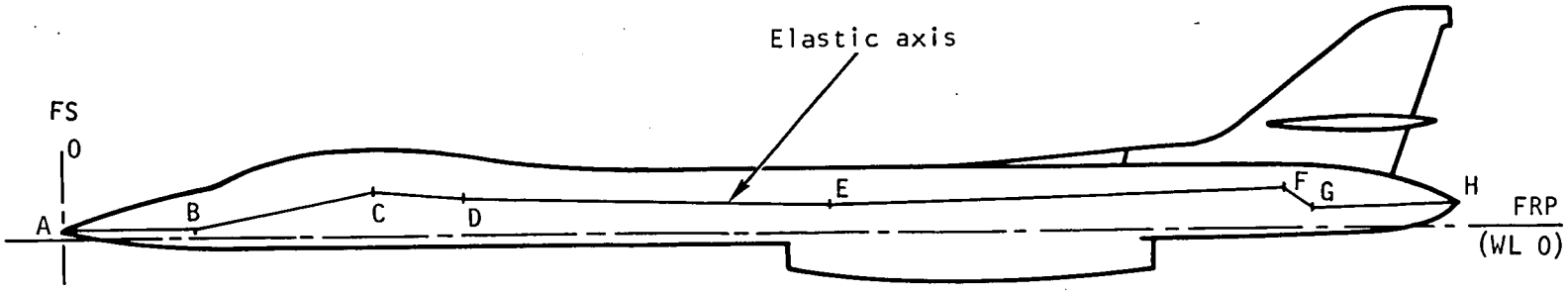

Elastic axis coordinates*

Point	Fus Sta	WL
A	0	38.6 (15.2)
B	406 (160)	34.0 (13.4)
C	1003 (395)	143.8 (56.6)
D	1283 (505)	123.2 (48.5)
E	2477 (975)	80.0 (31.5)
F	3937 (1550)	154.9 (61.0)
G	4013 (1580)	50.8 (20.0)
H	4430 (1744)	57.7 (22.7)

*Straight lines between these points

Figure 9. - Fuselage elastic axis refinement.

wing, fuselage, horizontal tail, and vertical tail. Also included were flexibly mounted engines/nacelles. The resultant mode shapes consisted of elastic axis deflections and rotations illustrated in figure 8.

Because the analyses were primarily oriented toward ride quality at the crew station, the free-free vibration modes were normalized at the most forward mass point at the nose of the aircraft. While most modes show a high degree of coupling among vehicle components, table IV identifies the main component (where this is possible) and lists the associated frequencies. In the analyses discussed herein, 10 symmetric modes and 12 antisymmetric modes were used. Discussions to follow later in this section describe the rationale used in selecting the modes shown.

When ground vibration test (GVT) data became available, they were used to upgrade the modal data. Symmetric orthogonal modes were successfully extracted from such tests. First, the effects of the soft support system were removed from the measured orthogonal set of modes. These data were next used, with proper fuel weights included, to analytically obtained orthogonal free-free modes at the desired weight condition. It was not possible, however, to directly extract an orthogonal set of antisymmetric modes from GVT data. To obtain usable, consistent, antisymmetric modal data reflecting test results, a technique was used of adjusting local stiffness data until a successful approximation of the measured data were obtained analytically. Then, as in the symmetric case, the effects of the soft suspension were deleted and the desired fuel weights adeed analytically to obtain orthogonal antisymmetric modes. The data of table IV are typical of those based on the GVT data obtained as described. It is to be noted also that structural damping was extracted; these data were obtained using the oscillation decay method. Figures 10 and 11 present typical symmetric and antisymmetric mode vector plots.

The computer programs used to determine the aerodynamic data require vibration mode shapes to be defined on a grid system whose chords are parallel to the free stream. Thus the basic mode shapes were interpolated to find point deflections along streamwise chords for all lifting surfaces. (See figure 12.) The mode-deflection data on the grid system shown were used as input to the Doublet Lattice Program where interpolations to the Doublet Lattice grid system were made and required slope data determined within the program.

AERODYNAMIC DATA

The Doublet Lattice aerodynamic theory was used to obtain most of the aerodynamics due to the flexible structure. In addition, extensive wind

TABLE IV. - TYPICAL ANALYTICAL STRUCTURAL MODE DATA

Wt = 119,296.8 kg (263 000 lb)
$\Lambda = 65^{o}$

Mode no.	Mode description	Frequency Hz	Structural[a] damping g_s
	Symmetric		
1	Wing, first bending	2.22	0.062
2	Fuselage, first bending	2.84	.094
3	First nacelle	3.26	.024
4	Horizontal tail, first bending	4.19	.028
5	Wing, fore and aft bending	4.23	.052
6	Fuselage, second bending	6.28	.016
7	Wing, second bending	7.57	.022
8	Horizontal tail, fore and aft bending	8.31	.064
9	Fuselage, third bending	11.15	.055
10	Horizontal tail, first torsion	27.35	.042
	Antisymmetric		
1	First nacelle	1.73	.145
2	Wing, first bending	2.41	.054
3	Horiz tail, first bending	3.51	.043
4	Horizontal tail, first bending	3.96	.025
5	Horizontal tail, fore and aft bending	4.14	.049
6	Wing, fore and aft bending	4.20	.031
7	Fuselage, first bending	5.58	.032
8	Wing, second bending	6.96	.031
9	Vertical tail, first bending	7.21	.019
10	Fuselage, second torsion	9.72	.078
11	Fuselage, second bending	10.30	.022
12	Vertical tail, first torsion	35.34	.020

[a]Determined from ground vibration tests

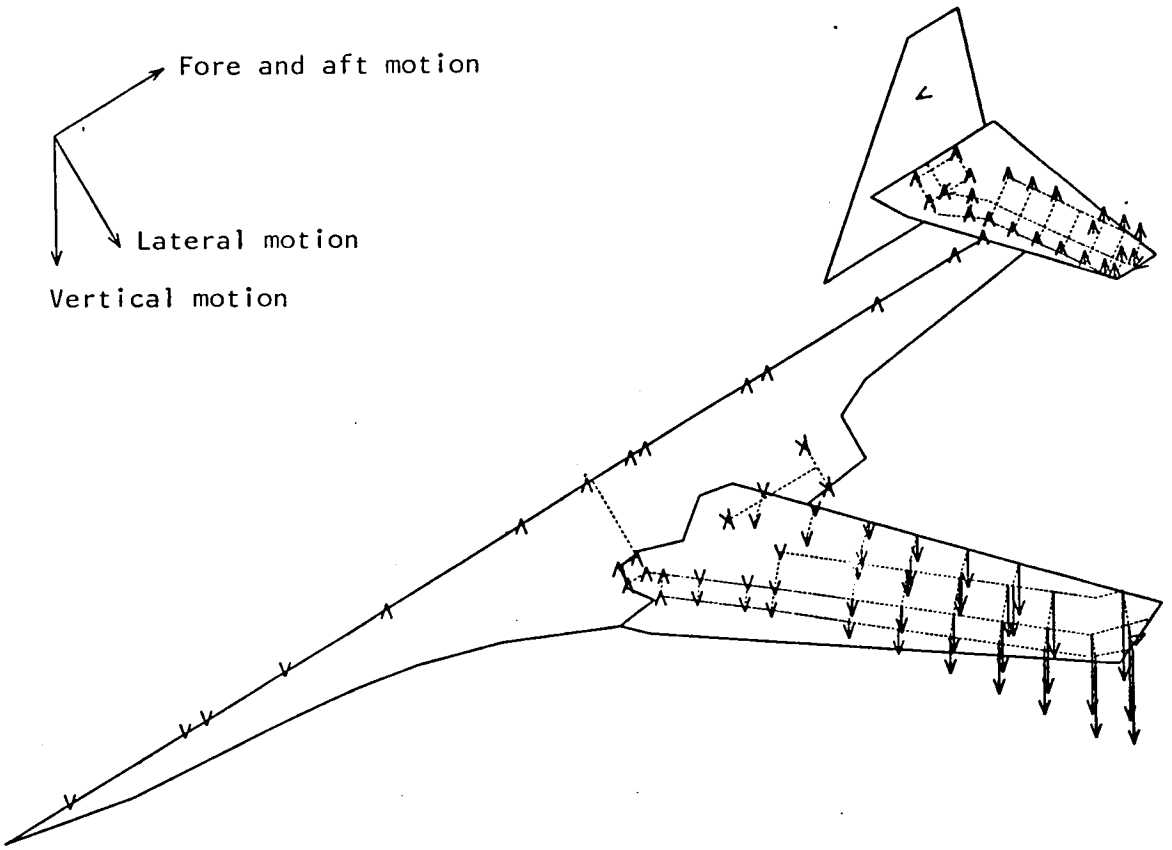

Figure 10. - Typical symmetric mode vector plot.

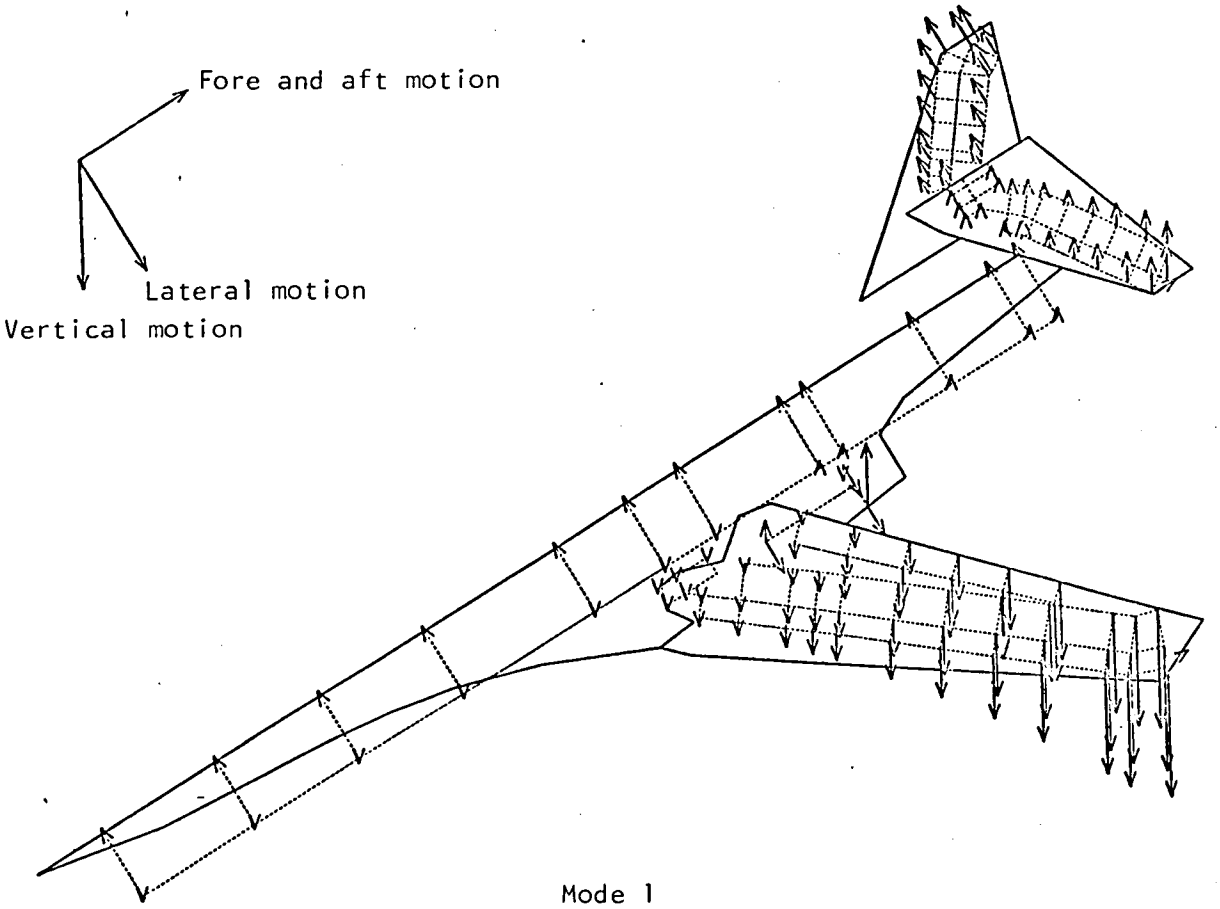

Figure 11. - Typical antisymmetric mode vector plot.

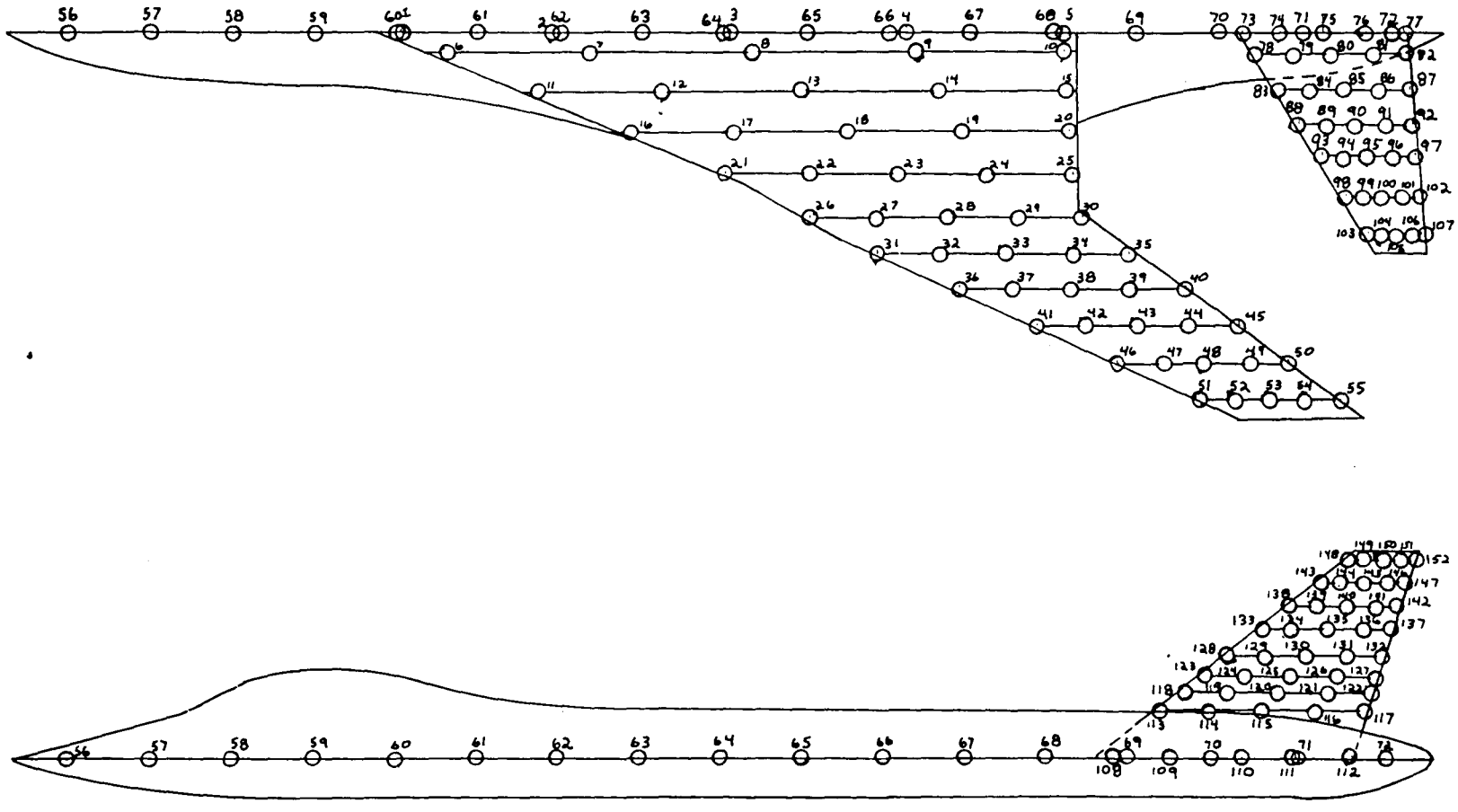

Figure 12. - Typical structural mode deflection grid points.

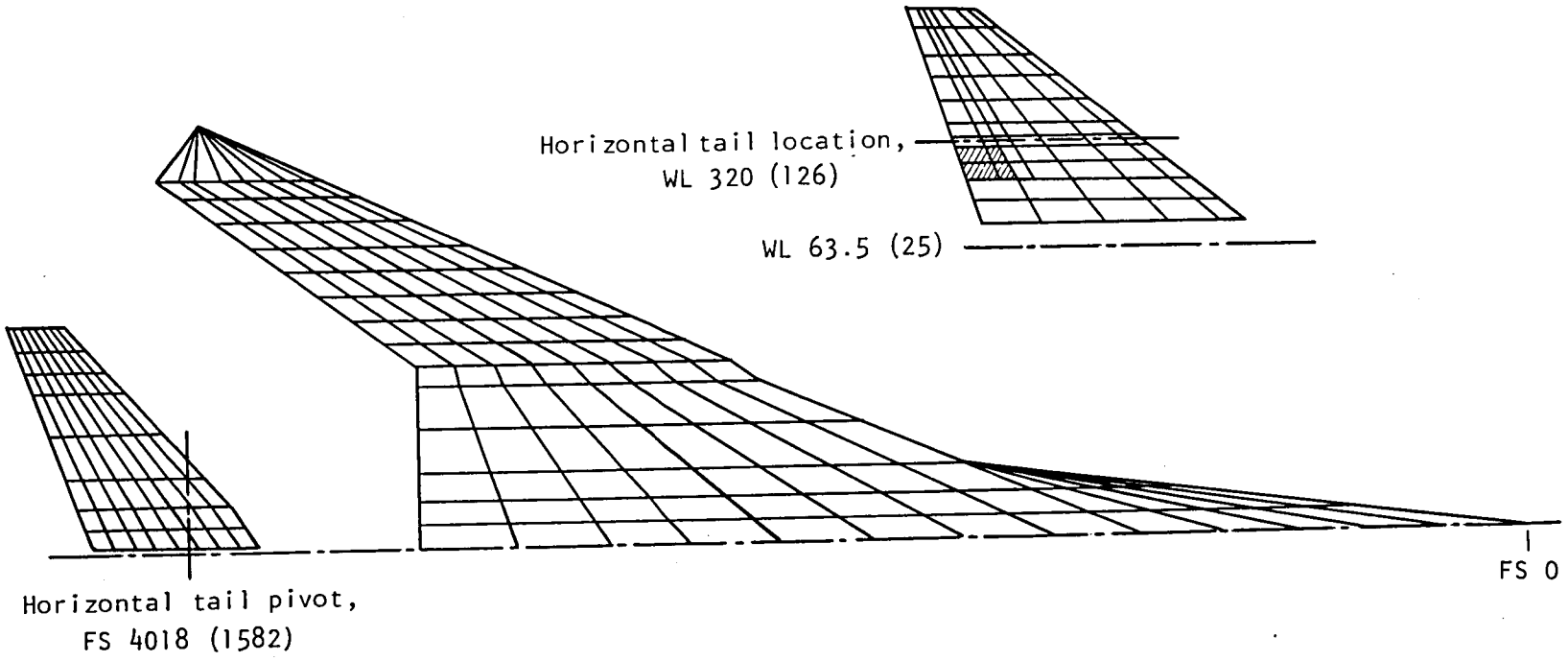

Figure 13. - Panelling and box grid for Doublet Lattice aerodynamics program.

tunnel data were also generated to obtain static, rigid-body force and moment-coefficient data along with pressure-distribution data. These two data sources were correlated (to be described) and used as input to the flexible aircraft analyses.

The panelling, box grid, and control-surfaces setup for the Doublet Lattice Program are shown in figure 13. The wing and fuselage forebody had five main panels with a total of 151 boxes. The horizontal tail had two panels and a total of 64 boxes; the horizontal tail was put in, also, as an all-movable control surface. The vertical tail had two panels and 73 boxes. In addition, the vertical tail had an end plate at its base consisting of one panel with 30 boxes. As shown in figure 13, the lower rudder control surface was also modeled.

For longitudinal-symmetric data, including control effectiveness and gust data, the wing/forebody and horizontal tail were run as shown in figure 13. This same wing/forebody arrangement was used along with the full empennage (horizontal tail, vertical tail, and end plate) to obtain lateral-directional-antisymmetric, whole-vehicle data. Vertical tail gust data, lower rudder control effectiveness, and differential horizontal tail effectiveness data were obtained by running the empennage plus end plate as an entity. For fuselage side gust and generalized aerodynamic forces, a modified slender body theory was used which made use of wind tunnel developed side-force distribution data.

It is to be noted that the SMCS vanes were not modeled for the Doublet Lattice Program. The aerodynamics for the vane were obtained from wind tunnel tests as described in reference 1. None of the vane-related aerodynamics were frequency dependent. The reduced frequency (k) determined on the basis of an assumed frequency of 10 Hz (62.8 rad/sec), the highest frequency range that vane is expected to be effective at M = 0.85, is

$$k = \frac{\omega \bar{c}}{2V_o} = \frac{(62.8)(2.46)}{(2)(951)} = 0.0812$$

Compared to k for the wing under the same circumstances

$$k = \frac{(62.8)(15.23)}{(2)(951)} = 0.503$$

This is a relatively low reduced frequency, and the aerodynamic unsteadiness effects are judged to be acceptably small. In retrospect, this appears to have been a valid judgement. In generating the structural-mode generalized force coefficients, the vane force was assumed to act at a point; i.e.,

FS 581.66 (229). Thus, $C_{\eta_{i_{\delta_{CV}}}} = C_{N_{\delta_{CV}}} \phi_i^{FS\ 581.66}$ for symmetric modes is an example.

In developing the Doublet Lattice paneling and box patterns, lifting-surface spanload distributions were compared to the wind tunnel-related data. The gap between the vehicle centerline and the first row of chordwise boxes of the horizontal tail is one of the devices used to obtain matched data sets for the horizontal tail. It was reasoned that with good matches of the lifting-surface spanloadings, the computer model developed would give valid answers for both rigid body and structural modes.

The point of view was adopted that the wind tunnel-related airload distribution for the rigid vehicle were the most accurate data available. Thus, the rigid vehicle aerodynamics couplings into the structural modes ($C_{\eta_{i_\alpha}}$ and $C_{\eta_{i_\delta}}$ data are examples) were computed using these distributions rather than Doublet Lattice theory, for the zero-frequency case. These data, in turn, were used to scale the frequency-dependent data produced by the Doublet Lattice Program. The $C_{\eta_{i\eta_j}}$ and $C_{\eta_{i\dot{\eta}_j}}$ data were used directly as generated by the program without scaling for both the symmetric and antisymmetric modes.

As an example of how the wind tunnel data and the Doublet Lattice frequency-dependent gust aerodynamic data were brought into agreement, consider the typical example of figure 14. Shown is the pitching-moment coefficient data due to a unit vertical gust velocity. The magnitude trends versus the reduced frequency, k, were assumed basically correct and all adjustments to match wind tunnel based data were made at low frequencies as illustrated. The data magnitude of the real component at zero frequency was adjusted to match the wind tunnel based data and then faired into the basic real curve at low reduced frequencies. For the case illustrated, the gust coefficient at zero frequency was determined from angle-of-attack data, $C_{m_{w_g}} = (C_{m_\alpha})/V_o$. This matching of the angle-of-attack and gust velocity data is essential to obtaining valid power spectral density responses due to gust data at low frequencies; a mismatch will produce a load factor response at zero frequency which is not there in the real world. In the real world, a stable aircraft will weathervane into the resultant velocity due to the combined motion and gust velocity and have no load factor at zero frequency.

As mentioned while discussing the analyses flow, the data produced by the Doublet Lattice Program must be reduced to the coefficient form of the equations of motion discussed in the previous section. In order to do this, the data are processed in the following manner.

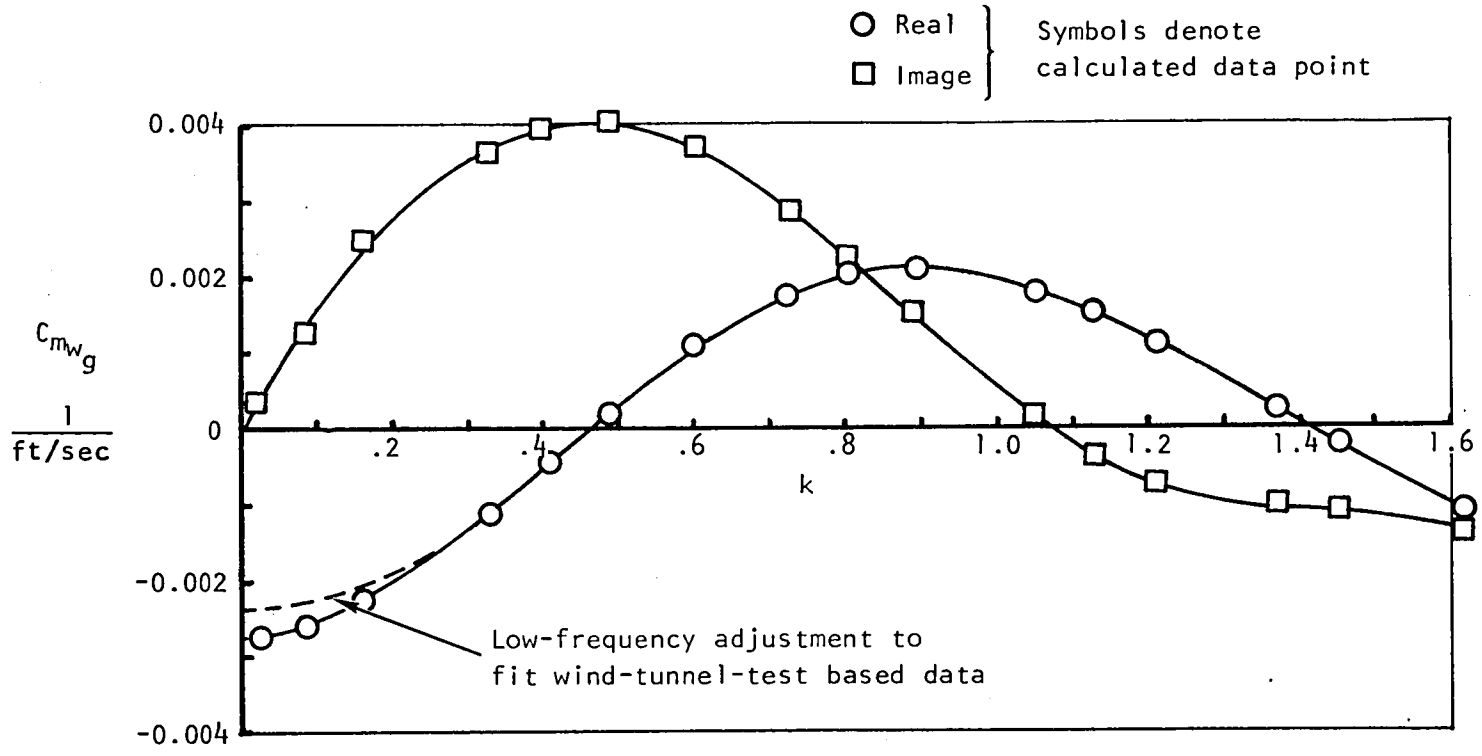

Gust reference point is FS 2649 (1043)

Figure 14. - Typical low-frequency adjustment made to analytical frequency-dependent aerodynamic data.

The program outputs data normalized to air density (2ρ) and to frequency (ω^2) as illustrated here using the dimensional lift force due to plunging L_h (for the whole vehicle), $[L_h/2\rho\omega^2]$. The division by two is because the data generated in the program are for half of a vehicle. ρ is assumed to be unity by the program. Velocity is determined by the data of Mach number and velocity of sound at the altitude selected. Frequency, ω, is input at a number of selected values.

Having this information, table V illustrates how the frequency-dependent coefficient data are developed as a function of frequency (or reduced frequency, k). Longitudinal-symmetrical coefficients are obtained using the information of table V; lateral-directional-antisymmetric coefficient data are obtained in a similar manner.

Reflected in table V is the sign convention built into the Doublet Lattice Program at Rockwell and the sign convention assumed for the equations of motion of tables I, II, and III. The only difference of importance to the understanding of the derivations of table V is the fact that lift force, L, of the Doublet Lattice Program is of opposite sense to the equation of motion normal force, N, and its associated coefficient, C_N. Otherwise, the pitching moment, M, and structural mode generalized forces, Q_i, are identical in definition.

As an aid in understanding how table V was assembled, the following example is given for the derivation of C_{N_α}.

For no pitching ($\theta = \dot{\theta} = 0$)

$$\alpha = \frac{\dot{h}}{V_o} = \frac{\omega h}{V_o}$$

therefore:

$$q_o S_w C_{N_\alpha} \alpha = - \left[L_h\right]_{IMAG} h \qquad \text{force units}$$

$$\frac{\rho}{2} V_o^2 S_w C_{N_\alpha} \alpha = - \left[L_h\right]_{IMAG} \left(\frac{V_o}{\omega}\right)\left(\frac{\omega}{V_o}\right) h$$

$$V_o^2 \frac{S_w}{4} C_{N_\alpha} = - \omega V_o \left[\frac{L_h}{2\rho\omega^2}\right]_{IMAG}$$

$$C_{N_\alpha} = - \left(\frac{\omega}{V_o}\right)\left(\frac{4}{S_w}\right)\left[\frac{L_h}{2\rho\omega^2}\right]_{IMAG}$$

TABLE V. - LONGITUDINAL-SYMMETRIC AERO COEFFICIENTS FROM DOUBLET LATTICE PROGRAM

$C_{N_\alpha} = -\left(\frac{\omega}{V_o}\right)\left(\frac{4}{S_w}\right)\left[\frac{L_h}{\omega^2 2\rho}\right]_{IMAG.}$	$C_{N_{\dot{\eta}_i}} = -\left(\frac{\omega}{V_o}\right)\left(\frac{4}{S_w}\right)\left[\frac{L_{\eta_i}}{\omega^2 2\rho}\right]_{IMAG.}$
$C_{m_\alpha} = \left(\frac{\omega}{V_o}\right)\left(\frac{4}{\bar{c}_w S_w}\right)\left[\frac{M_h}{\omega^2 2\rho}\right]_{IMAG.}$	$C_{m_{\dot{\eta}_i}} = \left(\frac{\omega}{V_o}\right)\left(\frac{4}{c_w S_w}\right)\left[\frac{M_{\eta_i}}{\omega^2 2\rho}\right]_{IMAG.}$
$C_{N_{\dot{\alpha}}} = \left(\frac{8}{\bar{c}_w S_w}\right)\left[\frac{L_h}{\omega^2 2\rho}\right]_{REAL}$	$C_{\eta_i\eta_j} = \left(\frac{\omega}{V_o}\right)^2\left(\frac{4}{S_w}\right)\left[\frac{Q_{i\eta_j}}{\omega^2 2\rho}\right]_{REAL}$
$C_{m_{\dot{\alpha}}} = -\left(\frac{8}{\bar{c}_w^2 S_w}\right)\left[\frac{M_h}{\omega^2 2\rho}\right]_{REAL}$	$C_{\eta_i\dot{\eta}_j} = \left(\frac{\omega}{V_o}\right)\left(\frac{4}{S_w}\right)\left[\frac{Q_{i\eta_j}}{\omega^2 2\rho}\right]_{IMAG.}$
$C_{N_q} + C_{N_{\dot{\alpha}}} = -\left(\frac{\omega}{V_o}\right)\left(\frac{8}{\bar{c}_w S_w}\right)\left[\frac{L_\theta}{\omega^2 2\rho}\right]_{IMAG}$	$C_{\eta_{i_\alpha}} = \left(\frac{\omega}{V_o}\right)\left(\frac{4}{S_w}\right)\left[\frac{Q_{ih}}{\omega^2 2\rho}\right]_{IMAG.}$
$C_{m_q} + C_{m_{\dot{\alpha}}} = \left(\frac{\omega}{V_o}\right)\left(\frac{8}{\bar{c}_w^2 S_w}\right)\left[\frac{M_\theta}{\omega^2 2\rho}\right]_{IMAG.}$	$C_{\eta_{i\dot{\alpha}}} = -\left(\frac{8}{\bar{c}_w S_w}\right)\left[\frac{Q_{ih}}{\omega^2 2\rho}\right]_{REAL}$
$C_{N_{\dot{q}}} = \left(\frac{16}{\bar{c}_w^2 S_w}\right)\left[\frac{\Delta L_\theta}{\omega^2 2\rho}\right]_{REAL}$	$C_{\eta_{iq}} + C_{\eta_{i\dot{\alpha}}} = \left(\frac{\omega}{V_o}\right)\left(\frac{8}{\bar{c}_w S_w}\right)\left[\frac{Q_{i\theta}}{\omega^2 2\rho}\right]_{IMAG.}$
$C_{m_{\dot{q}}} = -\left(\frac{16}{\bar{c}^3 S_w}\right)\left[\frac{\Delta M_\theta}{\omega^2 2\rho}\right]_{REAL}$	$C_{\eta_{i\dot{q}}} = -\left(\frac{16}{\bar{c}_w^2 S_w}\right)\left[\frac{\Delta Q_{i\theta}}{\omega^2 2\rho}\right]_{REAL}$
$C_{N_\delta} = -\left(\frac{\omega}{V_o}\right)^2\left(\frac{4}{S_w}\right)\left[\frac{L_\delta}{\omega^2 2\rho}\right]_{\substack{REAL \\ IMAG.}}$	$C_{\eta_{i_\delta}} = \left(\frac{\omega}{V_o}\right)^2\left(\frac{4}{S_w}\right)\left[\frac{Q_{i\delta}}{\omega^2 2\rho}\right]_{\substack{REAL \\ IMAG.}}$
$C_{m_\delta} = \left(\frac{\omega}{V_o}\right)^2\left(\frac{4}{\bar{c}_w S_w}\right)\left[\frac{M_\delta}{\omega^2 2\rho}\right]_{\substack{REAL \\ IMAG.}}$	$C_{N_{w_g}} = -\left(\frac{\omega}{V_o}\right)^2\left(\frac{4}{S_w}\right)\left[\frac{L_{w_g}}{\omega^2 2\rho}\right]_{\substack{REAL \\ IMAG.}}$
$C_{N_{\eta_i}} = -\left(\frac{\omega}{V_o}\right)^2\left(\frac{4}{S_w}\right)\left[\frac{L_{\eta_i}}{\omega^2 2\rho}\right]_{REAL}$	$C_{m_{w_g}} = \left(\frac{\omega}{V_o}\right)^2\left(\frac{4}{\bar{c}_w S_w}\right)\left[\frac{M_{w_g}}{\omega^2 2\rho}\right]_{\substack{REAL \\ IMAG}}$
$C_{m_{\eta_i}} = \left(\frac{\omega}{V_o}\right)^2\left(\frac{4}{\bar{c}_w S_w}\right)\left[\frac{M_{\eta_i}}{\omega^2 2\rho}\right]_{REAL}$	$C_{\eta_{iw_g}} = \left(\frac{\omega}{V_o}\right)^2\left(\frac{4}{S_w}\right)\left[\frac{Q_{iw_g}}{\omega^2 2\rho}\right]_{\substack{REAL \\ IMAG.}}$

The bracketed quantity [ ] here and in table V comes directly from the Doublet Lattice Program as a function of frequency.

One of the questions to be resolved in using a modal approach to aircraft flexibility modeling is the one of how many modes to use. The technique used to help make this decision for the described analyses is discussed here. First, the following criteria were developed as guides in the decision process. The modes contributing to main aeroelastic impacts on all short-period and Dutch-roll characteristics were to be included. The modes contributing to main aeroelastic impacts on control effectiveness were to be included. The modes contributing most to flexible fuselage motion at the pilot station and active control sensors were to be included.

Figure 15 is typical of the data generated to assist this mode selection process. For the longitudinal-symmetric case used as an illustration, some 25 whole-aircraft normalized modes were input to the Doublet Lattice Program and run at a frequency of $\pi/2$ (a frequency judged to be in the region of short period and Dutch roll frequency). These data then were reduced to aerodynamic coefficient form and entered into a program which calculates quasisteady flexible-to-rigid (F/R) ratios (refer to "Truncated Analytical Models") for all of the key aerodynamic derivatives (C_{N_α} and C_{m_α} are used as illustrations here). These F/R ratios are calculated as one mode after the other is eliminated. As a result, it is possible to identify the individual modes contributing most to a given derivative's aeroelastic impact.

After the preceding procedure is accomplished for all important derivatives, plots similar to figure 15 are assembled and inspected as a whole. Thus, those modes making important contributions to all derivatives are selected for retention.

As far as fuselage motion was concerned, as many modes as possible, having fuselage motion as a main component, were selected. Usually modes reflecting up to the third fuselage-bending and the second fuselage-torsion mode could be selected.

CONTROL-SURFACES INERTIA REACTION FORCES

The inertia reaction forces of the control surfaces are important inputs to the stability analyses of active control systems. The detailed final form of these inputs for the B-1 control surfaces are indicated in the equations of motion of the first part of this report. The basic approach that was used in developing these expressions will be discussed here, but each control-surface input will not be developed in detail.

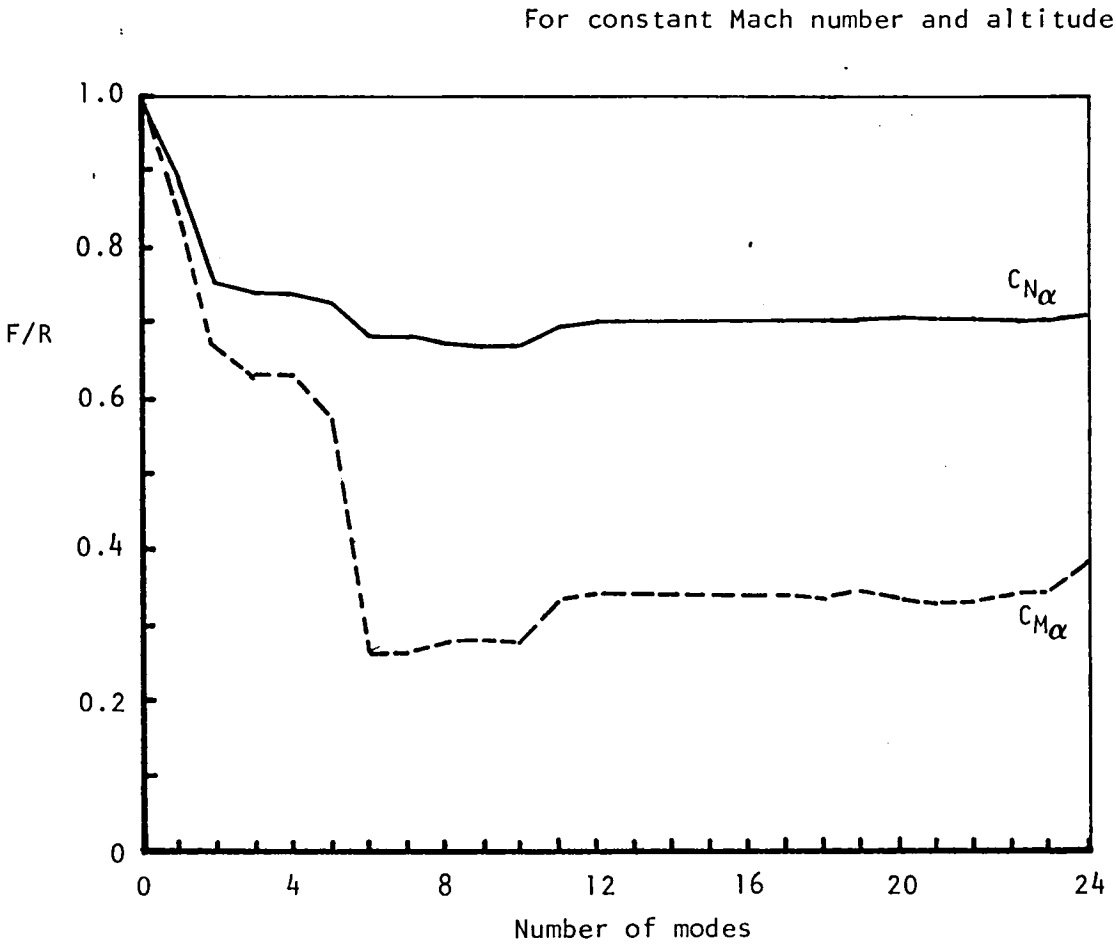

Figure 15. - Typical aeroelastic flexible-to-rigid ratio data for aerodynamic coefficients as a function of participating structural modes.

Figure 16a shows that when a typical control surface is accelerated in the positive sense of the deflection, a mass reaction force and moment are developed at the center of the mass of the control surface. This force and moment are reacted into the basic aircraft structure at the control surface hingeline as a force and moment as shown. The force acting on the aircraft is the force shown, and the moment acting about the aircraft center of gravity is $(\bar{\ell} m \ell + I_{HL})\ddot{\delta}$ where $\bar{\ell}$ is the distance between the control-surface hingeline and the aircraft center of gravity.

The generalized force acting on a typical structural mode due to control surface acceleration is illustrated in figure 16b where the specific example of a symmetric mode is used. Before getting into the specific example, consider the concept of a generalized force. A generalized force has units of work, that is m - N (foot-pounds). In this case, it is either force multiplied by mode deflection at the force application point, moment multiplied by mode slope at the moment application point, or both. A positive generalized force would act to increase the deflection (or virtual work) of the structural mode. Looking at the example in the figure, it can be seen, for the example shown, that the reaction force causes a generalized mode force increment of $-\phi_i^{HL} m \ell \ddot{\delta}$ and the reaction moment a generalized mode force increment of $+\phi_i'^{IL} I_{HL} \ddot{\delta}$.

The preceding development has proved an adequate representation for small control surfaces such as the B-1 SMCS control vane and lower rudder control surface. It is not accurate enough, however, for large control surfaces such as the all-movable horizontal tail. In this latter case, it was necessary to break up the mass characteristics of the surface onto a distributed grid system. Using the distributed mass data and the previously developed logic, generalized forces were developed for rigid body and structural modes. These data, developed using distributed masses, were input to the digital program which implements the equations of motion of table II using an equivalent point mass representation of the data.

During the B-1 development, checks of the pitch SCAS, with the aircraft on the ground resting on its landing gear, revealed a structural mode-coupling instability when excited with sharp horizontal tail control inputs. This instability could be analytically duplicated by using generalized control-surface inertia reaction forces developed employing the distributed mass approach but could not be duplicated using the single-point mass representation.

The inertia reaction forces are particularly important to the stability of SMCS with the aircraft on the ground. The inertia reaction forces have an opposite sense to the aerodynamic forces of the SMCS vanes. The stability of the system is established by these aerodynamic forces. Thus, if the aerodynamic forces disappear, the feedback sense is effectively reversed, producing an

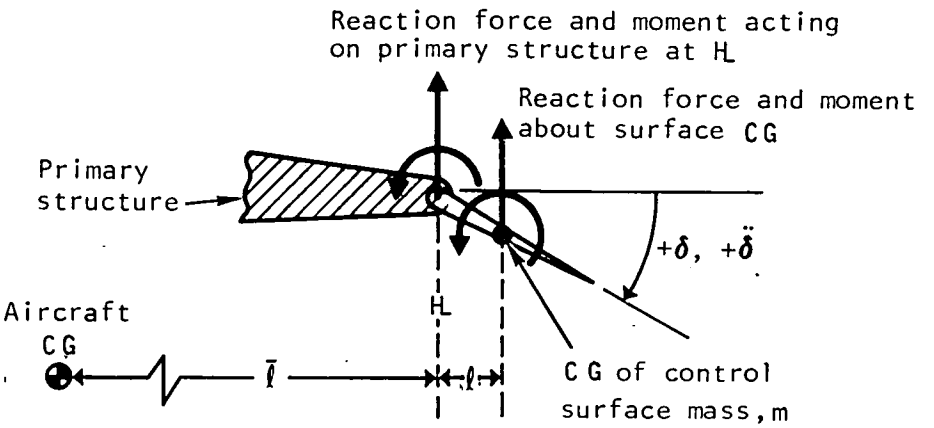

Force at aircraft CG = $+m\ell\ddot{\delta}$

Moment about aircraft CG = $-(\bar{\ell}m\ell + I_{H_L})\ddot{\delta}$
(pitch axis assumed for illustration)

(a) Rigid-body generalized forces

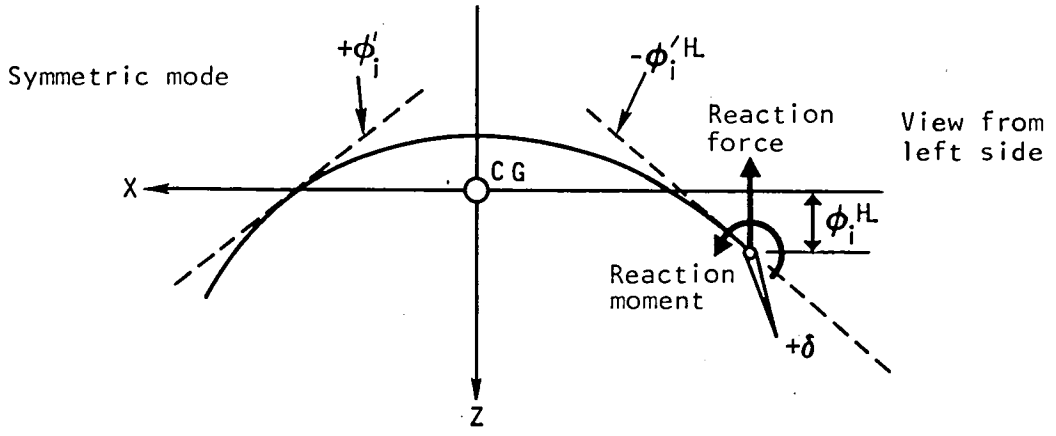

Note definitions of $+\phi_i'$ and $+\phi_i'^{H_L}$

Structural generalized forces = $-(\phi_i^{H_L} m\ell - \phi_i'^{H_L} I_{H_L})\ddot{\delta}$

(b) Structural generalized forces

Figure 16. - Typical control surface inertia reaction generalized forces.

instability. On the B-1, a switch on the landing gear prevents operating the SMCS while on the ground, precluding any inadvertant damage due to this potential instability.

ACTIVE CONTROL SYSTEMS

Two types of active control systems were included in the analyses pertaining to this study. One type, SCAS, is associated with control of whole-vehicle (short period and Dutch roll) modes of motion. The second type, SMCS, has the function to control fuselage structural motion to improve ride quality.

The block diagrams and analytical modeling of the SCAS are given in figures 17 through 19 and SMCS in figures 20 and 21. Flight condition-dependent gains are shown for M = 0.85 at SL. These figures indicate the type of sensors, compensations, gains, and actuator modeling assumed for each of the indicated systems. The control-surface deflection equations are cast in a form directly usable by the Rockwell response analyses programs. That is to say, the overall gain is indicated, system dynamics are represented by numerator and denominator roots of polynomials, and vehicle motions are defined as measured by the appropriate sensors.

COMPARISONS OF ANALYSES AND FLIGHT-TEST RESULTS

The ride quality indices, $\overline{H}_z$ and $\overline{H}_y$ (refer to reference 5 for detail definitions), for the vertical and lateral axes, respectively, cannot be measured directly in flight. One difficulty is the fact that the parameters are obtained from weighted power spectral density curves of crew-station accelerations, and the weighting can presently only be done as a postflight operation. Secondly, it is very difficult to precisely fly a specification vehicle weight at the specification Mach number and altitude. For the B-1, the approach has been to demonstrate that the analytical model can duplicate flight-test results and then proceed to use the verified model in the required ride quality analyses. It is the intent of this task to present the data matches which provided the verification and give an evaluation of the factors affecting the matches.

The flight-test data obtained for matching purposes were frequency responses of load factors at FS 571.5(225) due to SMCS vane inputs. Both vertical and lateral load-factor data were obtained. The flight condition flown was M = 0.85 at 762 meters (2500 feet). The vehicle weight was approximately 119 296 kilograms (263 000 pounds). Wing sweep was 65 degrees. Data were taken with all control systems inoperative; then, with only the SCAS

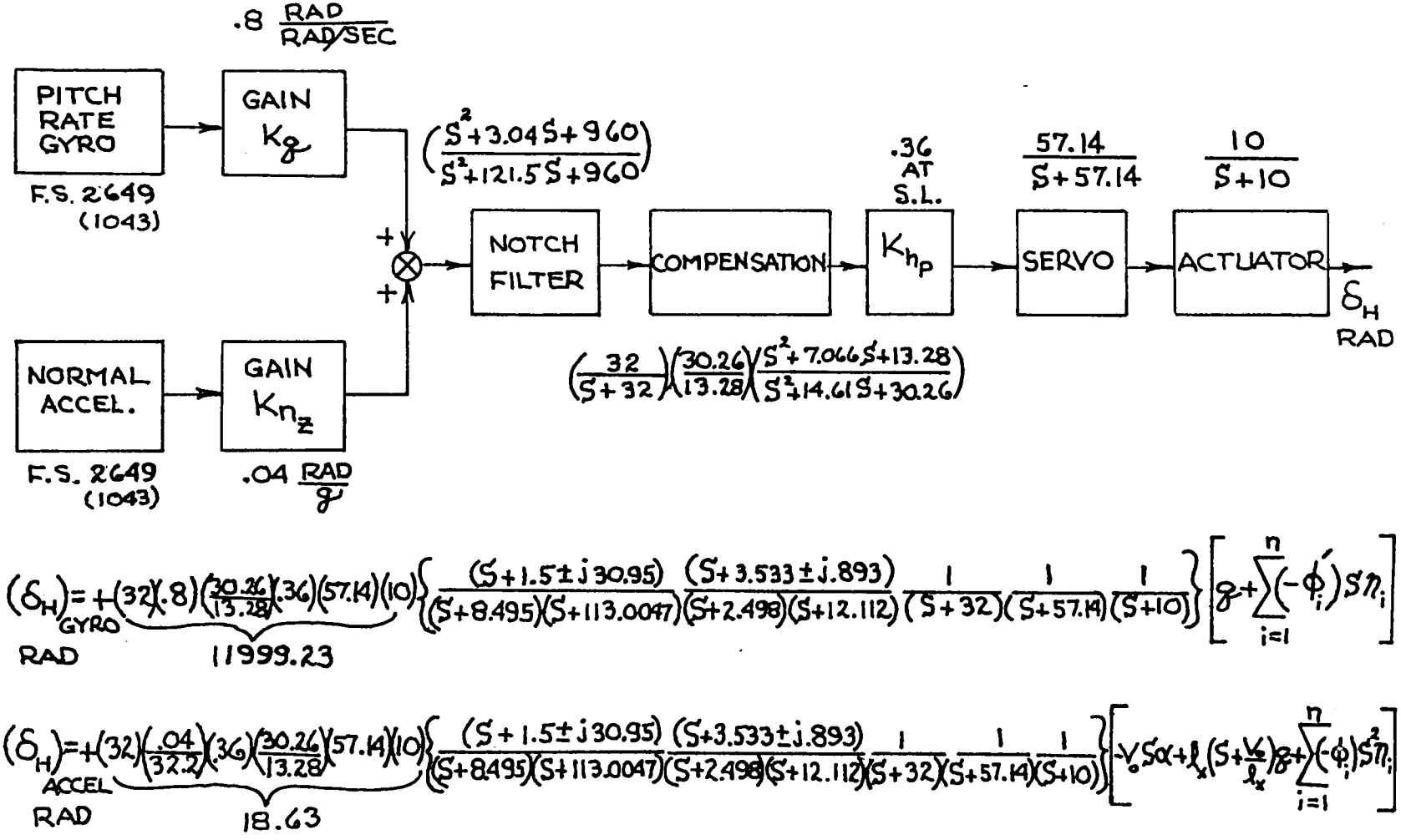

For flight condition of M = 0.85 at SL

Figure 17. - Pitch axis SCAS analytical model.

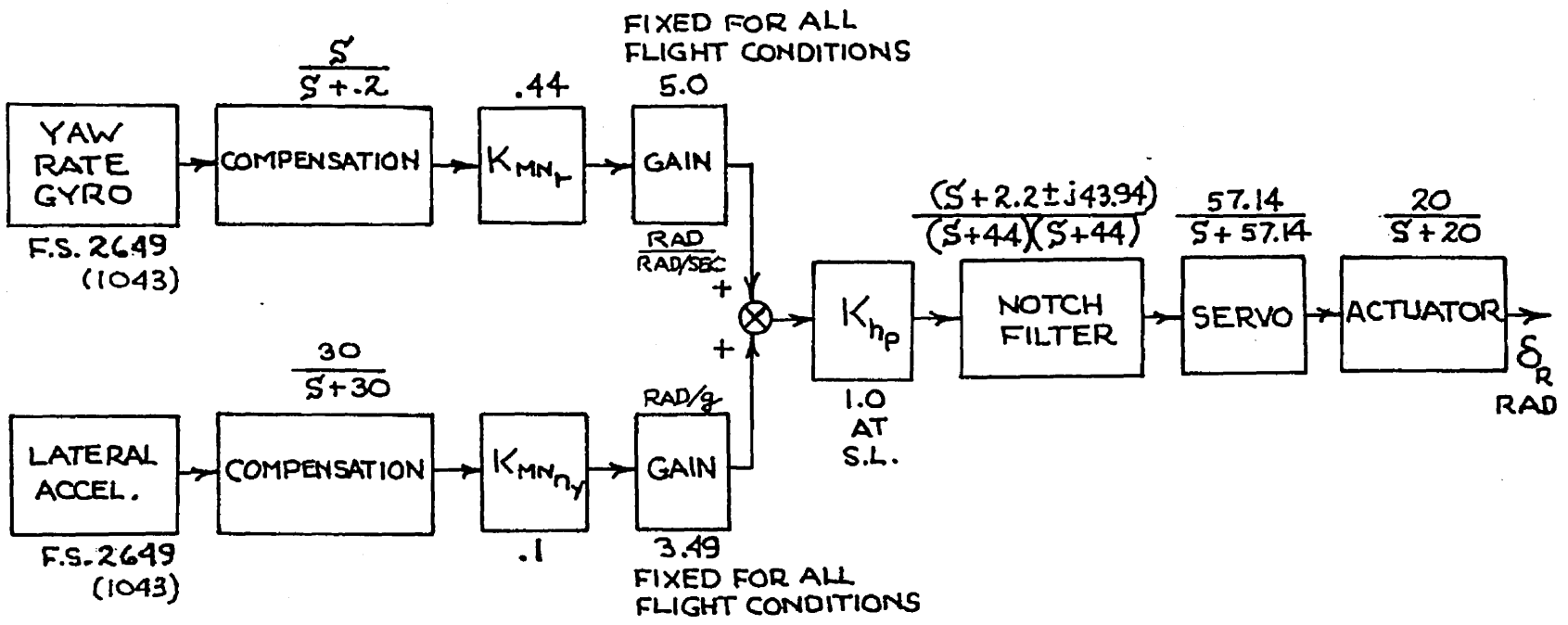

$$(\delta_R)_{GYRO} = +\overbrace{(.44)(5.0)(1.0)(57.14)(20)}^{2514.2}\left\{\left(\frac{S}{S+.2}\right)\left(\frac{S+2.2\pm j43.94}{(S+44)(S+44)}\right)\left(\frac{1}{S+57.14}\right)\left(\frac{1}{S+20}\right)\right\}\left[(0)\beta+(1.0)r+(0)p+\sum_{i=1}^{m}\phi_i S\eta_i\right]$$

RAD

$$(\delta_R)_{ACCEL.} = +\overbrace{\left(\frac{30}{32.2}\right)(.1)(3.49)(1.0)(57.14)(20)}^{371.59}\left\{\left(\frac{1}{S+30}\right)\left(\frac{S+2.2\pm j43.94}{(S+44)(S+44)}\right)\left(\frac{1}{S+57.14}\right)\left(\frac{1}{S+20}\right)\left(\frac{1}{S}\right)\right\}\left[V_o S^2\beta+l_x S\left(S+\frac{V_o}{l_x}\right)r-V_o\alpha_T\left(S+\frac{32.2}{V_o\alpha_T}\right)p+\sum_{i=1}^{m}\phi_i S^3\eta_i\right]$$

RAD

See note on figure 21

For flight condition of M = 0.85 at SL

Figure 18. - Yaw axis SCAS analytical model.

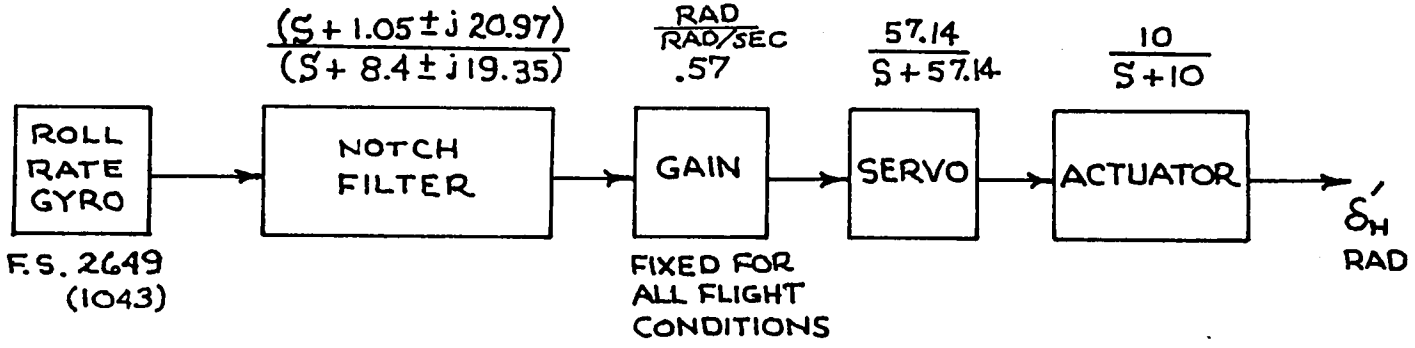

$$\delta'_{H_{RAD}} = -\overbrace{(.57)(57.14)(10)}^{325.7}\left\{\frac{(S+1.05\pm j20.97)}{(S+8.4\pm j19.35)}\frac{1}{(S+57.14)}\frac{1}{(S+10)}\right\}\left[(0)\beta+(0)r+(1.0)P+\sum_{i=1}^{m}\Phi_i^T S\eta_i\right]$$

For flight condition of M = 0.85 at SL

Figure 19. - Roll axis SCAS analytical model.

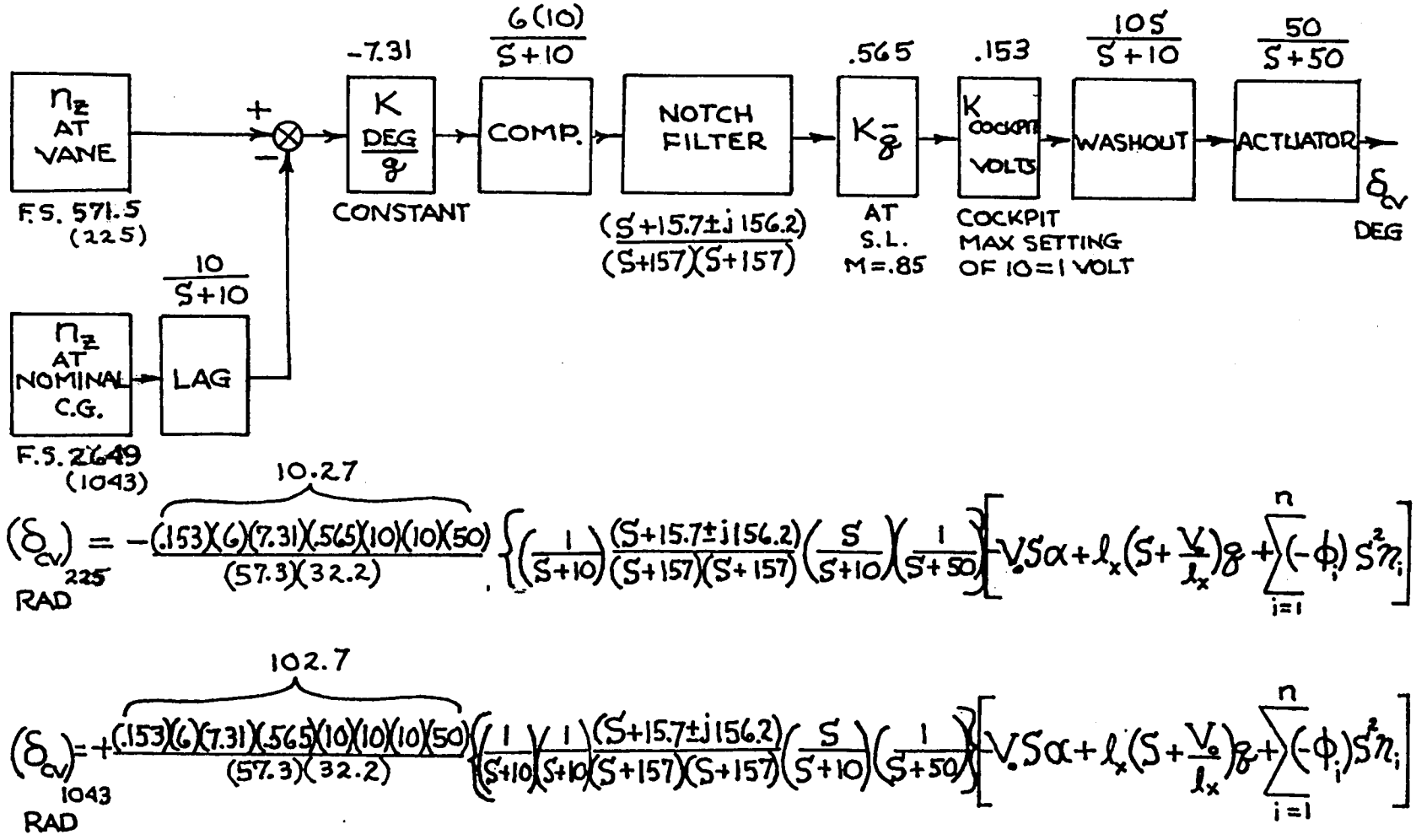

For flight condition of M = 0.85 at SL

Figure 20. - Vertical SMCS analytical model.

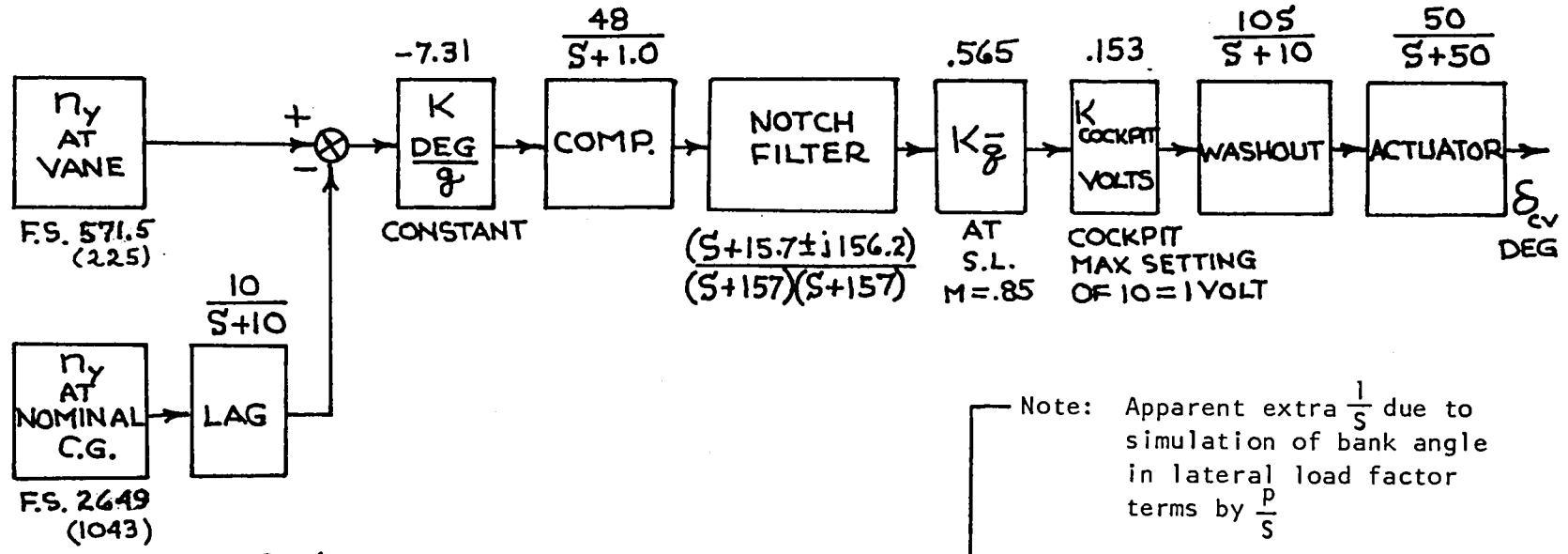

$$(\delta_{cv})_{225} = -\frac{\overbrace{(.153)(7.31)(48)(.565)(10)(50)}^{8.06}}{(57.3)(32.2)} \left\{\frac{1}{S+1.0}\right\}\left\{\frac{(S+15.7\pm j156.2)}{(S+157)(S+157)}\right\}\left\{\frac{S}{S+10}\right\}\left\{\frac{1}{S+50}\right\}\left\{\frac{1}{S}\right\}\left[V_o S^2\beta + l_x S\left(S+\frac{V_o}{l_x}\right)r - V_o\alpha_t\left(S+\frac{32.2}{V_o\alpha_t}\right)p + \sum_{i=1}^{3}\phi_i S^3\eta_i\right] \text{ RAD}$$

$$(\delta_{cv})_{1043} = +\frac{\overbrace{(.153)(7.31)(48)(.565)(10)(10)(50)}^{80.6}}{(57.3)(32.2)} \left\{\frac{1}{S+10}\right\}\left\{\frac{1}{S+1.0}\right\}\left\{\frac{(S+15.7\pm j156.2)}{(S+157)(S+157)}\right\}\left\{\frac{S}{S+10}\right\}\left\{\frac{1}{S+50}\right\}\left\{\frac{1}{S}\right\}\left[V_o S^2\beta + l_x S\left(S+\frac{V_o}{l_x}\right)r - V_o\alpha_t\left(S+\frac{32.2}{V_o\alpha_t}\right)p + \sum_{i=1}^{3}\phi_i S^3\eta_i\right] \text{ RAD}$$

For flight condition of M = 0.85 at SL

Figure 21. - Lateral SMCS analytical model.

operating; and finally, with both SCAS and SMCS (cockpit gains 1.5) operating. The forcing amplitude and frequency settings were set manually in the cockpit. The measured data were processed to obtain both magnitude and phase characteristics.

The analytical structural-mode characteristics for the data-match analyses were obtained from test and analysis sources. The symmetric structural modes were obtained directly from GVT. It was not possible to obtain a set of orthogonal modes for the antisymmetric case directly from the GVT. Instead, the analytical structural model was adjusted in stiffness until the frequency and mode-shape characteristics were as close to the observed characteristics as possible. In support of these tests, the basic vehicle weight characteristics (no fuel) were identified. For the specific data-matching analyses, fuel loadings were determined from measurements made during the flight-test period when the frequency responses were being executed.

The pitch SCAS characteristics used in the analyses were as described in figure 17; the yaw and roll SCAS were as described in figures 18 and 19, respectively. The vertical SMCS description is given in figure 20; and the lateral SMCS description is shown in figure 21.

Comparison of the analytical and flight-test results of the normal load factor of FS 571.5 (225) frequency response due to symmetric SMCS vane deflections (SMCS used as an excitation system) for the condition of no active controls (basic aircraft) are shown in figure 22. The three response peaks are (starting with the lowest frequency) first fuselage bending, second fuselage bending, and third fuselage bending, respectively; there is some influence on the second peak from the wing second bending. The quality of the match is considered excellent. To obtain this match, however, three adjustments were made to the original modal characteristics: (1) the wing first bending-mode frequency was reduced from 7.57 to 7.00 Hz, (2) the fuselage third-bending frequency was reduced from 11.15 Hz to 8.60 Hz (this latter change is substantial, and no reason has been found to explain why the original mode was off), and (3) the structural damping (g_s) for the fuselage third bending was changed from 0.055 to 0.025. Having made these adjustments for the basic aircraft responses, no additional adjustments were made to the analyses with control systems operating.

Figure 23 displays the data matches for the frequency response with the SCAS operating. Comparing the first peak-response magnitude of this figure with the previous figure, it can be seen that the SCAS excites this peak some. Again, the analytical-to-test data match is excellent.

Figure 24 shows the data matches for the frequency response with both the SCAS and SMCS operating. The effectiveness of the SMCS in damping the first fuselage-bending mode is demonstrated by these data. The data match is

Note: δ_{cv} is control surface deflection. The flight-test data measurements of the forcing command were analytically processed to remove effects of actuator dynamics, which were measured, in order to permit comparisons with analytical results on this and similar subsequent figures.

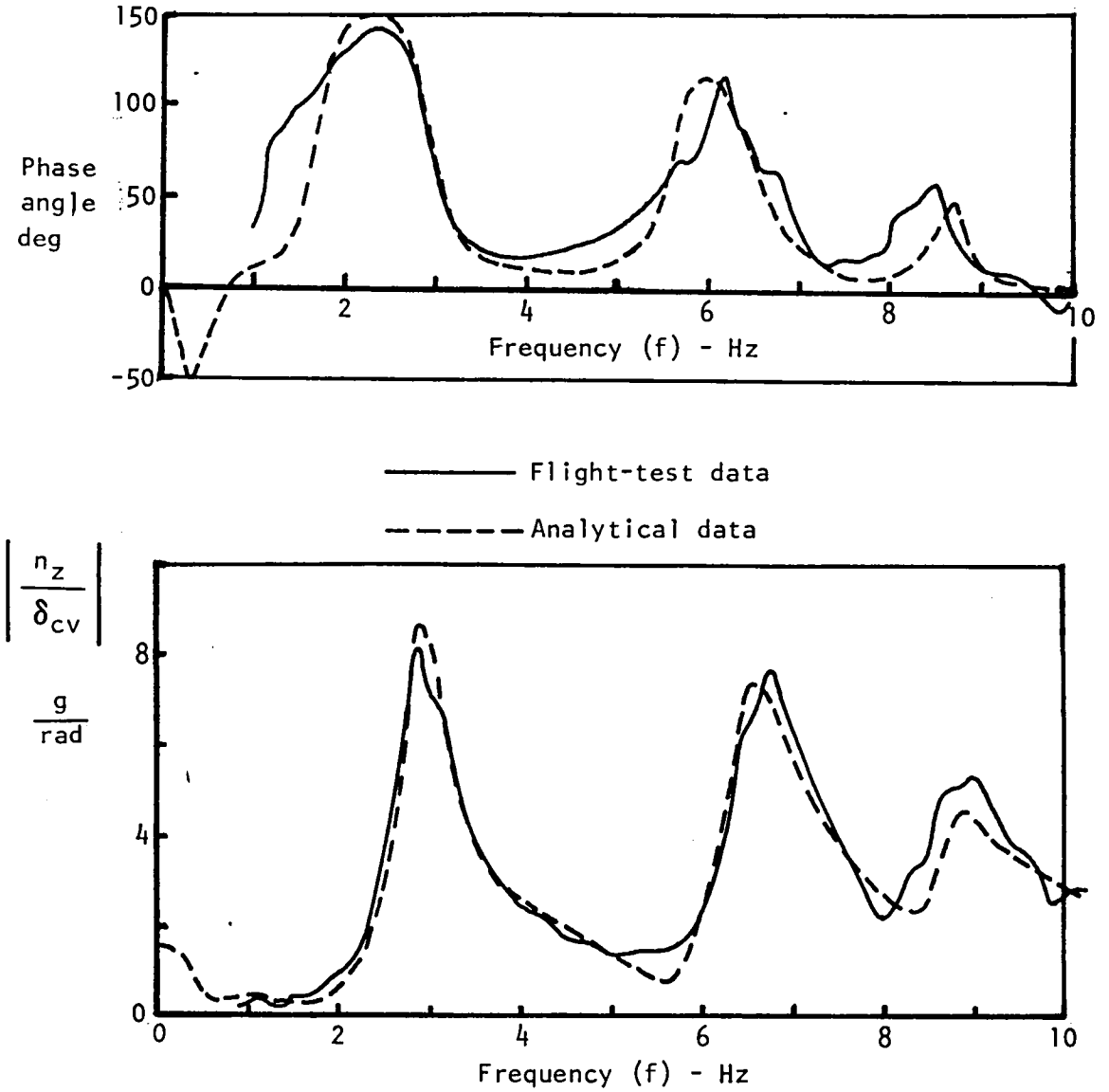

M = 0.85, alt = 762 m (2500 ft)
Wt = 119 296 kg (263 000 lb), Λ = 65°

Figure 22. - Comparison of flight test and analytical data, frequency response of normal load factor at FS 571.5 (225) due to SMCS vane deflection, SCAS off, SMCS off.

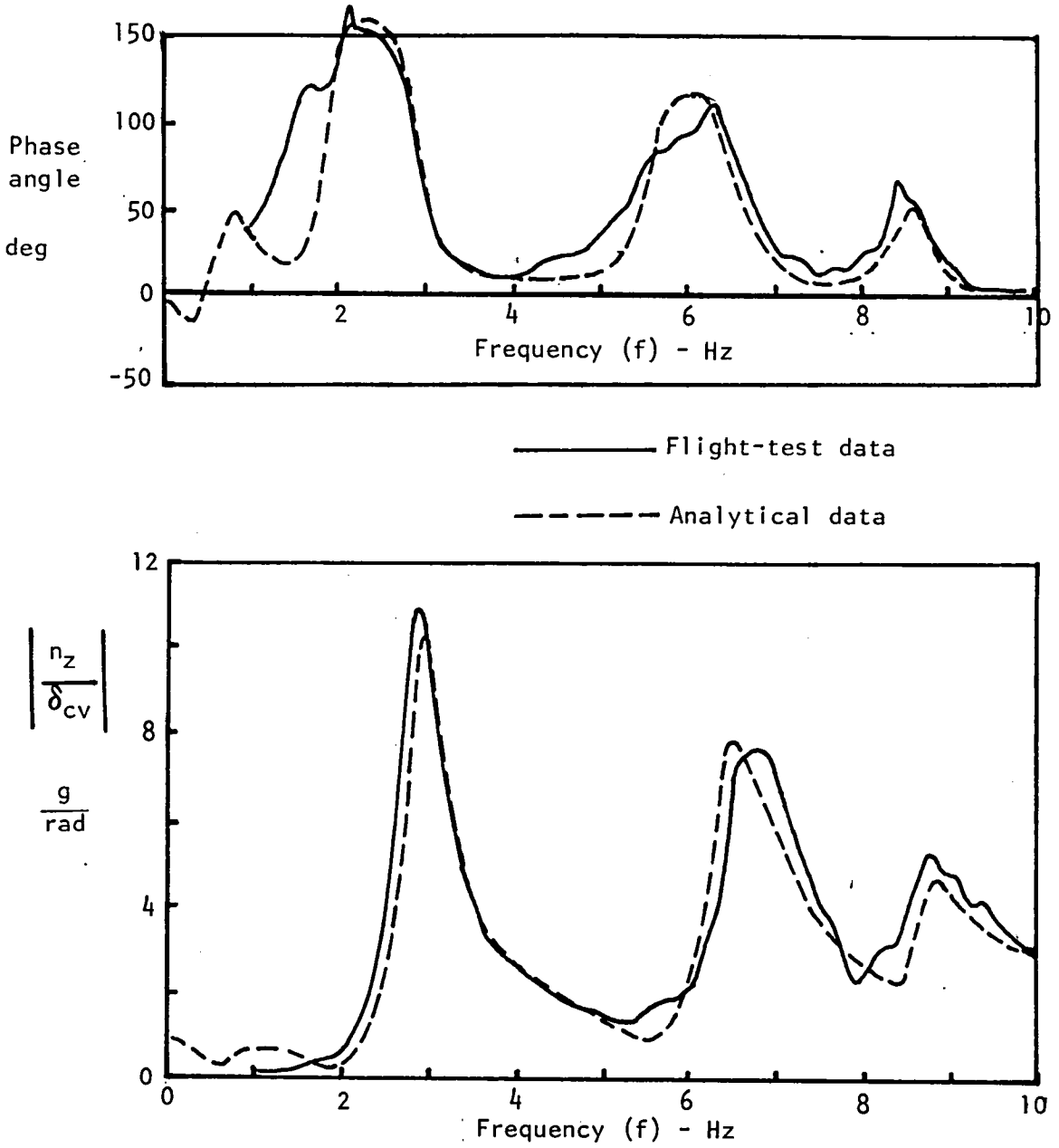

M = 0.85, alt = 762 m (2500 ft)
Wt = 119 296 kg (263 000 lb), $\Lambda = 65°$

Figure 23. - Comparison of flight test and analytical data, frequency response of normal load factor at FS 571.5 (225) due to SMCS vane deflection, SCAS on, SMCS off.

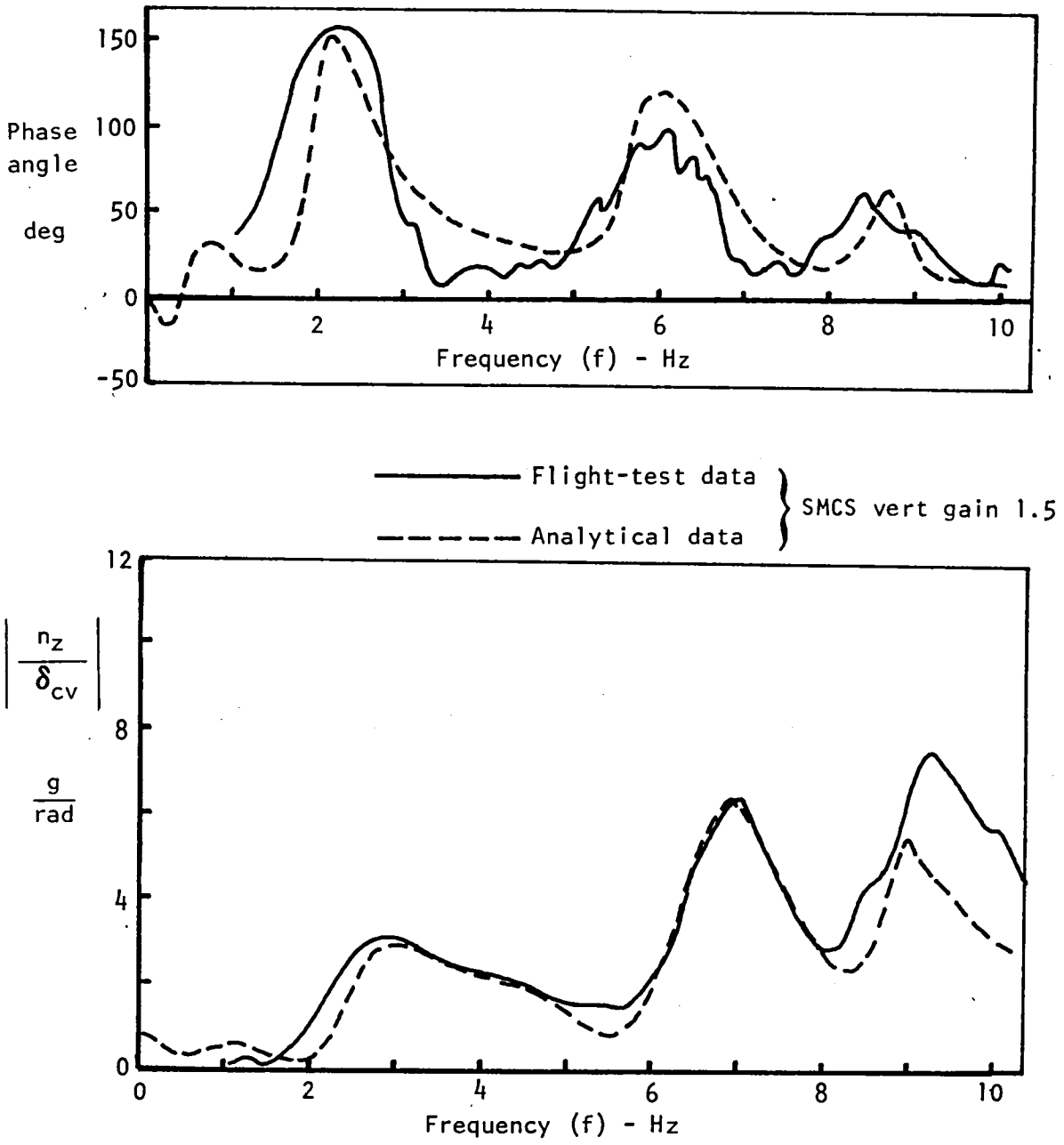

Figure 24. - Comparison of flight test and analytical data, frequency response of normal load factor at FS 571.5 (225) due to SMCS vane deflection, SCAS on, SMCS on.

excellent for the first two response peaks and fair for the third peak. The lack of better fit for this third peak was initially attributed to SMCS actuator modeling in this higher frequency range; however, using the flight-test-derived actuator model of figure 25 did not substantially improve the match to the flight-test data in the 8 to 10 Hz frequency range as shown in figure 26.

The comparison of the frequency response lateral load factor at FS 571.5 (225) due to differential SMCS vane deflections for the basic vehicle is shown in figure 27. The comparison is fair; the frequencies of the three peak responses are duplicated by the analyses, but the amplitude of the low-frequency peak is off by a considerable amount. The phase angle is matched reasonably well in the midfrequency range only; specific reasons for why the data do not match better are not known. The peaks are identified (starting with the low-frequency peak) as the wing fore and aft mode with a large fuselage side-bending component, fuselage first side bending, and second fuselage torsion. This last peak in the analysis was obtained by dropping the frequency for this mode from 9.72 to 7 Hz; although this mode was the only logical one to adjust, there is no reason known for the noted discrepancy. Having made this logical adjustment for the basic vehicle description, no other adjustments were made when the control systems were operated.

The data comparison of figure 28 are for the case of SCAS operating. The data are similar to the basic aircraft response of figure 27. Again, the agreement of analysis to test data is only fair.

In figure 29, the frequency response comparisons are made for the case of SCAS and SMCS operating. The trend of the analyses and the flight-test data are similar; i.e., the first and second peaks are attenuated but the peak around 7 Hz is increased by the SMCS operation.

The implications of these analytical/flight-test data comparisons are important to the B-1 ride quality verification. The data imply that the vehicle analytical stiffness and mass characteristics, whole-vehicle control-surface aerodynamics, SMCS vane aerodynamics and inertia reaction forces, and SCAS and SMCS modeling are fairly accurate. Thus, the ride quality characteristics can be calculated with considerable accuracy at specification or any other set of flight conditions. The longitudinal-symmetric aircraft characteristics have been more accurately described then the lateral-directional-antisymmetric set.

The aircraft ride quality characteristics have been calculated using the described data set and have been presented in reference 1, pages 56 and 57.

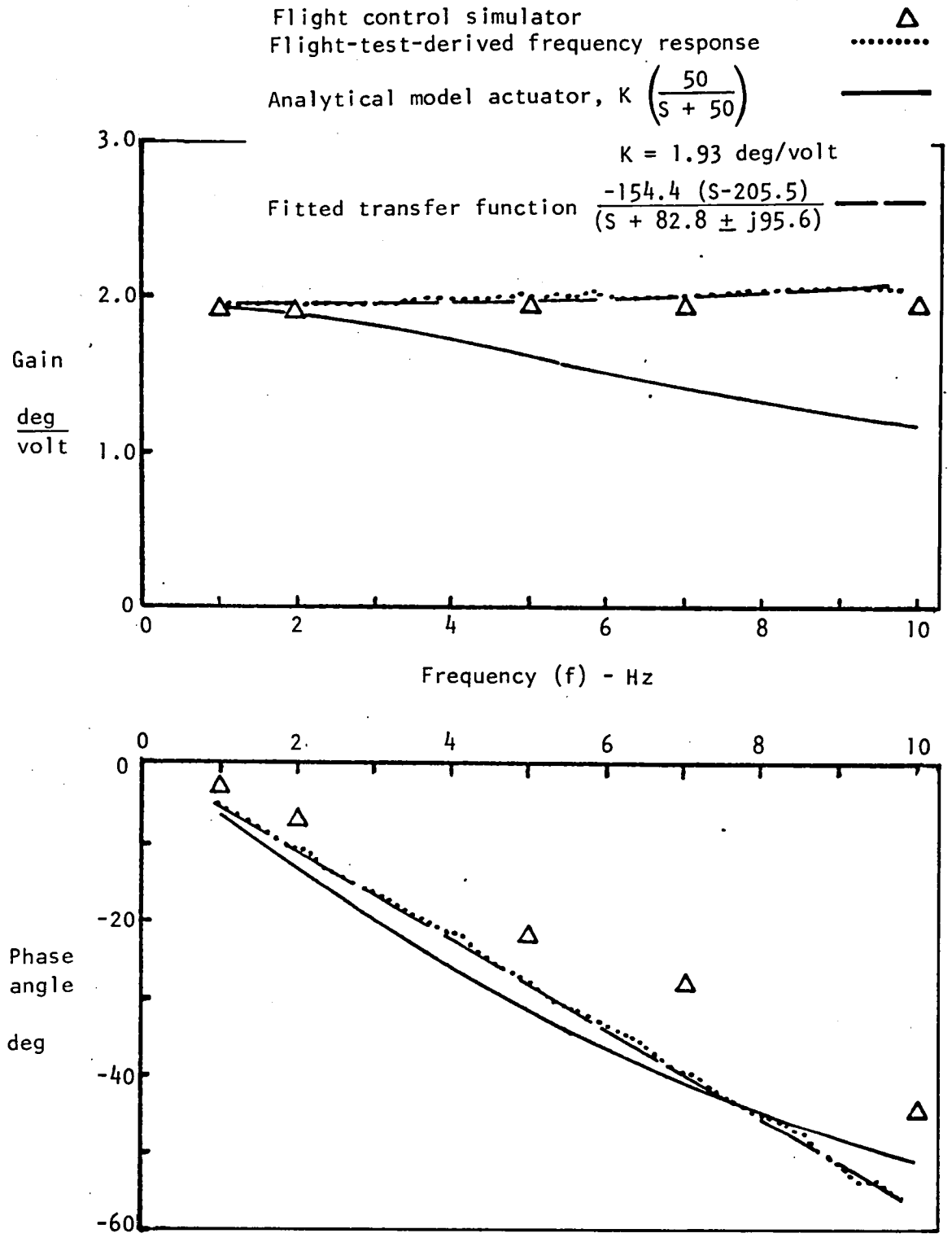

Figure 25. - Comparison of analytical SMCS actuator models to flight and simulator test data.

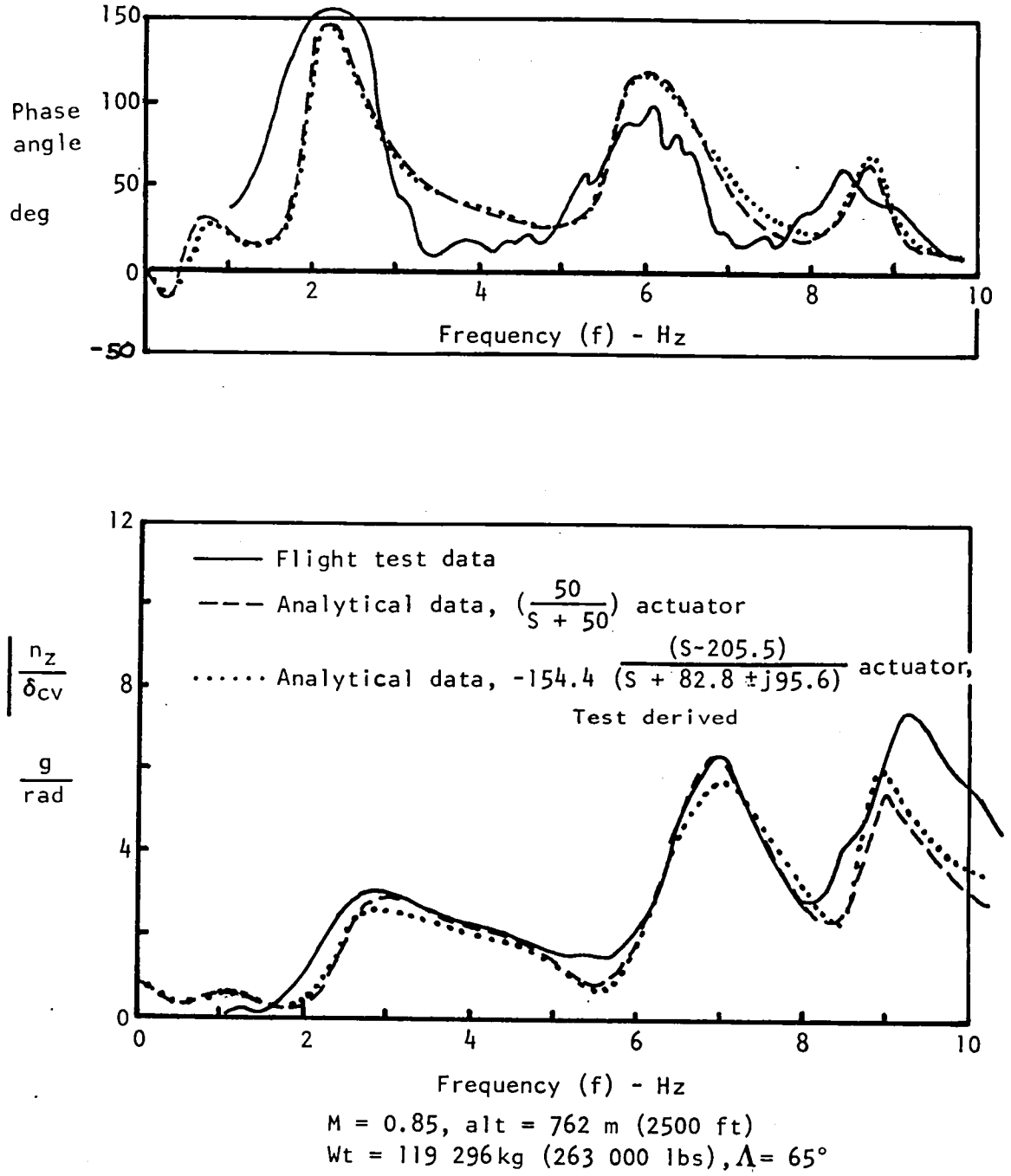

Figure 26. - Effect of test-derived SMCS actuator model, frequency response of normal load factor at FS 571.5 (225) due to SMCS vane deflection, SCAS on, SMCS on.

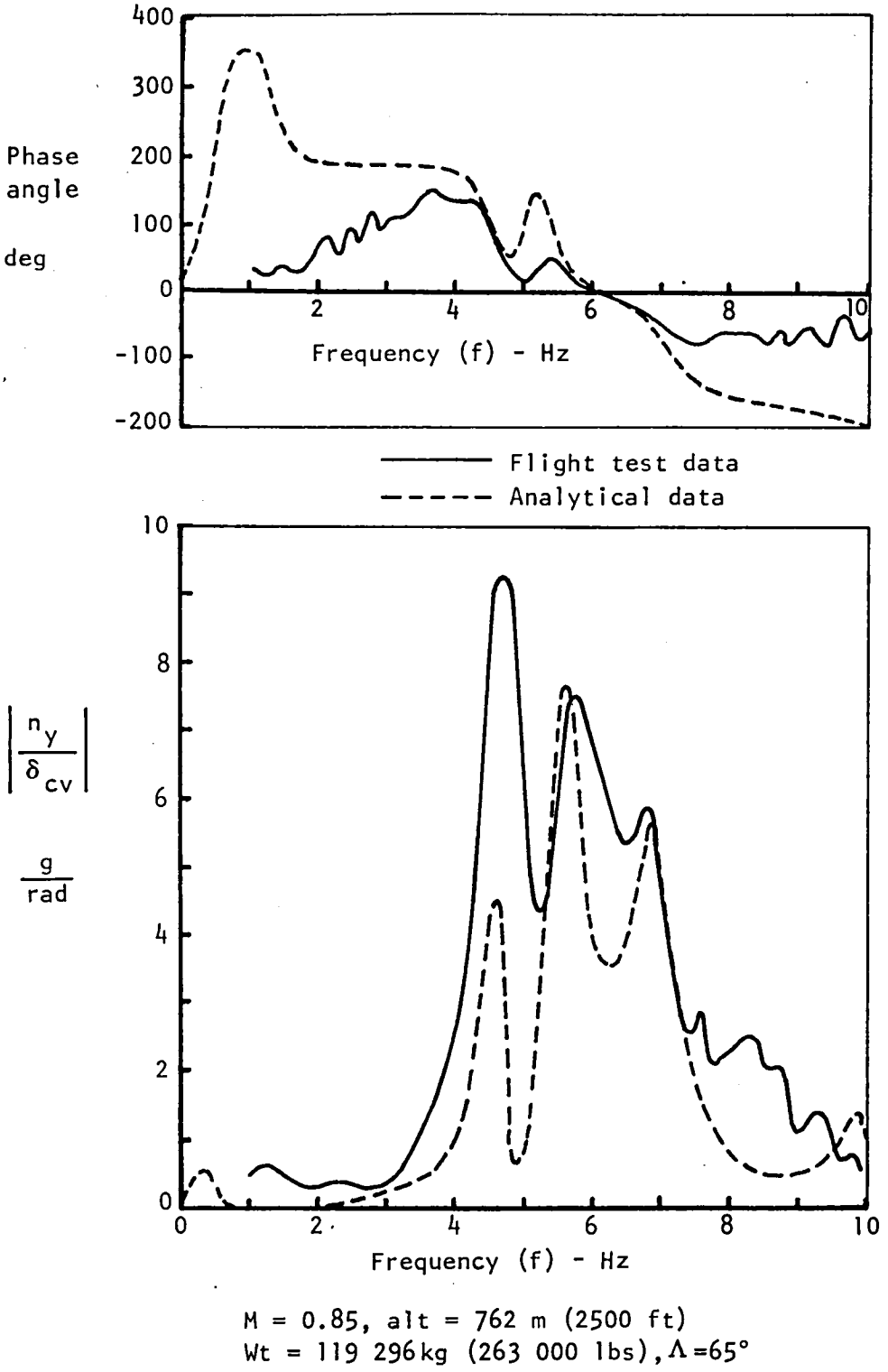

Figure 27. - Comparison of flight test and analytical data, frequency response of lateral load factor at FS 571.5 (225) due to SMCS vane deflection, SCAS off, SMCS off.

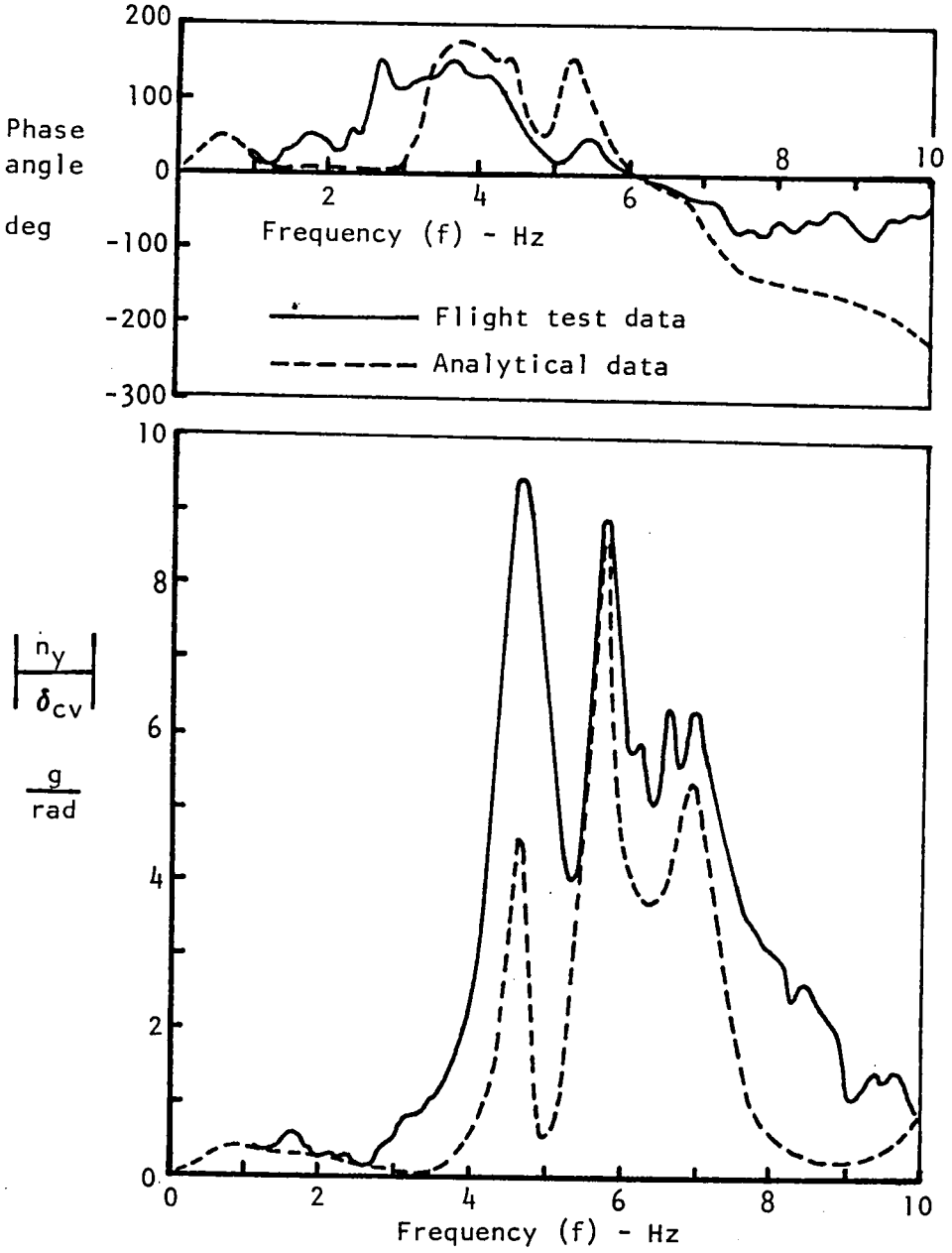

M = 0.85, alt = 762 m (2500 ft)
Wt = 119 296 kg (263 000 lb), Λ = 65°

Figure 28. - Comparison of flight test and analytical data, frequency response of lateral load factor at FS 571.5 (225) due to SMCS vane deflection, SCAS on, SMCS off.

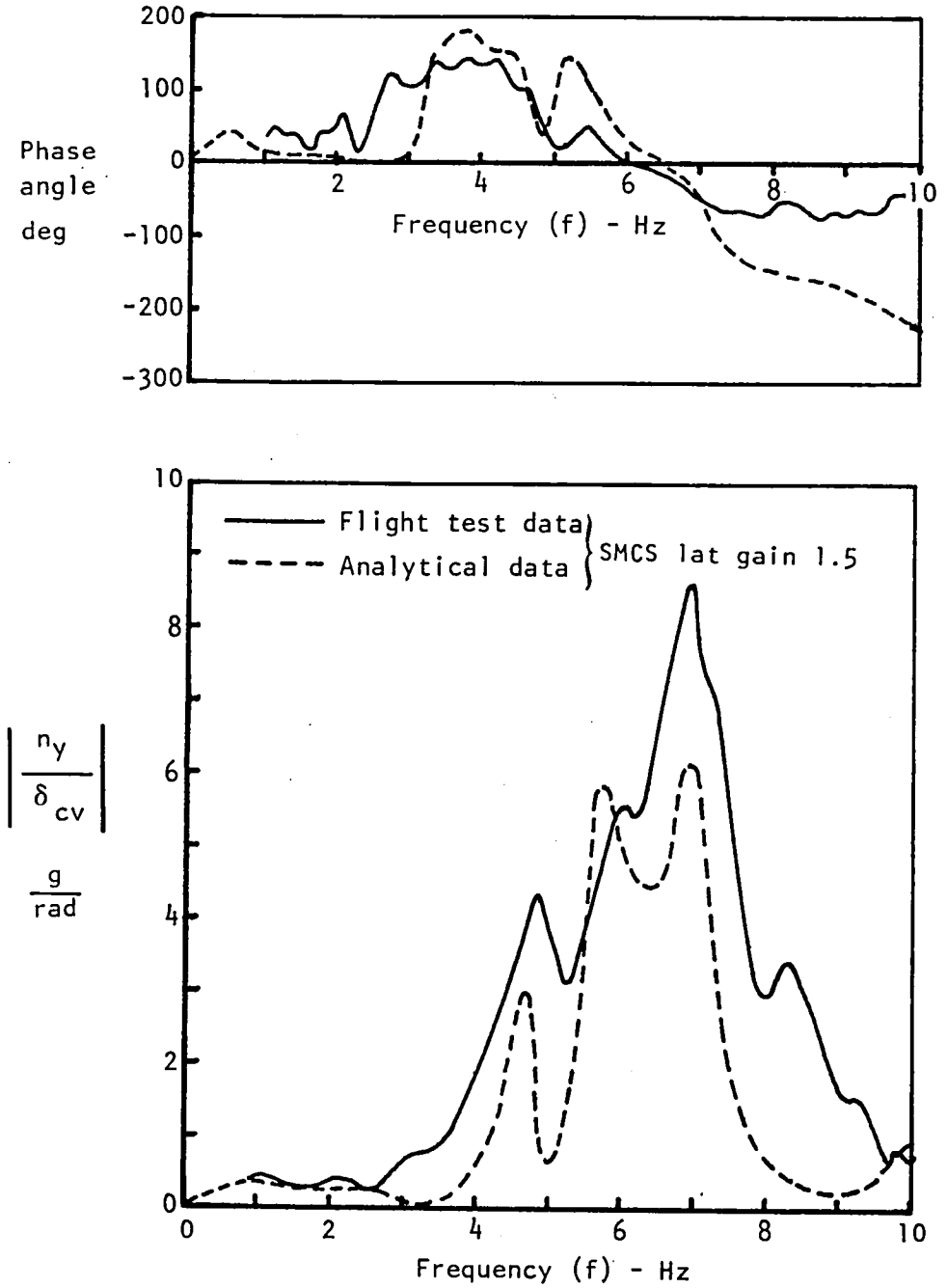

Figure 29. - Comparison of flight test and analytical data, frequency response of lateral load factor at FS 571.5 (225) due to SMCS vane deflection, SCAS on, SMCS on.

FORWARD SMCS SENSOR PACKAGE RELOCATION

On the whole, the SMCS has worked well in improving the ride quality of the low-altitude, high-speed flight regime operating at cockpit setting gains of 1.5 in the vertical and 1.5 in the lateral. The lateral axis performance, however, has been below that of the vertical.

As part of the ongoing investigation to determine how to improve the lateral SMCS performance, the data shown in figure 30 were obtained. The data shown are power spectral density (PSD) plots of the pilot station lateral acceleration response due to turbulence measured during flight 1-20 while flying at M = 0.80 at about 305 meters (1000 feet) altitude. The data show that the SMCS, with the lateral gains set at 1.5, significantly reduces the key peak response at 4.5 Hz, slightly modifies a second peak at 6 Hz, and increases the response significantly at 7 Hz. The net effect is an improvement in ride quality but not a large one. When the pilot increased the lateral gain to 2.2, there was a dramatic increase of the approximately 7 Hz response to a level which was felt by the crew to be not acceptable even though the 4.5 and 6 Hz responses were further reduced.

The comparison of the flight-test and analytical lateral acceleration frequency responses due to vane excitation shown in figure 29 demonstrated that the analytical model could reproduce the essence of 7 Hz increased response. A study of the analysis results indicated that the two peak responses at 4.5 and 6 Hz are due to fuselage side bending components in these modes while the response at 7 Hz is the fuselage second torsional mode. Figure 31 will assist in showing how the response phenomenon observed occurs. Key in the analysis is the location of the SMCS sensor package at fuselage station FS 571.5 (225), WL 142.24 (56) and BP 60.96 (24). Both the vertical and lateral accelerometers are located in this package. As the vanes are differentially deflected, a side force and a torque are created. The lateral accelerometer sees lateral acceleration due to both the side force and torque. When the lateral acceleration signals are sent through the SMCS, the side bending-induced signals are properly phased but the torsion-induced signals are adversely phased, resulting in a reduced gain margin of the 7 Hz mode. It is also important to note that the vertical accelerometer also sees the torque-induced motion, and undesirable SMCS symmetrical vane motions are caused by lateral SMCS operation. Data, however, have shown this not to be a large influence.

Analyses shown in figure 32 indicate that observed adverse torsion coupling, as well as the coupling into the vertical axis, could be eliminated or attenuated by relocating the SMCS sensor package close to the fuselage centerline and near the elastic axis. Since there would be no lateral moment arm, the coupling to the vertical axis would actually result in the torsional signal phasing being favorable.

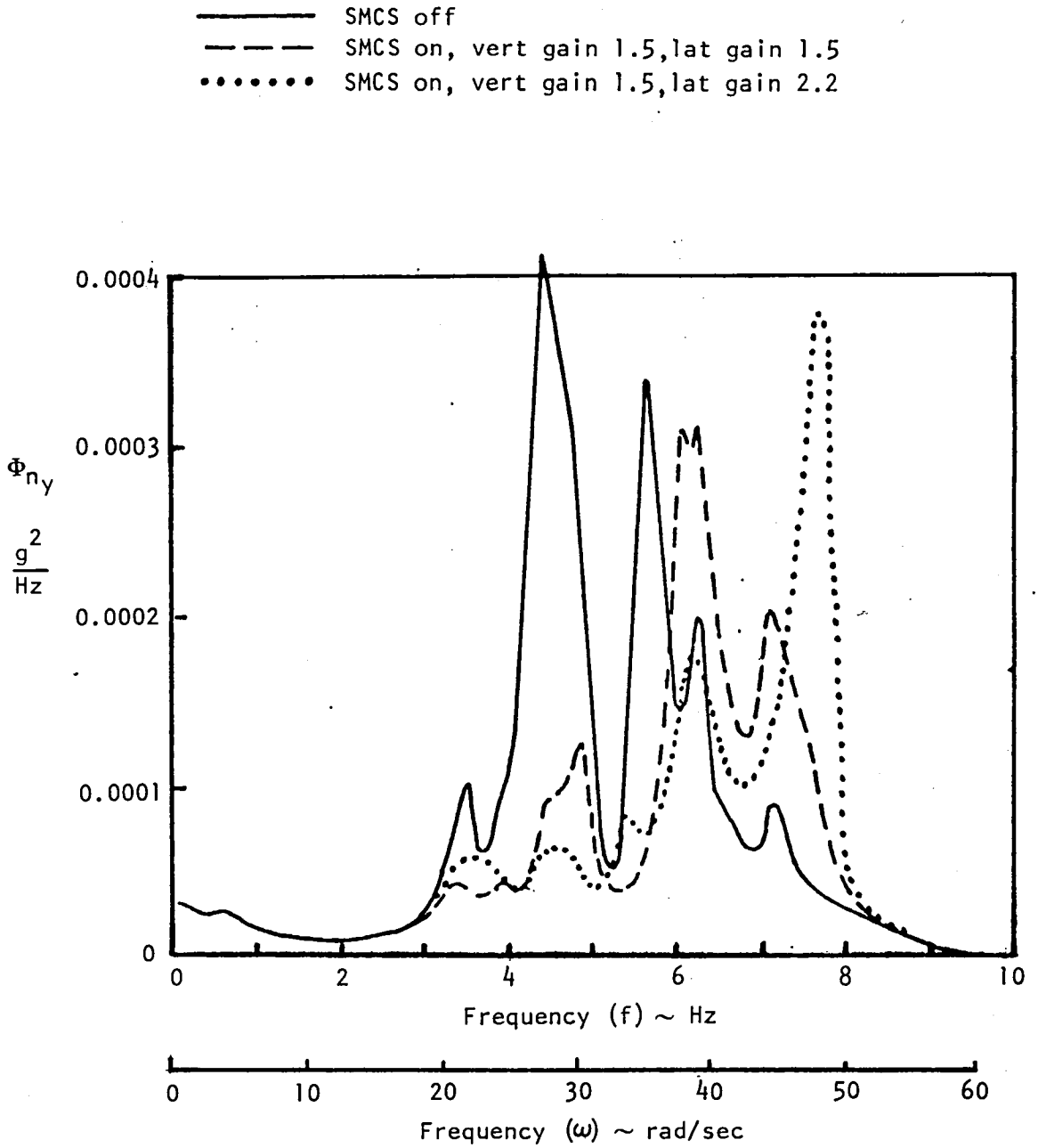

Figure 30. - Effect of SMCS lateral gain on power spectral density of lateral load factor at pilot station FS 746.8(294).

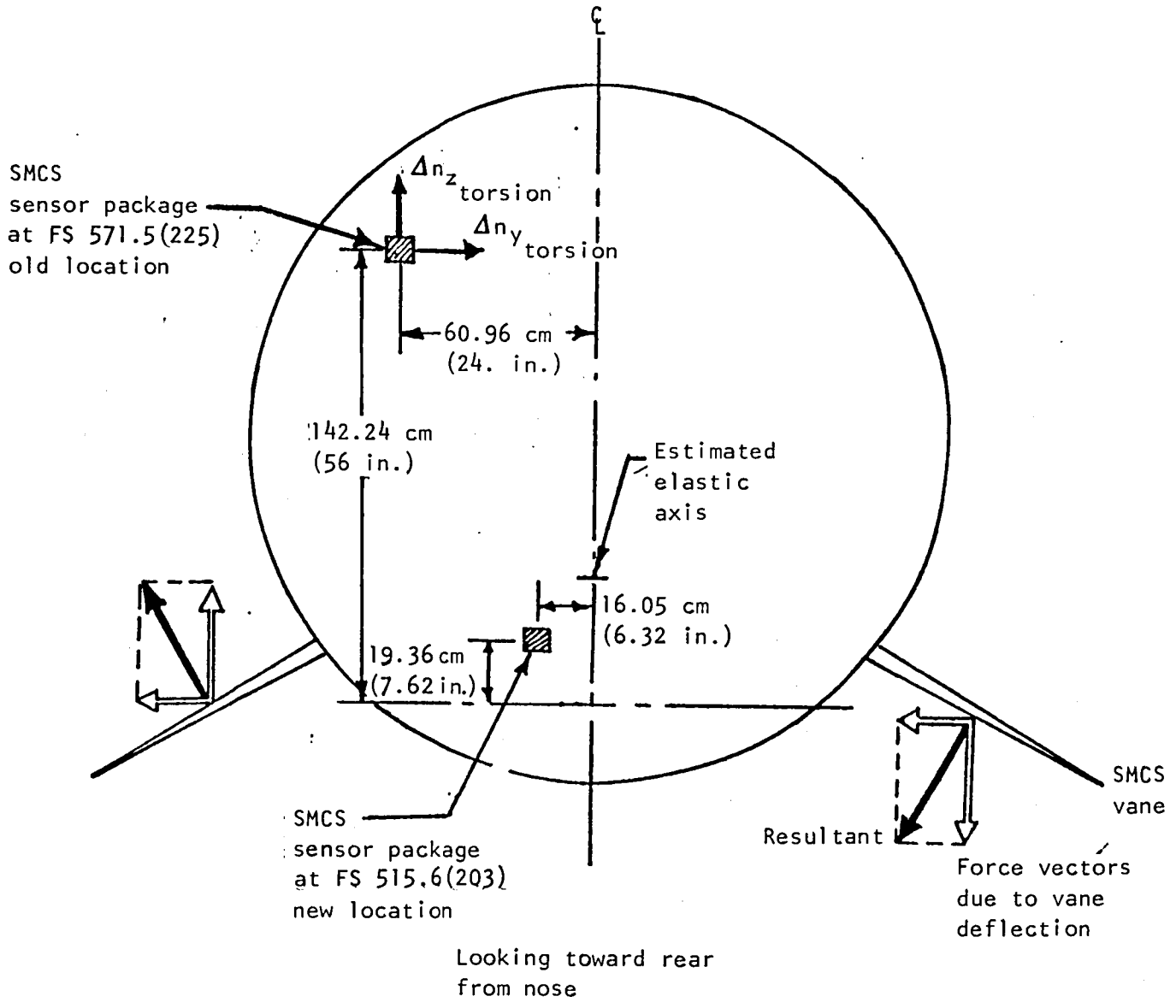

Figure 31. - SMCS sensor package locations and coupling characteristics.

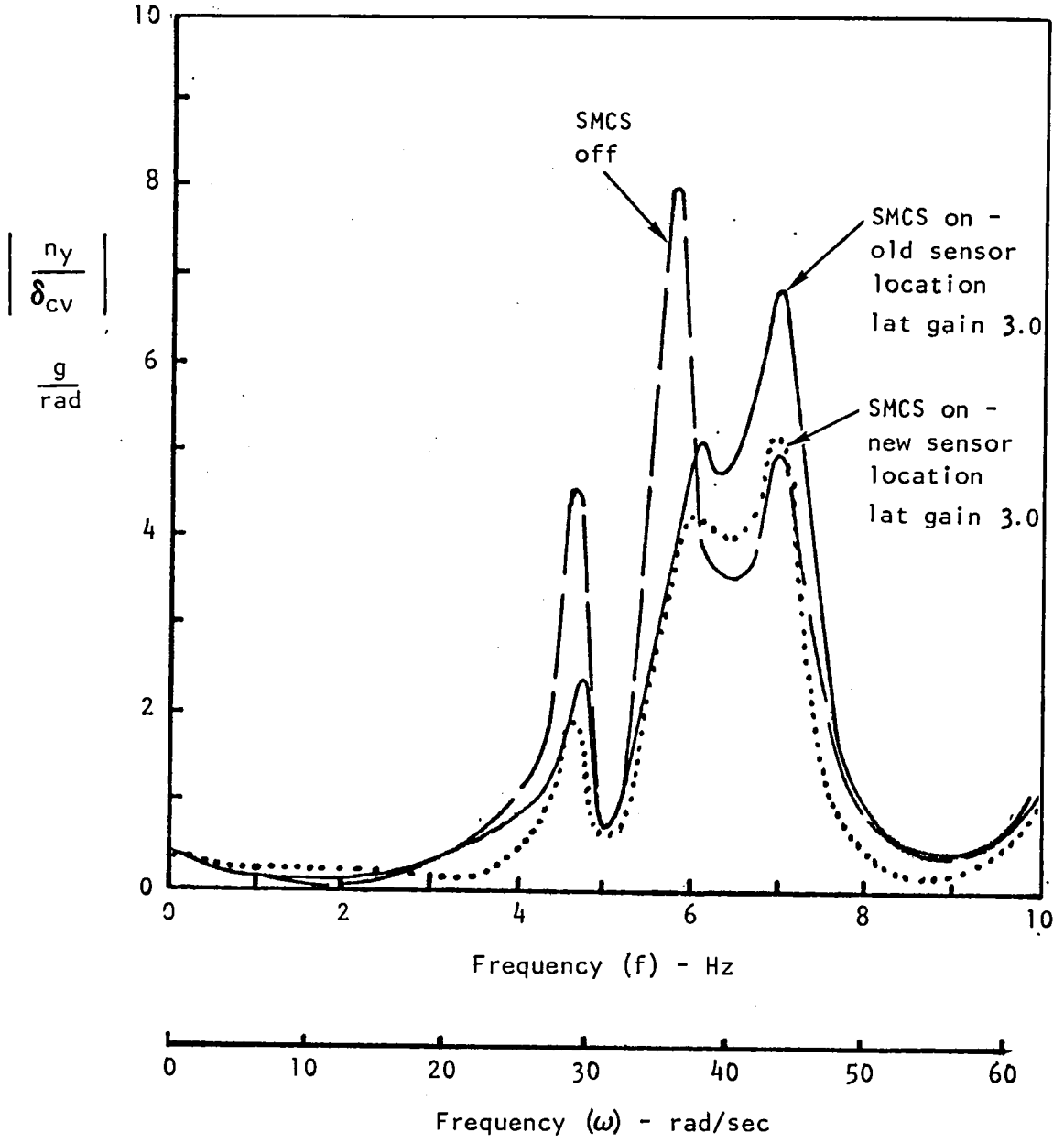

M = 0.85, alt = 762 m (2500 ft)
Wt = 119 387 kg (263 000 lb), Λ = 65°

Figure 32. - Effect of SMCS sensor package location on lateral load factor at FS 571.5 (225) due to differential vane deflection, analytical data.

The advantages of moving the SMCS package may be summarized as follows:

(1) Higher lateral gains could be used to improve lateral ride quality.

(2) Higher effective vertical gains (due to a farther forward sensor location) would improve vertical ride quality.

(3) The coupling of lateral vane inputs to the vertical axis would be eliminated.

As substantiated by both pilot comment and flight-test data, the original SMCS considerably improved the ride quality. However, the gains in the system were limited to values below those originally intended by the coupling described herein and not by system maximum capability. Based on the described advances, action was taken to move the forward SMCS sensor package to the new location at FS 515.6 (203), WL 19.36 (7.62) and BP 16.05 (6.32). This relocation was first accomplished on A/C-1 and then on A/C-2; this modification was never accomplished on A/C-3. A/C-4 has the sensor package at the new location.

SMCS stability tests were initially performed at high altitude to evaluate the forward SMCS sensor package relocation effects. The flight condition/configuration was M = 0.85, altitude 6096 meters (20 000 feet) and weight 119 297 kilograms (263 000 pounds).

The first fuselage vertical bending-mode damping obtained from the pitch-pulse transient data is shown in figure 33 and is seen to be a linear function of the SMCS gain. All other modes were stable at the indicated gain conditions. The first fuselage bending-mode damping with the SMCS forward accelerometer relocated (flight 1-41) is compared with the results with the accelerometer in its previous location (flight 1-7). The mode damping appears to be significantly larger at the higher gains with the new sensor location.

The lateral bending modes were not stimulated significantly by the rudder pulses, so that similar damping characteristics could not be obtained. However, the lateral SMCS was stable for all values of gain tested (maximum cockpit knob setting of 6). Results obtained with the previous sensor location (flight 1-7) showed the SMCS to be unstable at a setting of 6.

Following the high-altitude test, stability tests were conducted at low altitude. The initial flight condition/configuration was M = 0.85, altitude 914.4 meters (3,000 feet), Λ = 65 degrees, and weight 119 297 kilograms (263 000 pounds). The excitations were horizontal tail and rudder pulses. First, each axis was tested to a maximum gain for that axis (V-gain = 3.0 and L-gain = 3.0, respectively). Following this, tests were conducted with the

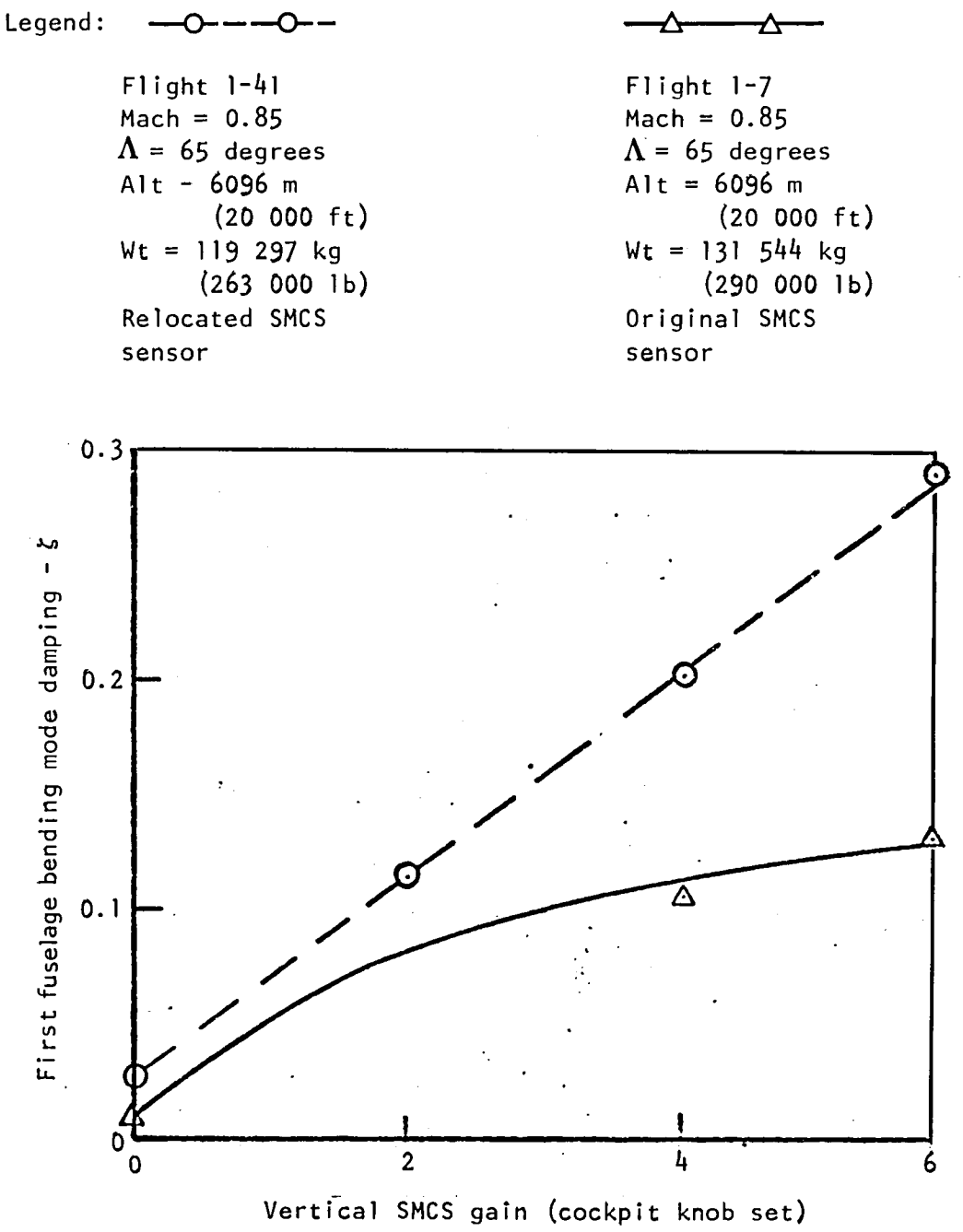

Figure 33. - First fuselage vertical bending mode damping versus SMCS gains for original and relocated forward sensor package.

SMCS operating in each axis simultaneously. The maximum combined setting was V-gain and L-gain = 3.0. The quality of the response data was such that the damping factor could not be numerically determined; however, these qualitative data indicated that the SMCS was stable.

Following the horizontal tail and rudder pulse-stability checks, SMCS response to SMCS vane excitation evaluations were made. Figure 34 contains the vertical-axis-response data. Shown are the normal load factor at FS 515.6 (203) (sensor location) frequency response due to SMCS symmetric vane deflections for SMCS off and SMCS on at vertical gains of 1.5 and 1.8. These data show good performance for the vertical SMCS and are not significantly different from the similar data of figure 24 for the SMCS forward sensor package at the original location.

Figure 35 shows the lateral load factor at FS 515.6 (203) (sensor location) frequency responses due to differential SMCS vane deflections for SMCS off and on at lateral gains of 1.5 and 2.2. As shown, the large 5 Hz (approximate) first fuselage lateral bending mode was significantly attenuated at the higher gain without the previously noted large adverse torsional coupling response at approximately 7 Hz.

Figure 36 shows the lateral load factor at FS 746.8 (294) (pilot station) frequency responses due to differential SMCS vane deflections for the SMCS off and on at lateral gains of 1.5 and 2.2. As on the previous plot, the large 5 Hz first fuselage lateral bending mode was significantly attenuated at higher gains. The 7 Hz response, however, shows a slight increase in magnitude over the zero gain response.

Additional data similar to that just described, but at a higher weight condition, are shown in figures 37 and 38. These data indicate less attenuation of the 5 Hz mode and more excitation of the next higher frequency mode peak.

Remembering that the lateral nominal gain setting is 1.5, all of these data indicated a substantial net improvement in lateral load-factor response due to the SMCS.

To further check out the relocated forward sensor package, tests were conducted at the off-design condition at M = 0.55, altitude 762 meters (2500 feet), Λ = 55 degrees. Figure 39 presents the normal load factor at FS 515.6 (203) frequency response due to symmetric SMCS vane deflection for SMCS off and on at vertical gains 2.5 and 3.0. These data show good performance for the vertical SMCS at this off-design condition.

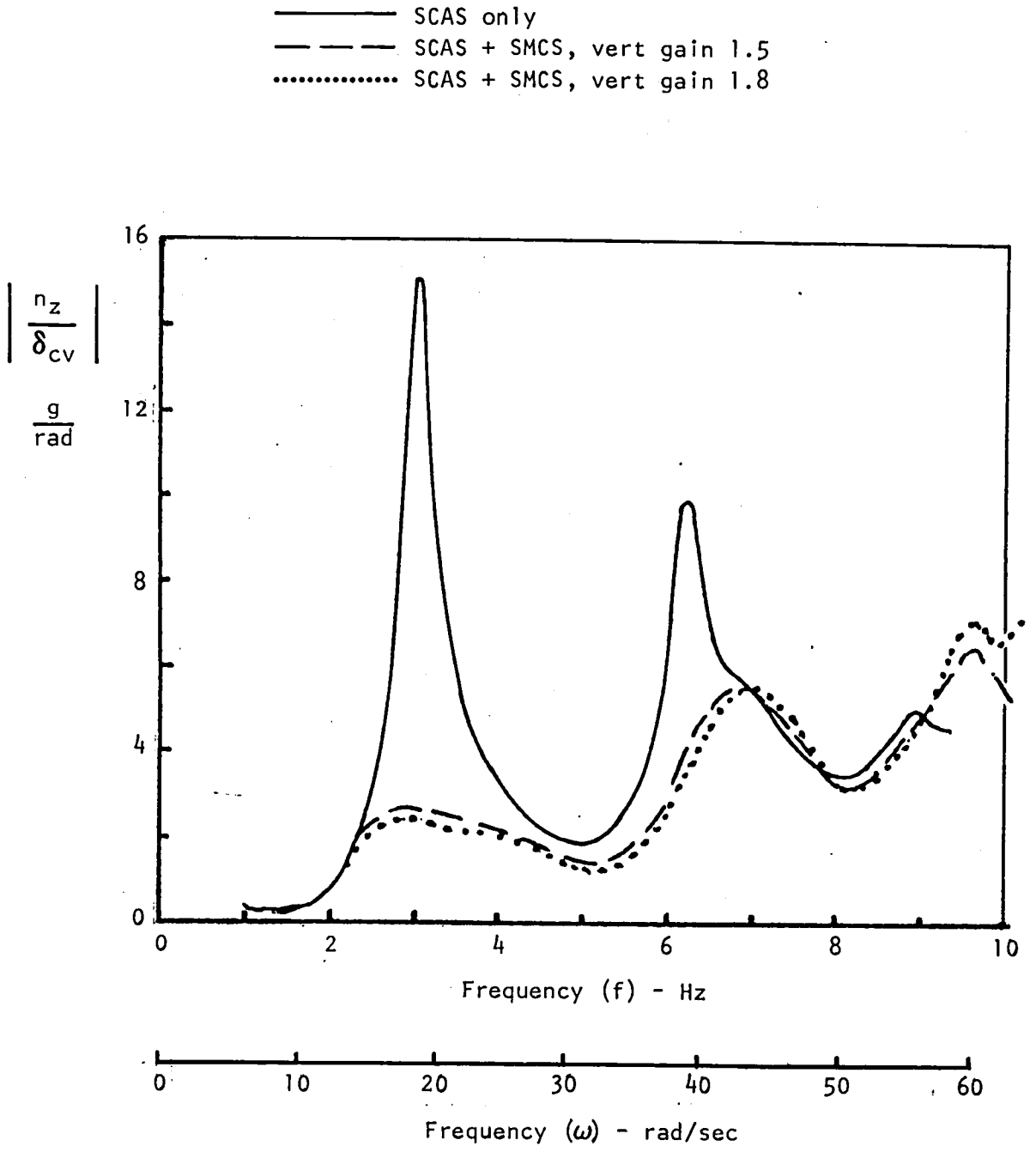

Figure 34. - SMCS vertical axis performance with relocated forward sensor package, frequency response of normal load factor at FS 515.6 (203) due to SMCS vane deflection, case 1.

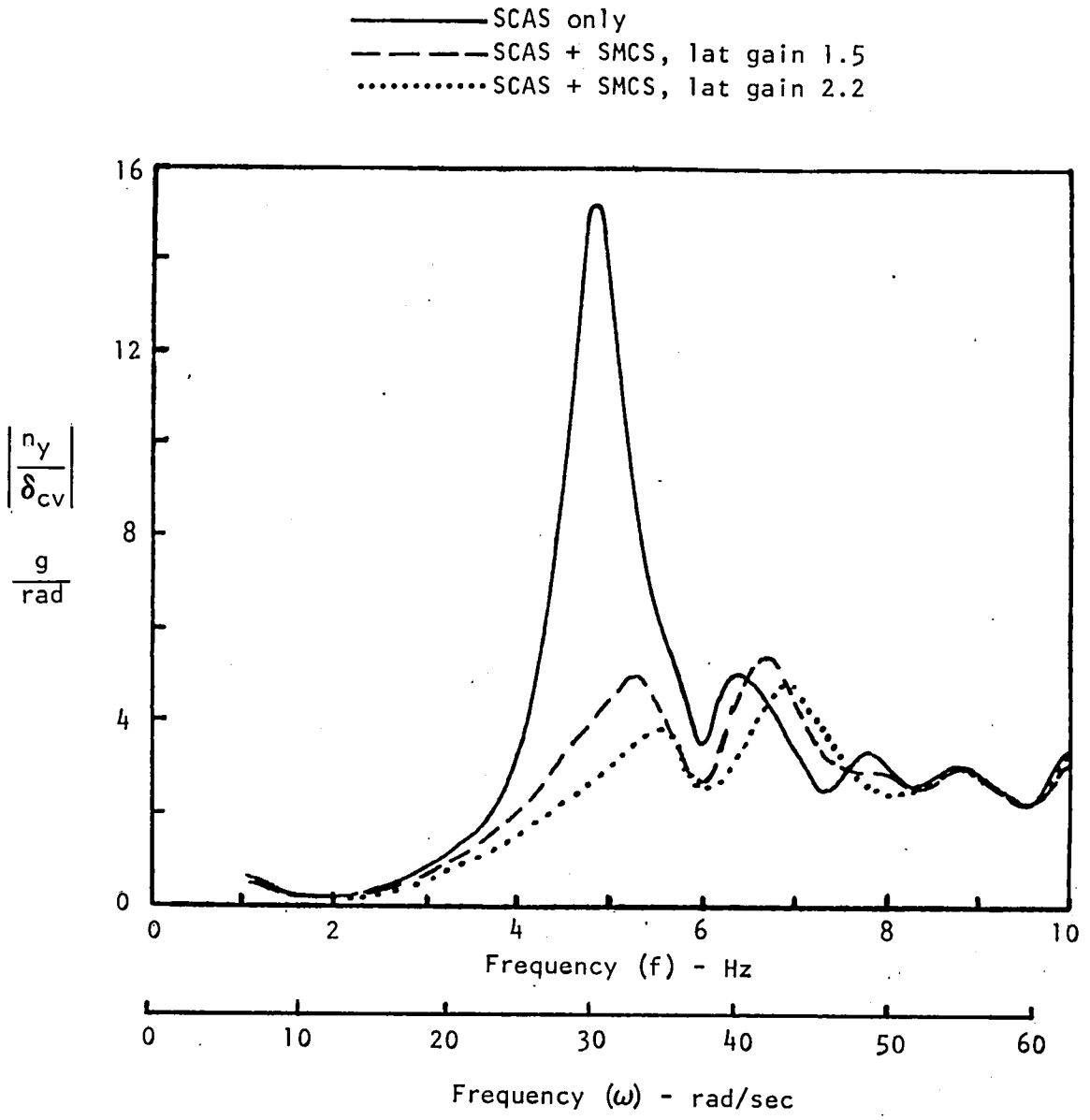

M = 0.85, alt = 914m (3000 ft)
Wt = 122 018kg (269 000 lbs), Λ = 65°

Figure 35. - SMCS lateral axis performance with relocated forward sensor package, frequency response of lateral load factor at FS 515.6 (203) due to SMCS differential vane deflection, case 1.

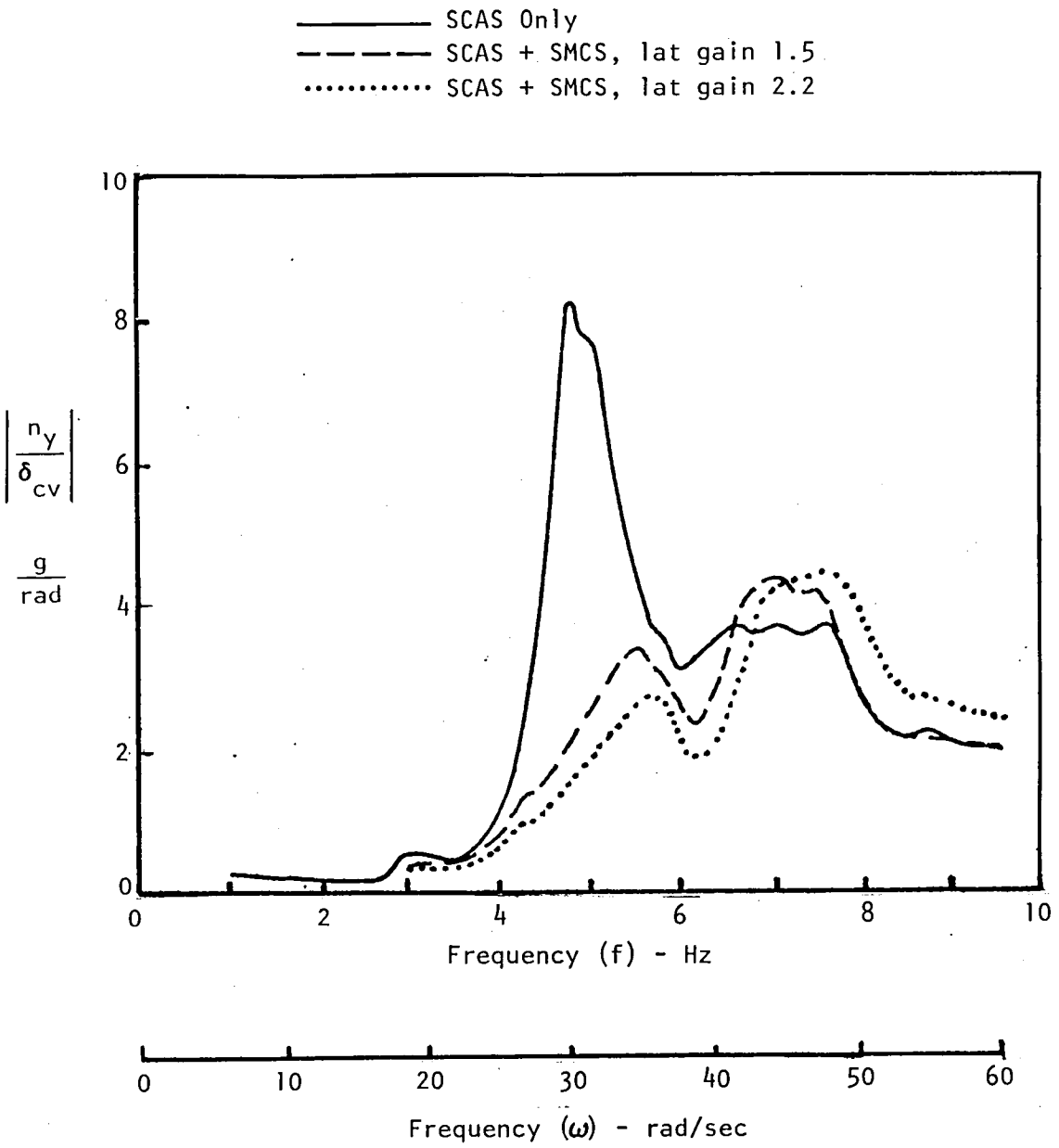

M = 0.85, alt = 914m (3000 ft)
Wt = 122 018kg (269 000 lb), Λ = 65°

Figure 36. - SMCS lateral axis performance with relocated forward sensor package, frequency response of lateral load factor at FS 746.8 (294) due to SMCS differential vane deflection, case 1.

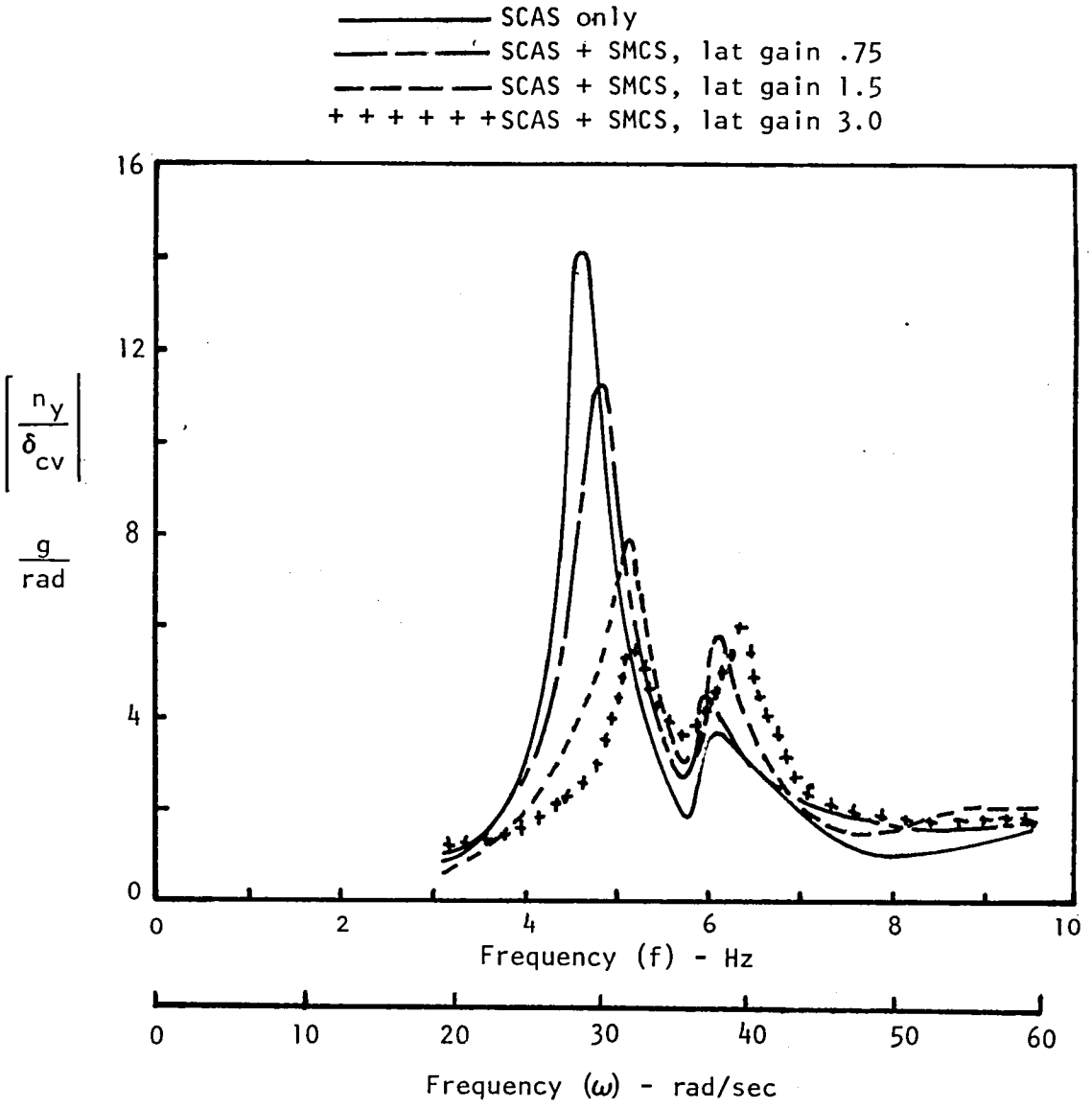

M = 0.85, alt = 487 m (1600 ft)
Wt = 139 709 kg (308 000 lb), Λ = 65°

Figure 37. - SMCS lateral axis performance with relocated forward sensor package, frequency response of lateral load factor at FS 515.6 (203) due to SMCS differential vane deflection, case 2.

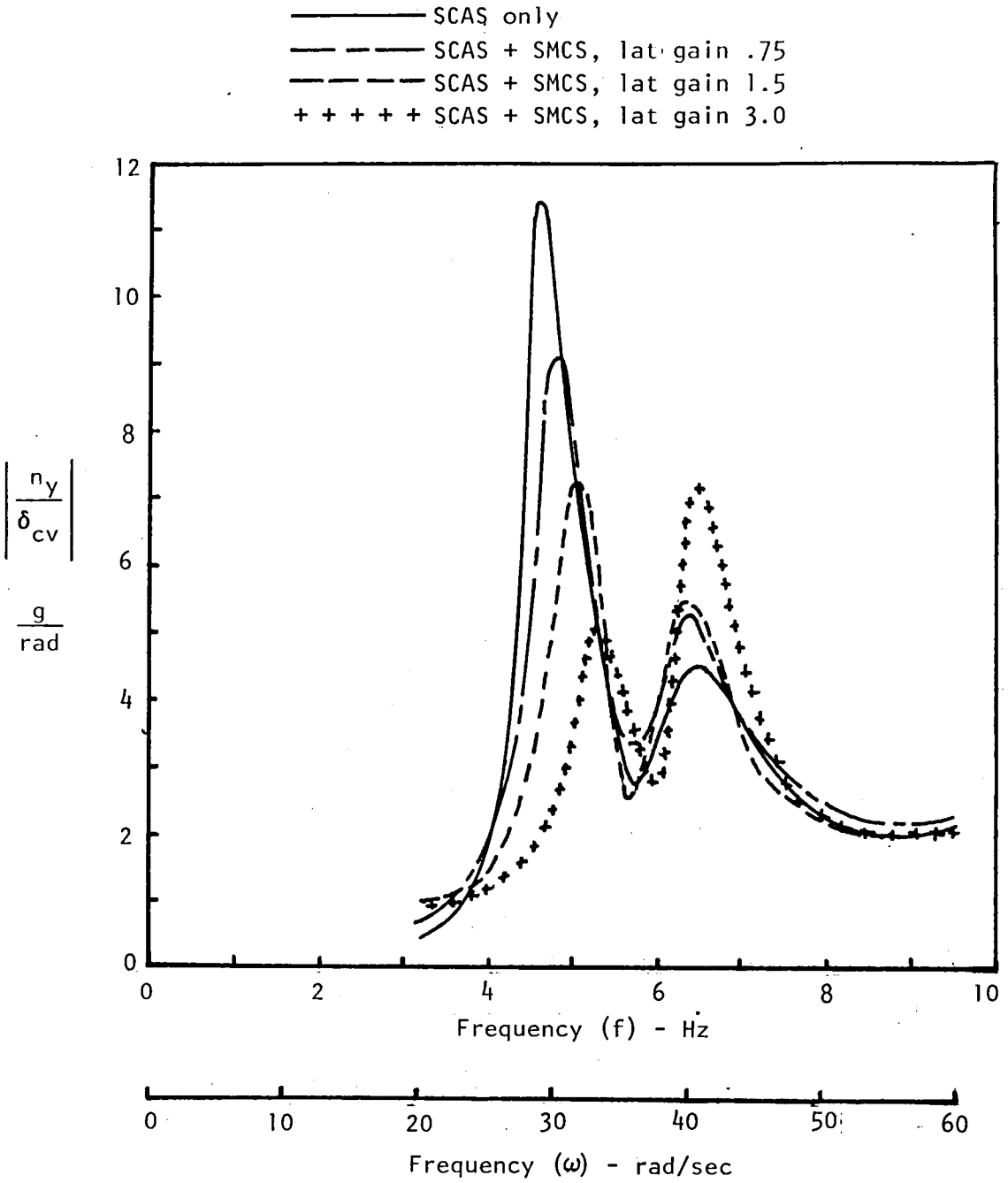

Figure 38. - SMCS lateral axis performance with relocated forward sensor package, frequency response of lateral load factor at FS 746.8 (294) due to SMCS differential vane deflection, case 2.

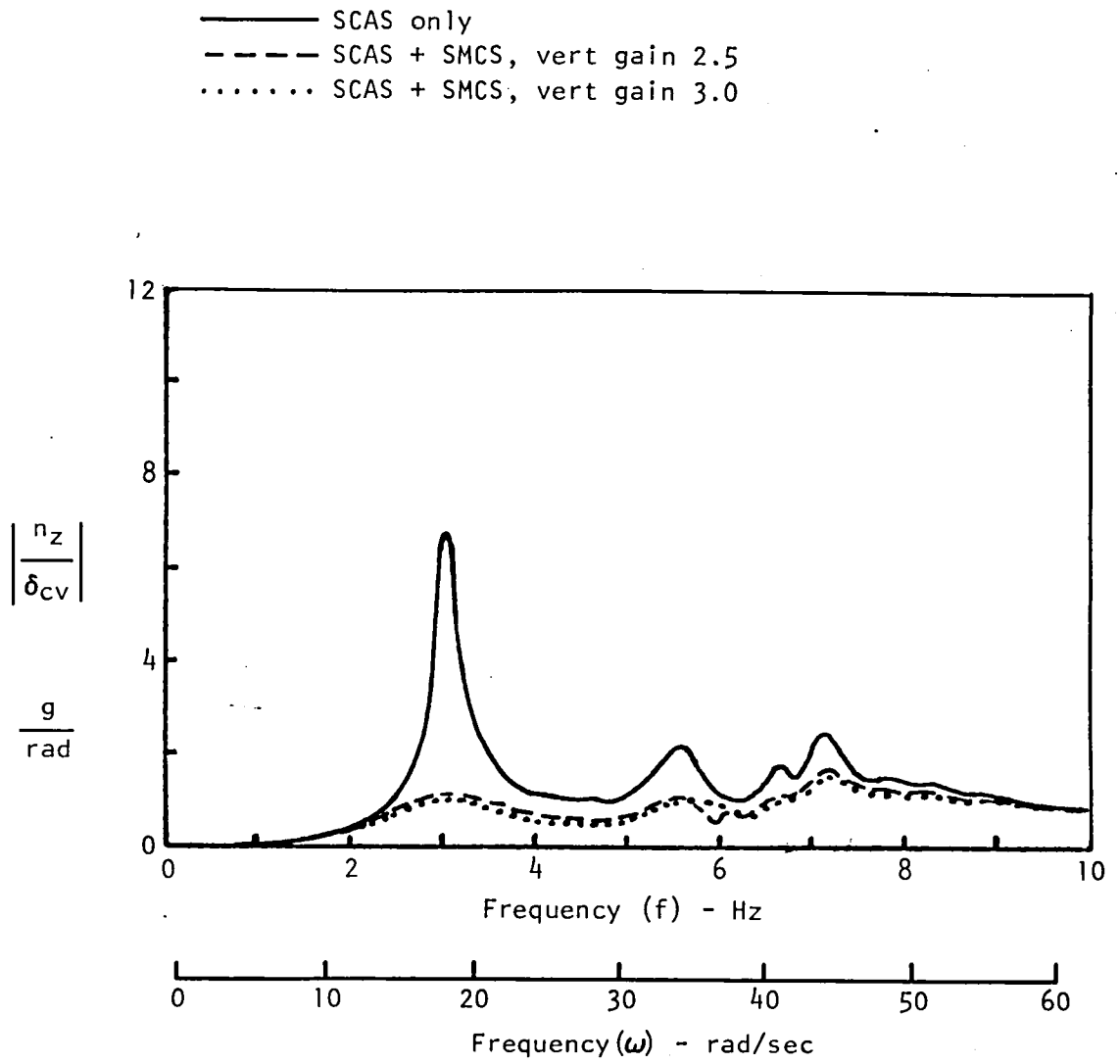

Figure 39. - SMCS vertical axis performance with relocated forward sensor package, frequency response of normal load factor at FS 515.6 (203) due to SMCS vane deflection, case 2.

Figure 40 shows the lateral load factor at FS 515.6 (203) frequency response due to differential deflection of the SMCS vanes for the SMCS off and on at lateral gains of 2.5 and 3.7. As shown, the large 5 Hz first lateral side-bending mode was significantly attenuated at the higher gains without the previously noted adverse torsional response at approximately 7 Hz.

In addition to the preceding frequency response data, SMCS performance data in turbulence were obtained to evaluate the relocated forward SMCS sensor package. Figure 41 is a power spectral density plot of the pilot station (FS 746.8 (294)) vertical load-factor response due to turbulence with the SMCS off and on at vertical gains of 1.5 and 1.9. As shown, the SMCS was very effective in attenuating the first fuselage vertical bending response.

The power spectral density of the load-factor response was normalized to unit root mean square (RMS) gust intensity (σ_{w_g}) as derived from the angle of attack (α vane) data. This is not an accurate technique but is the best available in absence of gust boom data. A similar normalization (σ_{v_g}) has been attempted for the lateral axis data using sideslip (β vane) data.

Figure 42 shows the lateral load-factor response at the pilot station with the lateral SMCS gain zero but the vertical gains at 0, 1.5, and 1.9. Since there is no mechanism for the vertical axis SMCS motion to couple into the lateral axis, these data indicate the level of repeatability of the lateral data.

Figure 43 contains vertical load-factor response data at the pilot station with the SMCS off and on at vertical gains of 1.5 and 1.9, together with lateral gains of 1.5 and 2.2, respectively. Comparisons of these data with the data of figure 41 show that little or no coupling of the lateral axis activity is evident in the vertical axis response.

Figure 44 shows the SMCS performance in the lateral axis at FS 515.6 (203) with the SMCS off and lateral gains of 1.5 and 2.2. These data show that the 5 Hz (approximately 30 radians per second) first fuselage lateral bending mode is significantly attenuated at both gain settings. However, at gain setting 1.5, the second fuselage lateral bending-mode peak response near 6 Hz remains about the same in magnitude but shifts slightly upward in frequency. At lateral gain of 2.2, a significant increase in magnitude develops with this frequency shift.

Similar data to figure 44 for the pilot station are shown in figure 45. These data show the 5 Hz mode reduction but indicate an increased coupling with gain increase of the higher modes.

Attention is directed to the power spectral density scales for figures 44 and 45. The data of figure 45 are a factor of 100 smaller than figure 44.

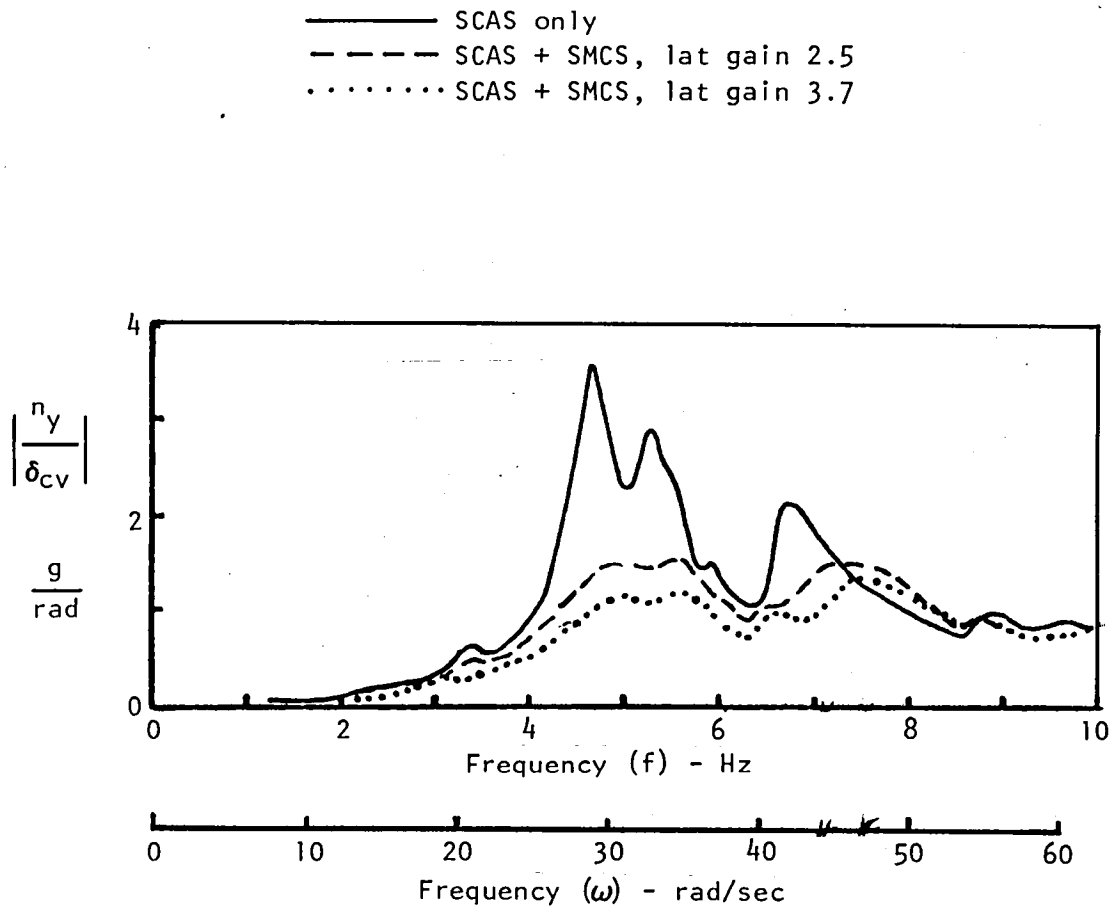

M = 0.55, alt = 762 m (2500 ft)
Wt = 129 276 kg (285 000 lbs), Λ= 55°

Figure 40. - SMCS lateral axis performance with relocated forward sensor package, frequency response of lateral load factor at FS 515.6 (203) due to SMCS differential vane deflection, case 3.

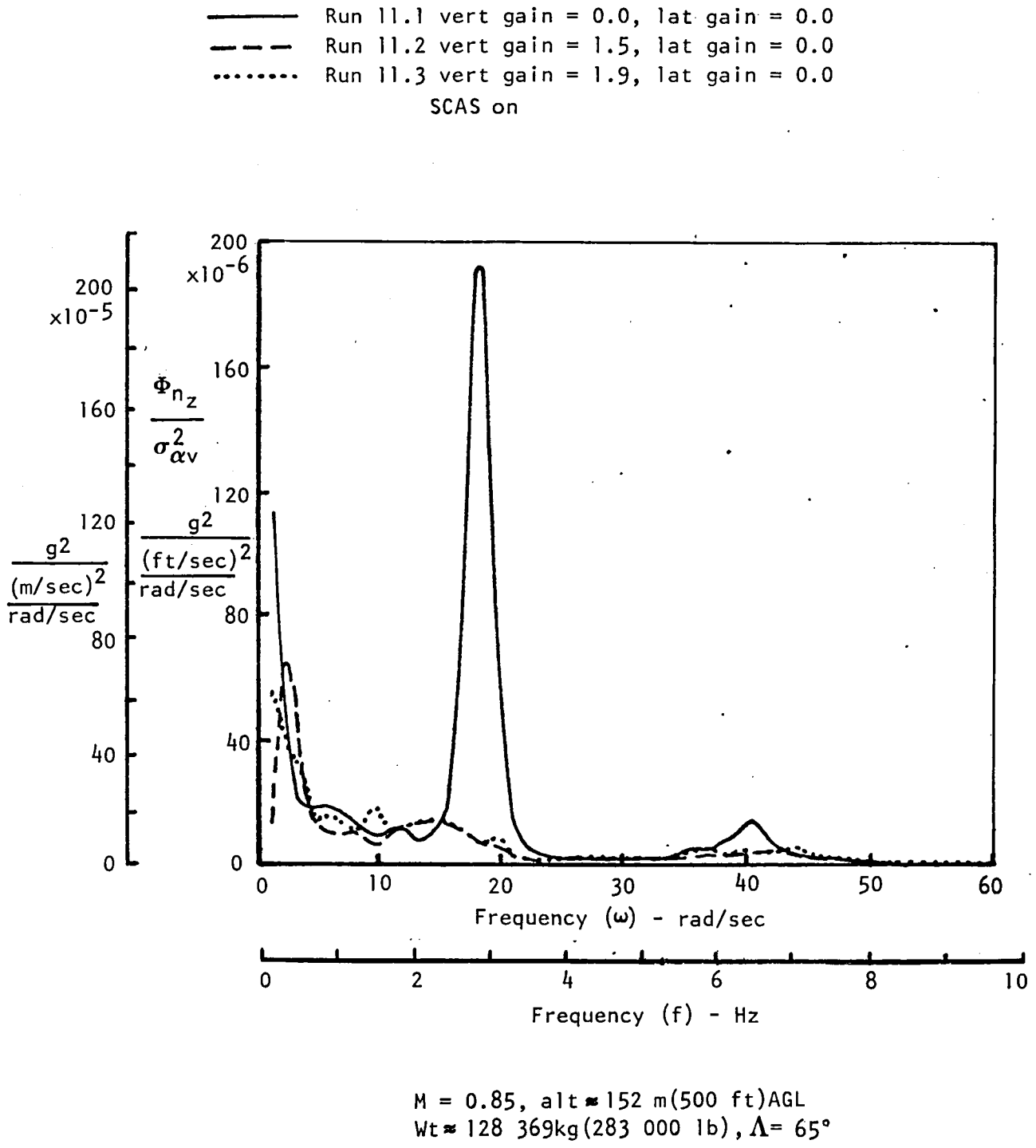

Figure 41. - SMCS performance with relocated sensor, PSD of vertical load factor at FS 746.8(294) - pilot station, case 1.

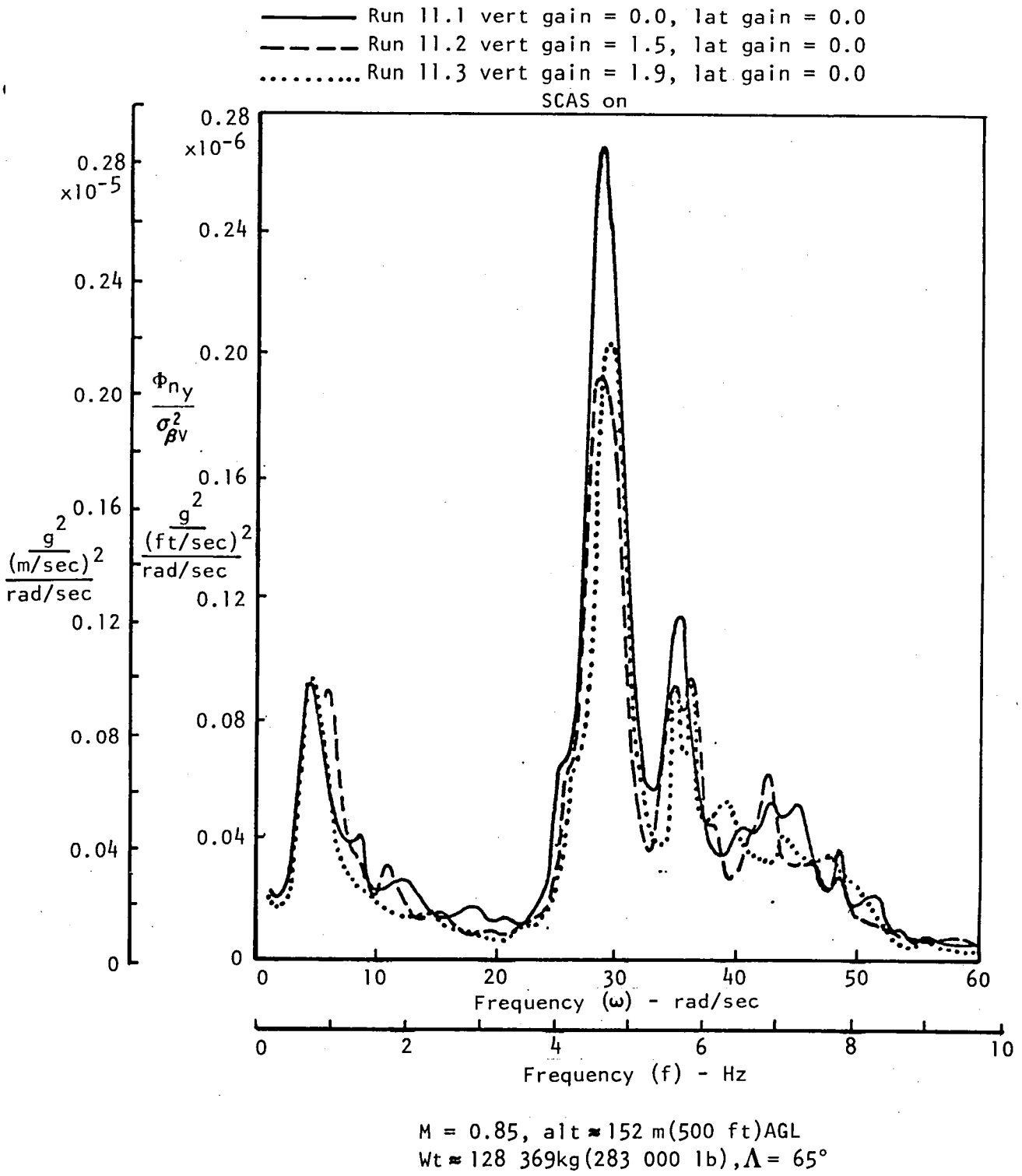

Figure 42. - SMCS performance with relocated sensor, PSD of lateral load factor at FS 746.8(294) - pilot station, case 1.

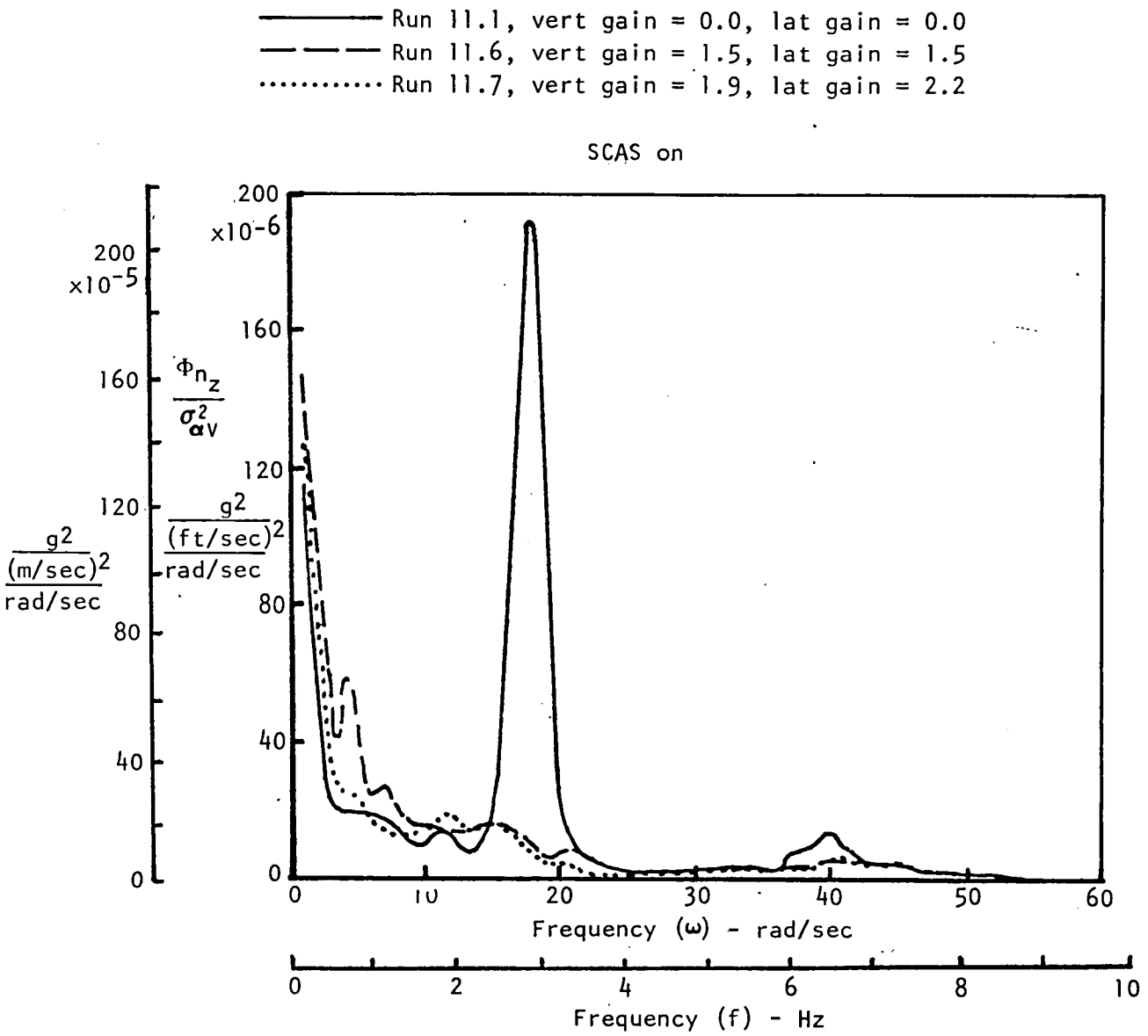

Figure 43. - SMCS performance with relocated sensor PSD of vertical load factor at FS 746.8(294) - pilot station, case 2.

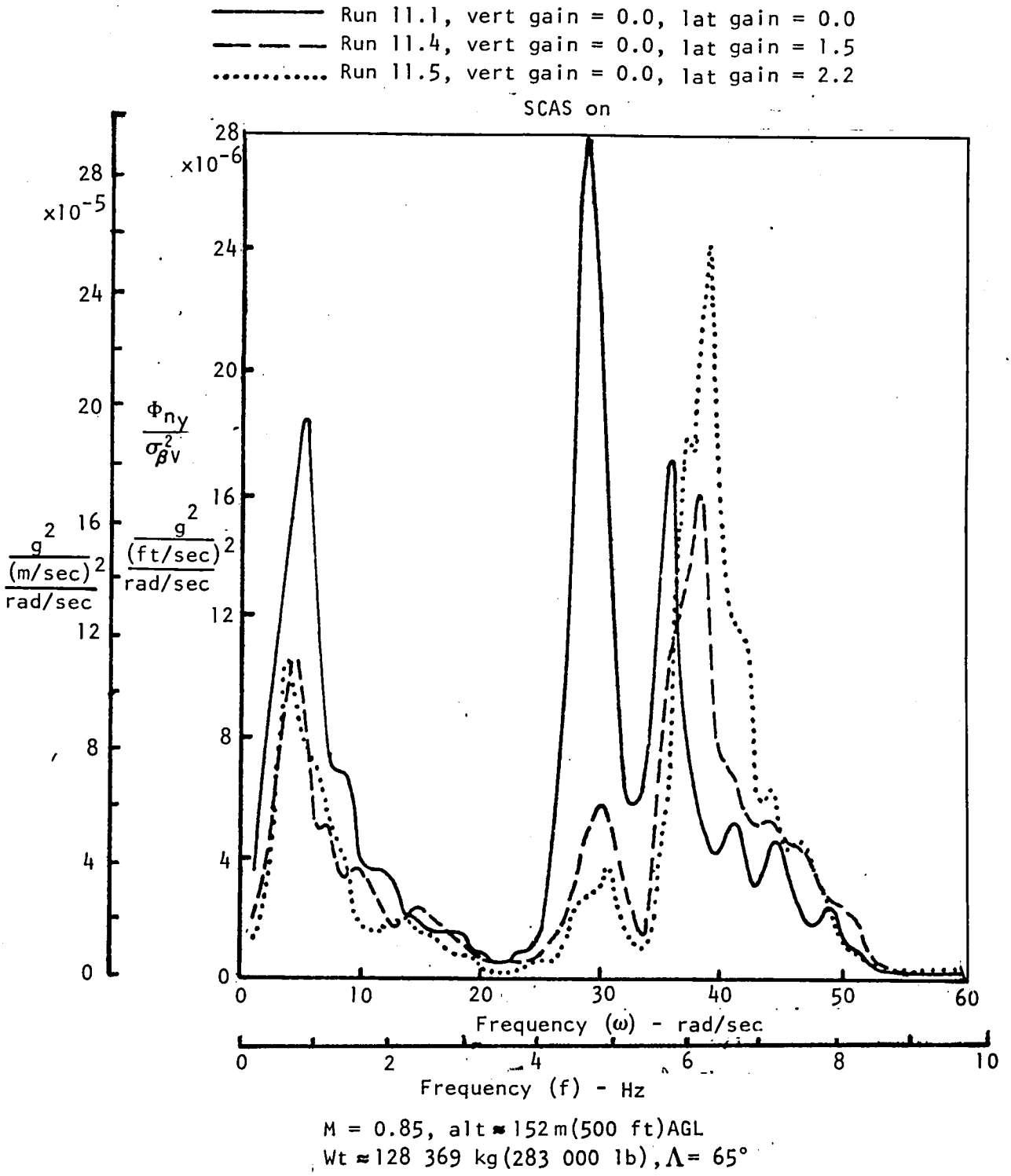

Figure 44. - SMCS performance with relocated sensor, PSD of lateral load factor at FS 515.6(203) - sensor location, case 1.

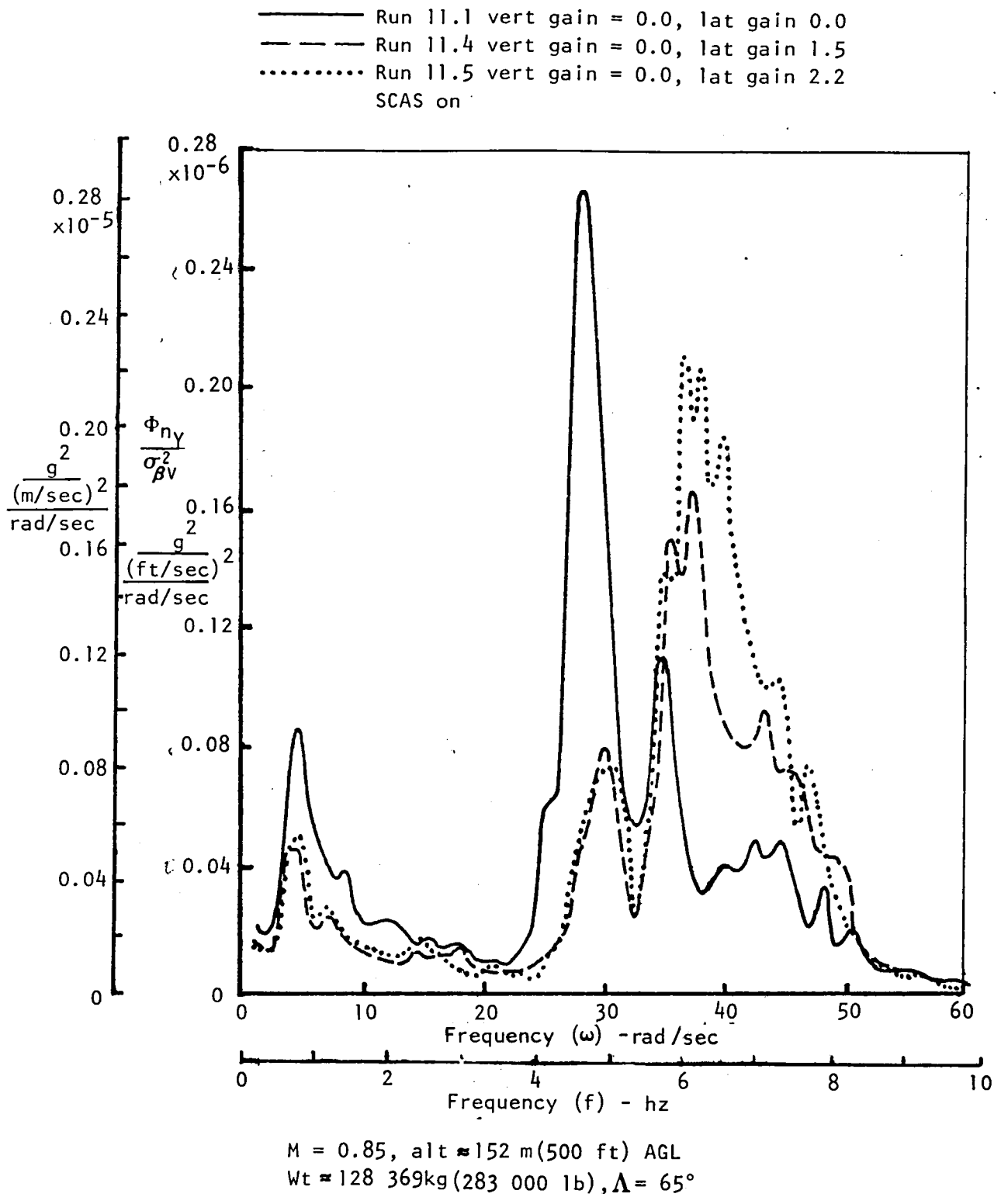

M = 0.85, alt ≈ 152 m(500 ft) AGL
Wt ≈ 128 369kg(283 000 lb), Λ = 65°

Figure 45. - SMCS performance with relocated sensor, PSD of lateral load factor at FS 746.8(294) - pilot station, case 2.

This large response difference between two fuselage stations which are relatively close is not reasonable. Figure 45 data are believed to be the data in error. Subsequent to flight 1-56, the accelerometer at the pilot station was found to be unable to hold a calibration and was replaced. Because the pilot station response is of prime importance in ride quality evaluations, it was requested that the data of flight 1-55 be rerun. This could not be accomplished in the schedule; however, the data of this flight do have limited value and are presented here for completeness.

Figures 46 and 47 are similar to the data of figures 44 and 45, respectively, but with the vertical SMCS on together with the lateral SMCS.

All of the data in figures 41 through 47 were obtained at an aircraft weight of approximately 128 369 kilograms (283 000 pounds). Data similar to figures 44 and 45 are shown in figures 48 and 49, respectively, for a weight of approximately 120 204 kilograms (265 000 pounds). Comparisons of these data indicate more adverse high-frequency mode coupling with increasing lateral gains for the lighter weight configuration.

It is concluded that the frequency response data show a significant improvement in pilot-station response due to relocation of the lateral accelerometer. The PSD data of the lateral response at the pilot station, however, still show considerable high-frequency mode excitation. Taking all evidence into account, the lateral SMCS still appears to provide a net lateral response improvement for the nominal lateral gain of 1.5.

TRUNCATED ANALYTICAL MODELS

As previously mentioned, the flexible analytical model of the B-1 used in SMCS design analyses has been described using normalized vibration modes of the structure. The model used 10 symmetric and 12 antisymmetric modes in most analyses. In developing analytical models to support moving base simulator studies, however, it was found that this number of modes caused computer equipment requirements to become excessive. The challenge was to retain the accurate aeroelastic impact on short-period and Dutch-roll characteristics and the main essence of the structural dynamic motion as seen at the pilot station and SCAS and SMCS sensors.

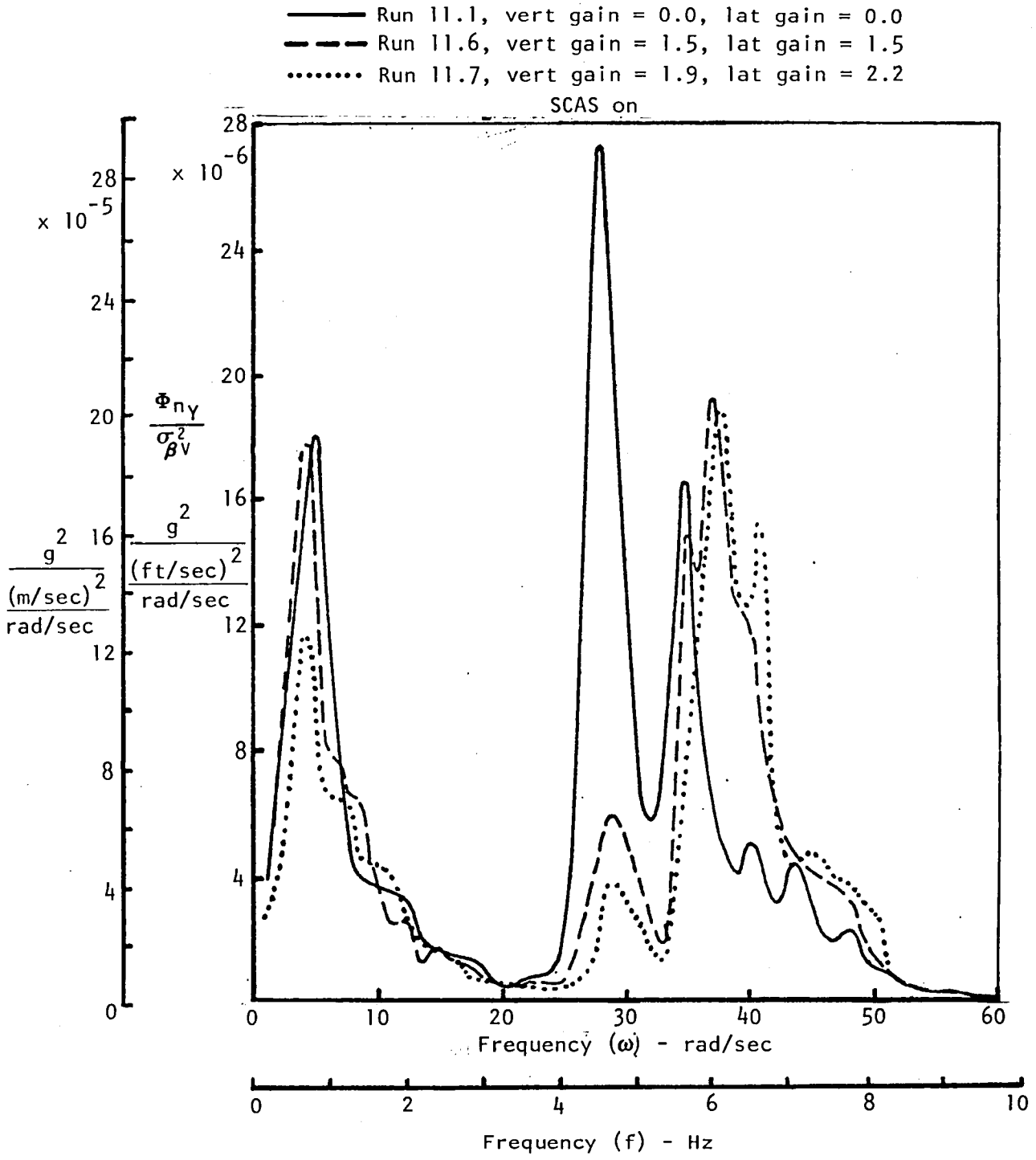

M = 0.85, alt ≈ 152 m (500 ft) AGL
Wt ≈ 128 369 kg (283 000 lb), Λ = 65°

Figure 46. - SMCS performance with relocated sensor, PSD of lateral load factor at FS 515.6 (203) - sensor location, case 2.

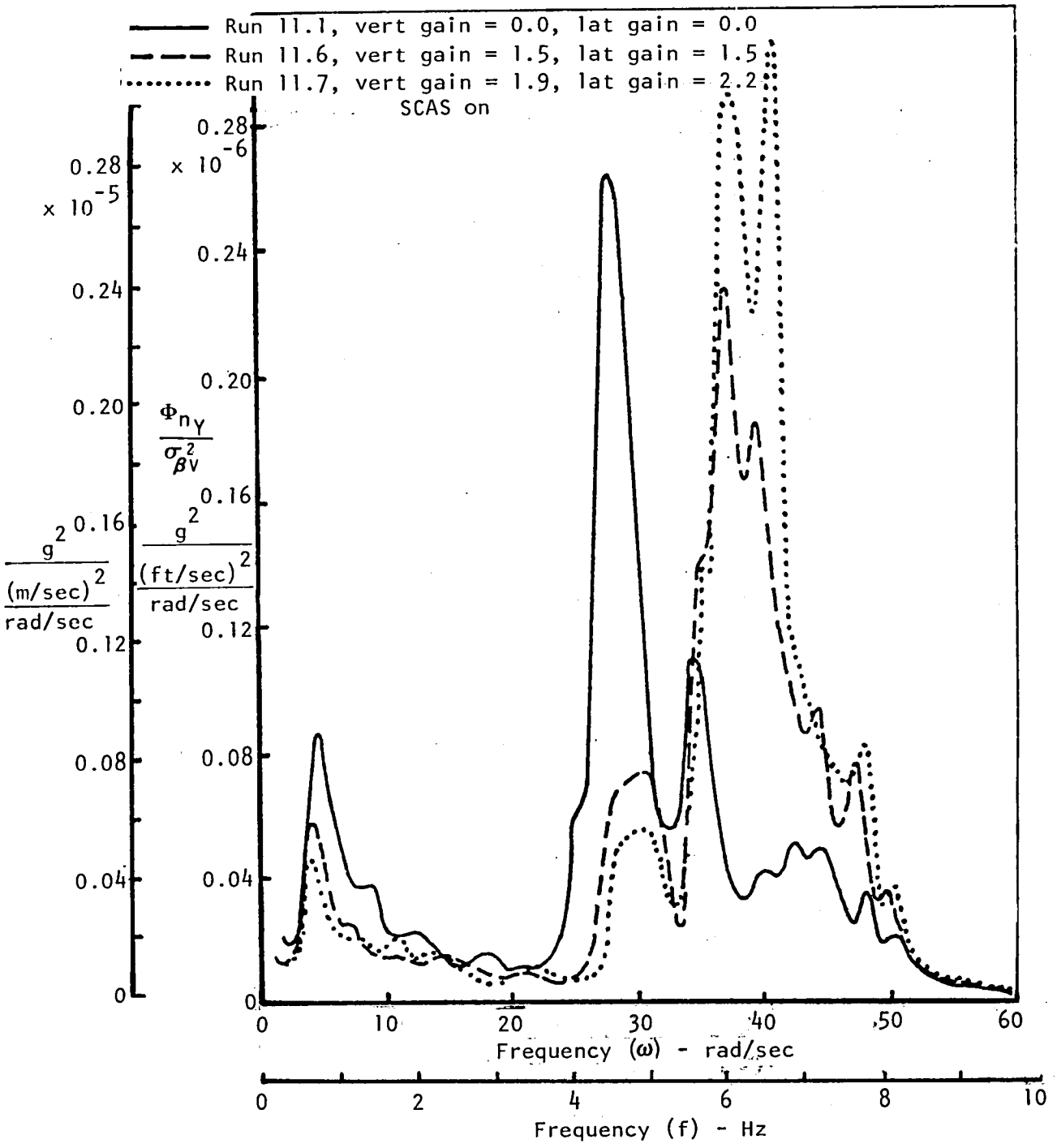

M = 0.85, alt ≈ 152 m (500 ft) AGL
Wt ≈ 128 369 kg (283 000 lb), Λ = 65°

Figure 47. - SMCS performance with relocated sensor, PSD of lateral load factor at FS 746.8 (294) - pilot station, case 3.

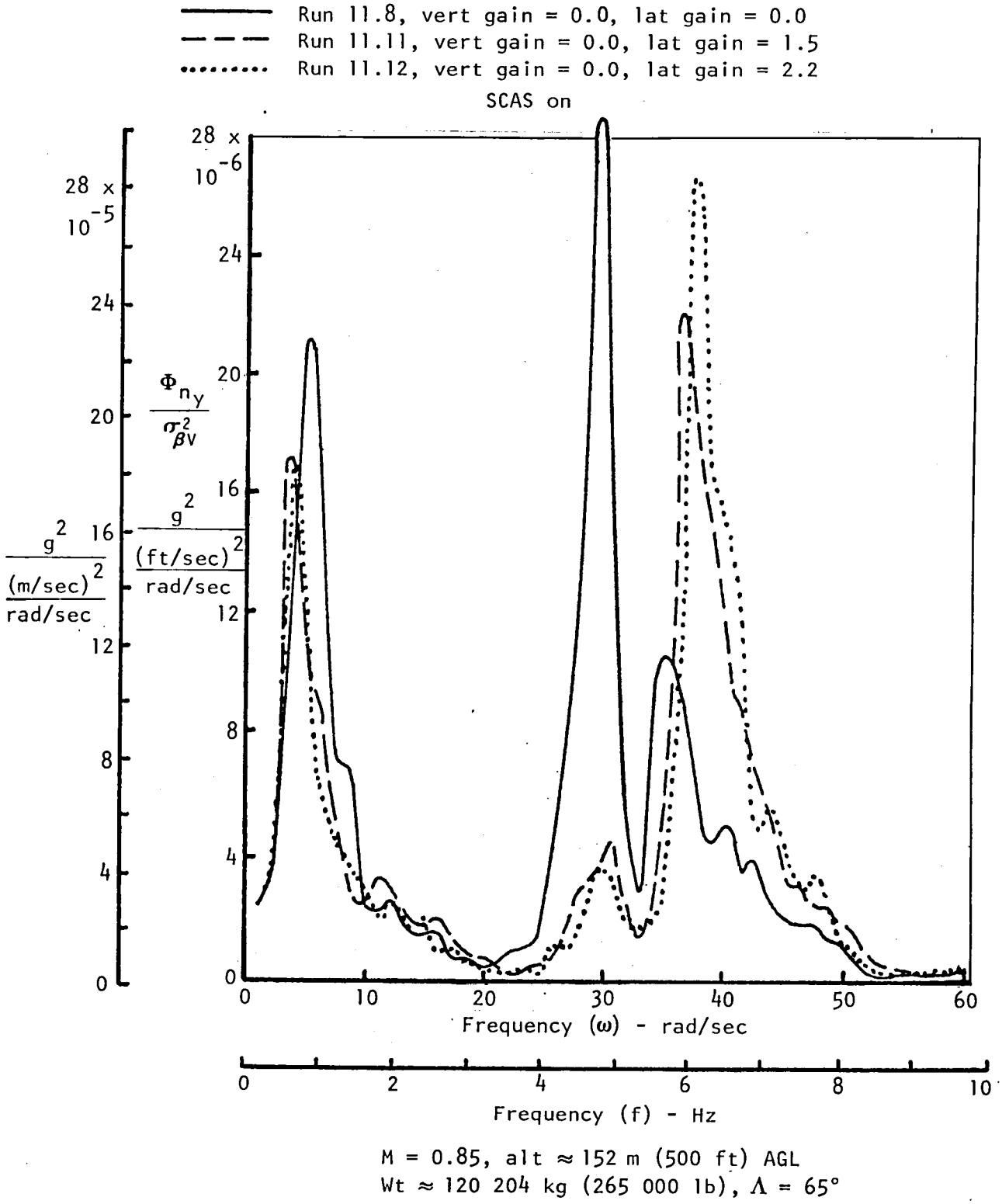

Figure 48. - SMCS performance with relocated sensor, PSD of lateral load factor at FS 515.6 (203) - sensor location, case 3.

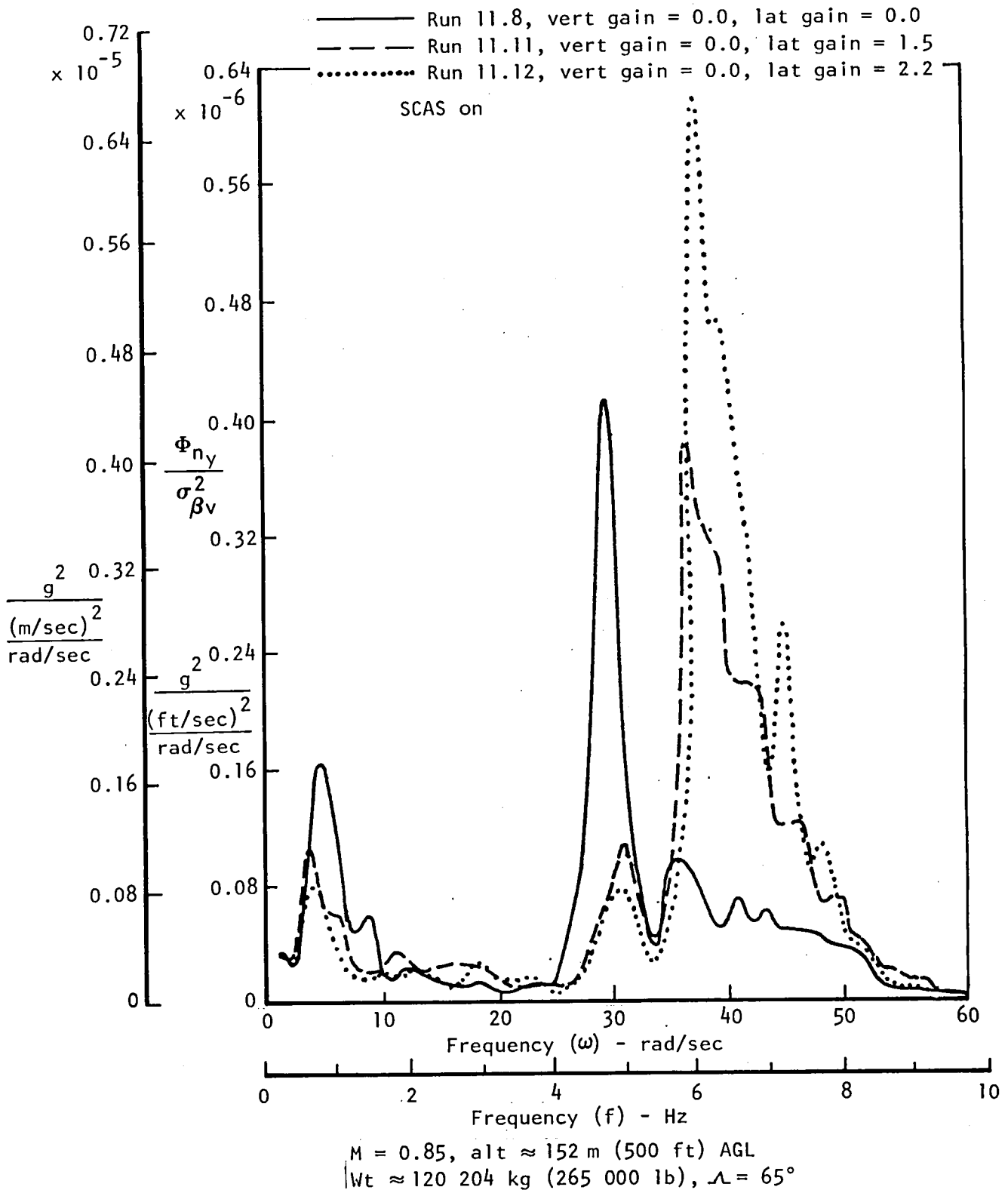

Figure 49. - SMCS performance with relocated sensor, PSD of lateral load factor at FS 746.8 (294) - pilot station, case 4.

Dynamic analyses were conducted to identify the key modes contributing to dynamic motion at the pilot station (the SMCS sensor was nearby) and SCAS sensors located at the nominal center-of-gravity (CG) location. The technique will be illustrated using the longitudinal-symmetric case. In this instance, the normal acceleration frequency responses at the pilot station and SCAS sensors, due to excitation by the horizontal tail, were employed as criteria to judge the degree of accuracy achieved with truncated models.

Thus, given a flexible aircraft described by rigid-body modes plus a number of structural dynamic modes, the structural dynamic mode set is truncated while none of the quasistatic aeroelastic effects of the eliminated modes are lost.

The data used to modify the aerodynamic derivatives are generated by the method described herein and are identified as F/R ratios, or $[\ ]_F/[\ ]_R$. The approach to generating the F/R ratios is as follows:

(1) Select sufficient modes to represent accurately the dynamic characteristics of the real system.

(2) Assume those modes not selected for the dynamic simulation to be quasistatic.

(3) Excite the quasistatic modes with the aerodynamic loadings associated with the dynamic modes, control-surface displacements, and rigid-body displacements. The loads picked up in each mode are determined by solving the simultaneous modal equations.

(4) The solutions to the preceding equations provide the information necessary to calculate the F/R ratios used to correct the aerodynamic derivatives of the rigid-body and structural dynamic modes selected for the simulation.

The equations to be used in the example are as follows:

Rigid-Body Plunge and Pitch Modes

$$\dot{\alpha} = +q + \left(\frac{g}{V_0}\right)\cos\theta\cos\Phi - \left(\frac{\rho_0 S_w}{m V_0}\right)\Big\{\underbrace{C_{N_\alpha}\alpha + C_{N_{\dot\alpha}}\left(\frac{\bar c_w}{2V_0}\right)\dot\alpha + C_{N_q}\left(\frac{\bar c_w}{2V_0}\right)q + C_{N_\delta}\delta}_{\text{RIGID VEHICLE AERO COEFFICIENTS}} + \sum_{i=1}^{n}\underbrace{\left[C_{N_{\eta_i}}\eta_i + C_{N_{\dot\eta_i}}\left(\frac{\dot\eta_i}{V_0}\right)\right]}_{\text{AEROELASTIC CORRECTION}}\Big\}$$

$$\dot{q} = +\left(\frac{\bar{q}_0 S_w \bar{c}_w}{I_y}\right)\Big\{\underbrace{C_{m_\alpha}\alpha + C_{m_{\dot\alpha}}\left(\frac{\bar{c}_w}{2V_0}\right)\dot\alpha + C_{m_q}\left(\frac{\bar{c}_w}{2V_0}\right)q + C_{m_\delta}\delta}_{\text{RIGID VEHICLE AERO COEFFICIENTS}} + \underbrace{\sum_{i=1}^{n}\left[C_{m_{\eta_i}}\eta_i + C_{m_{\dot\eta_i}}\left(\frac{\dot\eta_i}{V_0}\right)\right]}_{\text{AEROELASTIC CORRECTION}}\Big\}$$

Symmetric Structural Modes, i = 1 to n

$$\ddot{\eta}_i = -g_{s_i}\omega_i\dot\eta_i - \omega_i^2\eta_i + \left(\frac{\bar{q}_0 S_w}{M_i}\right)\Big\{\underbrace{C_{\eta_{i\alpha}}\alpha + C_{\eta_{i\dot\alpha}}\left(\frac{\bar{c}_w}{2V_0}\right)\dot\alpha + C_{\eta_{iq}}\left(\frac{\bar{c}_w}{2V_0}\right)q + C_{\eta_{i\delta}}\delta}_{\text{RIGID VEHICLE/STRUCTURAL COUPLING AERO COEFFICIENTS}} + \sum_{j=1}^{n}\Big[\underbrace{C_{\eta_{i\eta_j}}\eta_j + C_{\eta_{i\dot\eta_j}}\left(\frac{\dot\eta_j}{V_0}\right)}_{\text{STRUCTURAL COUPLING AERO COEFFICIENTS}}\Big]\Big\}$$

Before approaching the details of defining the specifics of the truncated simulation, a brief description of the basic F/R technique is discussed. If all of the n structural equations were eliminated but the aeroelastic impact on the short period retained, the equations would appear as follows:

Rigid-Body Plunge and Pitch Modes

$$\dot\alpha = +q + \left(\frac{g}{V_0}\right)\cos\Theta\cos\Phi - \left(\frac{\bar{q}_0 S_w}{mV_0}\right)\Big\{\frac{[C_{N_\alpha}]_F}{[C_{N_\alpha}]_R}C_{N_\alpha}\alpha + \frac{[C_{N_{\dot\alpha}}]_F}{[C_{N_{\dot\alpha}}]_R}C_{N_{\dot\alpha}}\left(\frac{\bar{c}_w}{2V_0}\right)\dot\alpha + \frac{[C_{N_q}]_F}{[C_{N_q}]_R}C_{N_q}\left(\frac{\bar{c}_w}{2V_0}\right)q + \frac{[C_{N_\delta}]_F}{[C_{N_\delta}]_R}C_{N_\delta}\delta\Big\}$$

$$\dot{q} = +\left(\frac{\bar{q}_0 S_w \bar{c}_w}{I_y}\right)\Big\{\frac{[C_{m_\alpha}]_F}{[C_{m_\alpha}]_R}C_{m_\alpha} + \frac{[C_{m_{\dot\alpha}}]_F}{[C_{m_{\dot\alpha}}]_R}C_{m_{\dot\alpha}}\left(\frac{\bar{c}_w}{2V_0}\right)\dot\alpha + \frac{[C_{m_q}]_F}{[C_{m_q}]_R}C_{m_q}\left(\frac{\bar{c}_w}{2V_0}\right)q + \frac{[C_{m_\delta}]_F}{[C_{m_\delta}]_R}C_{m_\delta}\delta\Big\}$$

The F/R ratios shown, where all 10 structure modes are involved, are obtained as follows. The set of structural mode equations are set up as shown below and η_1 through η_{10} are solved for each of the indicated unit loadings of α, $(\bar{c}_w/2V_o)\,\dot{\alpha}$, $(\bar{c}_w/2V_o)\,q$, and δ, respectively.

$$\begin{bmatrix} \left[C_{\eta_1\eta_1} - \left(\frac{\omega_1^2 M_1}{g_o S_w}\right)\right] & C_{\eta_1\eta_2} \cdots C_{\eta_1\eta_{10}} \\ \vdots & \left[C_{\eta_2\eta_2} - \left(\frac{\omega_2^2 M_2}{g_o S_w}\right)\right] \cdots C_{\eta_2\eta_{10}} \\ C_{\eta_{10}\eta_1} & C_{\eta_{10}\eta_2} \cdots \left[C_{\eta_{10}\eta_{10}} - \left(\frac{\omega_{10}^2 M_{10}}{g_o S_w}\right)\right] \end{bmatrix} \begin{bmatrix} \eta_1 \\ \eta_2 \\ \vdots \\ \eta_{10} \end{bmatrix} = \begin{bmatrix} -C_{\eta_1\alpha} \\ -C_{\eta_2\alpha} \\ \vdots \\ -C_{\eta_{10}\alpha} \end{bmatrix}_{\text{FOR } \alpha = 1.0} \begin{bmatrix} -C_{\eta_1\dot{\alpha}}\left(\frac{\bar{c}_w}{2V_o}\right)\dot{\alpha} \\ -C_{\eta_2\dot{\alpha}}\left(\frac{\bar{c}_w}{2V_o}\right)\dot{\alpha} \\ \vdots \\ -C_{\eta_{10}\dot{\alpha}}\left(\frac{\bar{c}_w}{2V_o}\right)\dot{\alpha} \end{bmatrix}_{\text{FOR } \left(\frac{\bar{c}_w}{2V_o}\right)\dot{\alpha} = 1.0} \begin{bmatrix} -C_{\eta_1 q}\left(\frac{\bar{c}_w}{2V_o}\right) q \\ -C_{\eta_2 q}\left(\frac{\bar{c}_w}{2V_o}\right) q \\ \vdots \\ -C_{\eta_{10} q}\left(\frac{\bar{c}_w}{2V_o}\right) q \end{bmatrix}_{\text{FOR } \left(\frac{\bar{c}_w}{2V_o}\right) q = 1.0} \begin{bmatrix} -C_{\eta_1\delta}\,\delta \\ -C_{\eta_2\delta}\,\delta \\ \vdots \\ -C_{\eta_{10}\delta}\,\delta \end{bmatrix}_{\text{FOR } \delta = 1.0}$$

As an example of how the F/R ratios are developed, consider the derivative C_{N_α}. From the normal force equation where $\alpha = 1.0$ and all other rigid-body variables are zero, the following relationship is obtained.

$$[C_{N_\alpha}]_{FLEX} = [C_{N_\alpha}]_{RIGID} + C_{N_{\eta_1}}\eta_1 + C_{N_{\eta_2}}\eta_2 + \cdots C_{N_{\eta_{10}}}\eta_{10}$$

η_1 through η_{10} were obtained from the simultaneous solution of the previous equation set for a loading $C_{\eta_{i_\alpha}}$ for a unit value of α.

The expression is reformed to obtain the F/R ratio.

$$\frac{[C_{N_\alpha}]_F}{[C_{N_\alpha}]_R} = 1 + \frac{C_{N_{\eta_1}}\eta_1 + C_{N_{\eta_2}}\eta_2 + \cdots C_{N_{\eta_{10}}}\eta_{10}}{[C_{N_\alpha}]_R}$$

The F/R ratios

$$\frac{[C_{N\dot{\alpha}}]_F}{[C_{N\dot{\alpha}}]_R}\ ,\ \frac{[C_{Nq}]_F}{[C_{Nq}]_R}\ ,\ \frac{[C_{N\delta}]_F}{[C_{N\delta}]_R}$$

are obtained in a similar manner.

The extension to the pitching-moment coefficients follows the same line of logic.

Consider now the longitudinal-symmetric equations where three structural modes (1, 3, and 5) of the 10 are dynamic, but the quasistatic flexibility effects of the eliminated modes are retained. The bar over the coefficients indicates a modification due to the quasistatic effects of structural modes 2, 4, and 6 through 10. Typically $\bar{C}_N = ([\bar{C}_N]/[C_N])\ C_N$, where C_N is for a rigid vehicle.

Rigid-Body Plunge and Pitch Modes

$$\dot{\alpha} = +q + \left(\frac{g}{V_o}\right)\cos\Theta\cos\Phi - \left(\frac{\rho_o S_w}{mV_o}\right)\Big\{\bar{C}_{N_\alpha}\alpha + \bar{C}_{N_{\dot{\alpha}}}\left(\frac{\bar{c}_w}{2V_o}\right)\dot{\alpha} + \bar{C}_{N_q}\left(\frac{\bar{c}_w}{2V_o}\right)q + \bar{C}_{N_\delta}\delta$$
$$+ \bar{C}_{N_{\eta_1}}\eta_1 + \bar{C}_{N_{\eta_3}}\eta_3 + \bar{C}_{N_{\eta_5}}\eta_5 + \bar{C}_{N_{\dot{\eta}_1}}\left(\frac{\dot{\eta}_1}{V_o}\right) + \bar{C}_{N_{\dot{\eta}_3}}\left(\frac{\dot{\eta}_3}{V_o}\right) + \bar{C}_{N_{\dot{\eta}_5}}\left(\frac{\dot{\eta}_5}{V_o}\right)\Big\}$$

$$\dot{q} = +\left(\frac{\rho_o S_w \bar{c}_w}{I_Y}\right)\Big\{\bar{C}_{m_\alpha}\alpha + \bar{C}_{m_{\dot{\alpha}}}\left(\frac{\bar{c}_w}{2V_o}\right)\dot{\alpha} + \bar{C}_{m_q}\left(\frac{\bar{c}_w}{2V_o}\right)q + \bar{C}_{m_\delta}\delta + \bar{C}_{m_{\eta_1}}\eta_1 + \bar{C}_{m_{\eta_3}}\eta_3$$
$$+ \bar{C}_{m_{\eta_5}}\eta_5 + \bar{C}_{m_{\dot{\eta}_1}}\left(\frac{\dot{\eta}_1}{V_o}\right) + \bar{C}_{m_{\dot{\eta}_3}}\left(\frac{\dot{\eta}_3}{V_o}\right) + \bar{C}_{m_{\dot{\eta}_5}}\left(\frac{\dot{\eta}_5}{V_o}\right)\Big\}$$

Symmetric structural modes, i = 1, 3, 5

$$\ddot{\eta}_i = -2\zeta_{s_i}\omega_i\dot{\eta}_i - \omega_i^2\eta_i + \left(\frac{\rho_o S_w}{M_i}\right)\Big\{\bar{C}_{n_{i_\alpha}}\alpha + \bar{C}_{n_{i_{\dot{\alpha}}}}\left(\frac{\bar{c}_w}{2V_o}\right)\dot{\alpha} + \bar{C}_{n_{i_q}}\left(\frac{\bar{c}_w}{2V_o}\right)q + \bar{C}_{n_{i_\delta}}\delta$$
$$+ \sum_{j=1,3,5}\left[\bar{C}_{n_{i_{\eta_j}}}\eta_j + \bar{C}_{n_{i_{\dot{\eta}_j}}}\left(\frac{\dot{\eta}_j}{V_o}\right)\right]\Big\}$$

For mode 1 (typical of modes 3 and 5 also)

$$\ddot{\eta}_1 = -g_{s_1}\omega_1\dot{\eta}_1 - \omega_1^2\eta_1 + \left(\frac{\rho_o S_w}{M_1}\right)\left\{\bar{C}_{n_1\alpha}\alpha + \bar{C}_{n_{\dot{\alpha}}}\left(\frac{\bar{c}_w}{2V_o}\right)\dot{\alpha} + \bar{C}_{n_1 q}\left(\frac{\bar{c}_w}{2V_o}\right)q + \bar{C}_{n_1\delta}\delta\right.$$
$$\left. + \bar{C}_{n_1\eta_1}\eta_1 + \bar{C}_{n_1\eta_3}\eta_3 + \bar{C}_{n_1\eta_5}\eta_5 + \bar{C}_{n_1\dot{\eta}_1}\left(\frac{\dot{\eta}_1}{V_o}\right) + \bar{C}_{n_1\dot{\eta}_3}\left(\frac{\dot{\eta}_3}{V_o}\right) + \bar{C}_{n_1\dot{\eta}_5}\left(\frac{\dot{\eta}_5}{V_o}\right)\right\}$$

The F/R ratio corrections for these equations are obtained in the following manner. Assuming that structural modes 1, 3, and 5 will be dynamic, the simultaneous equations to be solved for unit loadings appear as follows:

$$\begin{bmatrix} C_{n_2\eta_2} - \left(\frac{\omega_2^2 M_2}{\rho_o S_w}\right) & C_{n_2\eta_4} & C_{n_2\eta_6} & \cdots & C_{n_2\eta_{10}} \\ C_{n_4\eta_1} & \left[C_{n_4\eta_4} - \left(\frac{\omega_4^2 M_4}{\rho_o S_w}\right)\right] & C_{n_4\eta_6} & \cdots & C_{n_4\eta_{10}} \\ C_{n_6\eta_1} & C_{n_6\eta_4} & \left[C_{n_6\eta_4} - \left(\frac{\omega_6^2 M_6}{\rho_o S_w}\right)\right] & \cdots & C_{n_6\eta_{10}} \\ \vdots & \vdots & \vdots & & \vdots \\ C_{n_{10}\eta_1} & C_{n_{10}\eta_4} & C_{n_{10}\eta_6} & \cdots & \left[C_{n_{10}\eta_{10}} - \left(\frac{\omega_{10}^2 M_{10}}{\rho_o S_w}\right)\right] \end{bmatrix} \begin{bmatrix} \eta_2 \\ \eta_4 \\ \eta_6 \\ \vdots \\ \eta_{10} \end{bmatrix} =$$

$$\begin{bmatrix} -C_{n_2\alpha} \\ -C_{n_4\alpha} \\ -C_{n_6\alpha} \\ \vdots \\ -C_{n_{10}\alpha} \end{bmatrix}, \begin{bmatrix} -C_{n_2\dot{\alpha}} \\ -C_{n_4\dot{\alpha}} \\ -C_{n_6\dot{\alpha}} \\ \vdots \\ -C_{n_{10}\dot{\alpha}} \end{bmatrix}, \begin{bmatrix} -C_{n_2 q} \\ -C_{n_4 q} \\ -C_{n_6 q} \\ \vdots \\ -C_{n_{10} q} \end{bmatrix}, \begin{bmatrix} -C_{n_2\delta} \\ -C_{n_4\delta} \\ -C_{n_6\delta} \\ \vdots \\ -C_{n_{10}\delta} \end{bmatrix}, \begin{bmatrix} -C_{n_2\eta_1} \\ -C_{n_4\eta_1} \\ -C_{n_6\eta_1} \\ \vdots \\ -C_{n_{10}\eta_1} \end{bmatrix}, \begin{bmatrix} -C_{n_2\eta_3} \\ -C_{n_4\eta_3} \\ -C_{n_6\eta_3} \\ \vdots \\ -C_{n_{10}\eta_3} \end{bmatrix}, \begin{bmatrix} -C_{n_2\eta_5} \\ -C_{n_4\eta_5} \\ -C_{n_6\eta_5} \\ \vdots \\ -C_{n_{10}\eta_5} \end{bmatrix}, \begin{bmatrix} -C_{n_2\dot{\eta}_1} \\ -C_{n_4\dot{\eta}_1} \\ -C_{n_6\dot{\eta}_1} \\ \vdots \\ -C_{n_{10}\dot{\eta}_1} \end{bmatrix}, \begin{bmatrix} -C_{n_2\dot{\eta}_3} \\ -C_{n_4\dot{\eta}_3} \\ -C_{n_6\dot{\eta}_3} \\ \vdots \\ -C_{n_{10}\dot{\eta}_3} \end{bmatrix}, \begin{bmatrix} -C_{n_2\dot{\eta}_5} \\ -C_{n_4\dot{\eta}_5} \\ -C_{n_6\dot{\eta}_5} \\ \vdots \\ -C_{n_{10}\dot{\eta}_5} \end{bmatrix},$$

The F/R ratio data for C_N and C_m coefficients, given the solution of these equations for unit loadings of α, $(\bar{c}_w/2V_o)\,\dot{\alpha}$, $(\bar{c}_w/2V_o)\,q$, and δ, are obtained as previously explained. The F/R ratio corrections to $C_{N_{\eta_i}}$, $C_{N_{\dot{\eta}_i}}$, $C_{m_{\eta_i}}$, and $C_{m_{\dot{\eta}_i}}$ are obtained as follows:

$$\frac{\bar{C}_{N_{\eta_1}}}{C_{N_{\eta_1}}} = 1 + \frac{C_{N_{\eta_2}}\eta_2 + C_{N_{\eta_4}}\eta_4 + C_{N_{\eta_6}}\eta_6 + \cdots C_{N_{\eta_{10}}}\eta_{10}}{C_{N_{\eta_1}}}$$

where η_2, η_4 and η_6 through η_{10} are obtained from the simultaneous solution of the previous equation set for unit η_1 loading.

$$\frac{\bar{C}_{N_{\eta_3}}}{C_{N_{\eta_3}}} \quad \text{and} \quad \frac{\bar{C}_{N_{\eta_5}}}{C_{N_{\eta_5}}}$$

are obtained for unit loadings of η_3 and η_5, respectively.

$$\frac{\bar{C}_{m_{\eta_1}}}{C_{m_{\eta_1}}}, \quad \frac{\bar{C}_{m_{\eta_3}}}{C_{m_{\eta_3}}}, \quad \text{and} \quad \frac{\bar{C}_{m_{\eta_5}}}{C_{m_{\eta_5}}}$$

are obtained using the pitching moment $\sum$ Relationships and the η_i solutions for the unit loading of η_1, η_3, and η_5, respectively.

The

$$\frac{\bar{C}_{N_{\dot{\eta}_1}}}{C_{N_{\dot{\eta}_1}}}, \quad \frac{\bar{C}_{N_{\dot{\eta}_3}}}{C_{N_{\dot{\eta}_3}}}, \quad \frac{\bar{C}_{N_{\dot{\eta}_5}}}{C_{N_{\dot{\eta}_5}}}, \quad \frac{\bar{C}_{m_{\dot{\eta}_1}}}{C_{m_{\dot{\eta}_1}}}, \quad \frac{\bar{C}_{m_{\dot{\eta}_3}}}{C_{m_{\dot{\eta}_3}}} \quad \text{and} \quad \frac{C_{m_{\dot{\eta}_5}}}{C_{m_{\dot{\eta}_5}}}$$

data are obtained in a similar manner for unit loadings of $(\dot{\eta}_1/V_o)$, $(\dot{\eta}_3/V_o)$, and $(\dot{\eta}_5/V_o)$.

The ratios for modifying the coefficients of the dynamic structural modes are obtained using the $\eta 2$, $\eta 4$, and $\eta 6$ through η_{10} responses of the simultaneous equations for unit loadings of η_1, η_3, η_5, $(\dot{\eta}_1/V_o)$, $(\dot{\eta}_3/V_o)$, and $(\dot{\eta}_5/V_o)$. Typically:

$$\frac{\bar{C}_{\eta_1 \eta_1}}{C_{\eta_1 \eta_1}} = 1 + \frac{C_{\eta_1 \eta_2}\eta_2 + C_{\eta_1 \eta_4}\eta_4 + C_{\eta_1 \eta_6}\eta_6 - - - C_{\eta_1 \eta_{10}}\eta_{10}}{C_{\eta_1 \eta_1}}$$

Where η_2, η_4, and η_6 through η_{10} are from unit η_1 loadings.

$$\frac{\bar{C}_{\eta_1 \dot{\eta}_1}}{C_{\eta_1 \dot{\eta}_1}} = 1 + \frac{C_{\eta_1 \eta_2}\eta_2 + C_{\eta_1 \eta_4}\eta_4 + C_{\eta_1 \eta_6}\eta_6 - - - C_{\eta_1 \eta_{10}}\eta_{10}}{C_{\eta_1 \dot{\eta}_1}}$$

Where η_2, η_4, and η_6 through η_{10} are from unit $(\dot{\eta}_1/V_o)$ loadings.

It can be shown that all of the quasistatic aeroelastic information is in the truncated modal equations by using the following logic for a typical rigid-body aerodynamic coefficient.

$$\underbrace{(F/R)_{\text{3-mode modified system}} \times (F/R)_{\text{7-mode quasistatic system}}}_{A} = \underbrace{(F/R)_{\text{10-mode quasi-static original system}}}_{B}$$

The following set of numbers for a test case of the technique illustrates the accuracy retained in the coefficients.

M=0.85 SL ?

Coefficient	F/R from A	F/R from B
C_{N_α}	0.752514	0.752519
$C_{N_{\dot{\alpha}}}$	1.015199	1.015201
C_{N_q}	0.661091	0.661086
C_{N_δ}	0.620383	0.620382
C_{M_α}	0.602100	0.602126
$C_{M_{\dot{\alpha}}}$	0.948420	0.948413
C_{M_q}	0.732947	0.732943
C_{M_δ}	0.588629	0.588754

Figure 50 illustrates the degree of quasistatic and dynamic aeroelastic information retained in the three structural modes plus corrections set of equations. Shown is the frequency response plot of the normal acceleration at pilot station and CG. Note that at zero frequency, the truncated model response overlays exactly the original 10-mode model response, indicating that all of the quasistatic information of the 10-mode model has been retained in the truncated model. Furthermore, the truncated model dynamic response is a good representation of the 10-mode model dynamic response.

Truncated dynamic equations may be developed for the lateral-directional-antisymmetric case in a manner similar to that shown here for the longitudinal-symmetric case.

ANALYSIS OF SMCS VANE AERODYNAMIC INTERFERENCE EFFECT

During the development of the SMCS vane configuration, wind tunnel tests were conducted to determine the aerodynamic characteristics of the vane. Fairly extensive aerodynamic interference effects were observed in the force and moment data for both the longitudinal and lateral cases during component buildup tests. Reference 1 contains some of these wind tunnel data and analysis of their sources; refer to this reference as background for the material to be presented here. It is the purpose of this section to report the results of an analytical study made to assess the importance of the vane aerodynamic interference effects on the dynamics of the aircraft response.

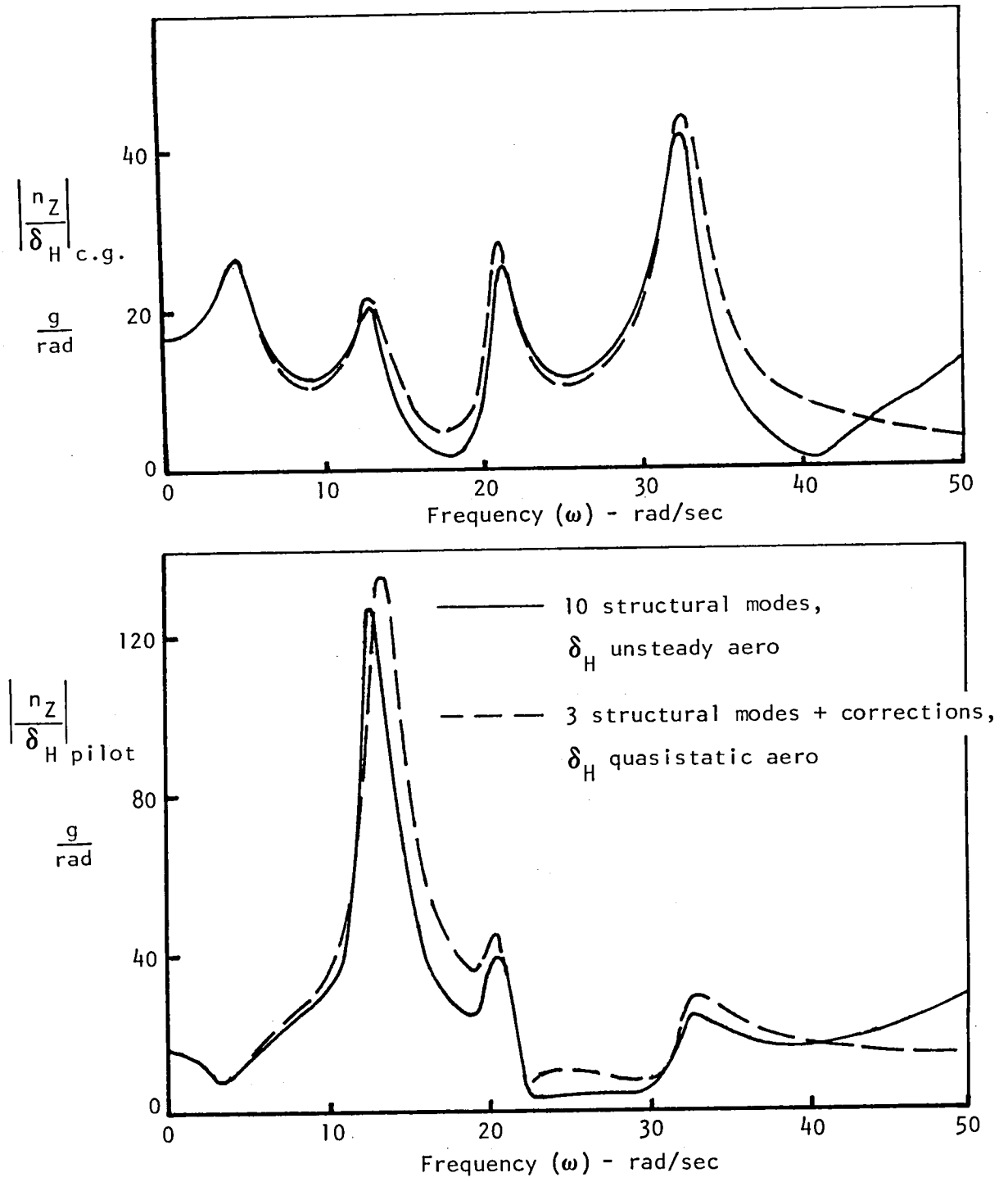

Figure 50. - Normal load factor due to horizontal tail frequency response comparisons of full and truncated dynamic analytical model, SCAS on.

The analyses conducted were made in the frequency domain where normal and lateral load-factor responses at the vane station were calculated due to SMCS vane oscillatory deflections at various frequencies. The main reason for doing this was that flight-test data existed for these frequency responses against which to check the reality of the interference effects modeled. Another reason was that the basic analytical model was available to conduct this study; only the vane aerodynamic characteristics had to be reworked to include the aerodynamic interference effects estimated. The following paragraphs describe how this was done and discusses the results of the analyses made. Finally, an evaluation is made of these interference factors relative to the importance to future similar designs.

Discussions of reference 1 identified general areas where the forces caused by vane deflections were acting. As shown in figure 51, they were on (1) vane itself, (2) forebody, (3) wing-aft body, and (4) empennage. As a simplification, it was assumed that these forces acted at point locations in each of the general areas identified. These point locations were determined from the wind tunnel test data of forces and moments for various stages of configuration buildup.

The SMCS vane alone force and moment coefficient data were determined analytically (reference 1) while the associated interference force and moment coefficients (C_N, C_m, C_y, C_ℓ, C_n) were determined directly from the wind-tunnel data. The structural mode generalized forces were calculated for each mode knowing the forces acting at the points defined previously and the structural mode deflections at these points ($F\phi_i$). However, before any of these data could be added, the transport time lag effect from the vane to the point of load impact had to be considered. In the frequency domain, this lag effect was included for each interference load by multiplying by

$$e^{-i\frac{\omega X}{V_o}},$$

where X is the distance (+ aft) from the vane station to the point in question, ω is the forcing frequency, and V_o the velocity.

Table VI shows the rigid-body and structural generalized force coefficient formulation for the SMCS vane, including intereference effects for the longitudinal-symmetric case. The SMCS vane lateral-directional-antisymmetric data, including interference effects, were assembled in an analogous manner.

The frequency response data of figures 22 through 24 and 27 through 29 are repeated here in figures 52 through 57. The normal load factor response data of figures 52 through 54 show that the interference effects modeled produce a

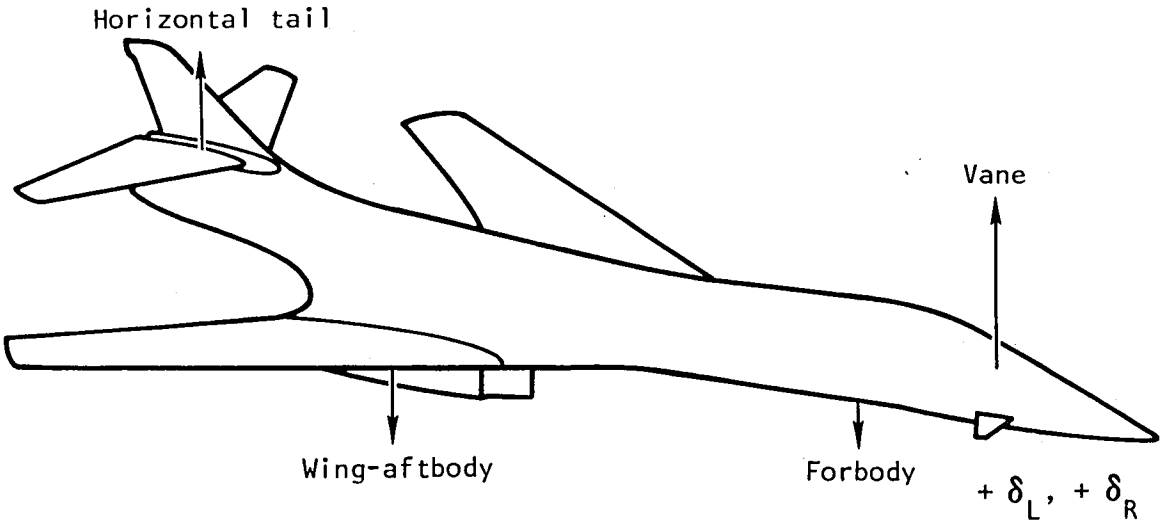

(a) Normal forces

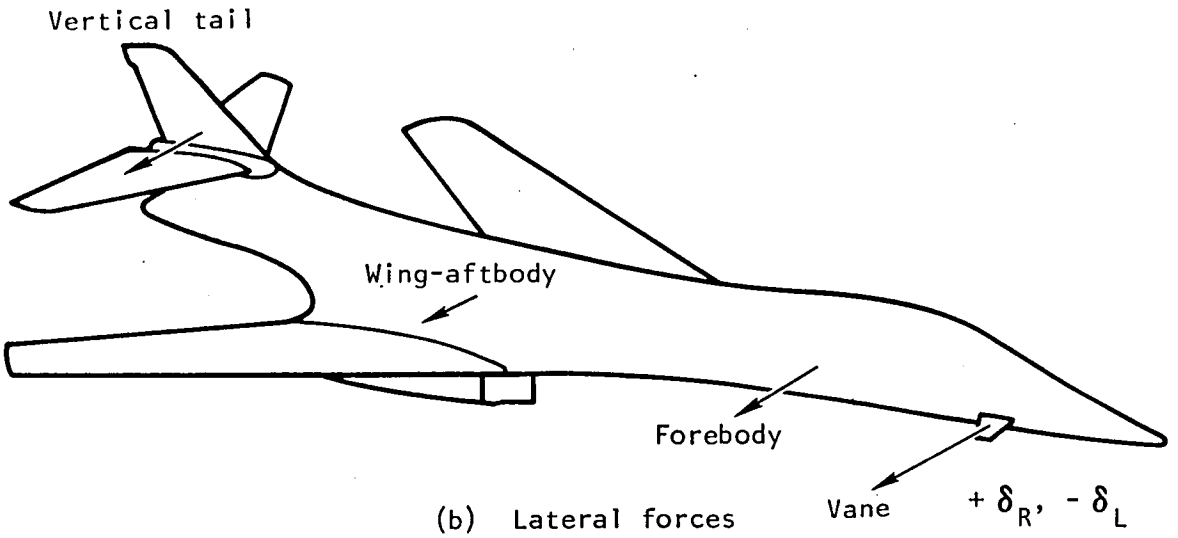

(b) Lateral forces

Figure 51. - Typical vane-induced interference forces.

TABLE VI. - SMCS VANE EFFECTIVENESS INCLUDING INTERFERENCE EFFECTS, LONGITUDINAL-SYMMETRIC CASE, FREQUENCY DOMAIN

$$C_{N_{\delta_{cv}}} = \left(C_{N_{\delta_{cv}}}\right)_{VANE} + \left(C_{N_{\delta_{cv}}}\right)_{FOREBODY} e^{-\frac{i\omega X_{FOREBODY}}{V_o}} + \left(C_{N_{\delta_{cv}}}\right)_{WING-AFTBODY} e^{-\frac{i\omega X_{WING-AFTBODY}}{V_o}} + \left(C_{N_{\delta_{cv}}}\right)_{H.TAIL} e^{-\frac{i\omega X_{H.TAIL}}{V_o}}$$

$$C_{m_{\delta_{cv}}} = \left(C_{m_{\delta_{cv}}}\right)_{VANE} + \left(C_{m_{\delta_{cv}}}\right)_{FOREBODY} e^{-\frac{i\omega X_{FOREBODY}}{V_o}} + \left(C_{m_{\delta_{cv}}}\right)_{WING-AFTBODY} e^{-\frac{i\omega X_{WING-AFTBODY}}{V_o}} + \left(C_{m_{\delta_{cv}}}\right)_{H.TAIL} e^{-\frac{i\omega X_{H.TAIL}}{V_o}}$$

$$C_{n_{i\delta_{cv}}} = \left(C_{N_{\delta_{cv}}}\right)_{VANE} \phi_i^{VANE} + \left(C_{N_{\delta_{cv}}}\right)_{FOREBODY} \phi_i^{FOREBODY} e^{-\frac{i\omega X_{FOREBODY}}{V_o}} + \left(C_{N_{\delta_{cv}}}\right)_{WING-AFTBODY} \phi_i^{WING-AFTBODY} e^{-\frac{i\omega X_{WING-AFTBODY}}{V_o}} + \left(C_{N_{\delta_{cv}}}\right)_{H.TAIL} \phi_i^{H.TAIL} e^{-\frac{i\omega X_{H.TAIL}}{V_o}}$$

TYPICAL FOR MODE i

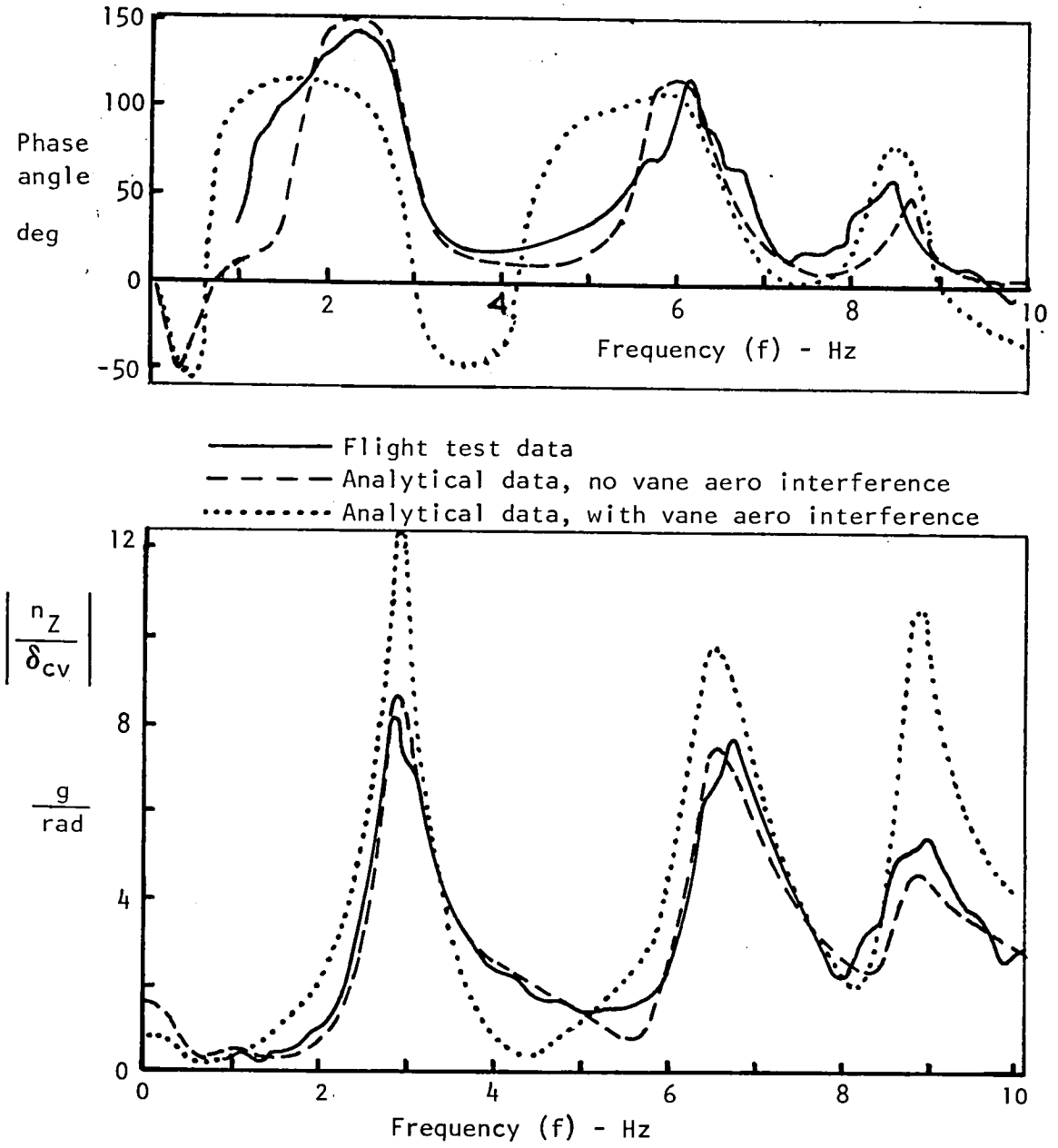

Figure 52. - Effect of SMCS vane aerodynamic interferences, frequency response of normal load factor at FS 571.5 (225) due to SMCS vane deflection, SCAS off, SMCS off.

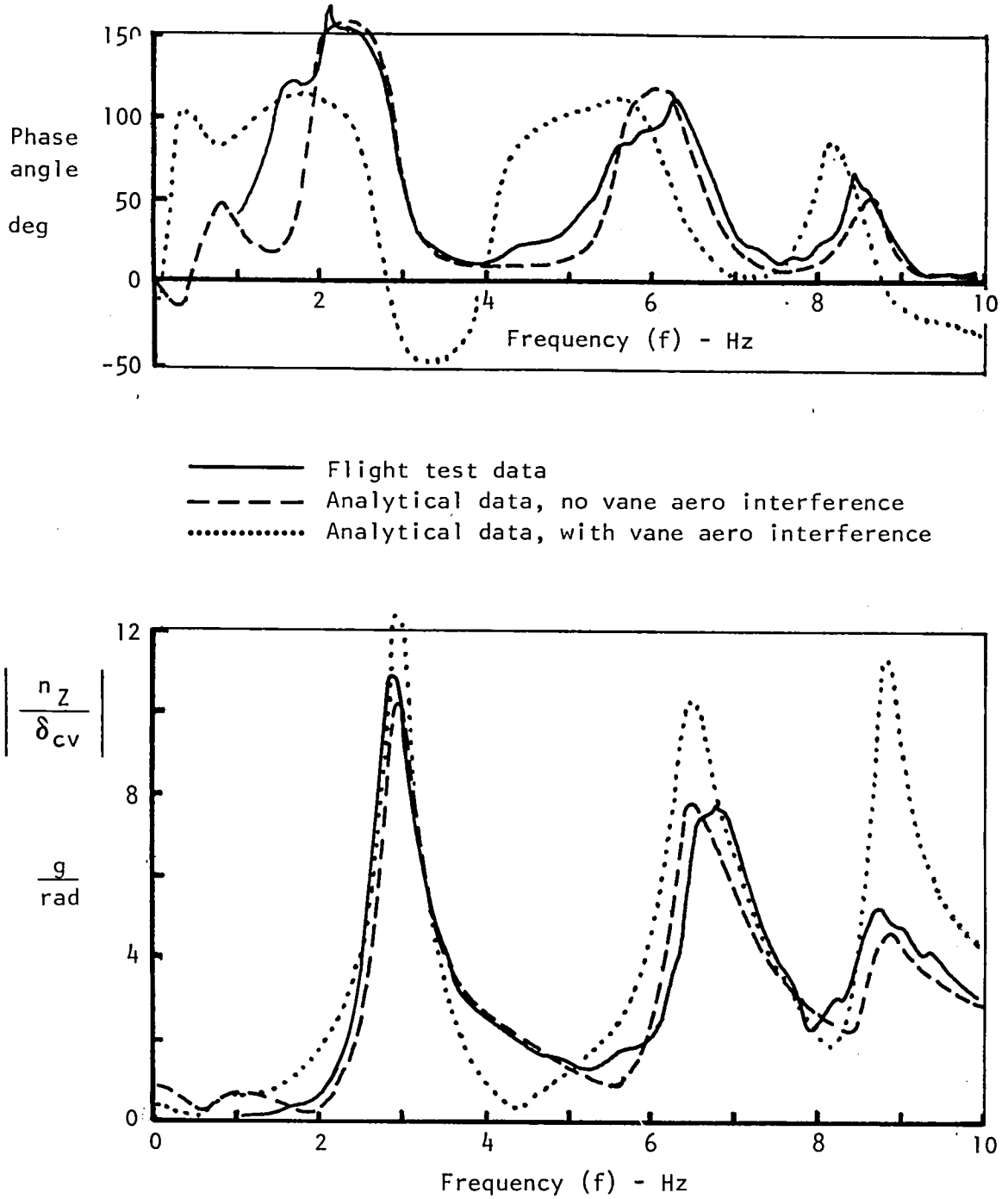

Figure 53. - Effect of SMCS vane aerodynamic interferences, frequency response of normal load factor at FS 571.5 (225) due to SMCS vane deflection, SCAS on, SMCS off.

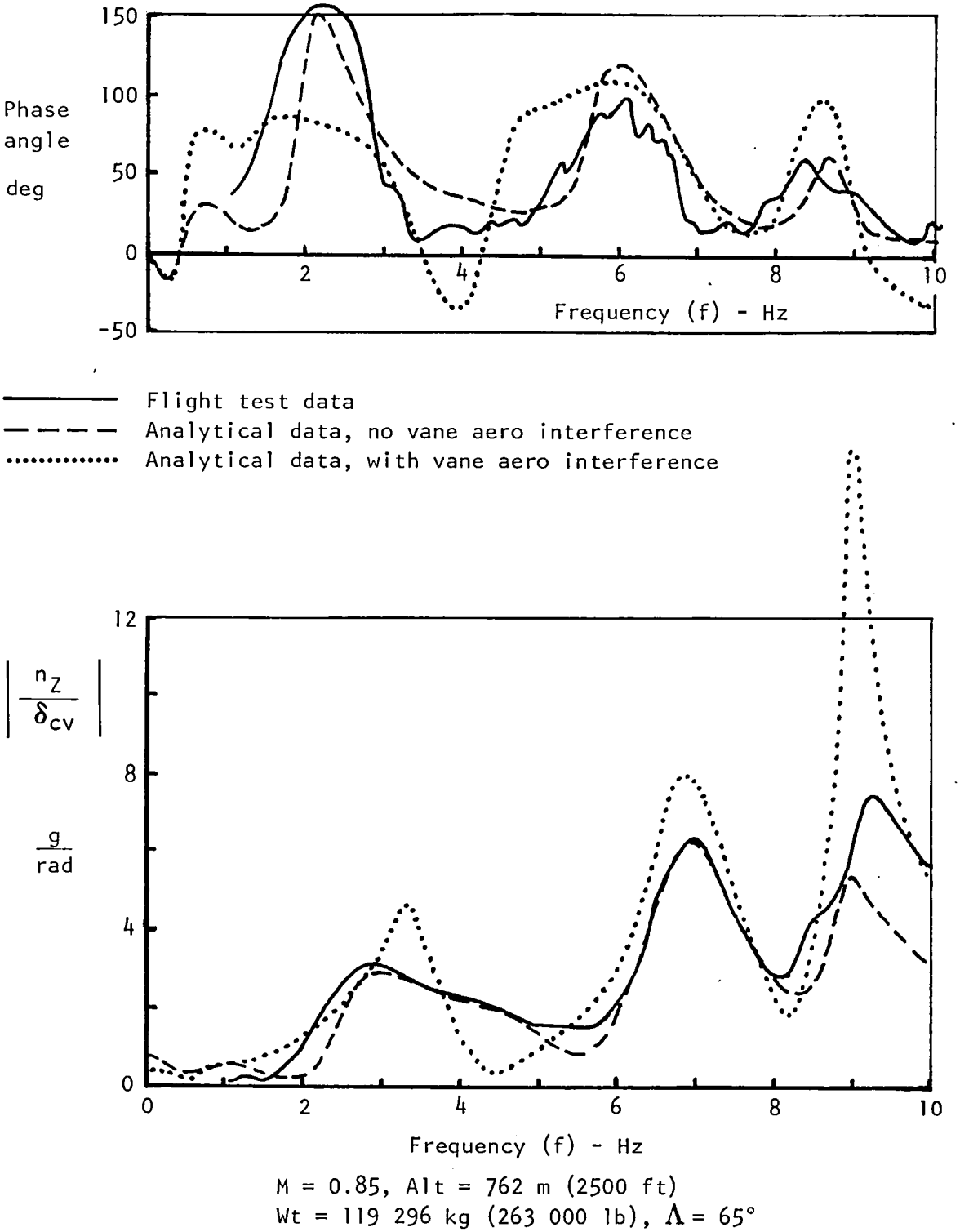

Figure 54. - Effect of SMCS vane aerodynamic interferences, frequency response of normal load factor at FS 571.5 (225) due to SMCS vane deflection, SCAS on, SMCS on.

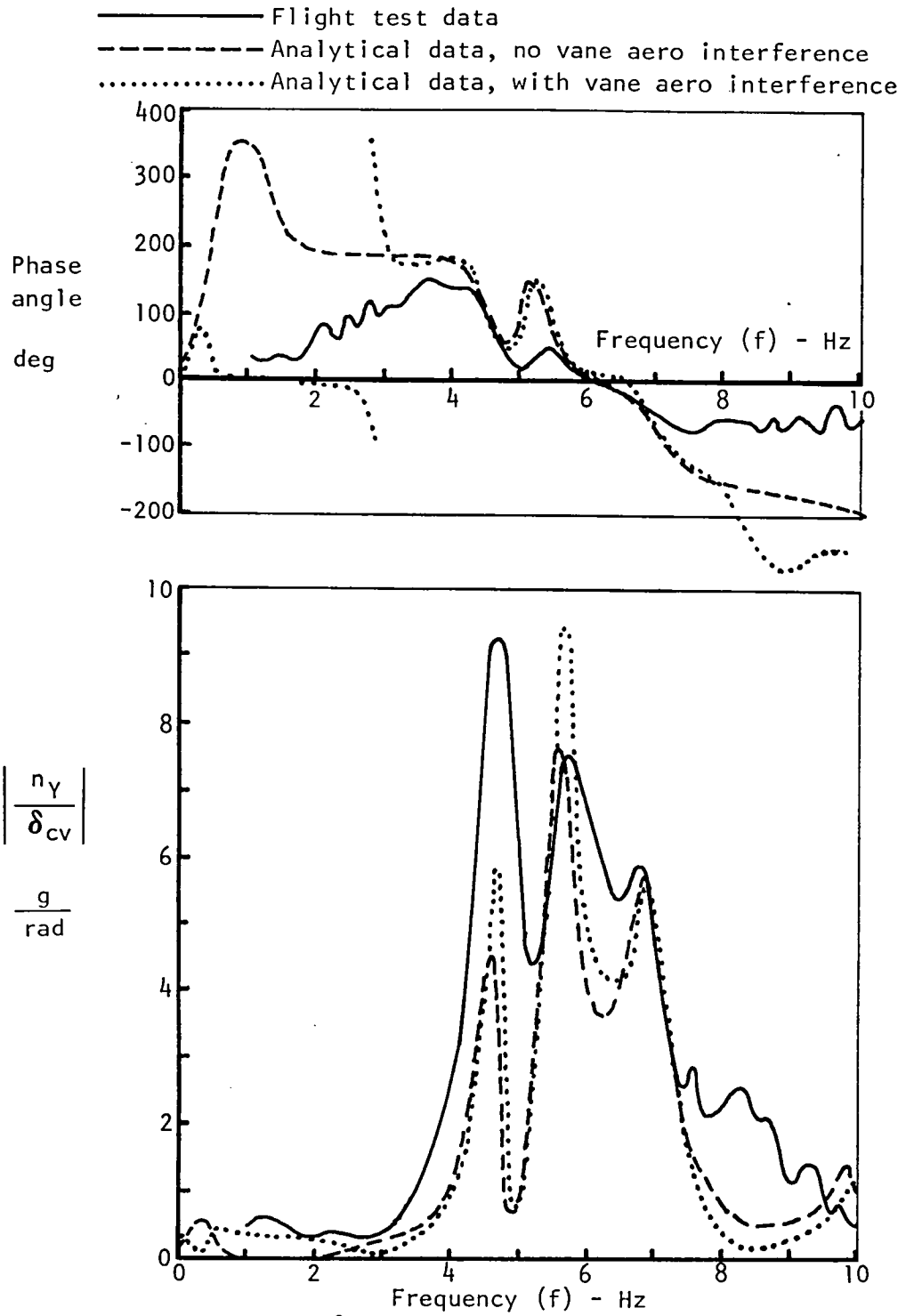

M = 0.85, alt = 762 m (2500 ft)
Wt = 119 296 kg (263 000 lb), Λ = 65°

Figure 55. - Effect of SMCS vane aerodynamic interferences, frequency response of lateral load factor at FS 571.5 (225) due to SMCS vane deflection, SCAS off, SMCS off.

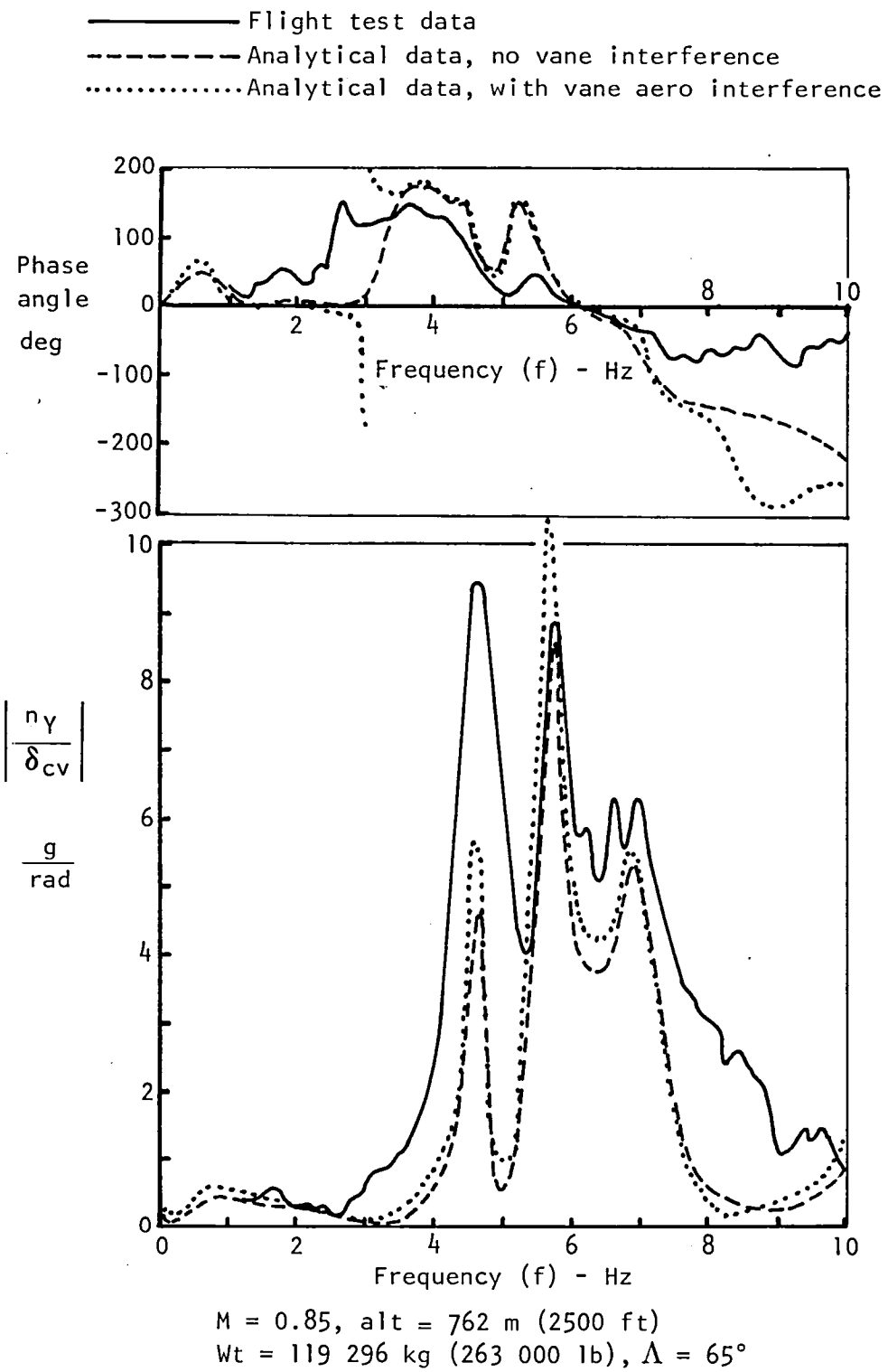

Figure 56. - Effect of SMCS vane aerodynamic interferences, frequency response of lateral load factor at FS 571.5 (225) due to SMCS vane deflection, SCAS on, SMCS off.

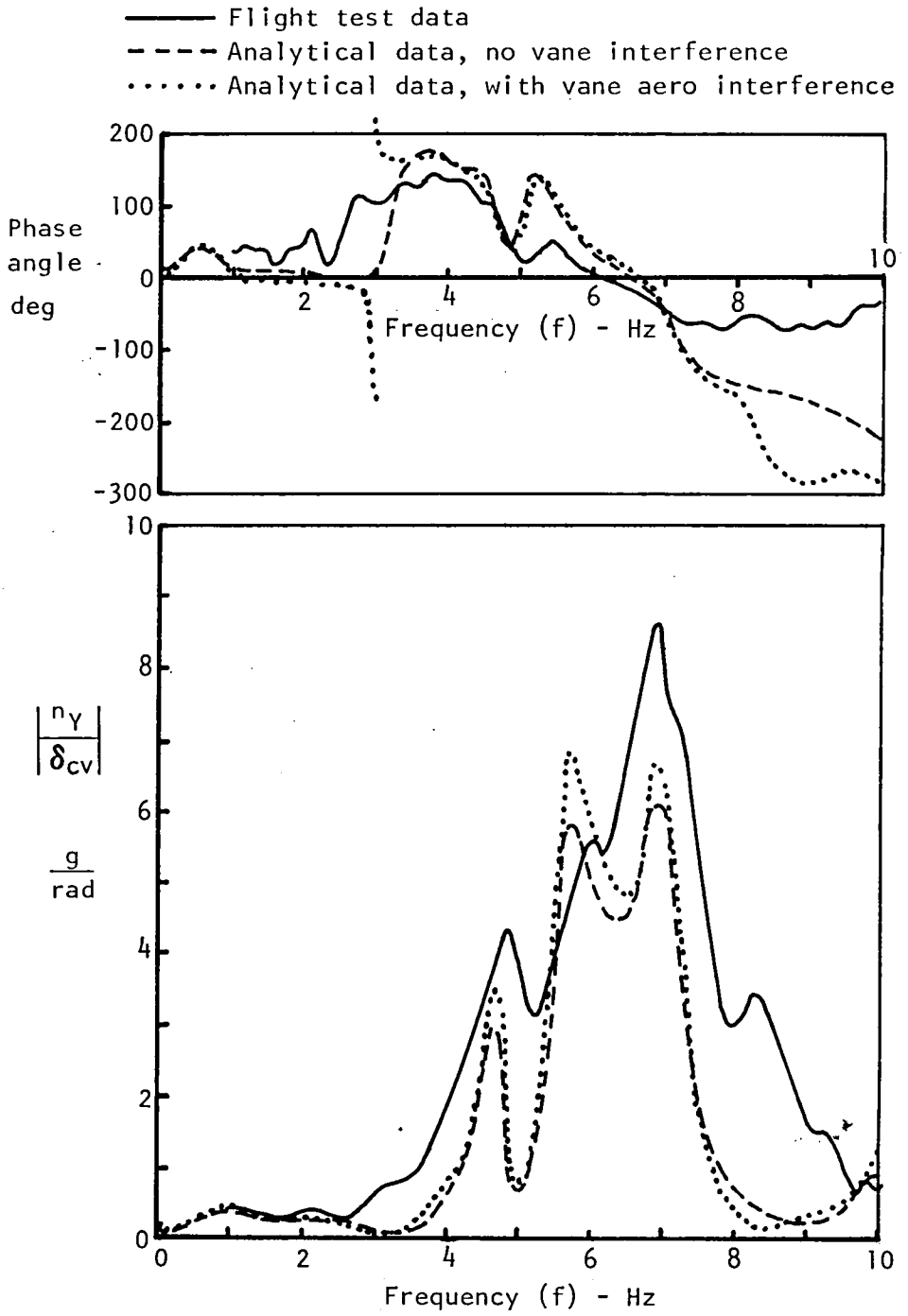

Figure 57. - Effect of SMCS vane aerodynamic interferences, frequency response of lateral load factor at FS 571.5 (225) due to SMCS vane deflection, SCAS on, SMCS on.

significant degradation of the analytical to flight-test-data matches in amplitude and phase. A similar, but less severe degradation of the lateral load factor analytical to flight-test data matches due to inclusion of the interferences is indicated in figures 55 through 57.

Why better agreements were not obtained of analytical results (with interference effects included) to flight-test data is difficult to assess. First, however, it is to be noted that the interference data were obtained using static measurement techniques, whereas the flight-test data were dynamic. The vane on the 0.036-scale force model from which most of the component buildup data were obtained produced small force readings of questionable accuracy for this type of study (moment data were judged more satisfactory). The 0.1-scale forebody model was judged to produce acceptable force and moment data. This, then, implies the need for more expensive and larger scale models tested, using dynamic techniques in order to support accurate analytical vane aerodynamic interference studies. The analytical to flight-test-data comparisons without interference effects displayed in the referenced figures are quite good, particularly for the normal load factors, and suggest that such an expensive approach is not warranted to obtain satisfactory aerodynamic design data. A key conclusion reached as a result of this interference analysis is that a static 0.1-scale forebody model is adequate for obtaining vane aerodynamics data that include the significant local fuselage interference effects; this model produced the basic data used in obtaining the best analytical to flight-test data match displayed in this report.

IMPACT OF SMCS ON SELECTED LOADS

BACKGROUND OF USING SMCS IN THE B-1 FATIGUE ANALYSIS

Because the SMCS system was designed to be fail-safe, not fail-operational, the original B-1 structural design concept was that the aircraft would have full structural integrity with or without the SMCS. That is to say, the structural loads for both design and fatigue analyses of the airframe were to be done with the SCAS operative and the SMCS inoperative. The B-1 SCAS was designed as triple-redundant, fail-operational, and (for the gust loads analysis) fully effective at all times.

During the B-1 design development, studies of the expected airframe loads were accomplished using the available weight, stiffness, and control systems data as it evolved. Several years into the program, it was found that filter changes in the symmetric SCAS were having a considerable impact on the forebody fatigue spectrum. Further analyses indicated that operating the SMCS minimized the effects of the SCAS changes and gave forebody loads of a more consistant magnitude. Also, the lower statistical load levels computed with the

SMCS active were thought to be more representative of those that would be seen in service usage. In view of these facts and with Air Force concurrence, it was decided that the B-1 symmetric fatigue analyses for the low-altitude penetration mission segments would be accomplished with the SMCS operating. Fatigue analyses for all other flight conditions and all design limit load analyses continued to be performed with only the SCAS activated.

GUST LOADS ANALYSIS DESCRIPTION

As with the ride quality analysis described earlier, the dynamic gust loads analysis performed was a generalized modal analysis where the equations of motion were solved in the frequency domain. This analysis used 14 modes of motion: plunge and pitch rigid-body modes and 12 symmetric free-free normal structural modes. Also included were two active control surfaces: the horizontal stabilizer and the structural mode control vane.

For the B-1 aircraft fatigue analysis, the missions for the expected service usage were each divided into segments. Flight conditions representing the mission segments were selected for analysis. For each flight condition, static aeroelastic trim loads (to be used as mean load levels) and gust dynamic response incremental loads were computed. Both the trim loads and gust incremental loads were issued for fatigue and fracture mechanics analyses as distributed grid loads. Along with the gust loads were the estimated time to be spent at the flight condition and a graph of the expected load exceedances per hour flight.

Aeroelastic loads for the steady-flight trim conditions were computed using wind tunnel-derived nonlinear aerodynamic data for the rigid and theoretically computed aeroelastic increment loads. These static aeroelastic calculations were performed with structural influence coefficients fixed at a point near the aircraft CG.

The gust response equations of motion that were used are presented as follows in matrix notation (ref. 6). See the appendix for symbol definitions.

$$\left[-\omega^2 \left[\overline{M} \right] + (1 + jg) \left[\overline{M} \right] \left[\Omega^2 \right] + \left[Q_M \right] + \left[Q_C \right] \left[T \right] \right] \left\{ q \right\} = - \left\{ Q_G \right\}$$

Frequency response functions of the generalized coordinates, q, were obtained by solving the equations for a unit sinusoidal gust input at each of 100 equally spaced frequencies.

GUST LOADS STRUCTURAL MODEL

A complete aircraft structural model was derived from structural flexibility influence coefficients generated by the B-1 Internal Loads Group using finite-element methods. These SIC's, which were used for both static and dynamic analyses, were for partially buckled skins so as to be representative of the aircraft stiffness at the design-limit load level. On the lifting surfaces, the SIC points were arranged in streamwise rows to make it easy to compute the required slopes and deflections for the aeroelastic analyses. Figure 58 shows the arrangement of SIC points, and table VII presents the structural degrees of freedom used in this model.

TABLE VII.- GUST LOADS MODEL STRUCTURAL DEGREES OF FREEDOM

Component	Motion Type					
	X	Y	Z	θ_x	θ_y	θ_z
Fuselage, fixed wing and fairings			57			
Nacelle, including engines	4	6	17	2	2	2
Moveable wing	4	4	58			
Horizontal stabilizer	2		45			
Total = 203 Σ	10	10	177	2	2	2

Normal elastic modes, free from rigid-body plunge and pitch constraints, were computed by the method of reference 7, as shown in the following equation.

$$[R]\,[SIC]\,[M]\,\{\phi\} = \frac{1}{\Omega^2}\,\{\phi\}$$

where:

$$\left[\,R\,\right] = \left[\,I\,\right] - \left[\,\phi^{RBM}\,\right]\left[\,\overline{M}_{RBM}\,\right]^{-1}\left[\,\phi^{RBM}\,\right]^{T}\left[\,M\,\right]$$

GUST LOADS AERODYNAMICS

Aerodynamic generalized forces were developed using the Doublet Lattice method with the wing-fuselage-horizontal-tail combination run at one time. Figure 58 presents a diagram of the aerodynamic panel arrangement. Geometry adjustments were made to the theoretical model to improve the correlation of the zero-frequency stability derivatives and pressure distributions with wind-tunnel test results. One particular adjustment was to leave a small gap at the root of the horizontal stabilizer. At each Mach number, the width of the gap was adjusted to get the best match of stabilizer C_{L_α} and spanwise loading. For the SMCS vane, the aerodynamics were run separately using the vane modeled with 30 boxes (5 chordwise and 6 spanwise) in the form of a symmetric inverted V. These data were correlated against the average wind-tunnel test data. Generalized vane forces due to modal motion and gust were then added to those from the wing-fuselage-horizontal combination. No attempt was made to simulate any vortex wake produced by the vane.

Deflections used to define the structural shape for aerodynamic calculations were selected from the SIC points available in the gust analysis model. It was found to be necessary to review the shape of each mode to insure that the deflections chosen defined a smooth shape with no sudden changes or reversals in slope. Points eliminated represented concentrated mass items and fairing-nacelle deflections that were not representative of the true wing-body streamwise shape.

Generalized forces due to modal, vane, and horizontal-tail motions and a unit sinusoidal vertical gust were computed at zero frequency and eight frequencies between zero and approximately 11 Hz. In the process of computing the aerodynamics, the downwash induction matrices generated were retained on magnetic files so that they could be used again with different mode shapes, thus saving considerable computing cost.

At each of the 100 solution frequencies required, generalized aerodynamic forces were obtained by spline-curve fits of real and imaginary parts of the generalized forces computed at the nine frequencies as previously described. To improve the quality of the spline interpolations of the gust forces, the gust reference point was transferred to a point just forward of the aircraft aerodynamic center. This transfer tends to flatten the curves; i.e., reduces the rate of oscillation of the functions with frequency. After fitting, the gust reference point was transferred back to the nose of the aircraft. For convenience, the gust reference point is normally placed at the nose of the aircraft so that when the solution frequency response functions are used to compute time histories due to a discrete gust input, the penetration of the gust starts at time equals zero.

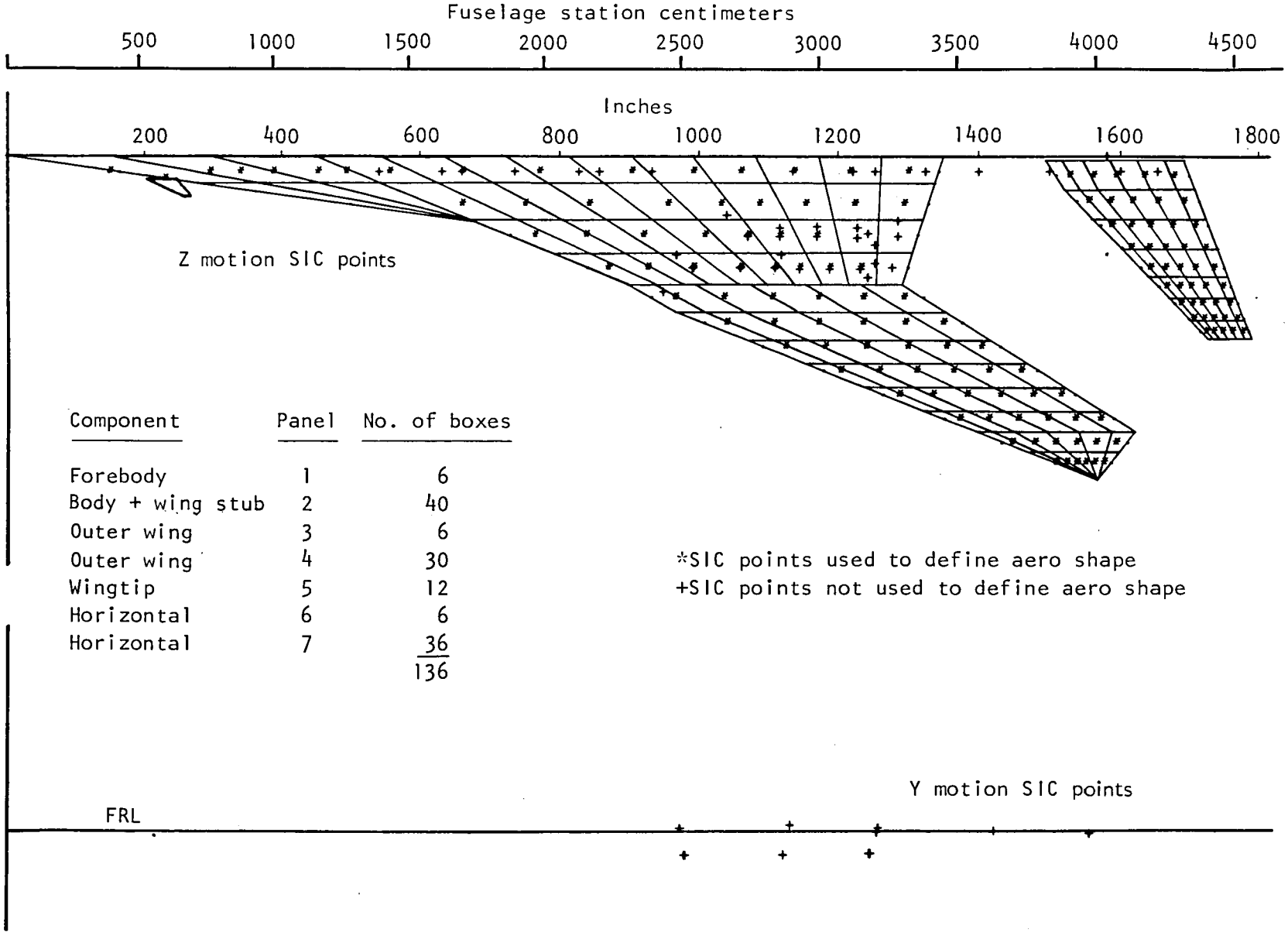

Figure 58. - Loads analysis SIC point locations and Doublet Lattice geometry.

Final adjustments were made by direct ratioing to bring the generalized forces in the rigid-body modes, due to rigid-body motions and gust, into agreement with the available wind tunnel measured values of C_{L_α} and C_{M_α}. Factors developed in the region of zero frequency were applied to the full range of solution frequencies.

GUST LOADS CONTROL SYSTEMS

Descriptions of the active control systems (ref. 8) used in this gust analysis are presented in figure 59. Also shown is the method used to form the transformation matrix, [T], for control-systems feedback, relating control-surface deflections to the generalized coordinates.

LOAD METHOD DISCUSSION

Gust response loads were computed at selected structural stations. (See figure 60.) The mode displacement method was used at each frequency of solution to compute distributed loads at the SIC points. Shears, moments, and torques were then computed by finite summations of the loads or the loads times the appropriate moment arms. Figure 61 presents the matrix equations used to perform the load computations. The mode displacement method finds a set of net external loads that are equivalent to the loads required to hold the structure in the deflected shape attained (ref. 3). To obtain accurate results, a linear superposition of the elastic modes that are used in the solution must give a good description of the structural deflections. This requires that at least several modes of vibrations that are primary to each structural component be included. Modes selected should not be restricted in frequency to the maximum Fourier frequency of the solution, but should be chosen to obtain all significant contributions to the structural deflections.

Although the final loads for structural analysis were issued as grid or mass point loads, it was necessary to compute shears and moments in order to keep the number of items used in the load calculations to a manageable size. On each structural component, a reference axis and load stations were established for computing the shears, moments, and torques. The LOAD GEOM matrix contained one row for each load item. Basically the LOAD GEOM row elements are: for a shear, ones in the columns required to select loads outboard of the load station axis, and for a moment or torque, the arms from the load station or reference axis to each required load point.

To improve the accuracy of the computed shears, moments, and torques, each load acting on a SIC point was considered to be a pressure evenly distributed over a load box around the point. For any load box cut by a load station axis, only the box area outboard of the axis was considered in

Symmetric SCAS at SL, $K_{hp} = .36$

$$\underset{\text{Degrees}}{\delta_H} = K_{hp}\underbrace{\left(\frac{30.26\,(S^2+7.066\,S+13.28)}{13.28\,(S^2+14.61\,S+30.26)}\right)}_{\text{Compensation}}\underbrace{\left(\frac{S^2+3.04\,S+960}{S^2+121.6\,S+960}\right)}_{\text{Notch}}\underbrace{\left(\frac{32}{S+32}\right)}_{\text{Low pass}}\underbrace{\left(\frac{3600}{S^2+55\,S+3600}\right)}_{\text{Servo}}\underbrace{\left(\frac{10}{S+10}\right)}_{\text{Actuator}}\left(2.05\,\Delta\eta_{z_{CG}}+0.716\,\dot{\theta}_{CG}\right)$$

Symmetric SMCS for M = .85 at SL, $K_{\bar{q}_o} = .565$

$$\underset{\text{Degrees}}{\delta_{cv}} = 6.58\,K_{\bar{q}_o}\underbrace{\left(\frac{(S^2+31.4S+(157)^2)}{(S^2+314S+(157)^2)}\right)}_{\text{Notch}}\underbrace{\left(\frac{10}{S+10}\right)}_{\text{Shaping}}\underbrace{\left(\frac{10\,S}{S+10}\right)}_{\text{Washout}}\underbrace{\left(\frac{654.7\,(S-255)}{(S+223)(S+729)}\right)}_{\text{Actuators}}\left(\Delta\eta_{z_{cv}}-\left(\frac{10}{S+10}\right)\Delta\eta_{z_{CG}}\right)$$

The matrix representing the control systems in the solution equations was formed as:

$$\underset{2,14}{\left[\;T(\omega)\;\right]} = \underbrace{\begin{bmatrix} P^H_{\eta_{z_{CG}}} & P^H_{\dot{\theta}_{CG}} & 0 \\ P^V_{\eta_{z_{CG}}} & 0 & P^V_{\eta_{z_{cv}}} \end{bmatrix}}_{\text{Gains x polynomials evaluated at } S = j\omega}\begin{bmatrix} \omega^2/g & & \\ & j\omega & \\ & & \omega^2/g \end{bmatrix}\underbrace{\begin{bmatrix} \phi_{CG,1} & \cdots & \phi_{CG,14} \\ \phi'_{CG,1} & \cdots & \phi'_{CG,14} \\ \phi_{CV,1} & \cdots & \phi_{CV,14} \end{bmatrix}}_{\text{Mode deflections and slopes at sensor locations}}$$

Where: CG = FS 2649 cm (1043 in), CV = FS 516 cm (203 in), $\phi' = \frac{d\phi}{dx}$

Figure 59. - Control systems for gust loads.

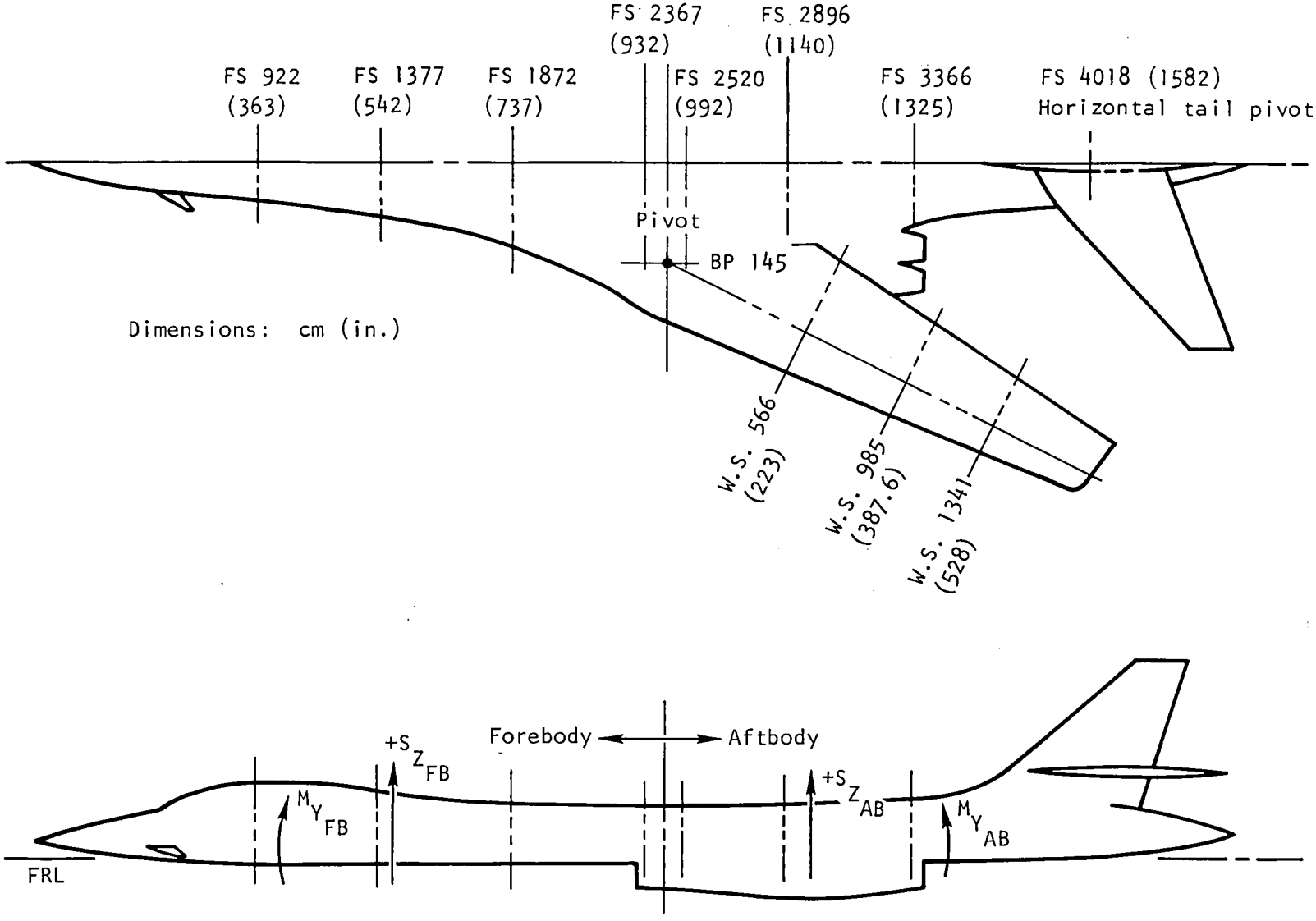

Figure 60. - Structural stations for gust loads analysis.

Point load at each mass point, by mode displacement method

$$\underset{N,1}{\left\{F(\omega)\right\}} = \underset{N,N}{\left[M\right]}\underset{N,NEM}{\left[\phi^{E}\right]}\underset{NEM,NEM}{\left[\Omega^{2}\right]}\underset{NEM,1}{\left\{q(\omega)\right\}}$$

Calculation of loads; shears, moments & torques

$$\underset{NLI,1}{\left\{LOADS(\omega)\right\}} = \underset{NLI,N}{\left[\begin{matrix}LOAD\\GEOM\end{matrix}\right]}\underset{N,1}{\left\{F(\omega)\right\}}$$

Acceleration at point i

$$a_i(\omega) = -\omega^2 \underset{1,NM}{\left\lfloor \phi_{i,1} \text{------} \phi_{i,NM} \right\rfloor} \underset{NM,1}{\left\{q(\omega)\right\}}$$

Pitch rate at point i

$$\dot{\theta}_i(\omega) = j\omega \underset{1,NM}{\left\lfloor \frac{d\phi_{i,1}}{dx} \text{------} \frac{d\phi_{i,NM}}{dx} \right\rfloor} \underset{NM,1}{\left\{q(\omega)\right\}}$$

Control surface deflections

$$\underset{2,1}{\left\{\begin{matrix}\delta_H(\omega)\\ \delta_V(\omega)\end{matrix}\right\}} = \underset{2,NM}{\left[T(\omega)\right]}\underset{NM,1}{\left\{q(\omega)\right\}}$$

Where:
- N = Number of mass points
- NM = Number of modes, rigid plus elastic
- NEM = Number of elastic modes
- NLI = Number of S, M, & T load items

Figure 61. - Load calculation equations.

computing the load. The moment and torsion arms for this load were taken to the centroid of the outboard area.

The partitioning of the load boxes was computer mechanized by subdividing a box cut by a load station axis into 100 small boxes (10 equal division on a side). Area ratio and centroid coordinates of each subbox were computed using as data the coordinates of the load box corner points. The area ratio was the ratio of the subbox area to the load box area. Coordinates of each subbox centroid were then checked, and all those outboard of the load station were retained. The retained subbox area ratios and area ratio moments were accumulated to obtain the total element values for the LOAD GEOM matrix.

Other load items computed were load factors at selected stations, pitch rate and acceleration, and control-surface deflections.

Frequency response functions resulting from these load item calculations were computer plotted for visual review and also saved on magnetic files for use in computing the load exceedance curves and in-phase component load conditions.

GUST STATISTICAL LOAD CALCULATIONS

For each load item, the turbulence response power spectrum, $\Phi_O(\omega)$, response quantities $\overline{A}$ and N_O, and a frequency of exceedance of load curve were computed. The methods used were as presented in reference 9 and as follows:

$$\Phi_O(\omega) = \Phi_W(\omega) \left|H(\omega)\right|^2$$

$$\overline{A} = \left[\int_O^\infty \Phi_O(\omega)\, d\omega\right]^{1/2}$$

$$N_O = \frac{3600\ V}{2\pi\overline{A}} \left[\int_O^\infty \omega^2\, \Phi_O(\omega)\, d\omega\right]^{1/2}$$

$$N(y) = N_O \left[P_1 \exp\left(\frac{-y}{b_1\overline{A}}\right) + P_2 \exp\left(\frac{-y}{b_2\overline{A}}\right)\right]$$

The Von Karman continuous turbulence spectrum was used with the gust scale L equal to 152.4 meters (500 feet). Also used were the sea-level vertical gust parameters for low-level contour flying: $P_1 = 1.0$, $b_1 = 0.823$ m/sec (2.70 ft/sec), $P_2 = 1 \times 10^{-5}$, and $b_2 = 3.246$ m/sec (10.65 ft/sec). In the calculations to compute $\bar{\Lambda}$ and N_o, the required integrations were performed from zero through the highest frequency of the analysis, approximately 11 Hz.

The load level that could be expected to be exceeded one time per airplane life in each mission segment was determined for each load item. This was done to define a set of loads that could be used to develop distributed loading conditions for the fatigue analysis. These load values were read from the exceedance curve of each item at one over the total number of flight hours for the mission segment. By nature, all of these loads were positive numbers, and although they were considered to represent a load-cycle condition, the phasing relationships between the loads were unknown.

LOAD PHASING

The problem of load phasing was solved by application of the correlation coefficient method to produce what are referred to as in-phase component load conditions. Reference 10 developed and used the correlation coefficient to express the statistical correlation between two gust response parameters.

$$\rho_{ij}\sigma_i\sigma_j = \int_0^\infty \text{Real} \left(\Phi_w(\omega)\ H_i(\omega)\ H_j^*(\omega) \right)\ d\omega$$

For this gust load analysis, correlation was developed between all of the load items. Correlation coefficients were not actually computed; but a matrix [B], the elements of which were proportional to $\rho_{ij}\sigma_i\sigma_j$, was developed. Here i and j indicate load item numbers and, thus, the corresponding [B] matrix row and column numbers.

$$\left[B \right] = \text{Real} \left[\left[H(\omega) \right] \left[\Phi_w(\omega) \right] \left[H^*(\omega) \right]^T \right]$$

Each column of [B] was then normalized on the diagonal element and weighted with the corresponding load item expected value.

$$\left[S \right] = \left[B \right] \left[\frac{1}{B_{ij}} \right] \left[E \right]$$

where:

$$i = j$$

Columns of the resulting [S] matrix represent load conditions where the diagonal elements are the load item expected values and the off-diagonal elements are the statistically in-phase components of the other load items.

CONDITION MATCHING

To develop distributed grid loads that matched the in-phase component load conditions the mode displacement method was again used. As shown in figure 61, this method can be used to compute distributed loads for a given set of generalized coordinates. For this matching problem, the shears, moments, and torques at each load station were known, and the solution had to be made for the generalized coordinates. The load generation matrix was defined as:

$$\left[\begin{matrix} \text{LOAD} \\ \text{GEN} \end{matrix} \right] = \left[\begin{matrix} \text{LOAD} \\ \text{GEOM} \end{matrix} \right] \left[M \right] \left[\phi^E \right] \left[\Omega^2 \right]$$

Then the coordinates and the shear, moment, and torque loads from the [S] matrix are related as:

$$\left\{ \text{SLOADS} \right\} = \left[\begin{matrix} \text{LOAD} \\ \text{GEN} \end{matrix} \right] \left\{ h \right\}$$

This equation is usually overdetermined, and the coordinates are solved for in a least-squares sense. Due to the large differences in magnitude of the shears and moments involved, the solution results generally provide a poor load match. To improve the solution quality, each load item was weighted so that it had equal magnitude and, thus, equal significance in the solution. By multiplying through by a diagonal matrix of one over the loads, the following equation was obtained.

$$\left\{ 1 \right\} = \left[\left[\frac{1}{\text{SLOADS}} \right] \left[\begin{matrix} \text{LOAD} \\ \text{GEN} \end{matrix} \right] \right] \left\{ h \right\}$$

Taking one column from the [S] matrix at a time, a general least-squares solution program was used to solve for the generalized coordinates. Distributed point loads for the in-phase matching conditions were then formed by the mode displacement method.

EXAMPLE CONDITION LOAD RESULTS

Load results for a B-1 aircraft low-altitude penetration condition of M = 0.85, altitude = SL, using sweep = 67.5 degrees, and weight = 140 614 kilograms (310 000 pounds) are presented in table VIII. Also, presented in figures 62 through 100 are plots of the load-item frequency-response functions, power spectrums, and load exceedance curves for the items listed:

(1) Wing, WS 985 (387.6), bending moment

(2) Forebody, FS 1377 (542), bending moment

(3) Forebody, FS 2367 (932), bending moment

(4) Normal load factor, n_z, at CG

(5) Normal load factor, n_z, at pilot

(6) Delta (deflection) of horizontal stabilizer

(7) Delta (deflection) of SMCS vane (SMCS on)

TABLE VIII. - LOAD COMPARISON, SMCS OFF VERSUS SMCS ON

Expected loads, increments from trim, one occurrence per 1000 hours
M = 0.85 at SL, wing sweep = 67.5°, wt = 140 616 kg (310 000 lb)

SCAS on

Load items		Loads			
		SMCS off		SMCS on	
Shear	WS 1341 (528)	38 330	(8 617)	39 149	(8 801)
Bend. mom.		67 232	(49 588)	69 567	(51 310)
Torsion		3 243	(2 392)	3 246	(2 394)
Shear	WS 985 (387.6)	80 406	(18 076)	78 622	(17 675)
Bend. mom.		278 977	(205 764)	280 389	(206 805)
Torsion		11 977	(8 834)	11 413	(8 418)
Shear	WS 566 (223)	123 958	(27 867)	117 842	(26 492)
Bend. mom.		698 319	(515 056)	681 015	(502 293)
Torsion		20 984	(15 477)	19 975	(14 733)
Shear	at wing pivot	171 710	(38 602)	155 567	(34 973)
Roll mom.		649 463	(479 022	612 953	(452 093)
Pitch mom.		1 355 627	(999 864)	1 280 991	(944 815)
Shear	at HT root	58 681	(13 192)	60 189	(13 531)
Roll mom.		237 236	(174 977)	238 159	(175 658)
Pitch mom.		126 113	(93 017)	127 587	(94 104)
FB mom.	FS 922 (363)	381 315	(281 245)	188 692	(139 173)
FB mom.	FS 1377 (542)	1 060 369	(782 092)	349 942	(258 105)
FB mom.	FS 1872 (737)	1 848 893	(1 363 680)	364 677	(268 973)
FB mom.	FS 2367 (932)	2 261 236	(1 667 810)	627 525	(462 841)
AB mom.	FS 2520 (992)	4 106 793	(3 029 030)	2 366 297	(1 745 300)
AB mom.	FS 2896 (1140)	2 438 061	(1 798 230)	1 100 992	(812 054)
AB mom.	FS 3366 (1325)	983 160	(725 145)	603 152	(444 864)
Nacelle S_Z		85 953	(19 323)	91 366	(20 540)
Δn_Z at CG		0.956		0.949	
Δn_Z at pilot		2.007		1.041	
δ horizontal, degrees		0.699		0.728	
δ mode vane, degrees		-		19.955	

Stations, cm (in.)
Shears, N (lb)
Moments and torques, N-m (lb-ft)

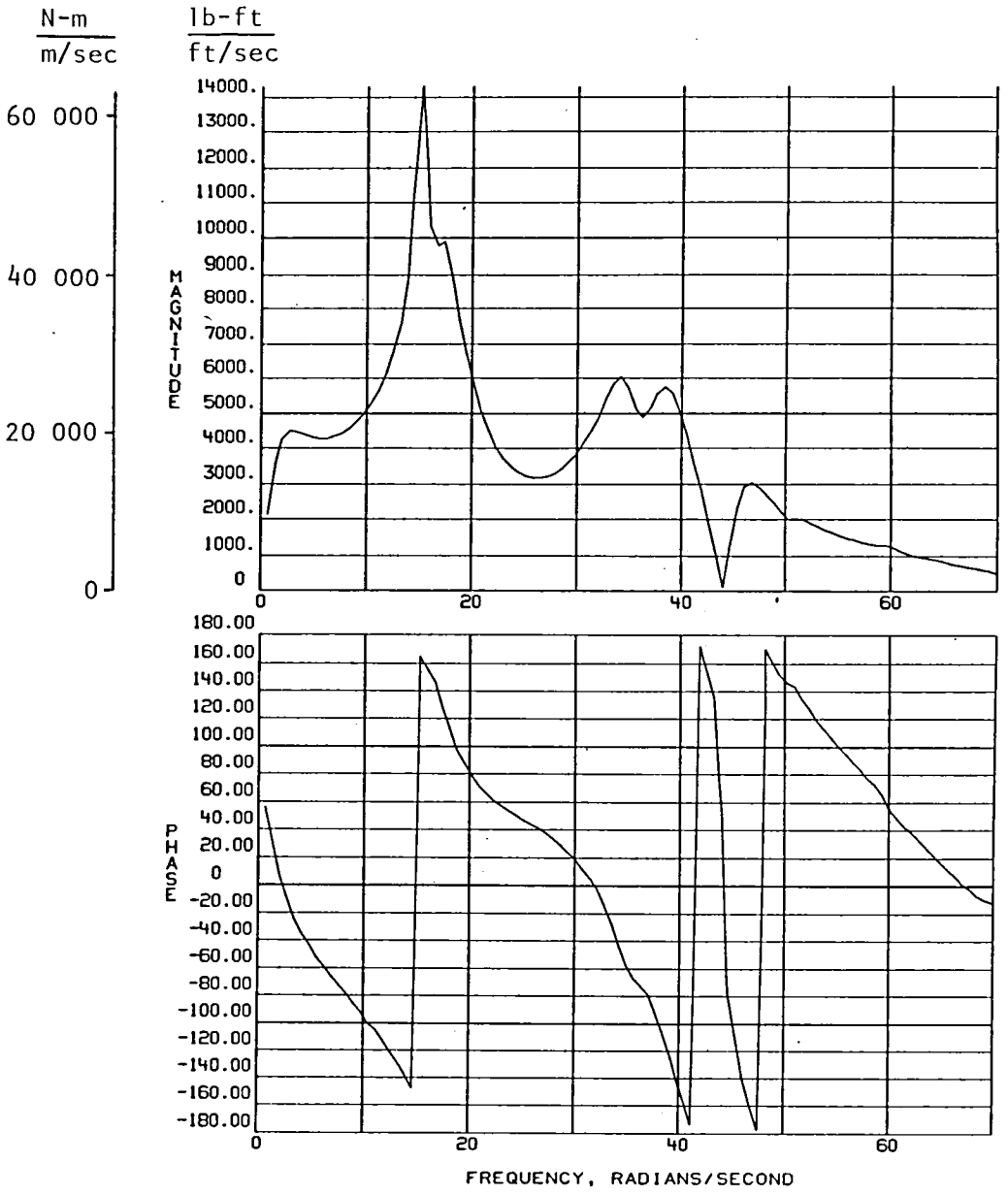

Figure 62. - SMCS off, wing bending moment frequency response - WS 985 cm (387.6 in.).

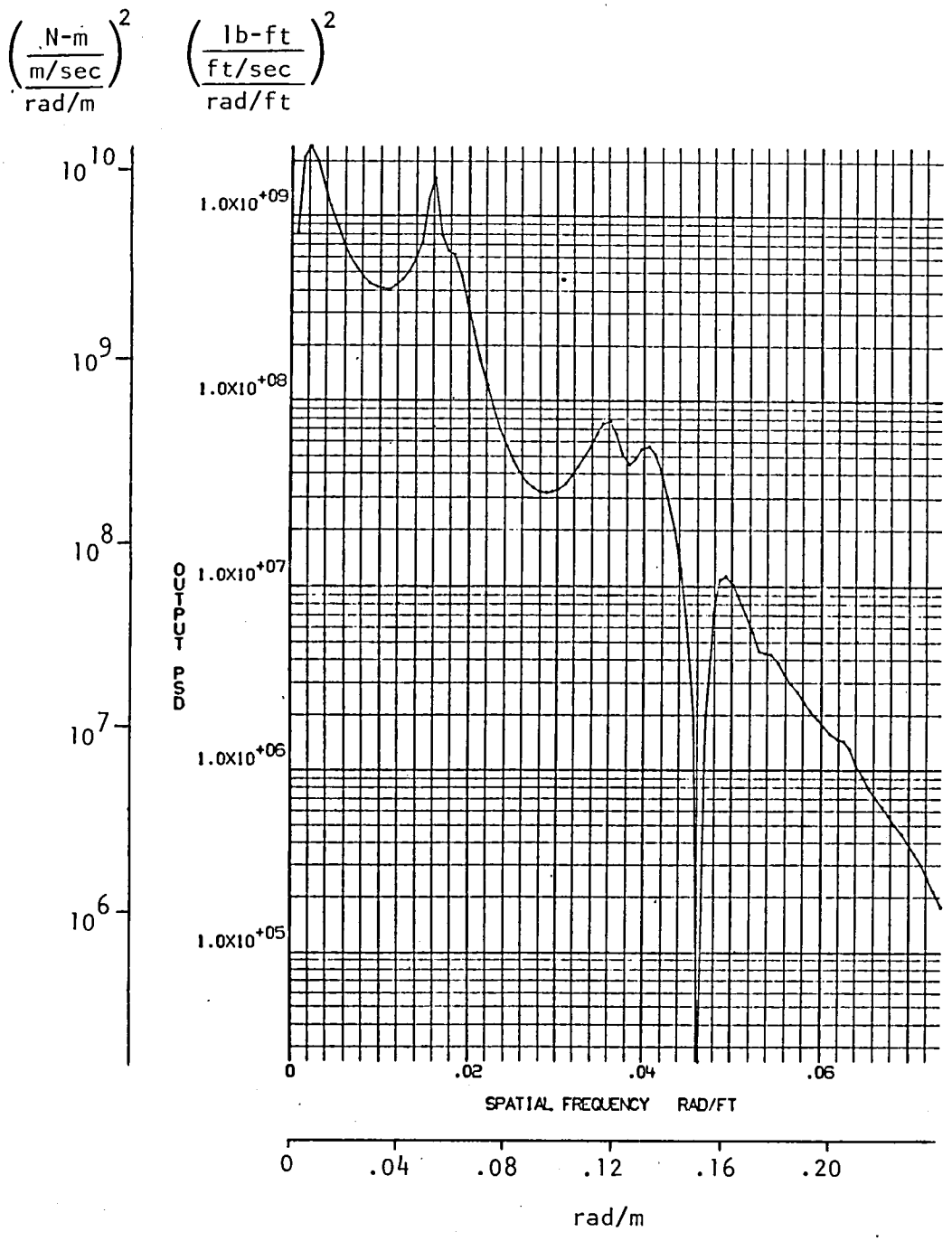

Figure 63. - SMCS off, wing bending moment response power spectrum - WS 985 cm (387.6 in.).

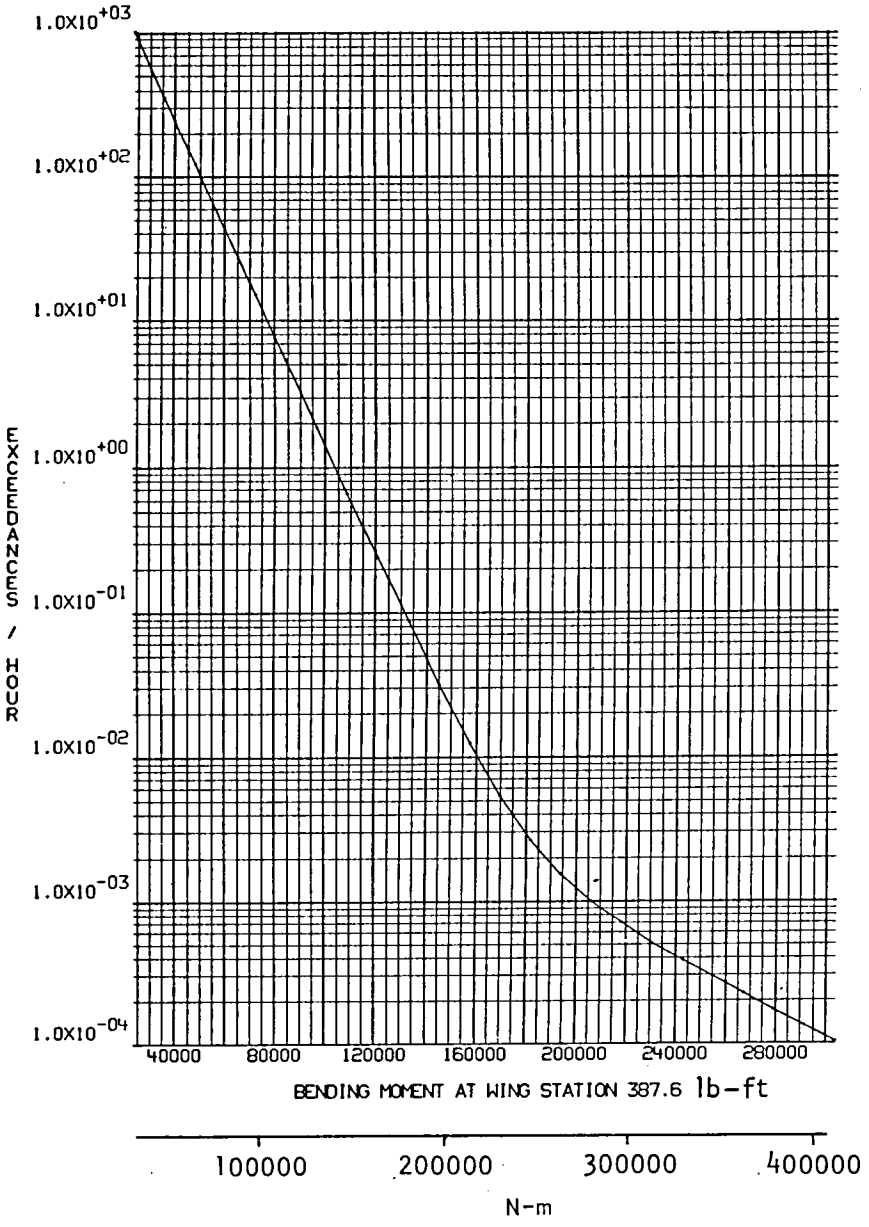

Figure 64. - SMCS off, wing bending moment exceedances - WS 985 cm (387.6 in.).

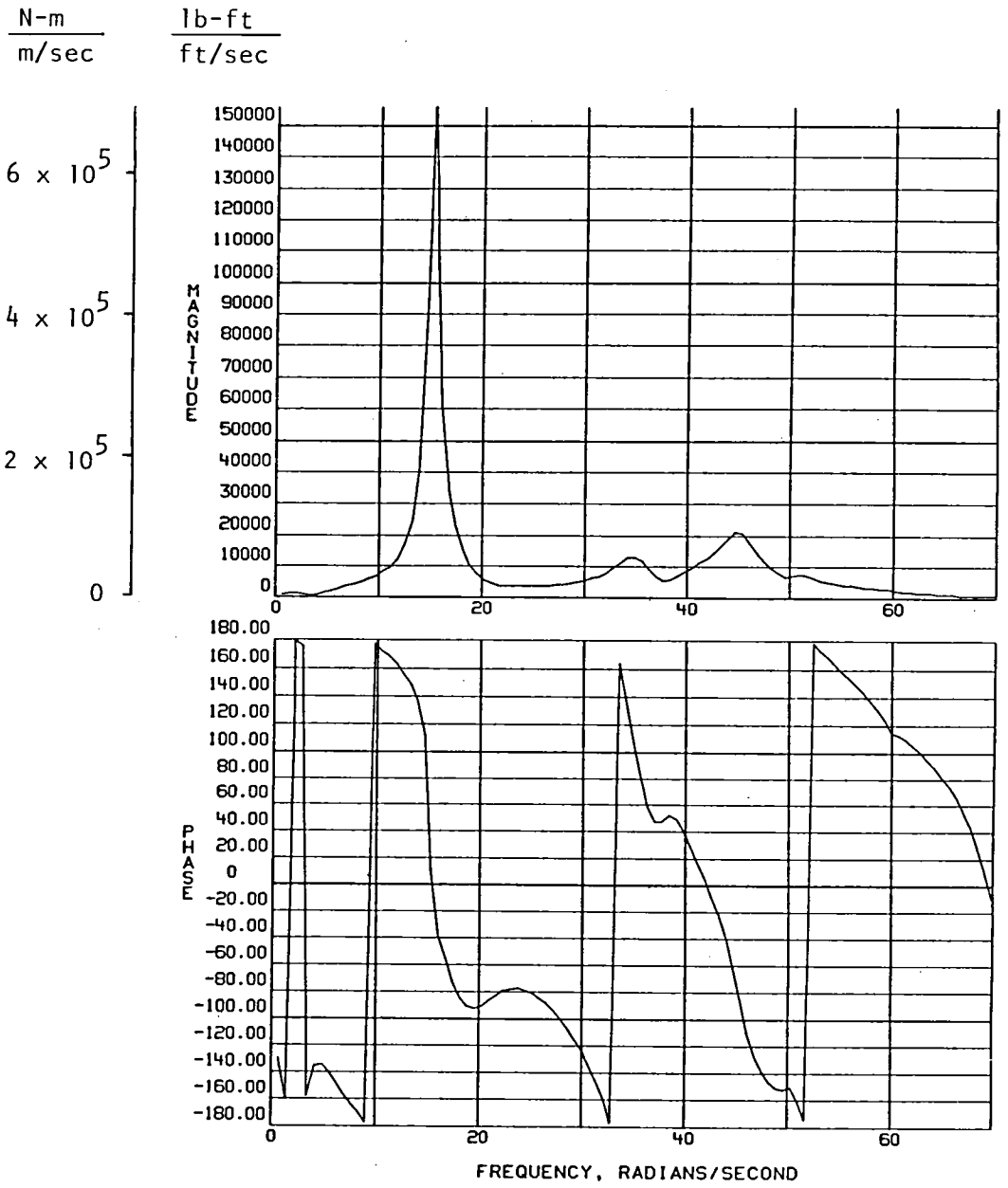

Figure 65. - SMCS off, forebody bending moment frequency response - FS 1377 cm (542 in.).

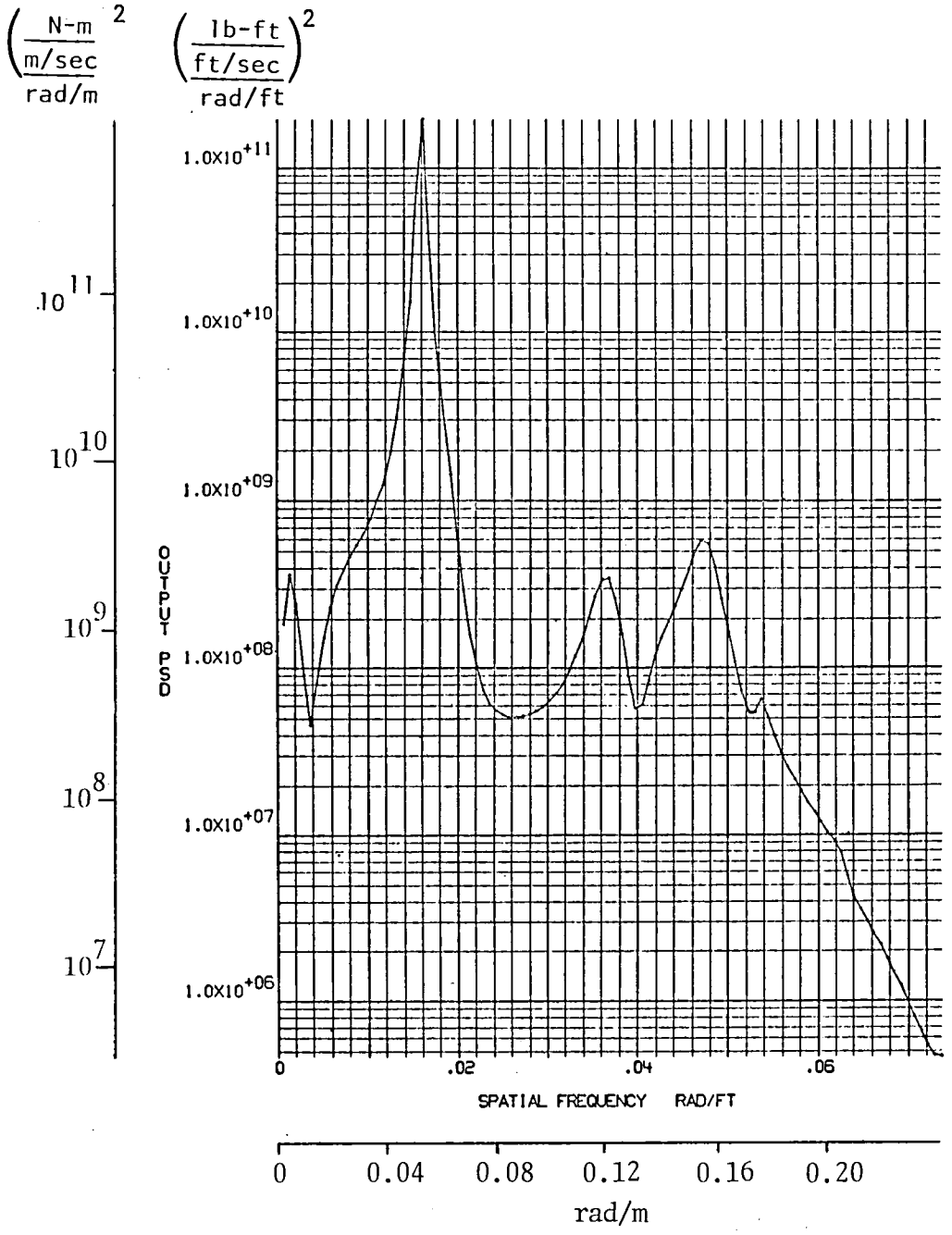

Figure 66. - SMCS off, forebody bending moment response power spectrum - FS 1377 cm (542 in.).

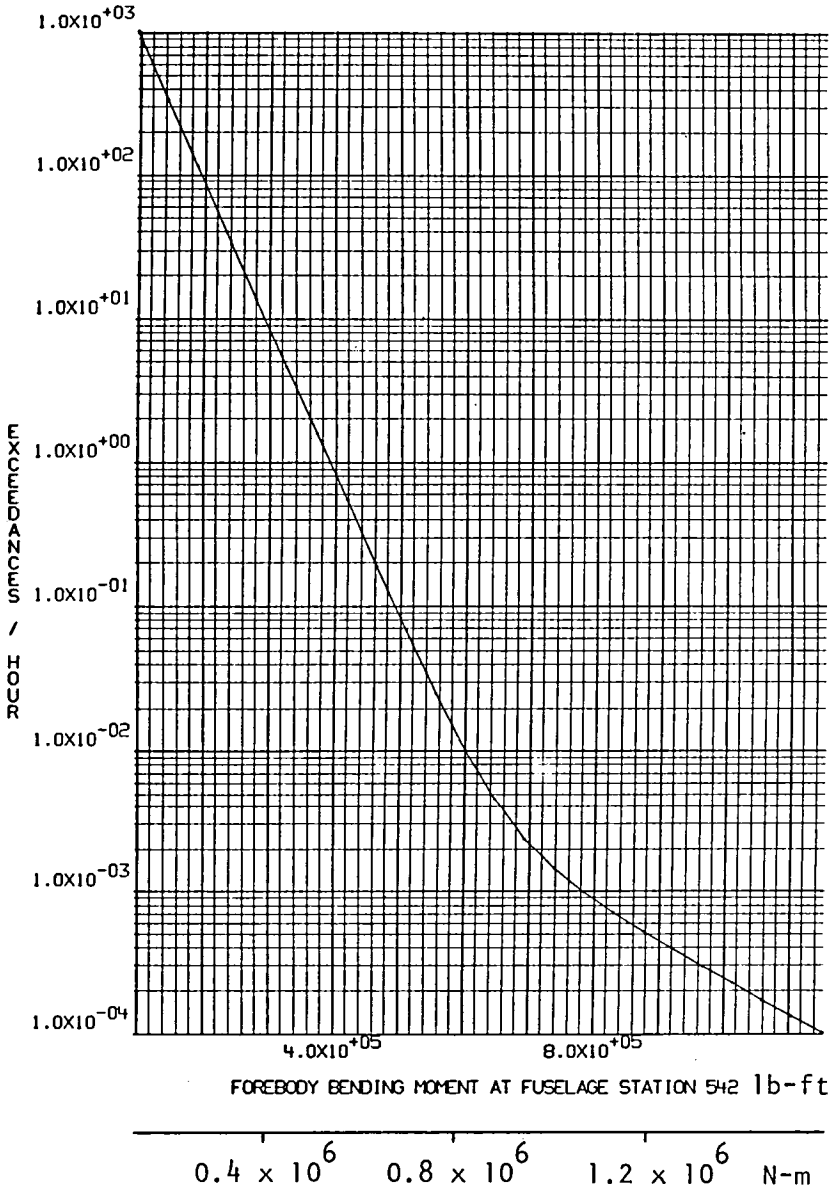

Figure 67. - SMCS off, forebody bending moment exceedances - FS 1377 cm (542 in.).

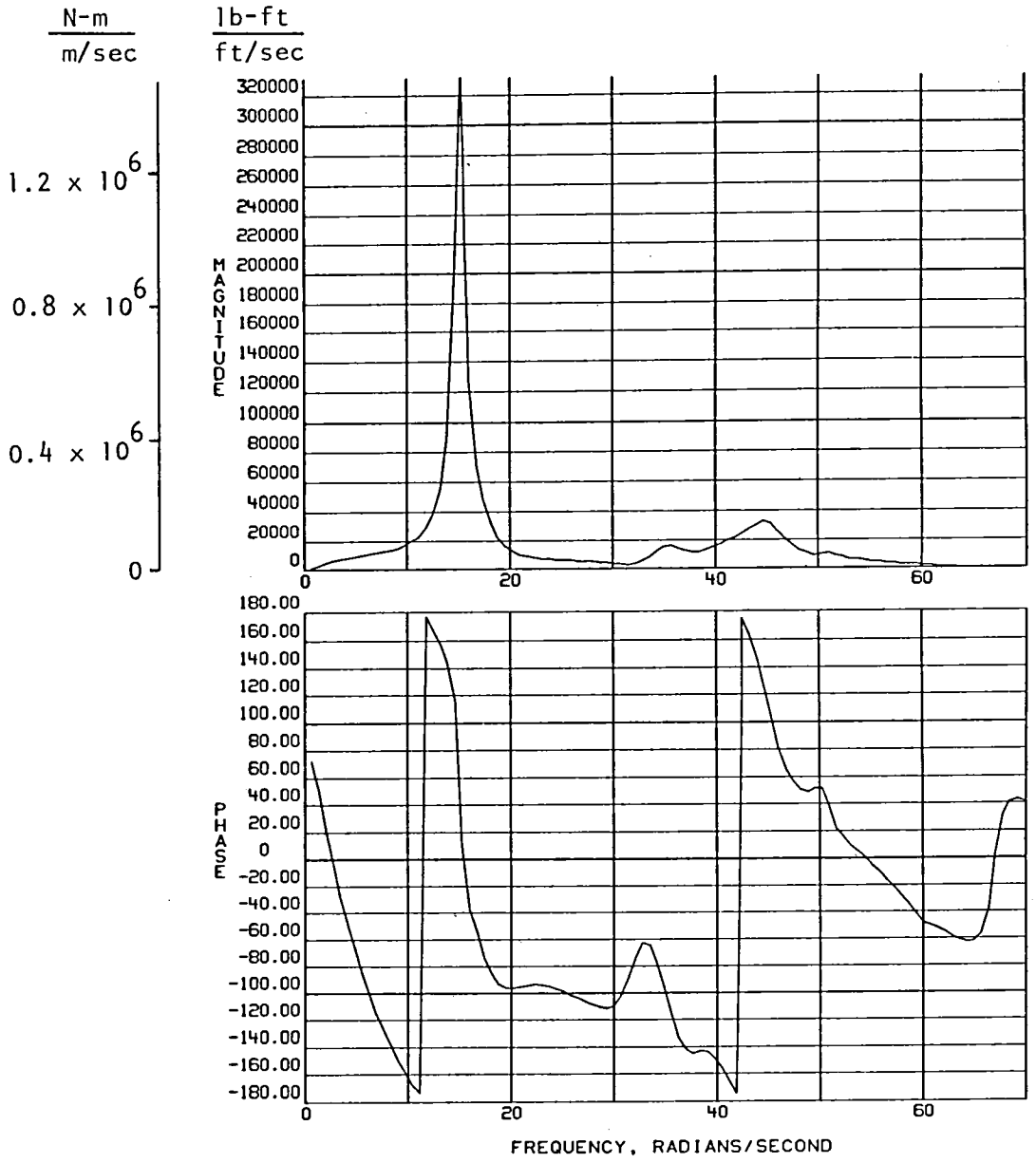

Figure 68. - SMCS off, forebody bending moment frequency response - FS 2367 cm (932 in.).

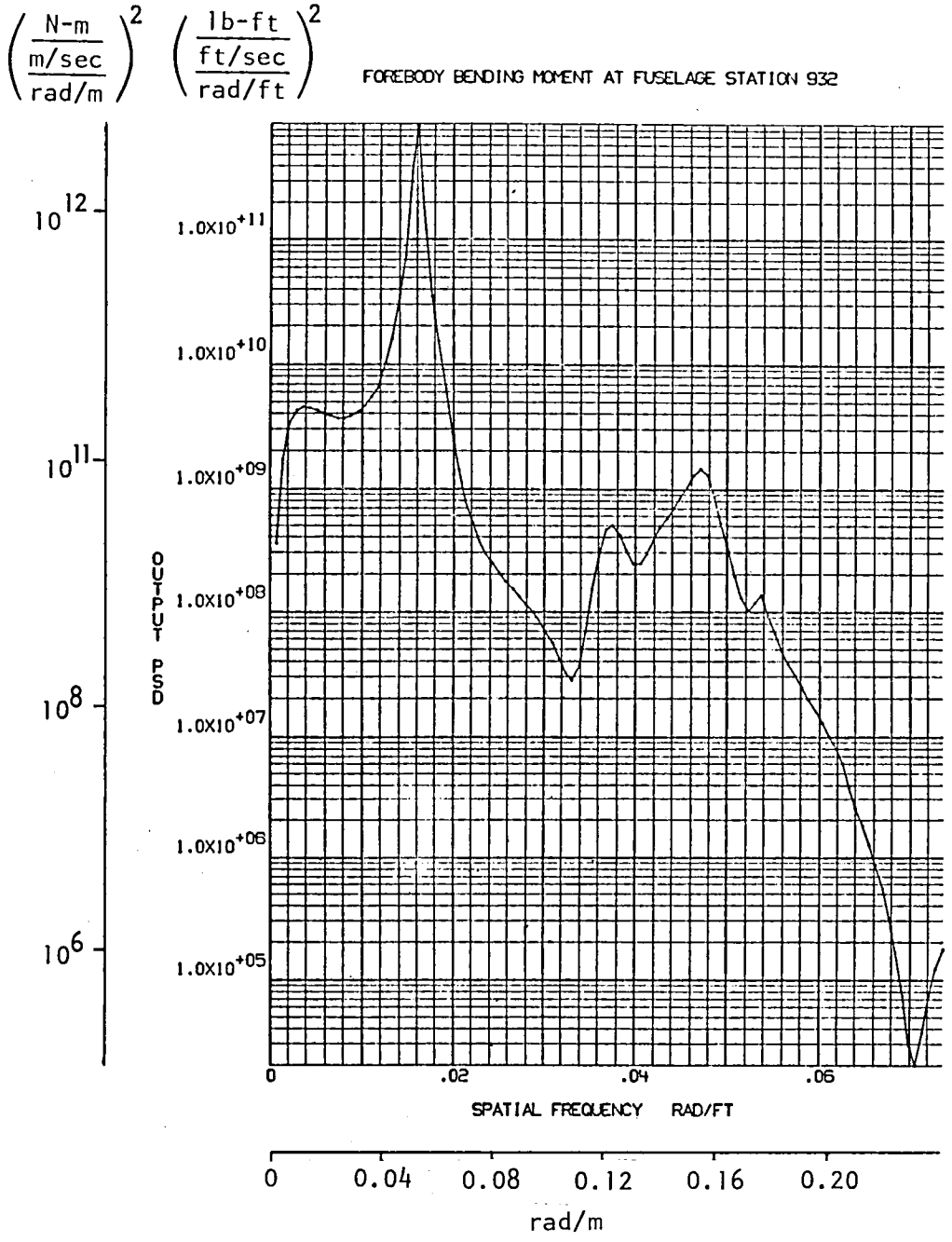

Figure 69. - SMCS of, forebody bending moment response power spectrum - FS 2367 cm (932 in.).

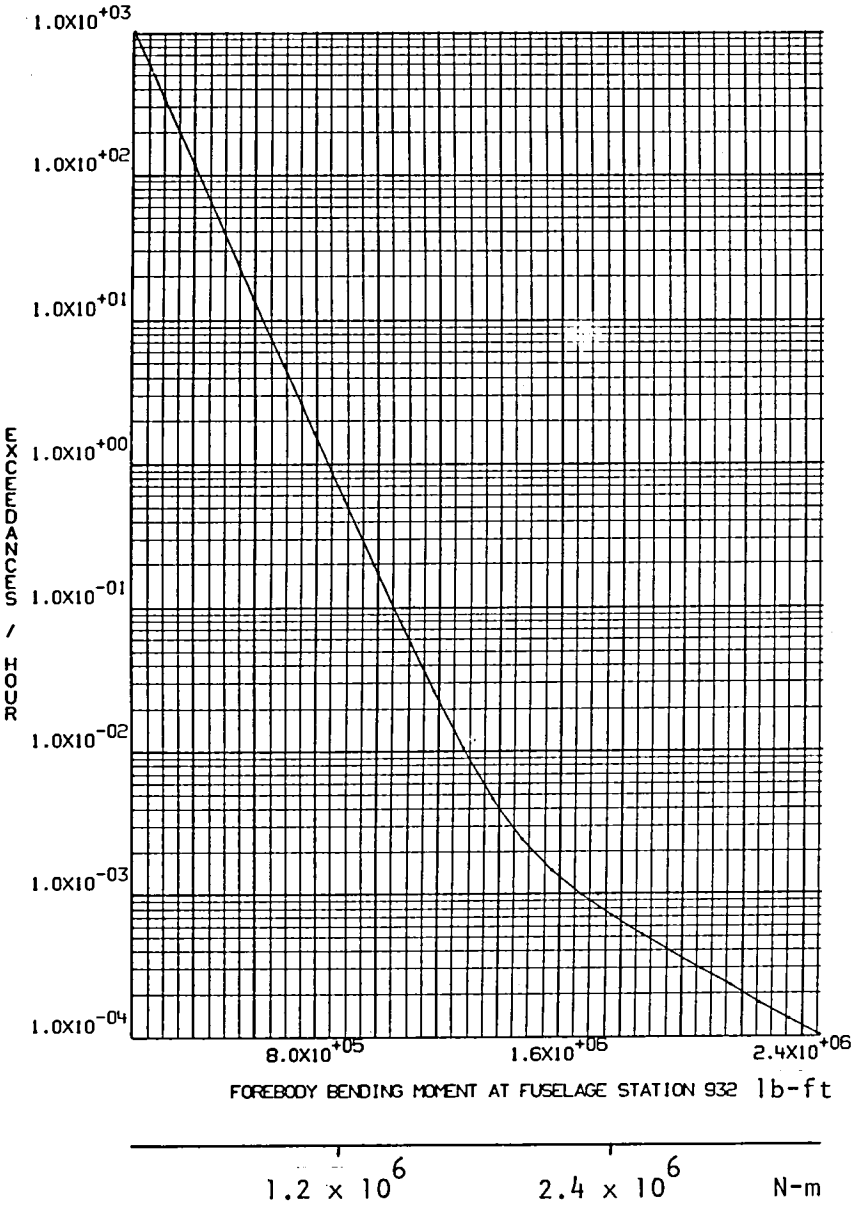

Figure 70. - SMCS off, forebody bending moment exceedances - FS 2367 cm (932 in.).

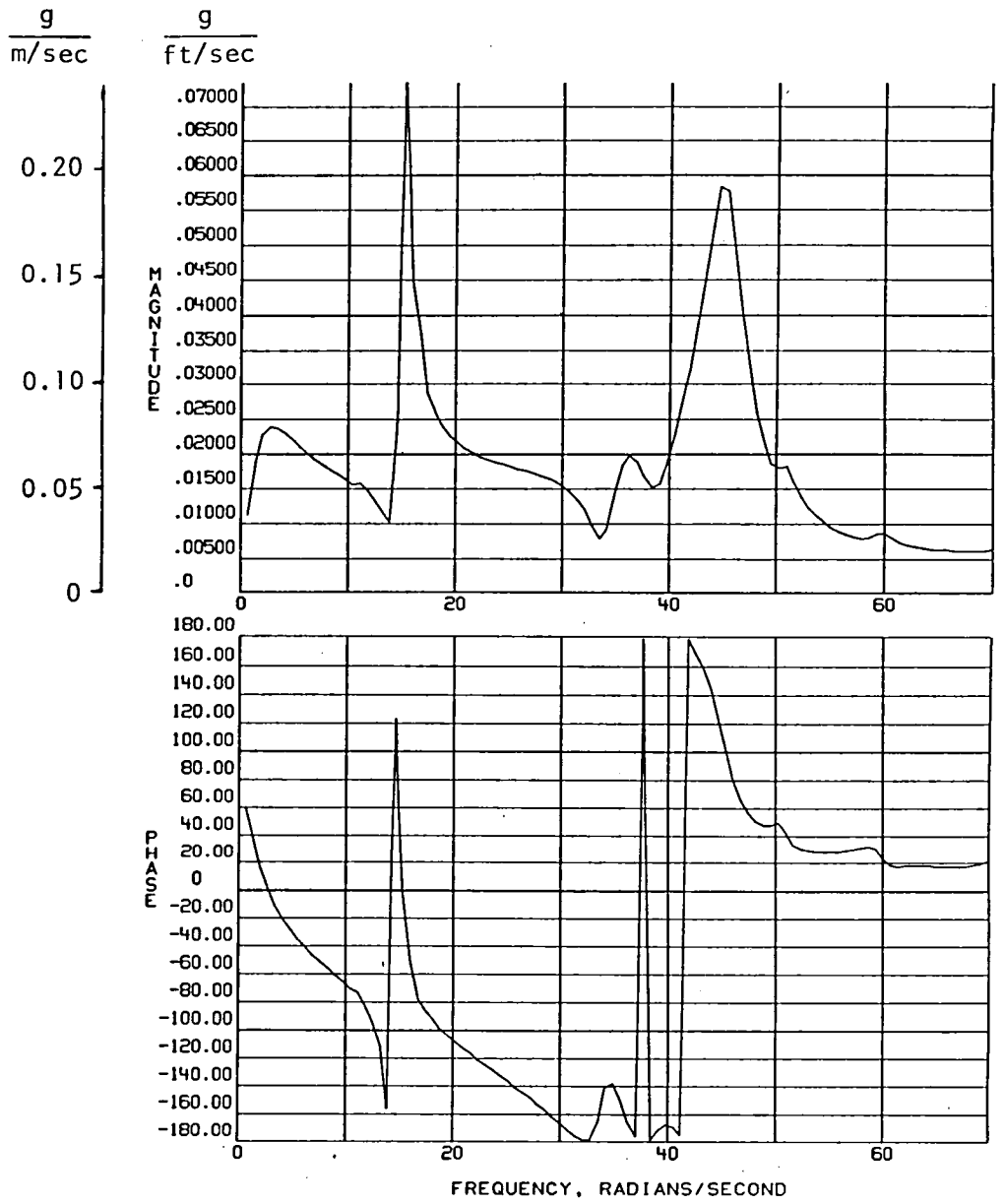

Figure 71. - SMCS off, normal load factor frequency response - aircraft CG.

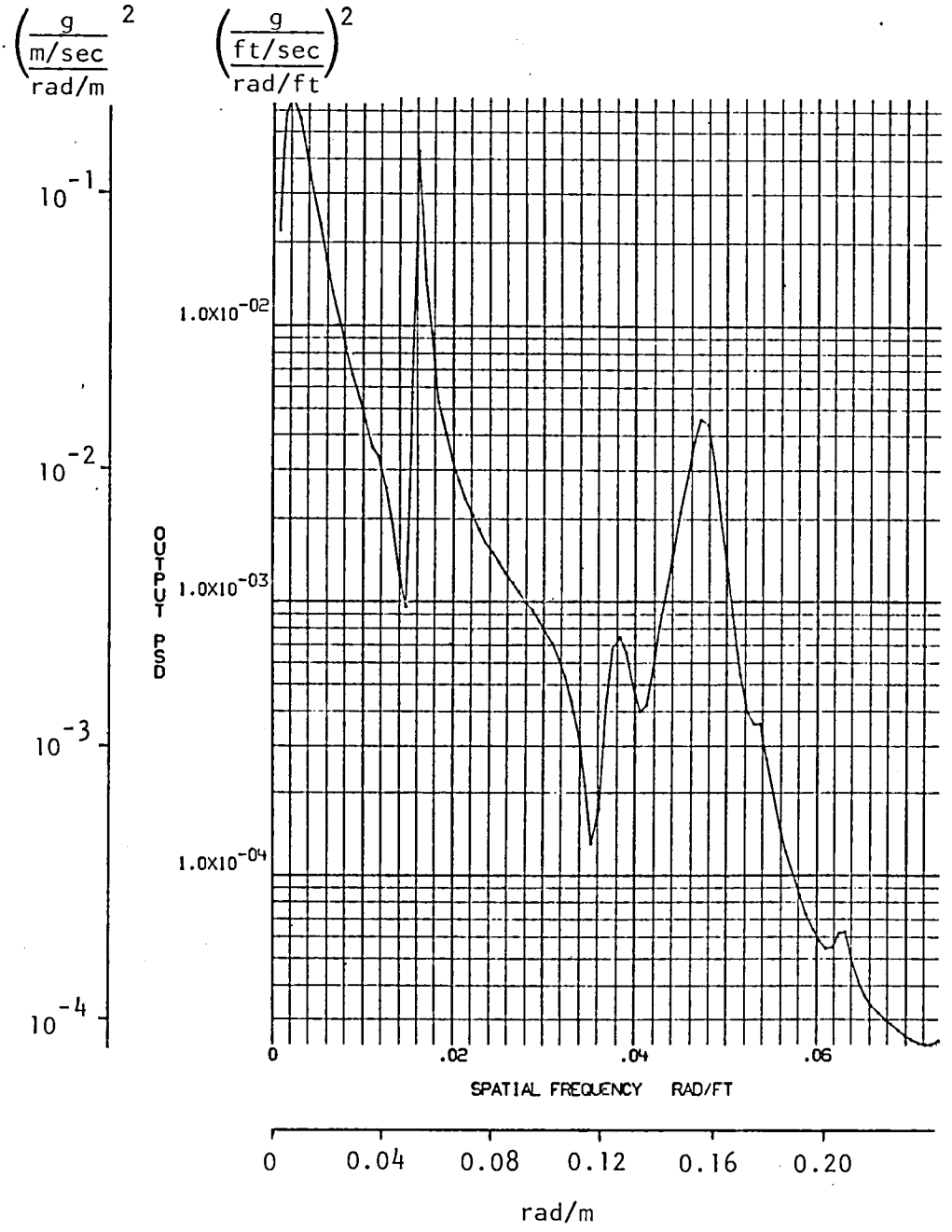

Figure 72. - SMCS off, normal load factor response power spectrum - aircraft CG.

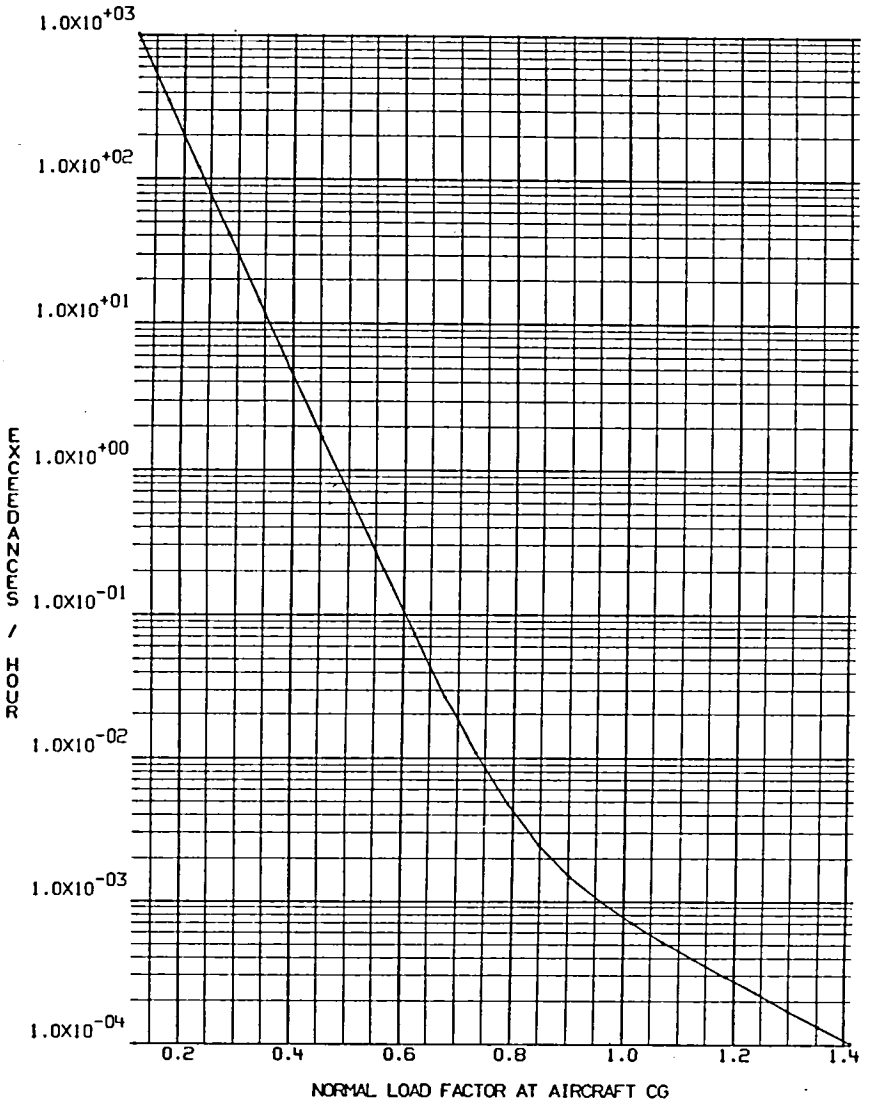

Figure 73. - SMCS off, normal load factor exceedances - aircraft CG.

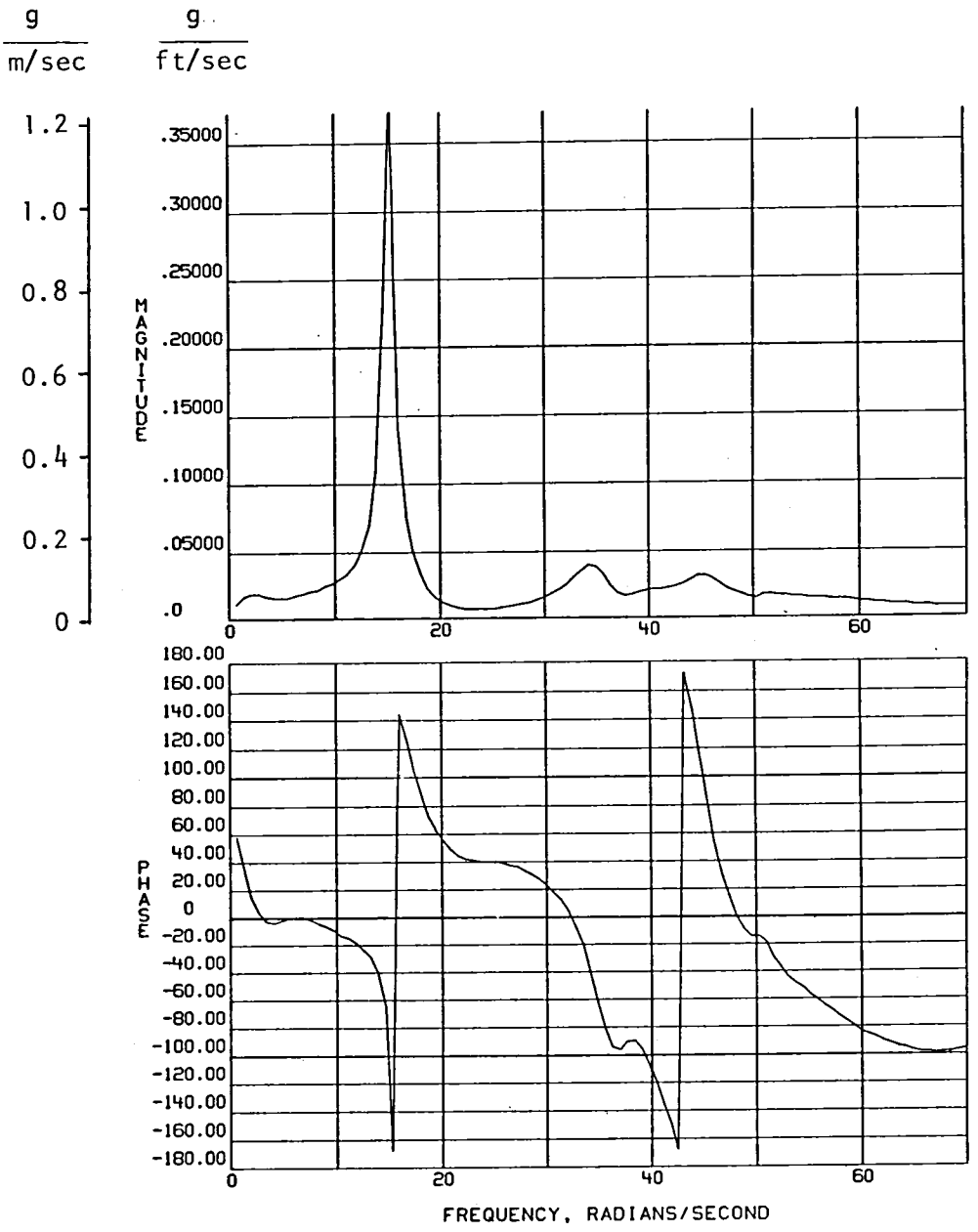

Figure 74. - SMCS off, normal load factor frequency response - pilot station.

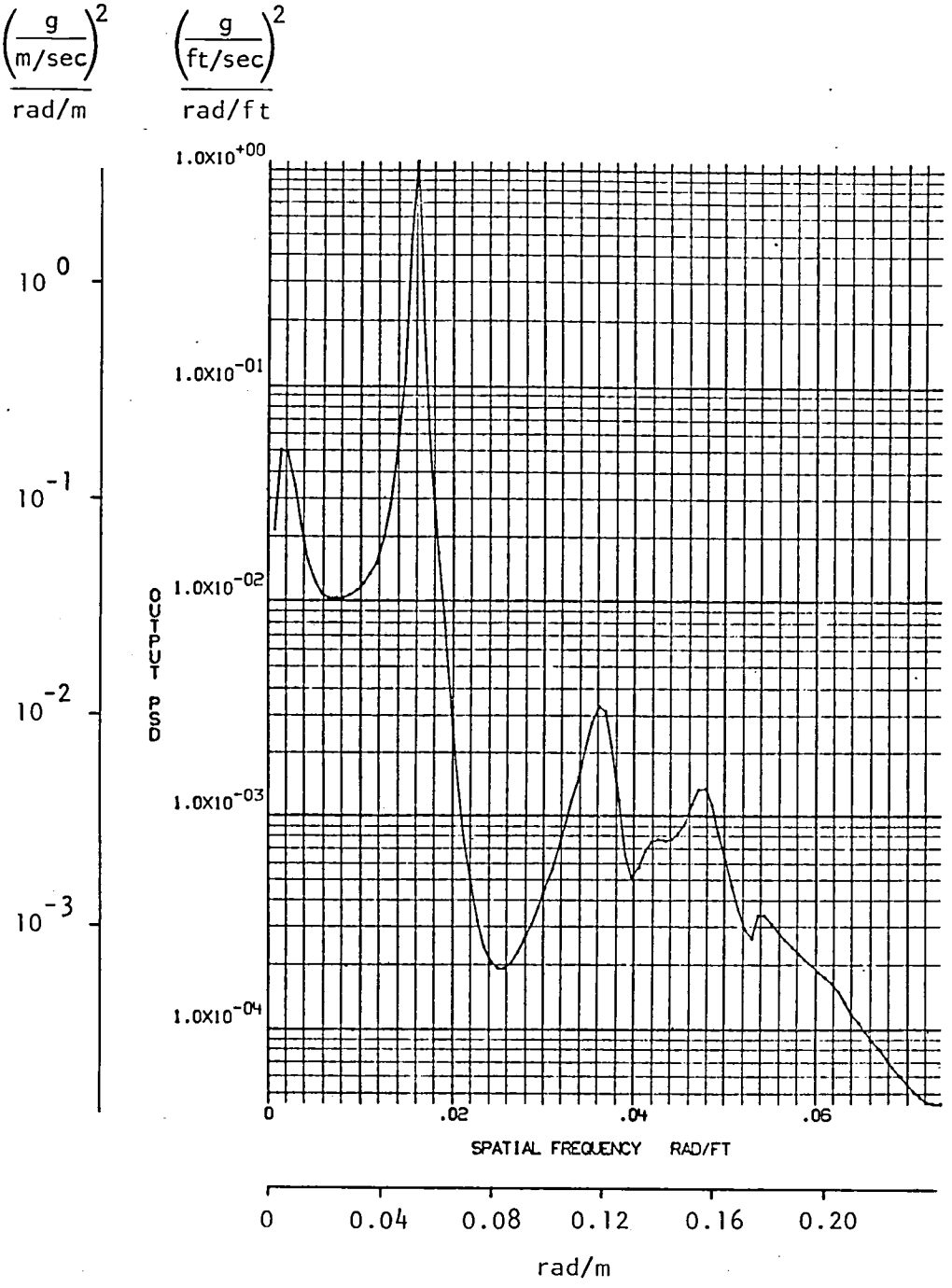

Figure 75. - SMCS off, normal load factor response power spectrum - pilot station.

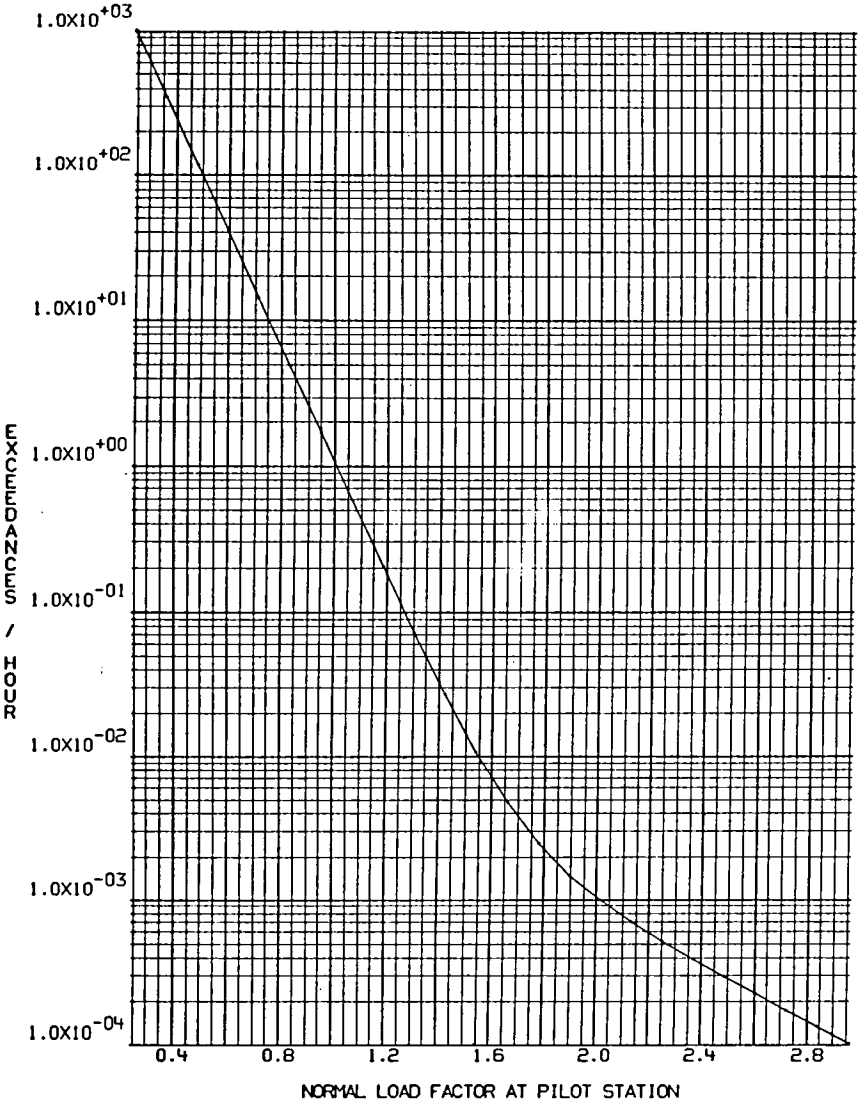

Figure 76. - SMCS off, normal load factor exceedances - pilot station.

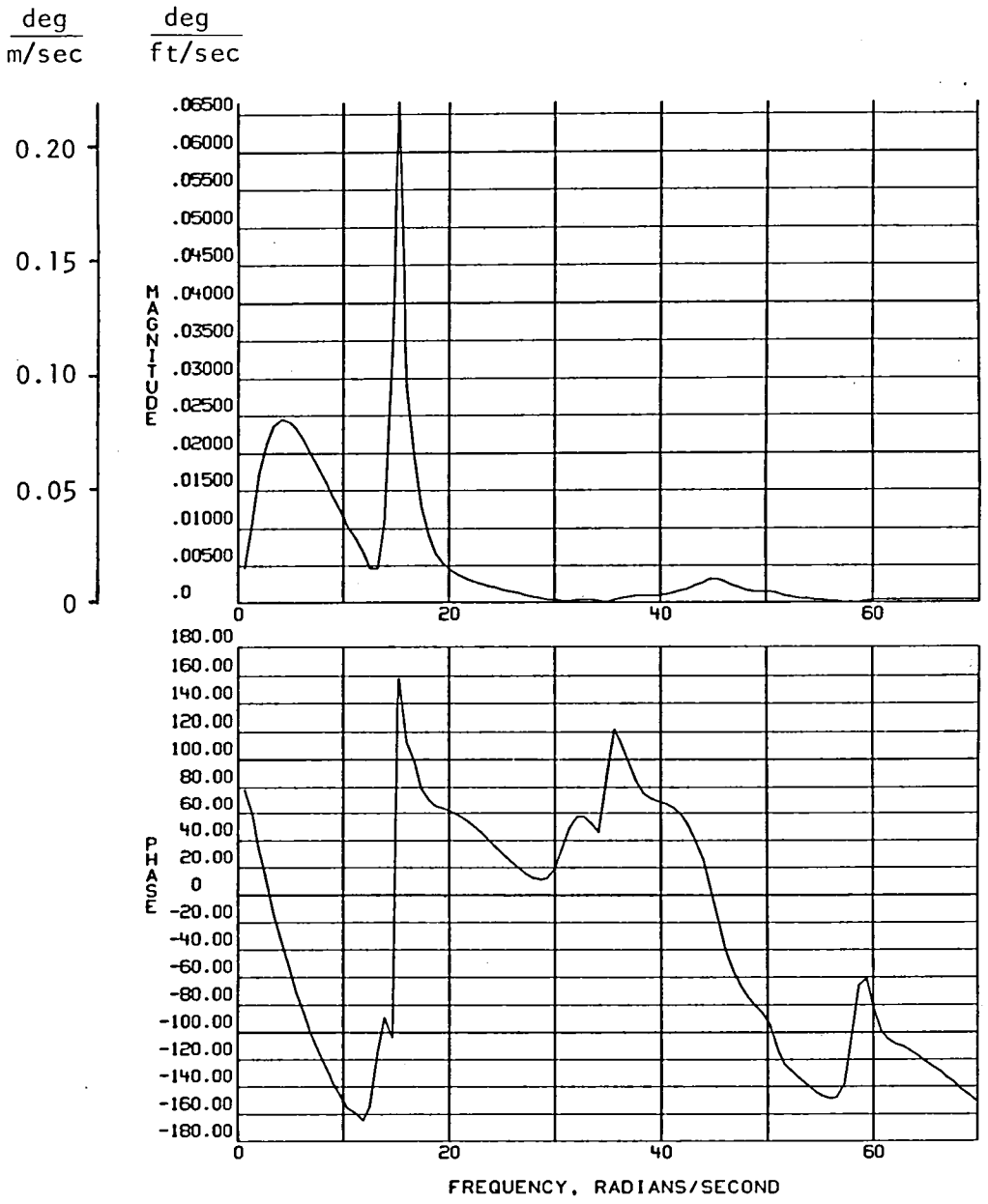

Figure 77. - SMCS off, delta horizontal stabilizer frequency response.

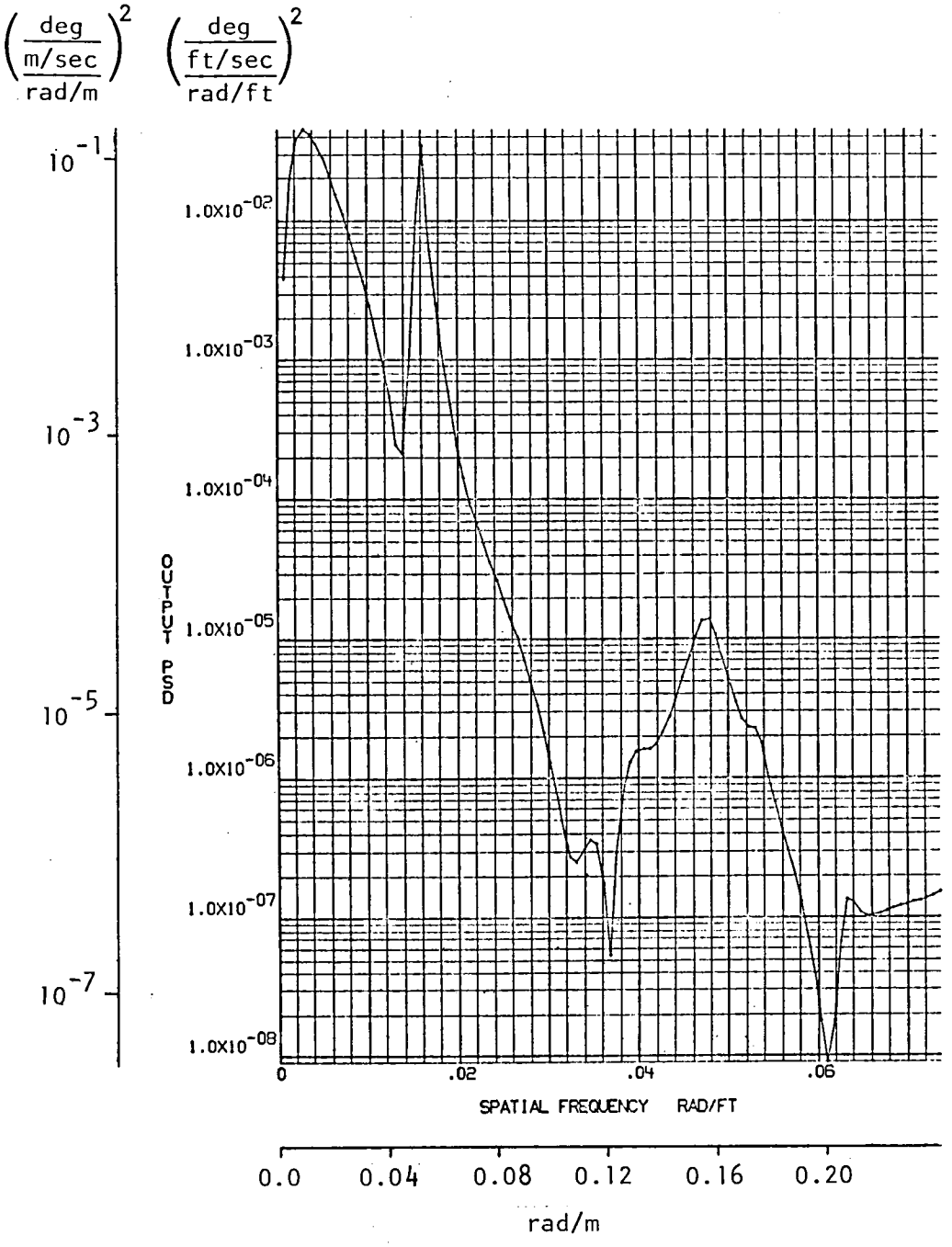

Figure 78. - SMCS off, delta horizontal stabilizer response power spectrum.

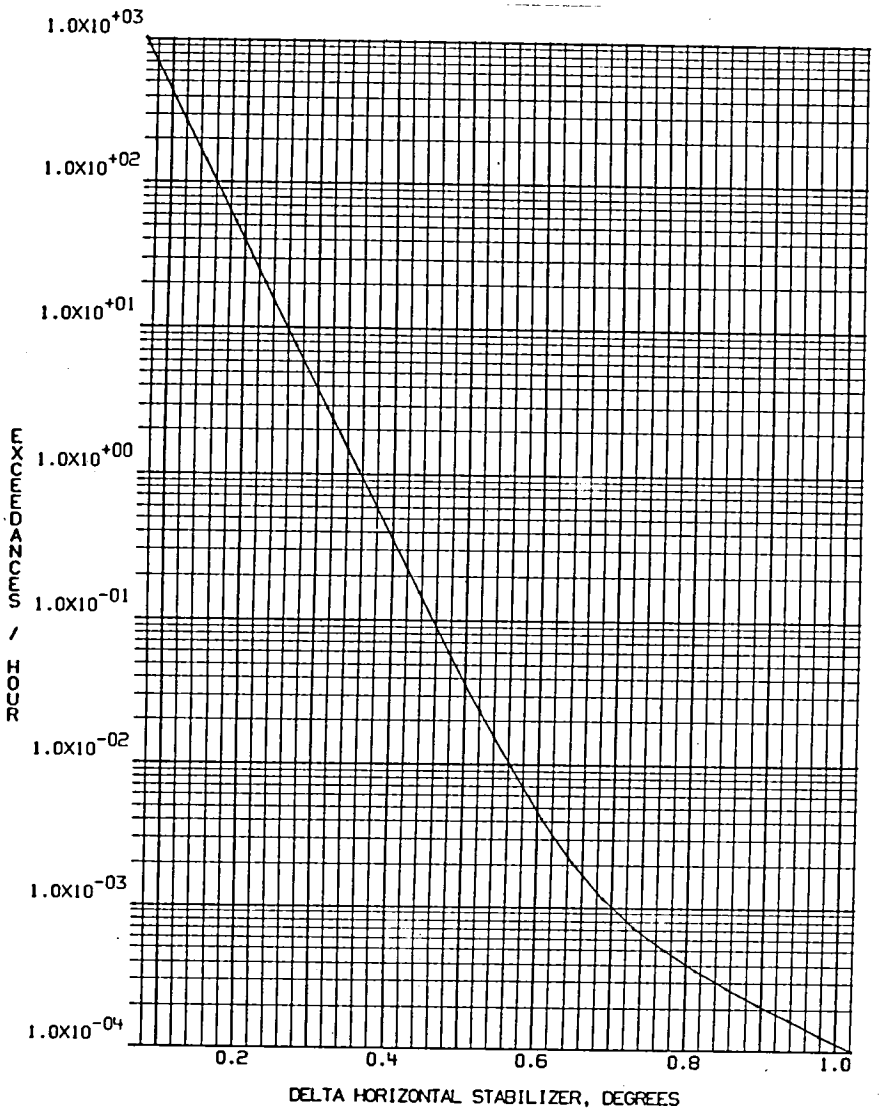

Figure 79. - SMCS off, delta horizontal stabilizer exceedances.

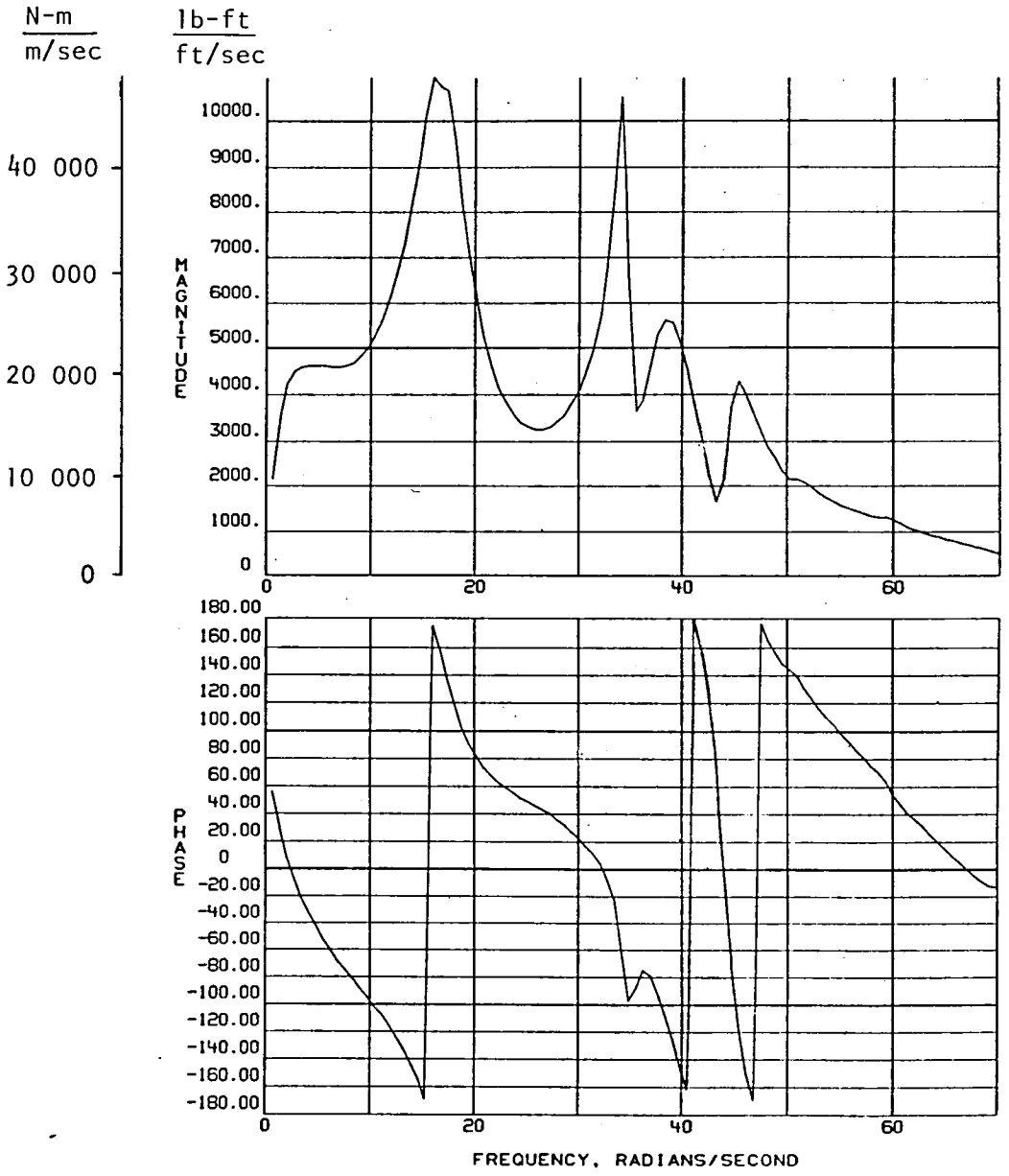

Figure 80. - SMCS on, wing bending moment frequency response - WS 985 cm (387.6 in.).

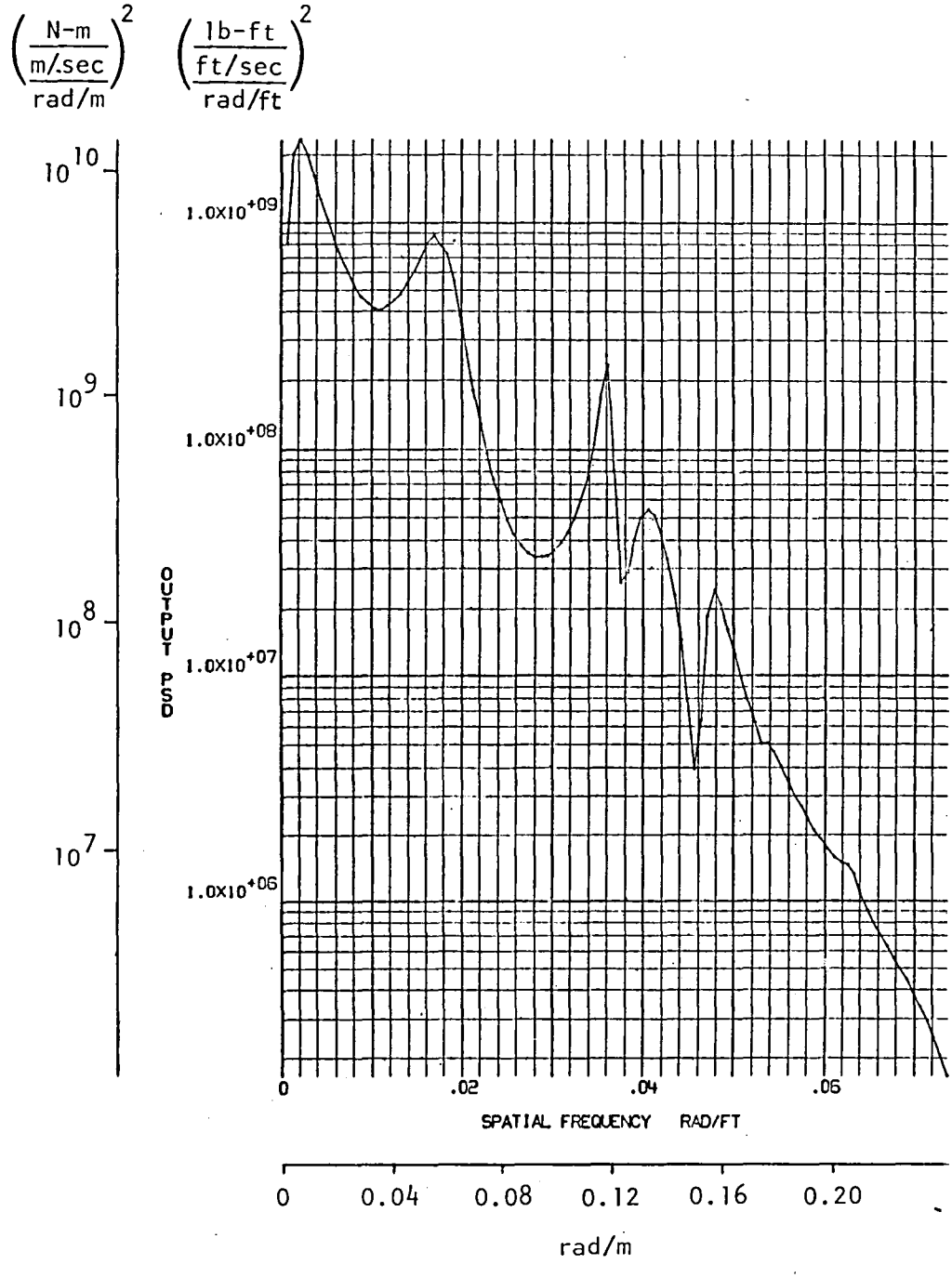

Figure 81. - SMCS on, wing bending moment response power spectrum - WS 985 cm (387.6 in.).

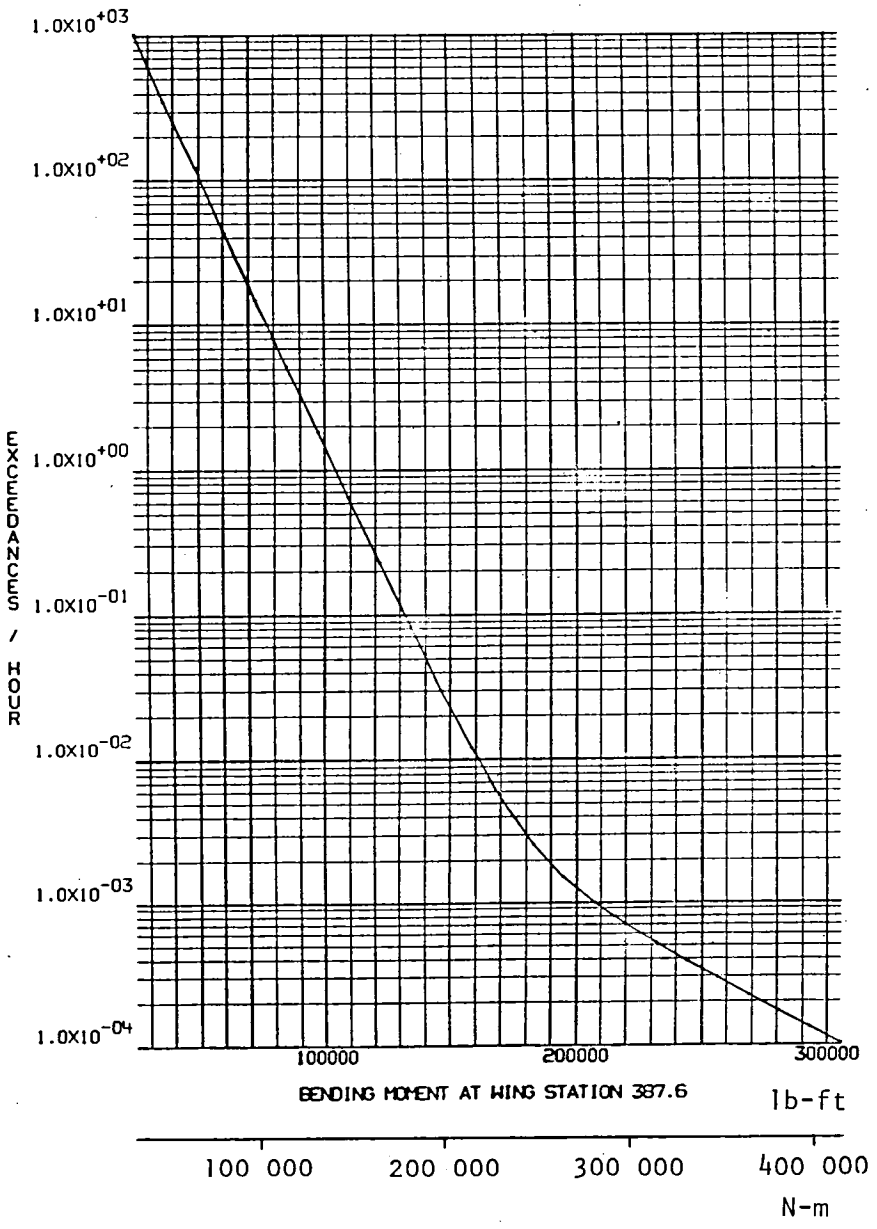

Figure 82. - SMCS on, wing bending moment exceedances - FS 985 cm (387.6 in.).

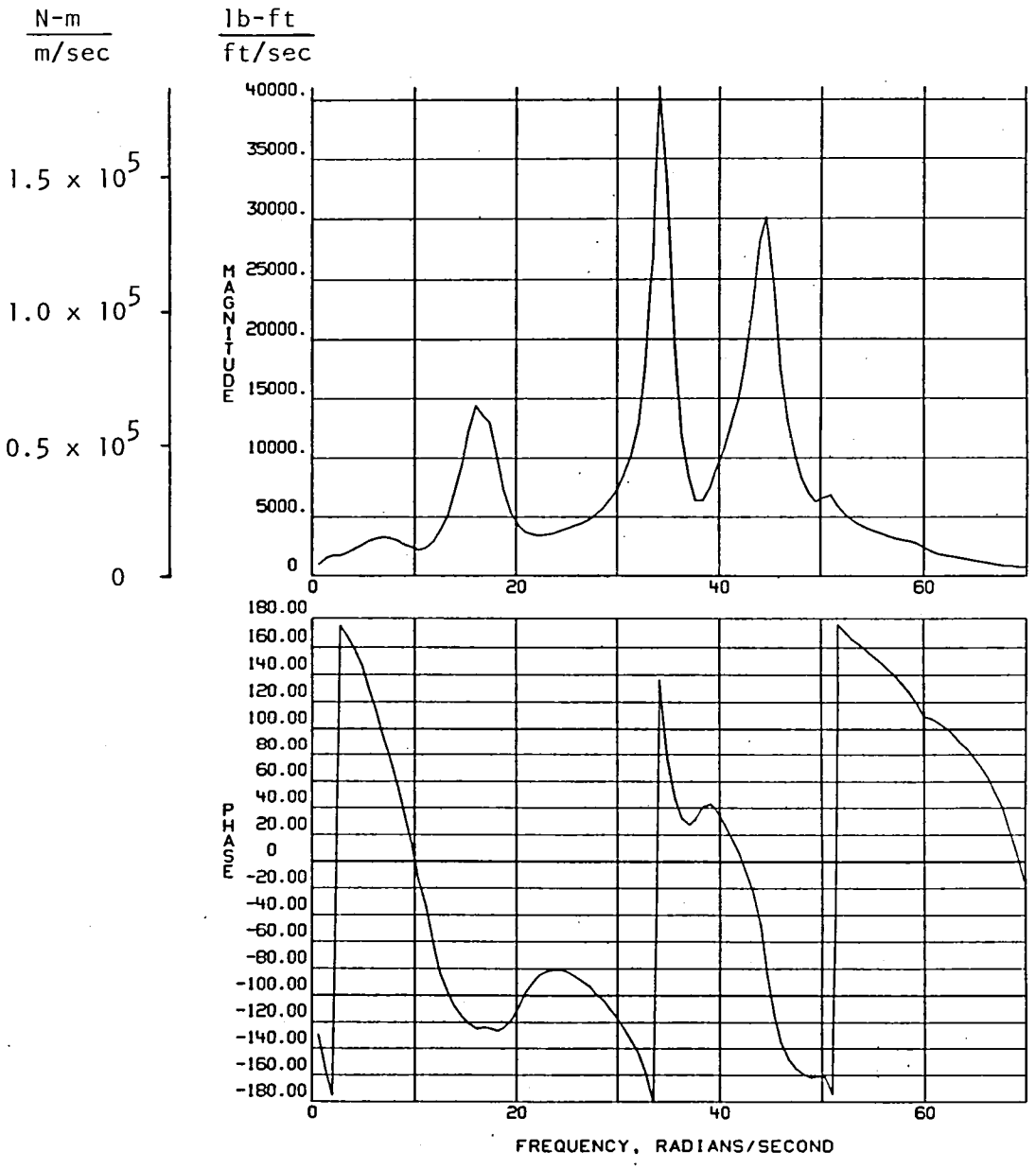

Figure 83. - SMCS on, forebody bending moment frequency response - FS 1377 cm (542 in.).

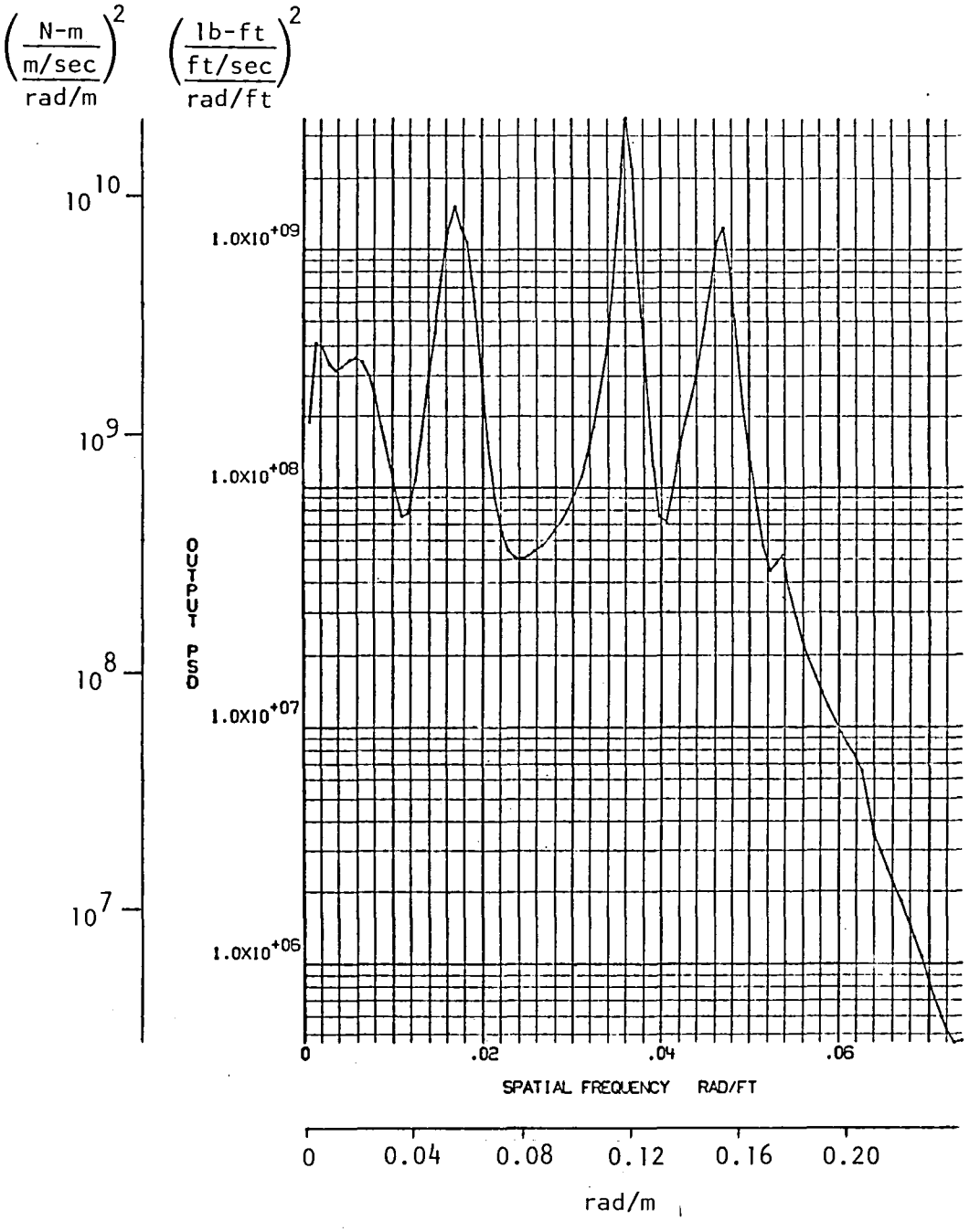

Figure 84. - SMCS on, forebody bending moment response power spectrum - FS 1377 cm (542 in.).

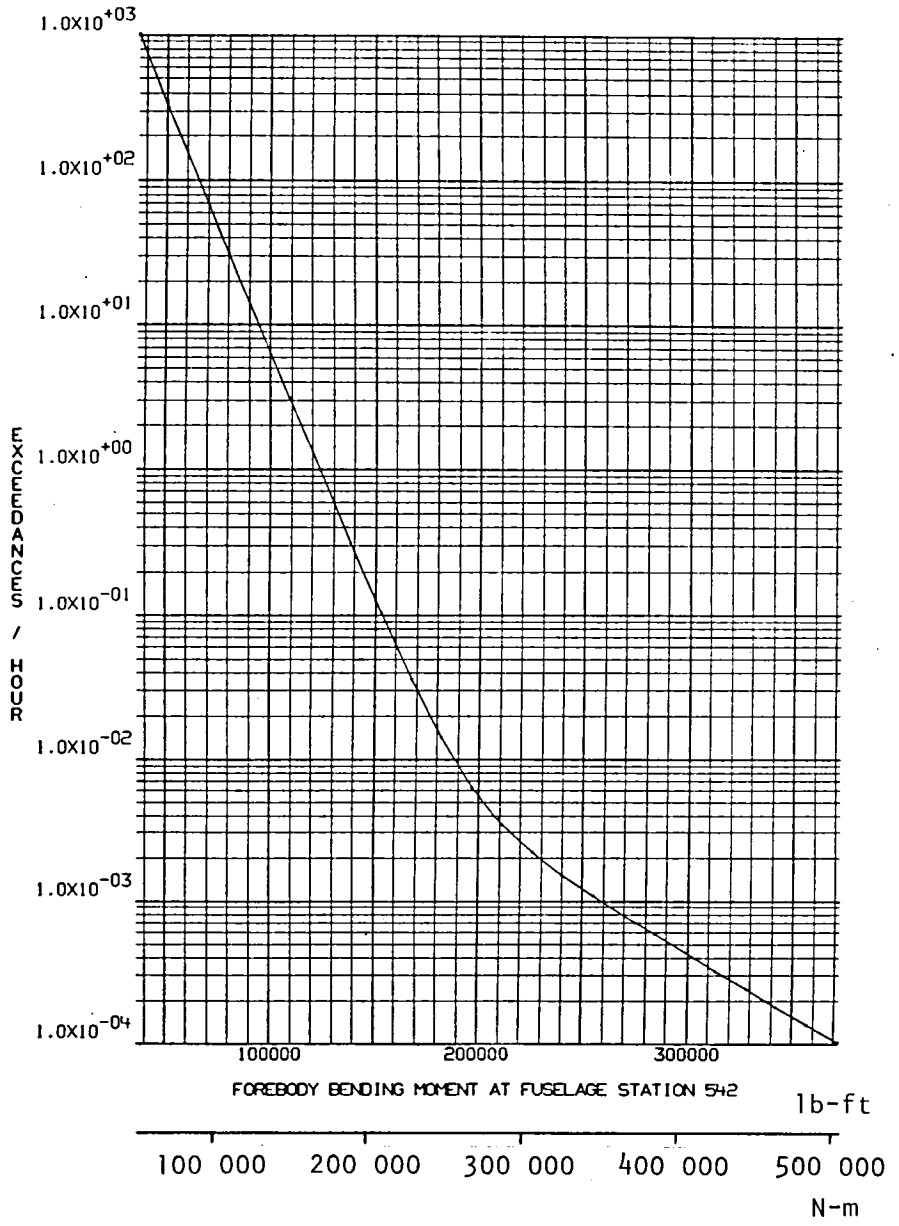

Figure 85. - SMCS on, forebody bending moment exceedances - FS 1377 cm (542 in.).

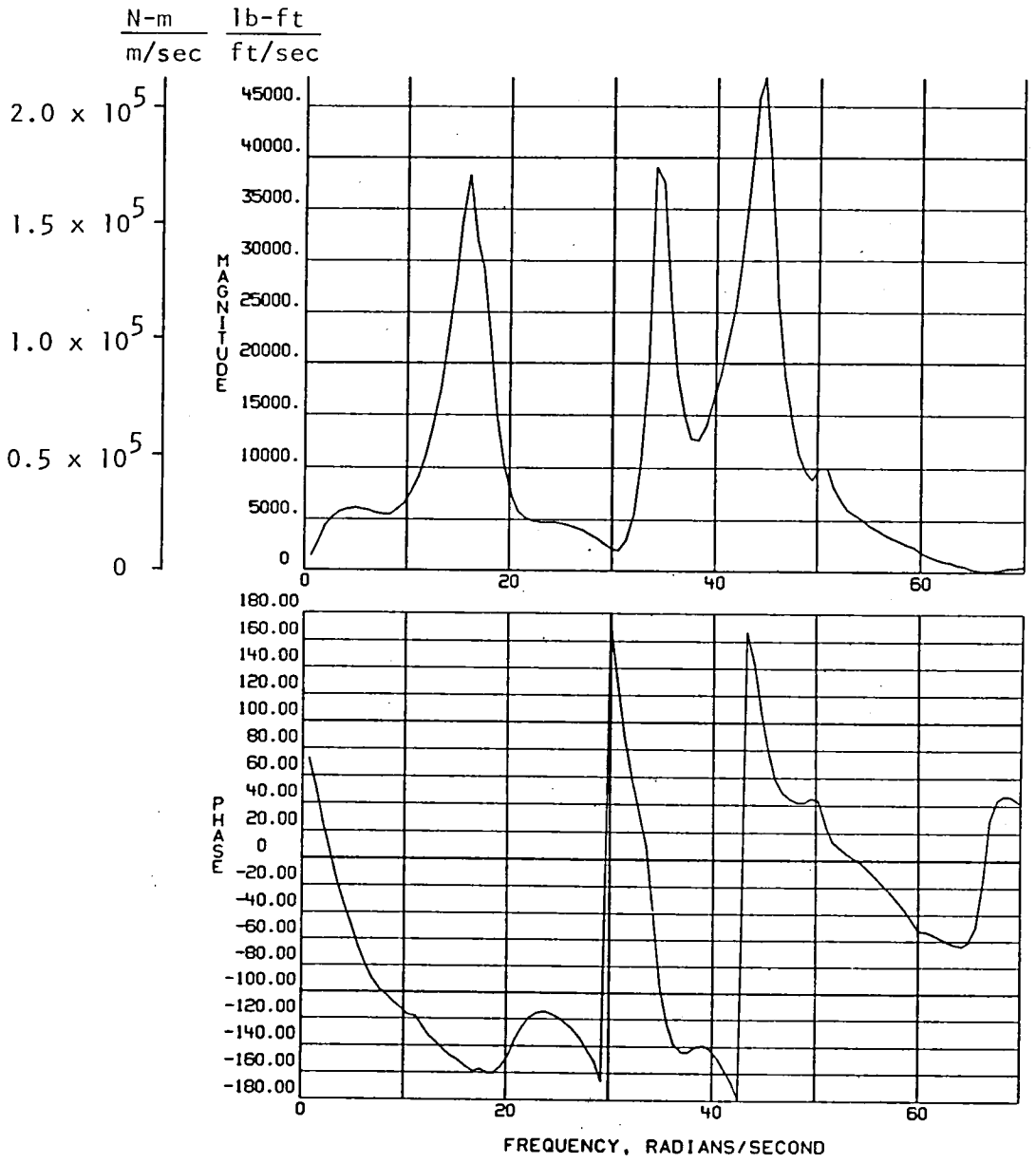

Figure 86. - SMCS on, forebody bending moment frequency response - FS 2367 cm (932 in.).

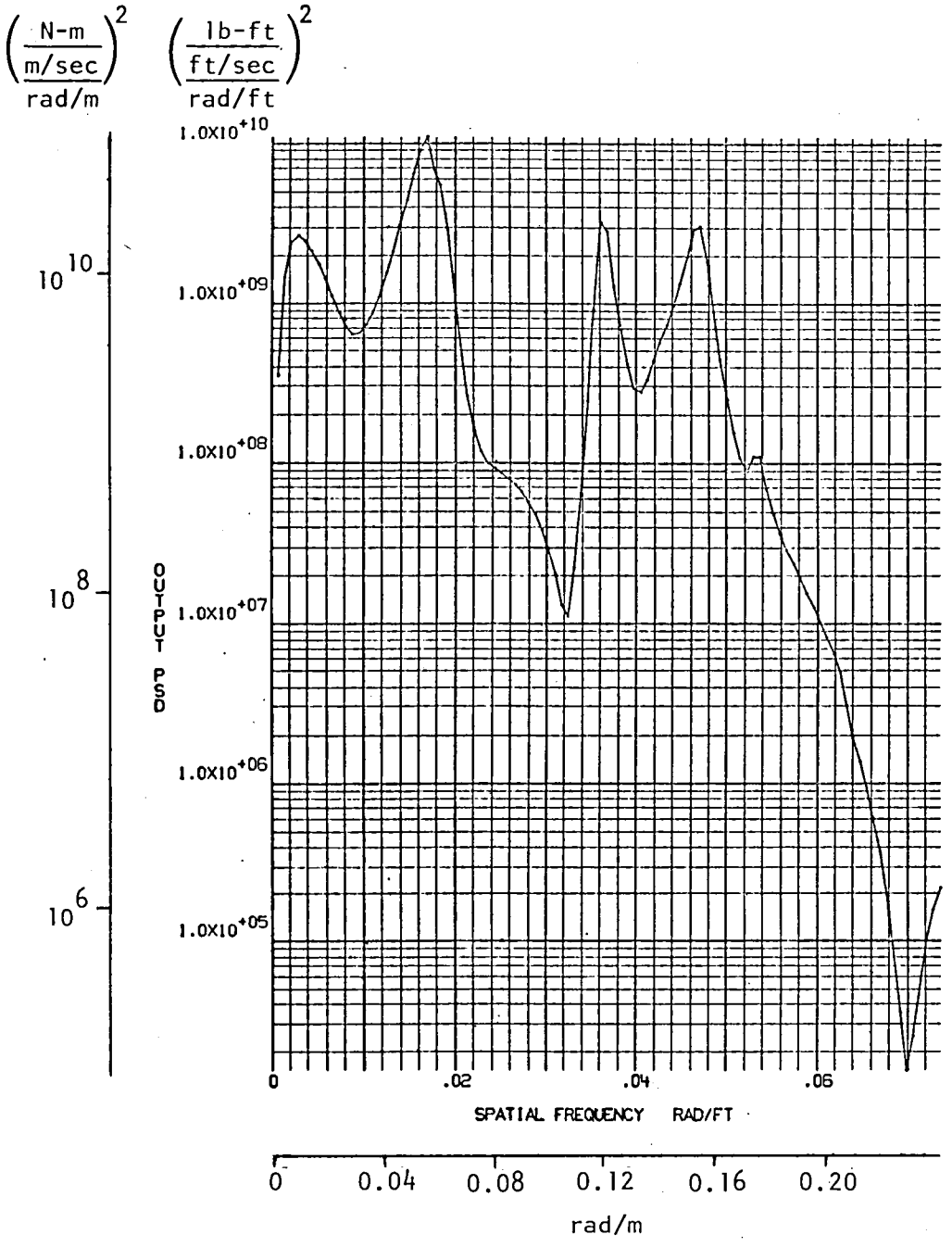

Figure 87. - SMCS on, forebody bending moment response power spectrum - FS 2367 cm (932 in.).

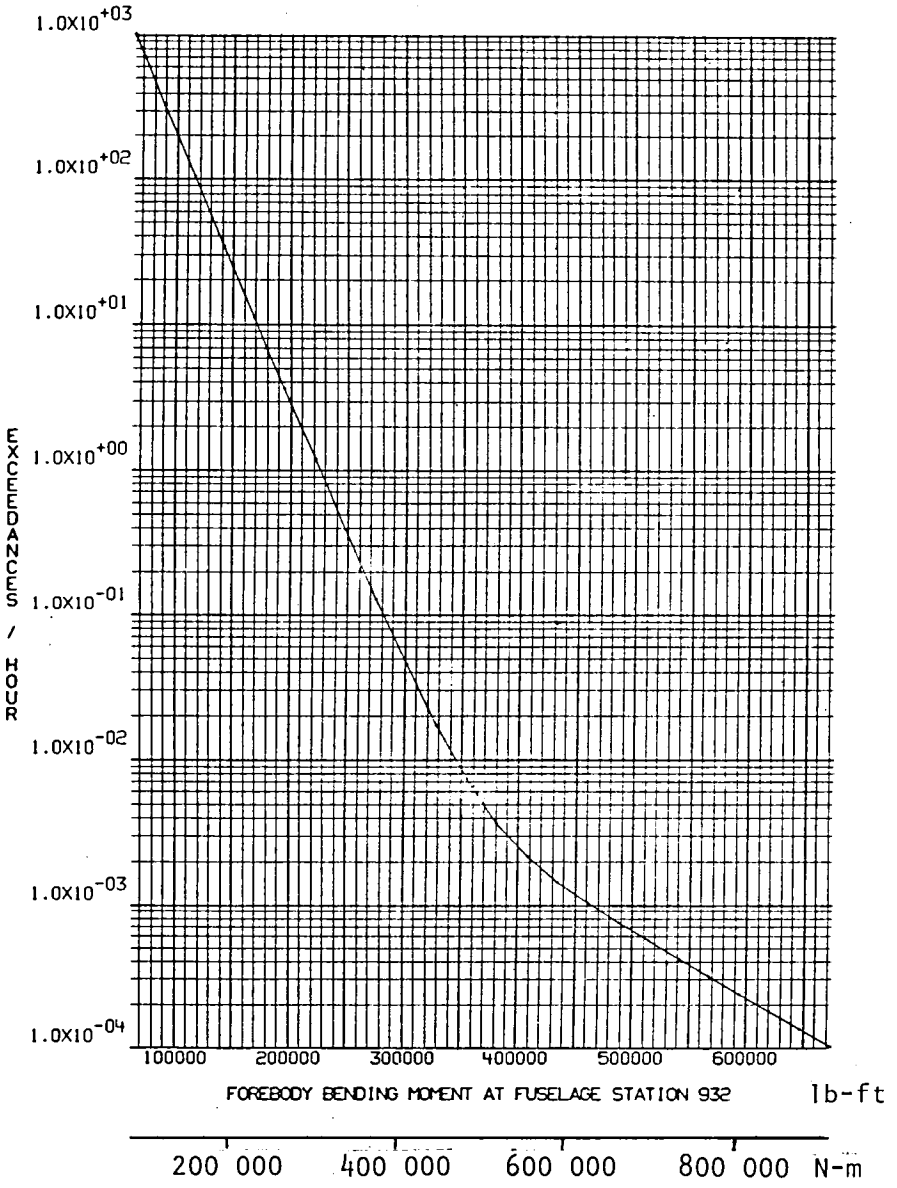

Figure 88. - SMCS on, forebody bending moment exceedances - FS 2367 cm (932 in.).

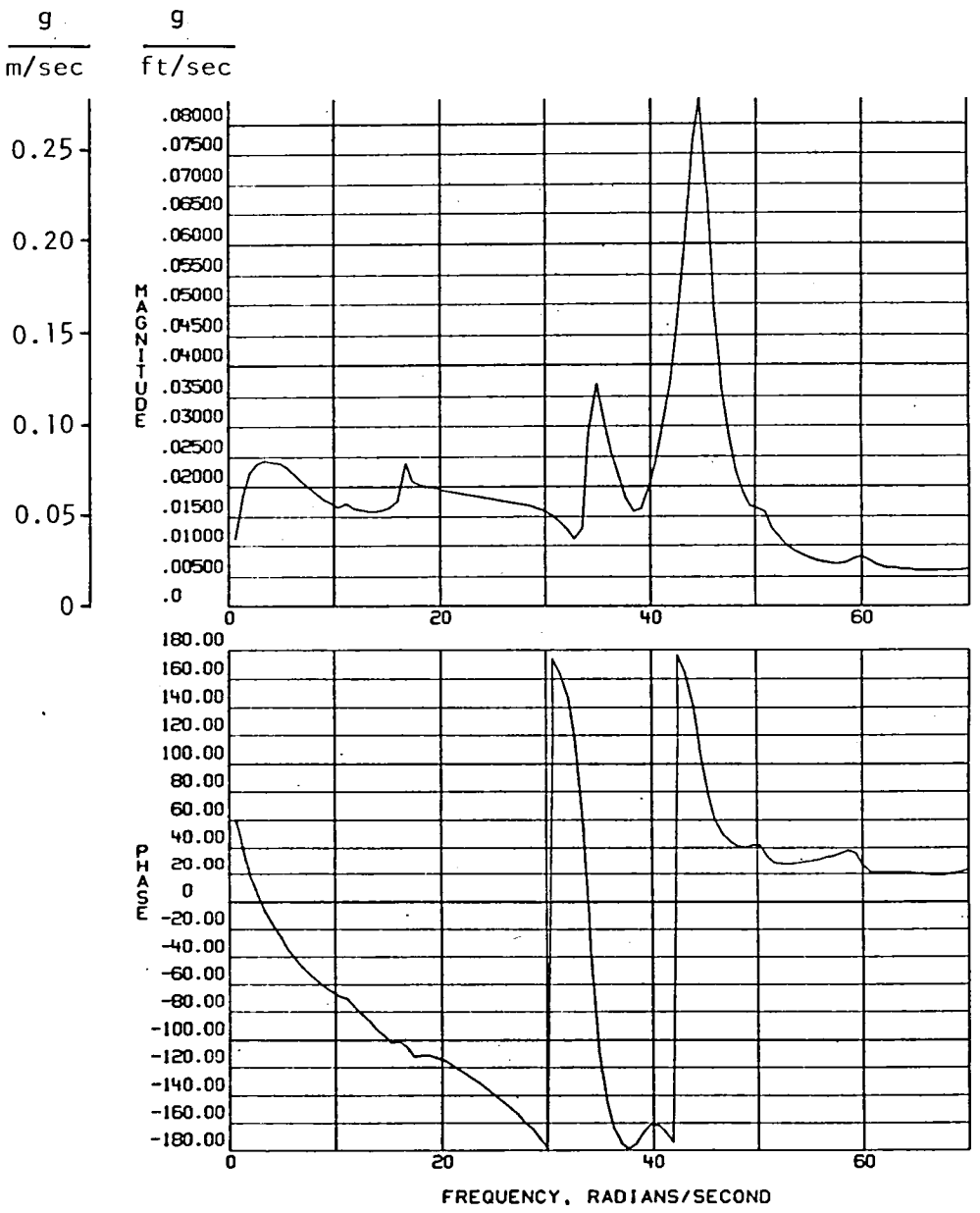

Figure 89. - SMCS on, normal load factor frequency response-aircraft CG.

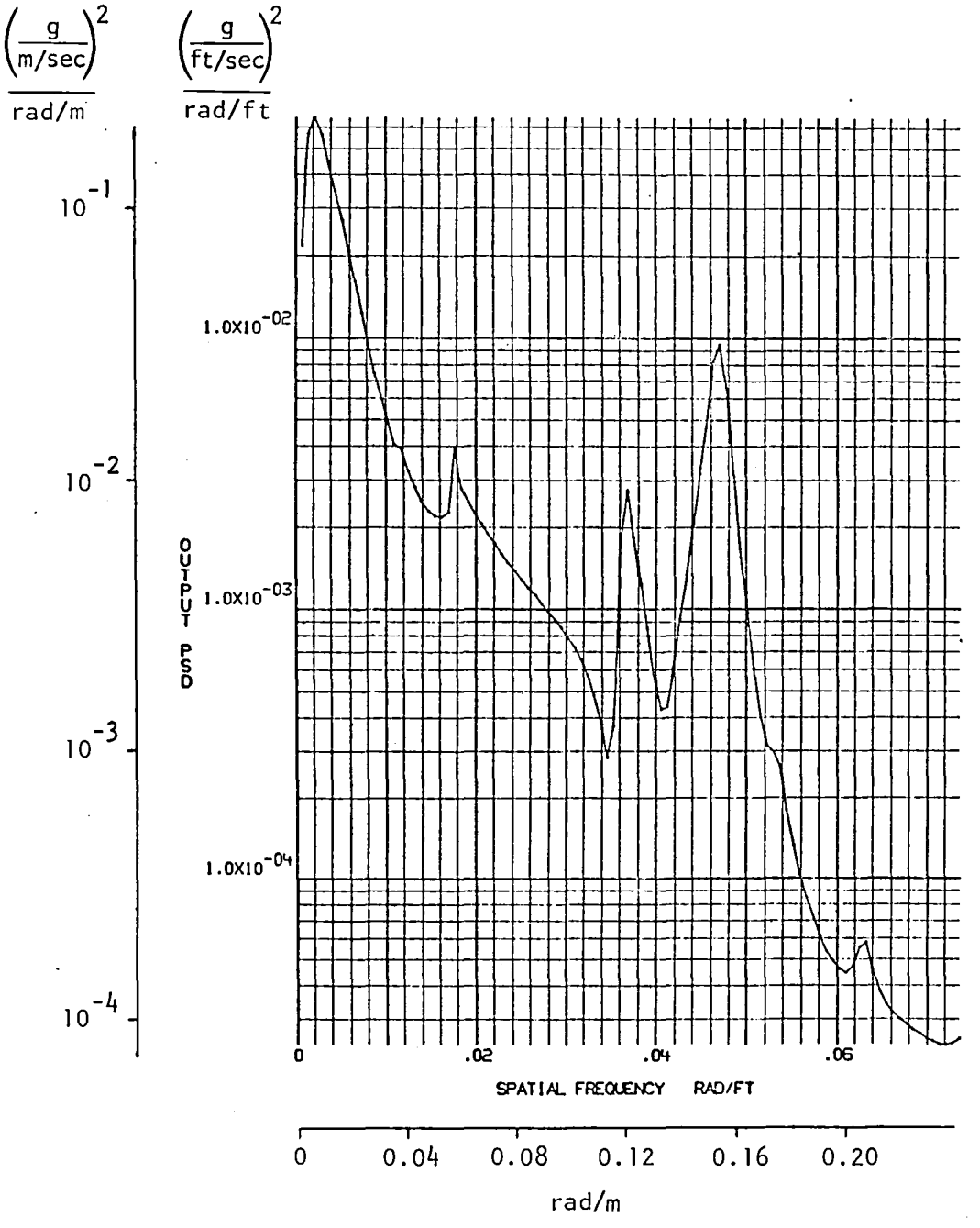

Figure 90. - SMCS on, normal load factor response power spectrum - aircraft CG.

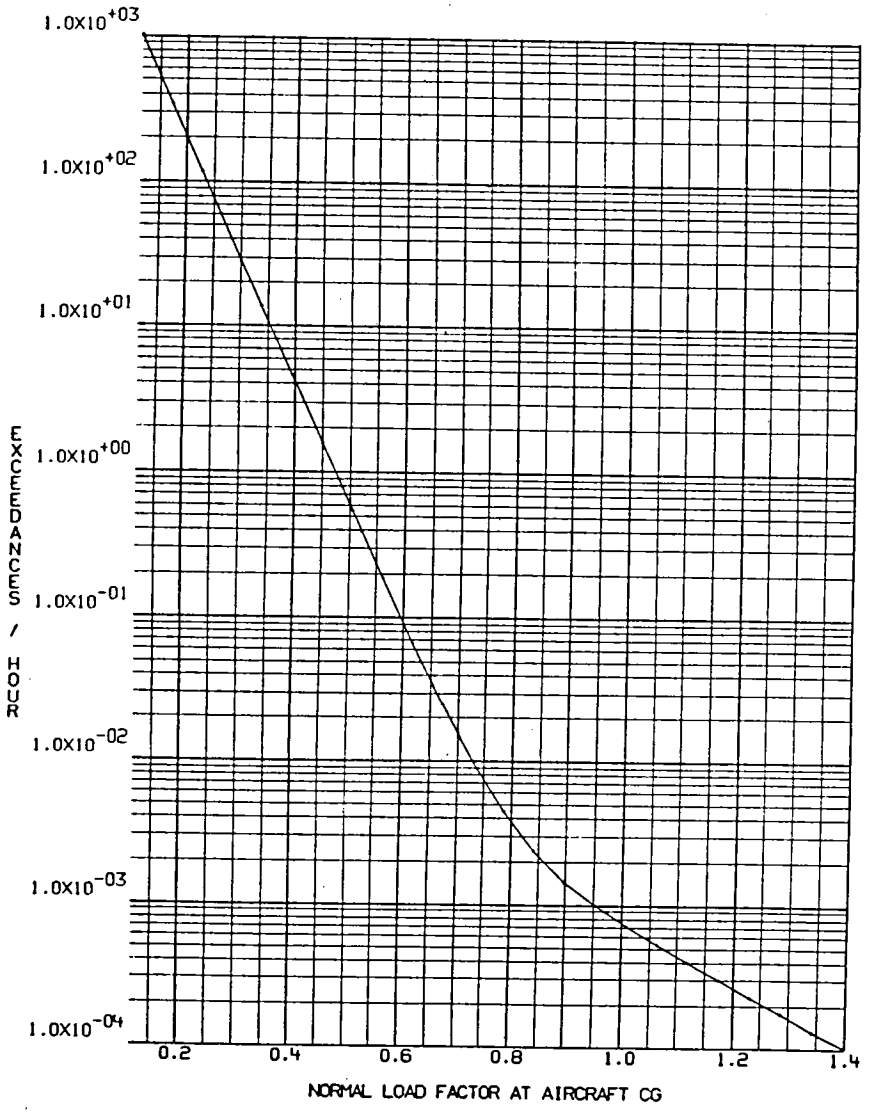

Figure 91. - SMCS on, normal load factor exceedances - aircraft CG.

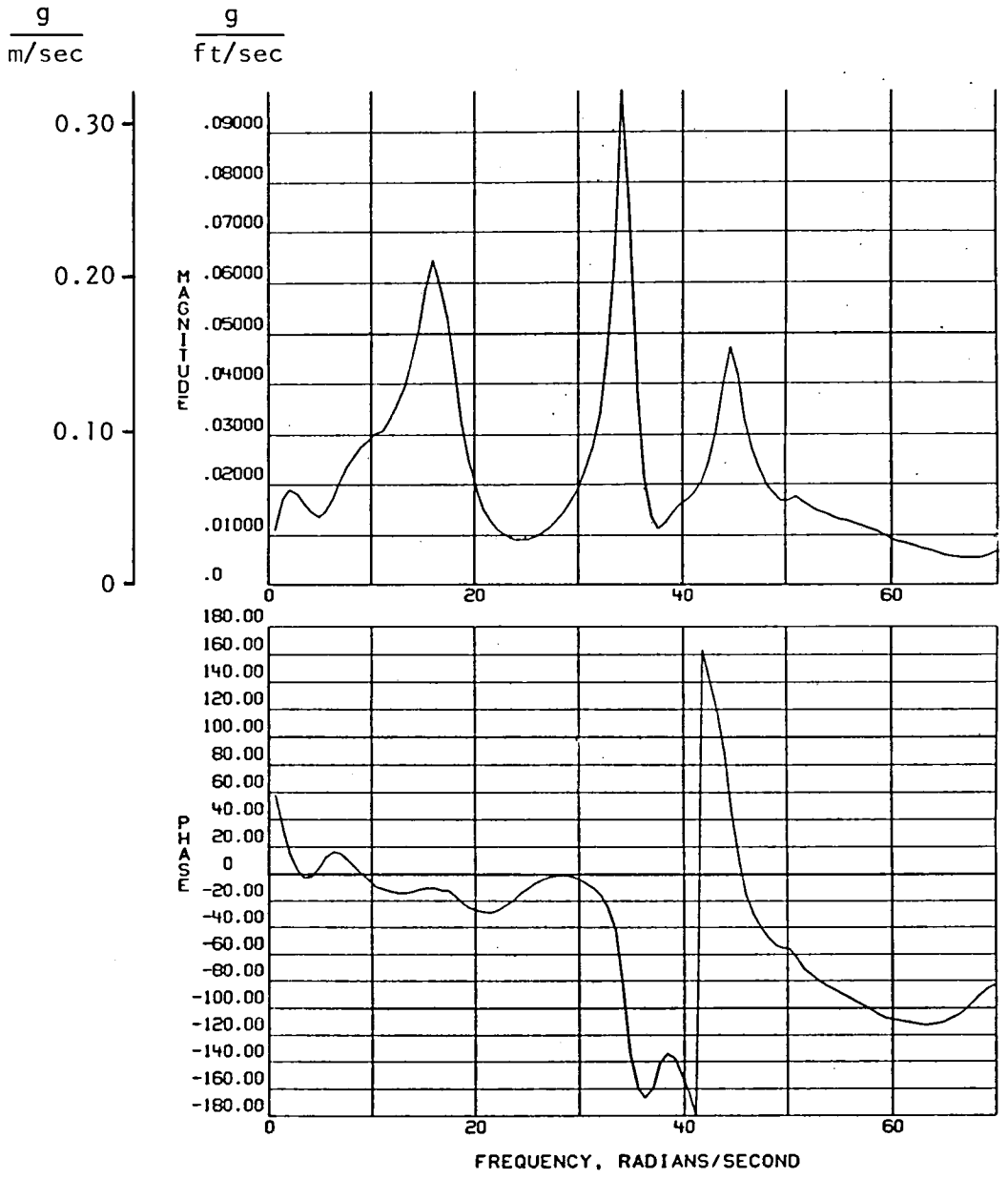

Figure 92. - SMCS on, normal load factor frequency response - pilot station.

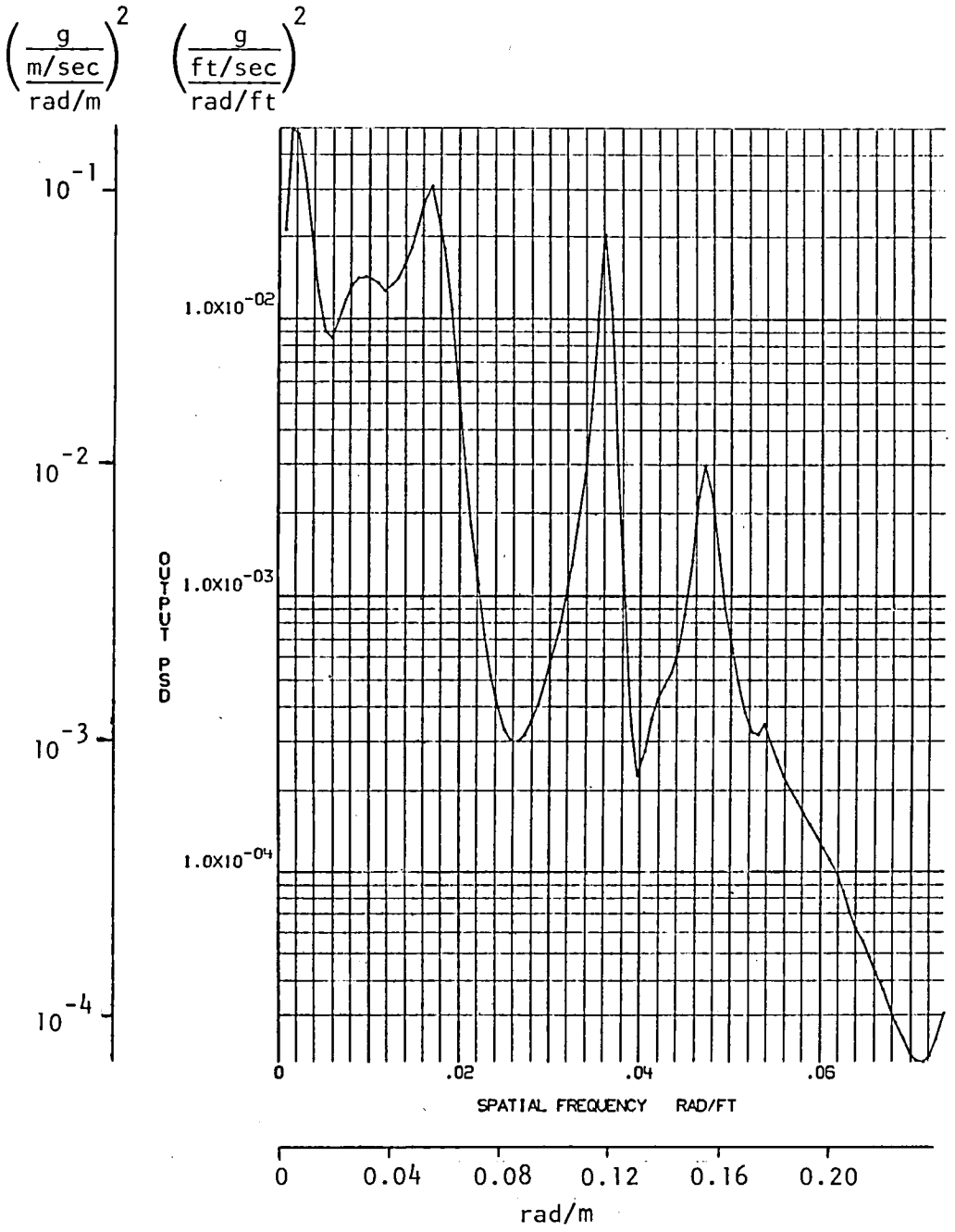

Figure 93. - SMCS on, normal load factor response power spectrum - pilot station.

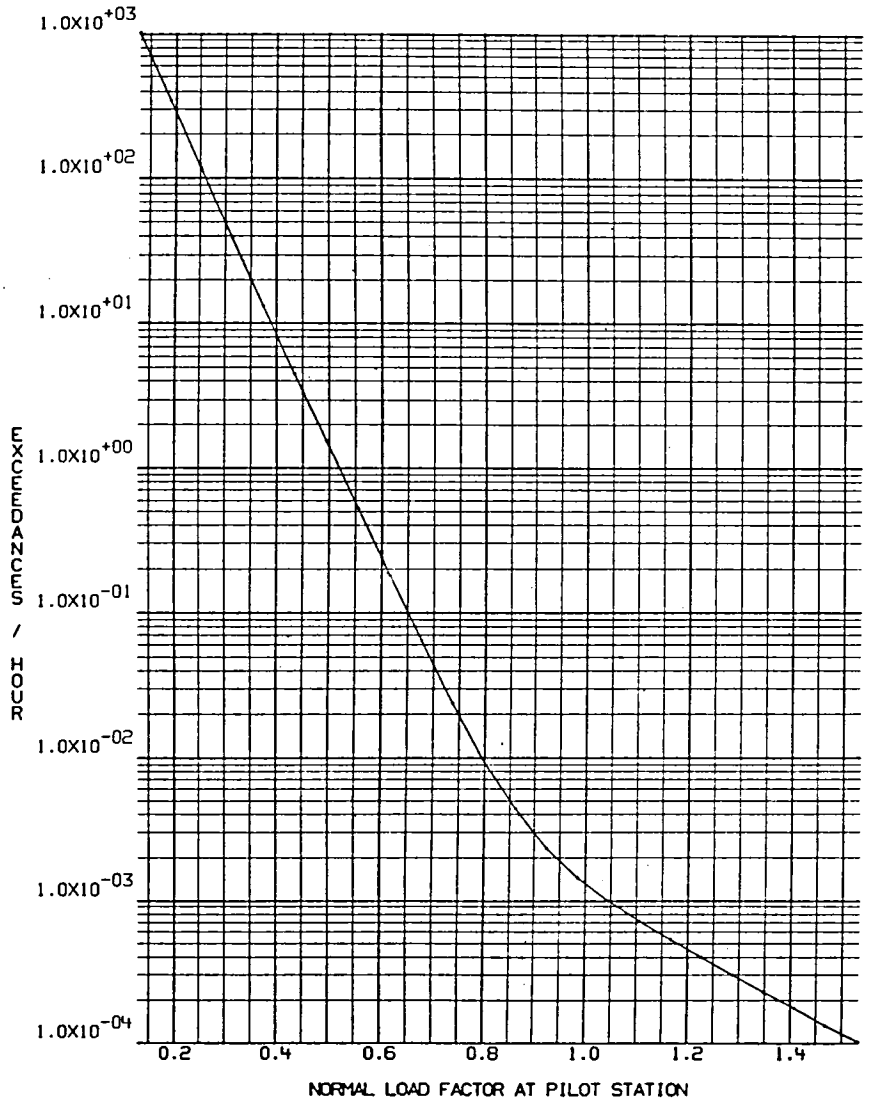

Figure 94. - SMCS on, normal load factor exceedances - pilot station.

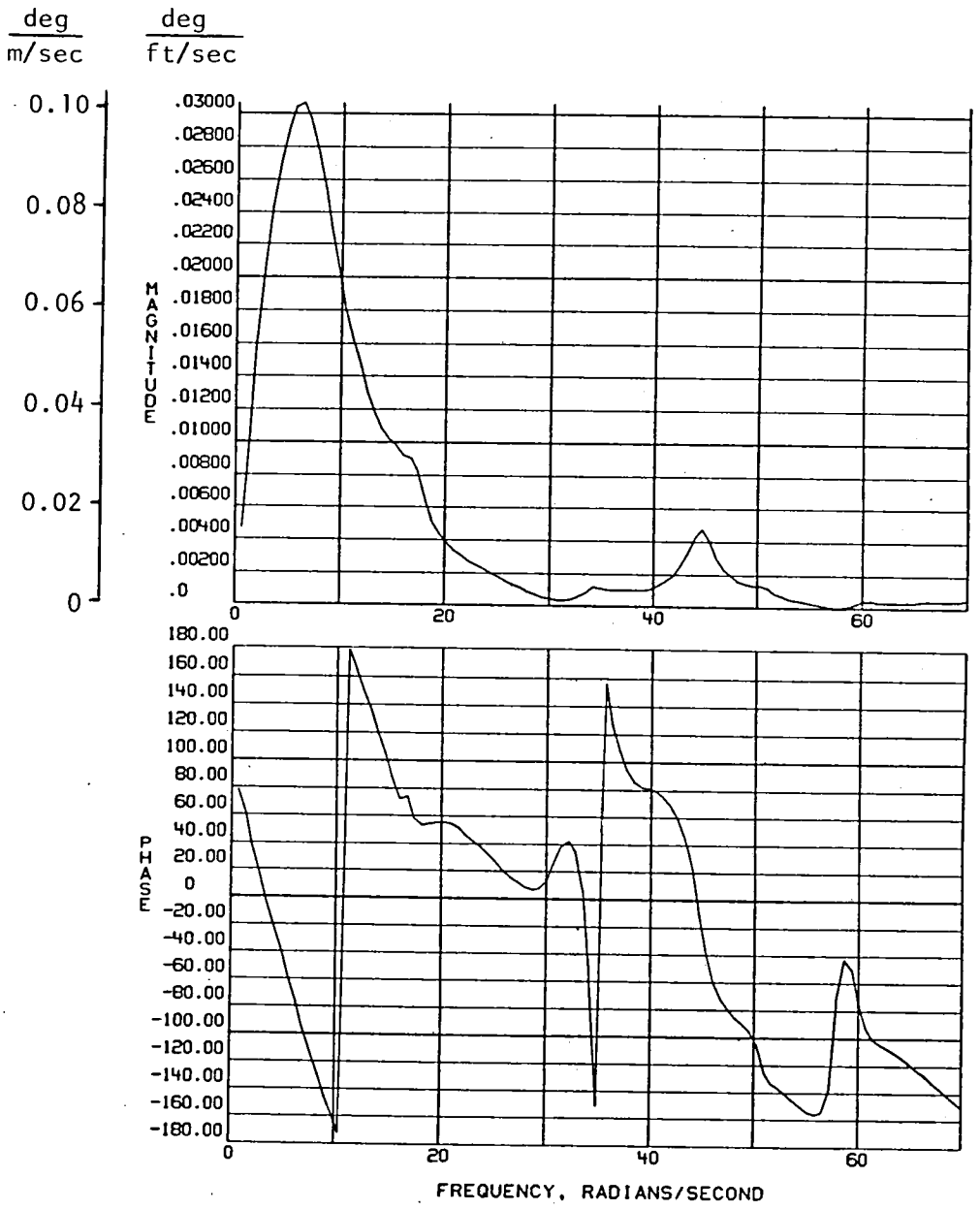

Figure 95. - SMCS on, delta horizontal stabilizer frequency response.

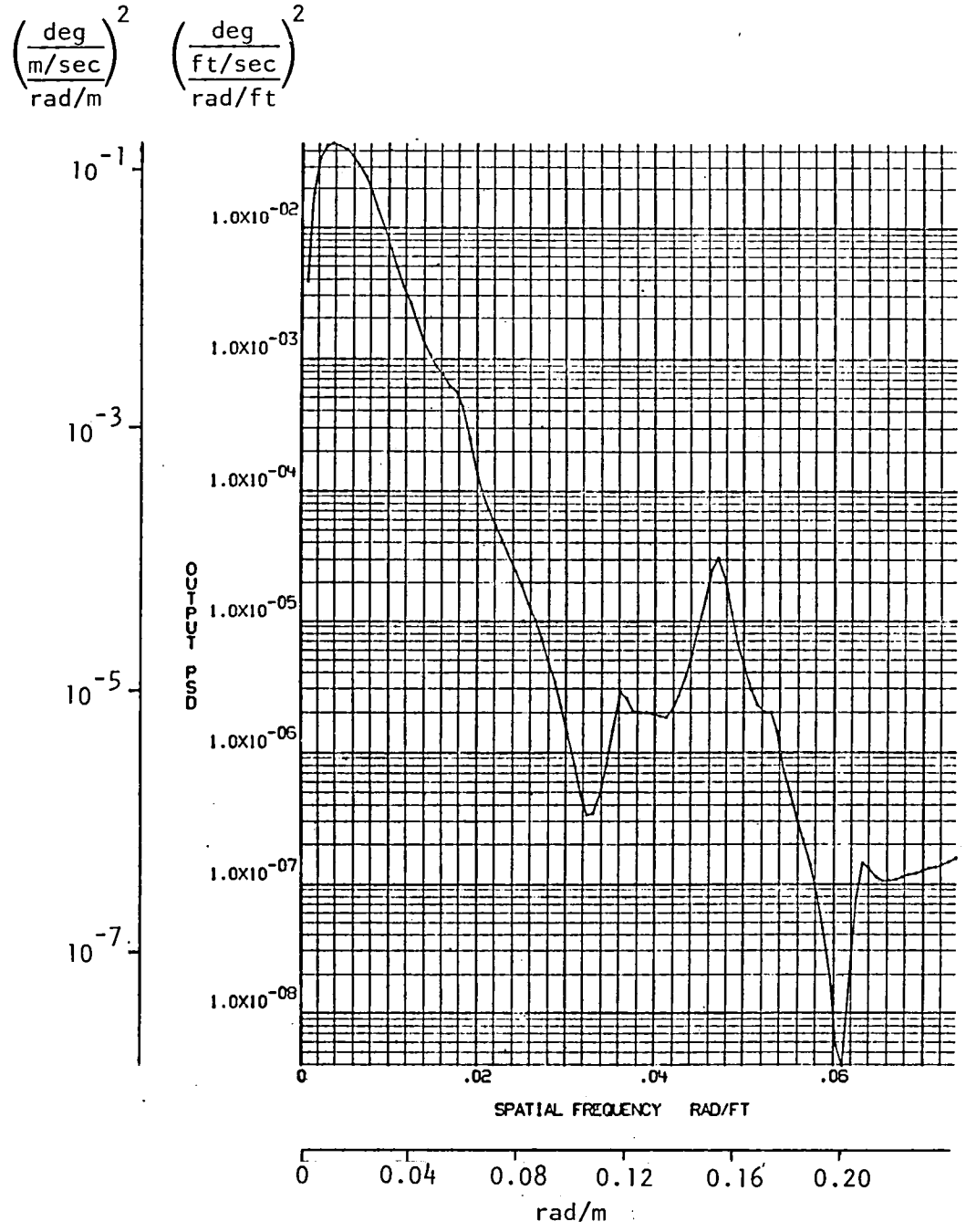

Figure 96. - SMCS on, delta horizontal stabilizer response power spectrum.

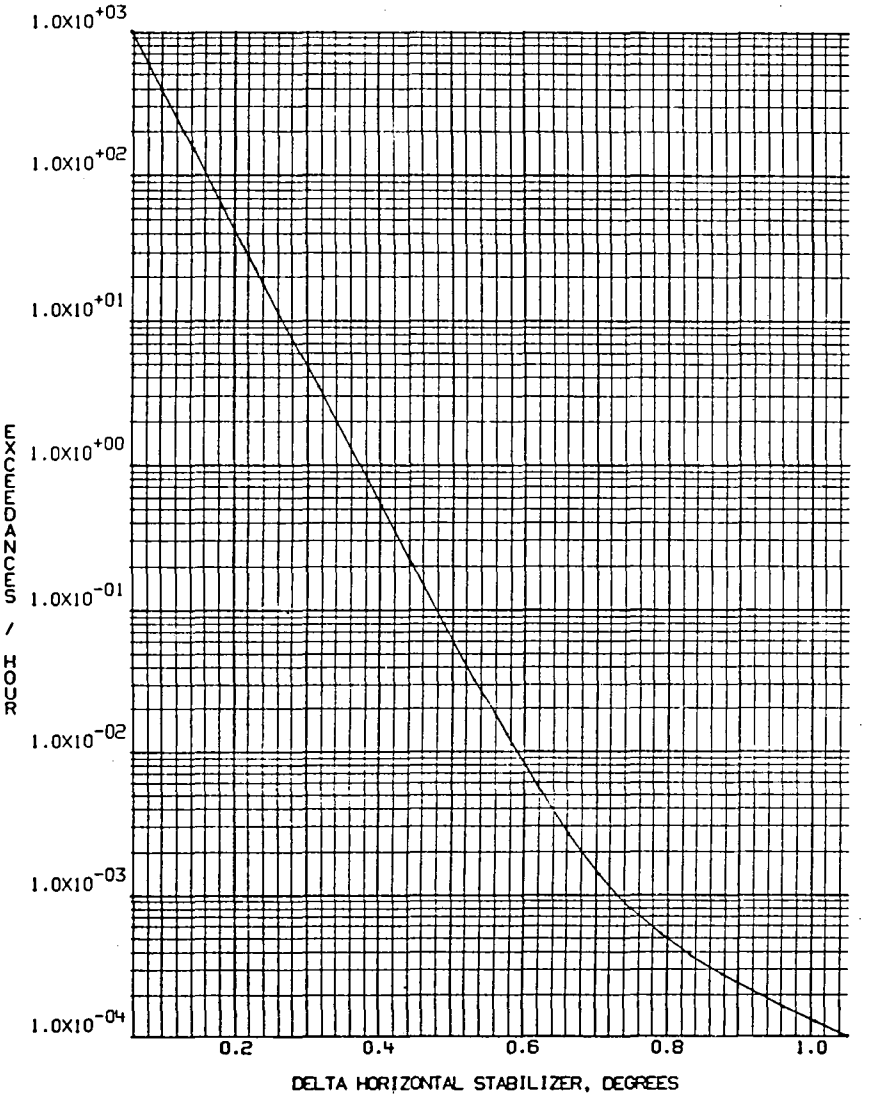

Figure 97. - SMCS on, delta horizontal stabilizer exceedances.

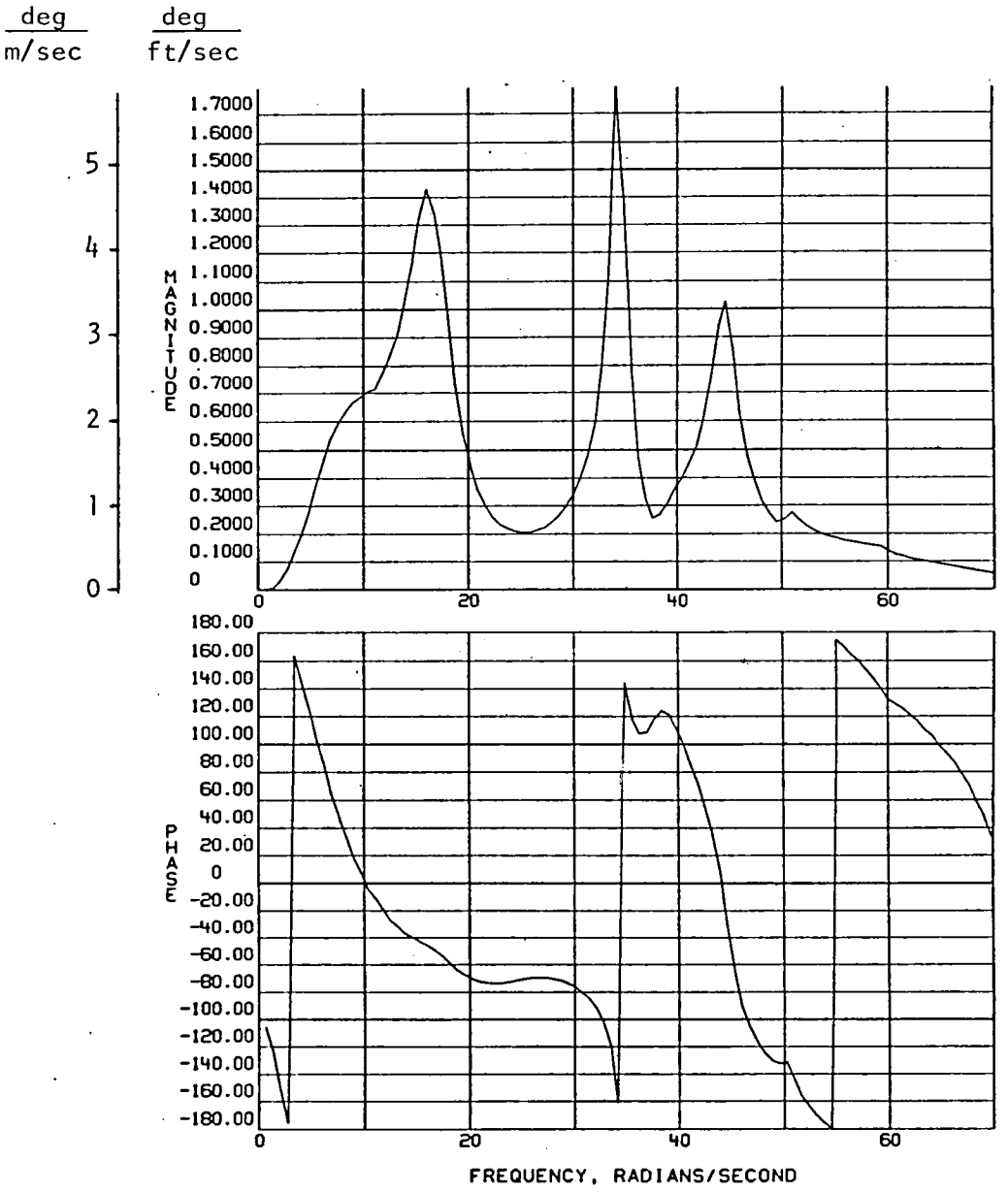

Figure 98. - SMCS on, delta mode control vane frequency response.

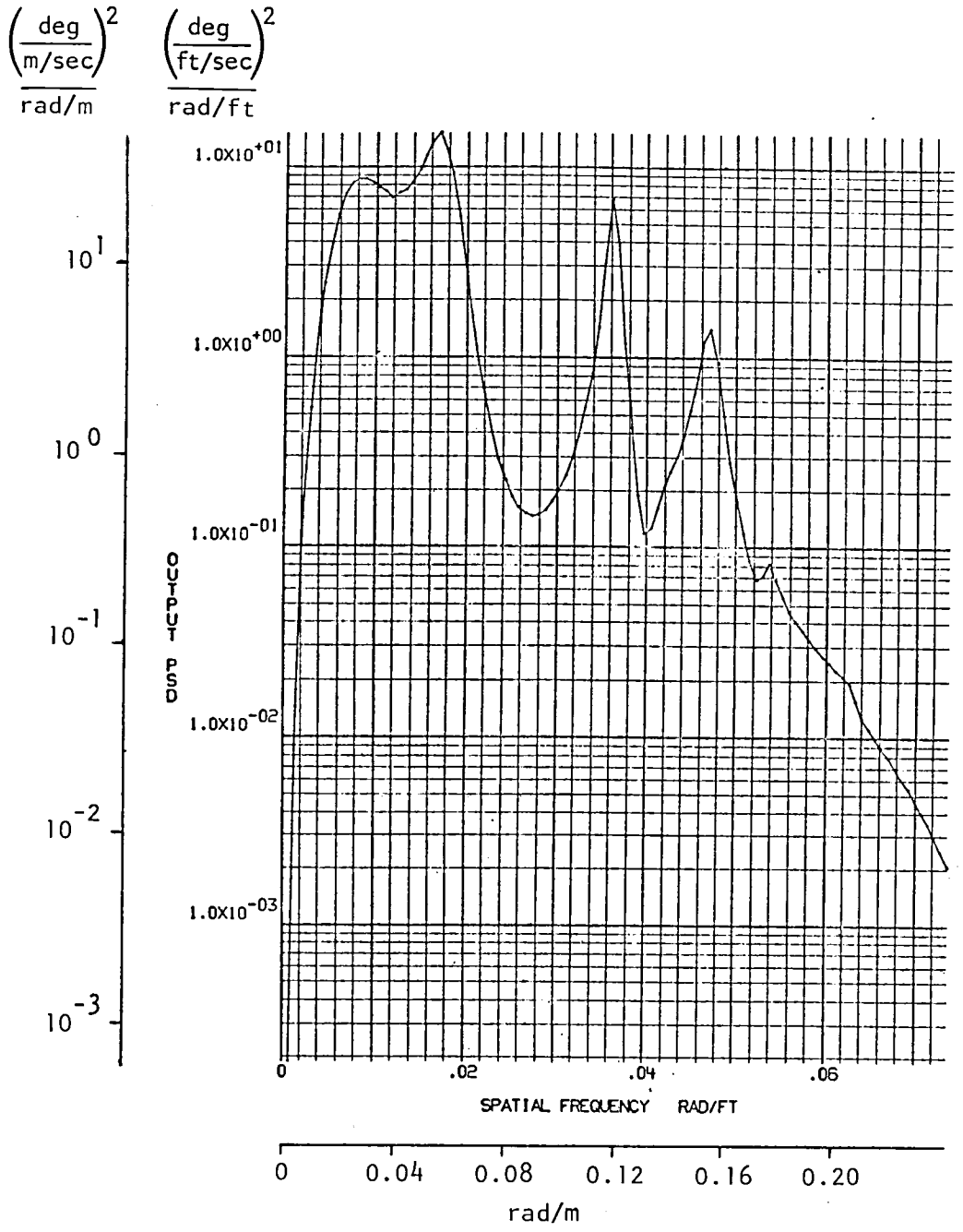

Figure 99. - SMCS on, delta mode control vane response power spectrum.

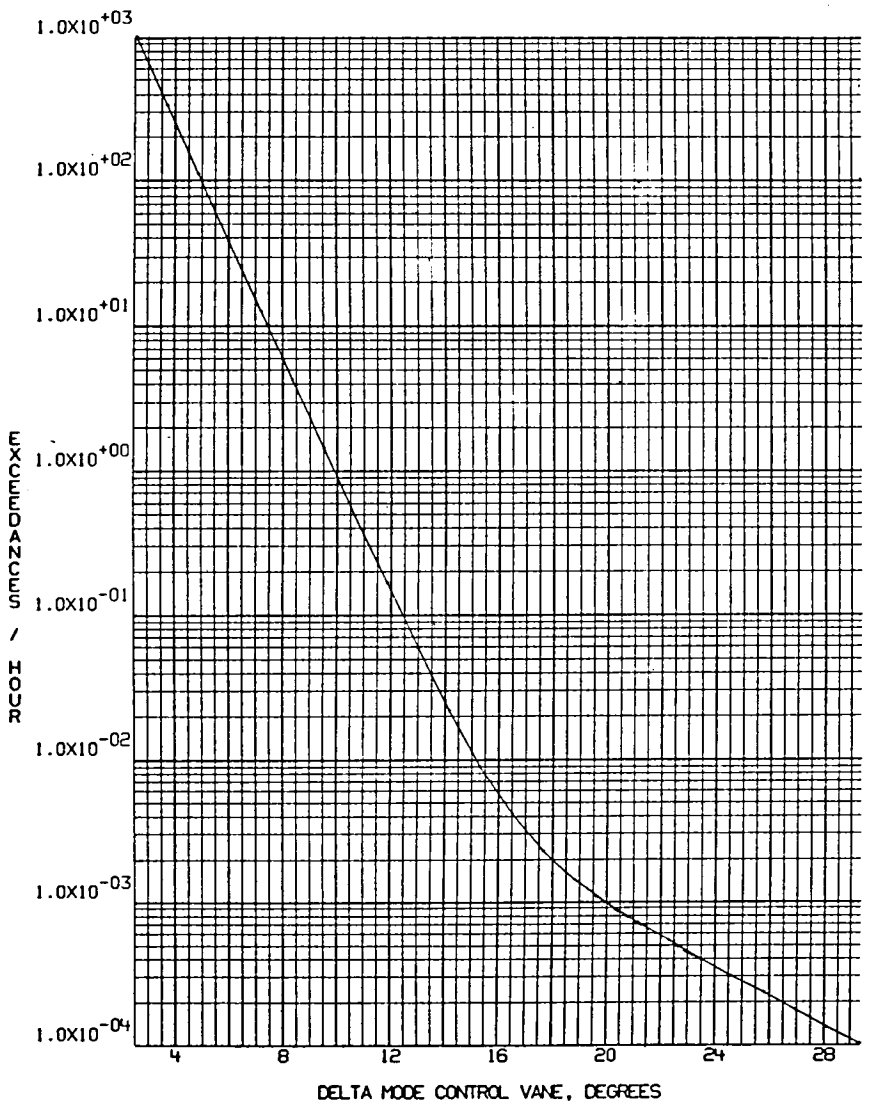

Figure 100. - SMCS on, delta mode control vane exceedances.

The tabular load summary results and the plots are presented for both SMCS off (gains = 0), and SMCS on. In either case, the SCAS was considered to be operating normally.

As can be seen in the summary table, the effect of the active SMCS was to substantially lower the fuselage forebody expected bending moments. Also lowered were the aft fuselage bending moments. The most obvious effect of the SMCS, as can be seen in the forebody frequency response and PSD plots, was to considerably suppress the response of the fuselage first bending mode. At the same time, the operation of the SMCS caused increased responses in some of the higher frequency structural modes. The effect of this increased modal activity, as seen in the fuselage and wing frequency response plots, was to cause slight increases in the wing tip, nacelle, and horizontal tail expected loads.

Although the effect of the SMCS activity dramatically reduced the magnitude of the forebody fatigue loads for low-altitude penetration, the total forebody fatigue spectrums were not so drastically reduced. The SMCS was not used during the high-altitude cruise mission segments. The large number of flight hours spent cruising and the higher wing lift curve slope at a 25-degree wing sweep, cause the expected loads to be relatively high. Thus, with the reduction in the low-altitude penetration loads, the cruise conditions became dominant in the forebody fatigue load spectrum.

SMCS VANE EFFECT ON INLET/ENGINE CHARACTERISTICS

The objective of this section is to briefly describe and summarize B-1 flight-test results that identify effects of ingesting vortices generated by the SMCS vanes into the inlet. Although vortices generated by the SMCS vanes were ingested frequently, no engine incidents relating to operation of the SMCS were identified during the approximately 1200 flight hours accumulated to date. This program included more than 200 flights with three aircraft and 29 engines. Wind-tunnel results with sub- and full-scale models were summarized in reference 1.

Portions of specific flights were dedicated to demonstrating operational suitability during aircraft maneuvers with the SMCS vanes deflected. Emphasis was placed on exploring combinations of SMCS vanes deflection angles and aircraft maneuvers during operation at Mach 0.85. Effects on inlet total-pressure recovery and engine-face distortion were measured by a 40-probe instrumentation matrix at the inlet/engine aerodynamic interface plane (AIP). Instrumentation, including an automatic in-flight calibration system, and flight-test procedures are described. Results are summarized to document this B-1 experience as an aid to future programs employing similar systems. Nomenclature associated with this section may be found in the appendix.

TEST DESCRIPTION

The B-1 propulsion system is arranged in two nacelles under the fixed portion of the wing as shown in figure 101. Each nacelle contains two independent two-dimensional (2-D) external compression inlets and two General Electric F-101 afterburning turbofan engines. Relative locations between the SMCS vanes and inlet nacelles are also shown.

Most flight tests investigating inlet characteristics with the SMCS vanes deflected were conducted with the simulated, fixed-inlet configuration shown in figure 102. Ramp configuration for both inlets consists of the initial two ramps set at 7 degrees. On the inboard inlet, the third ramp is set at 5 degrees. In the outboard inlet, the third ramp is set at 9 degrees. Small differences between inboard and outboard ramp configurations reflect an attempt to maintain good performance characteristics during both subsonic and supersonic operation. The movable cowl lip is shown in its normal, takeoff, and landing positions. Duct flow area distributions are shown in figure 103. Maximum flow area is based on an average third ramp angle of 7 degrees. Design flow area is shown for reference and represents supersonic operation with a variable geometry inlet.

Inlet boundary-layer air is removed through porous surfaces on the second movable ramp, throat panel, and small regions on the upper and lower end plates. The bleed air is collected in two compartments. The air exits from the forward compartment through fixed louvers and from the aft compartment through two-position doors. The doors are open above Mach 1.4 and closed at lower speeds. Aft bleed doors were closed during all tests with the SMCS activated.

A bypass system operates at supersonic speeds above Mach 1.4 to match the inlet supply and engine demand. The bypass doors open to compensate for reduced engine airflow such as occur on a hot day or during low-power settings. The bypass doors remained closed during all tests with the SMCS activated.

The SMCS vane configuration is defined in reference 1. Flight-test provisions included a black box located in the crew compartment to drive the SMCS vanes to a fixed deflection angle. From this position, the vanes could also be driven at selected frequencies to oscillate ±10 degrees. Using these provisions to generate full-scale vane deflections, flight tests were conducted to identify wake ingestion effects during combined aircraft maneuvers and engine throttle transients as measured at the inlet/engine AIP.

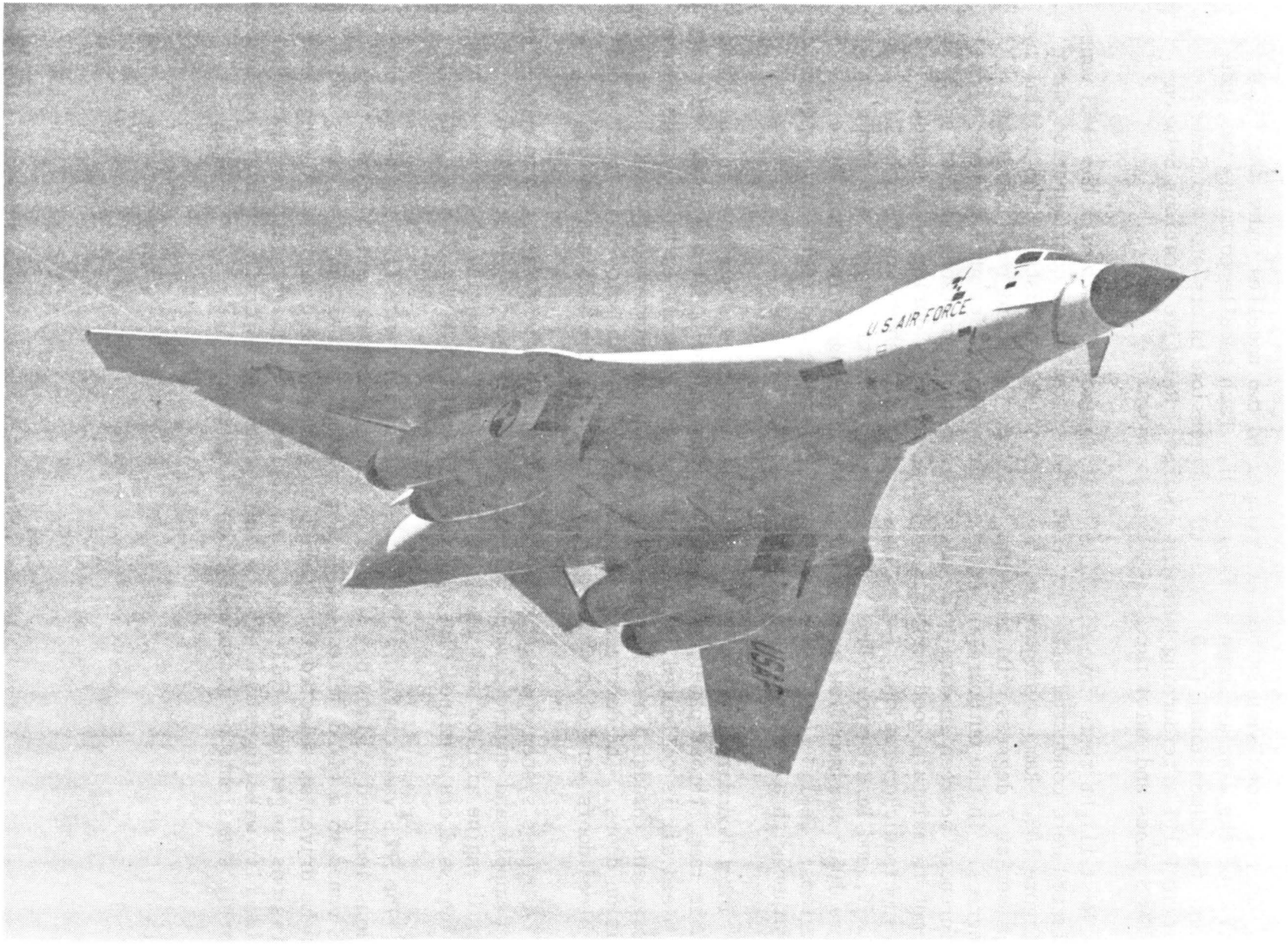

Figure 101. - B-1 flight test aircraft, wings swept 65 degrees.

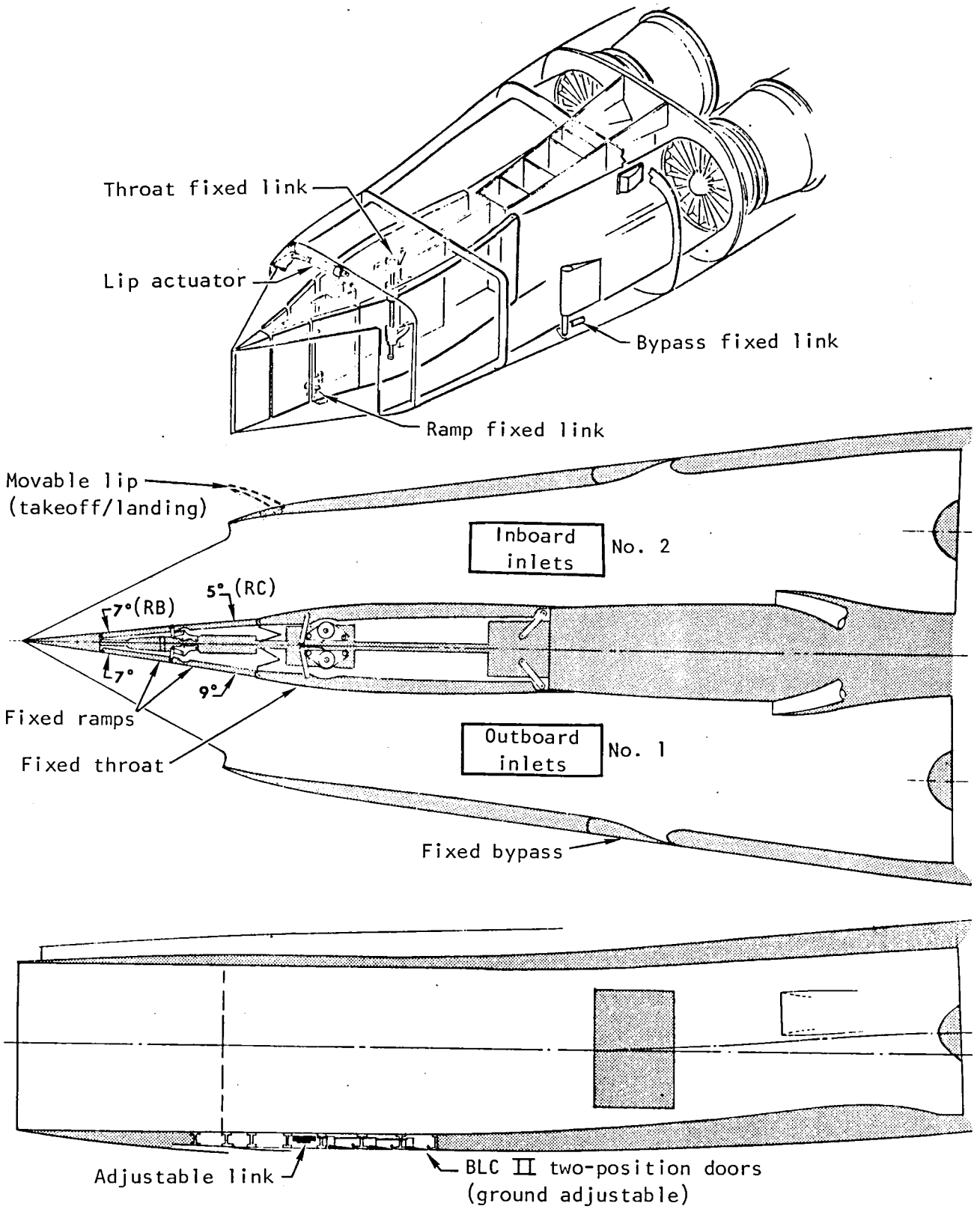

Figure 102. - B-1 air induction system.

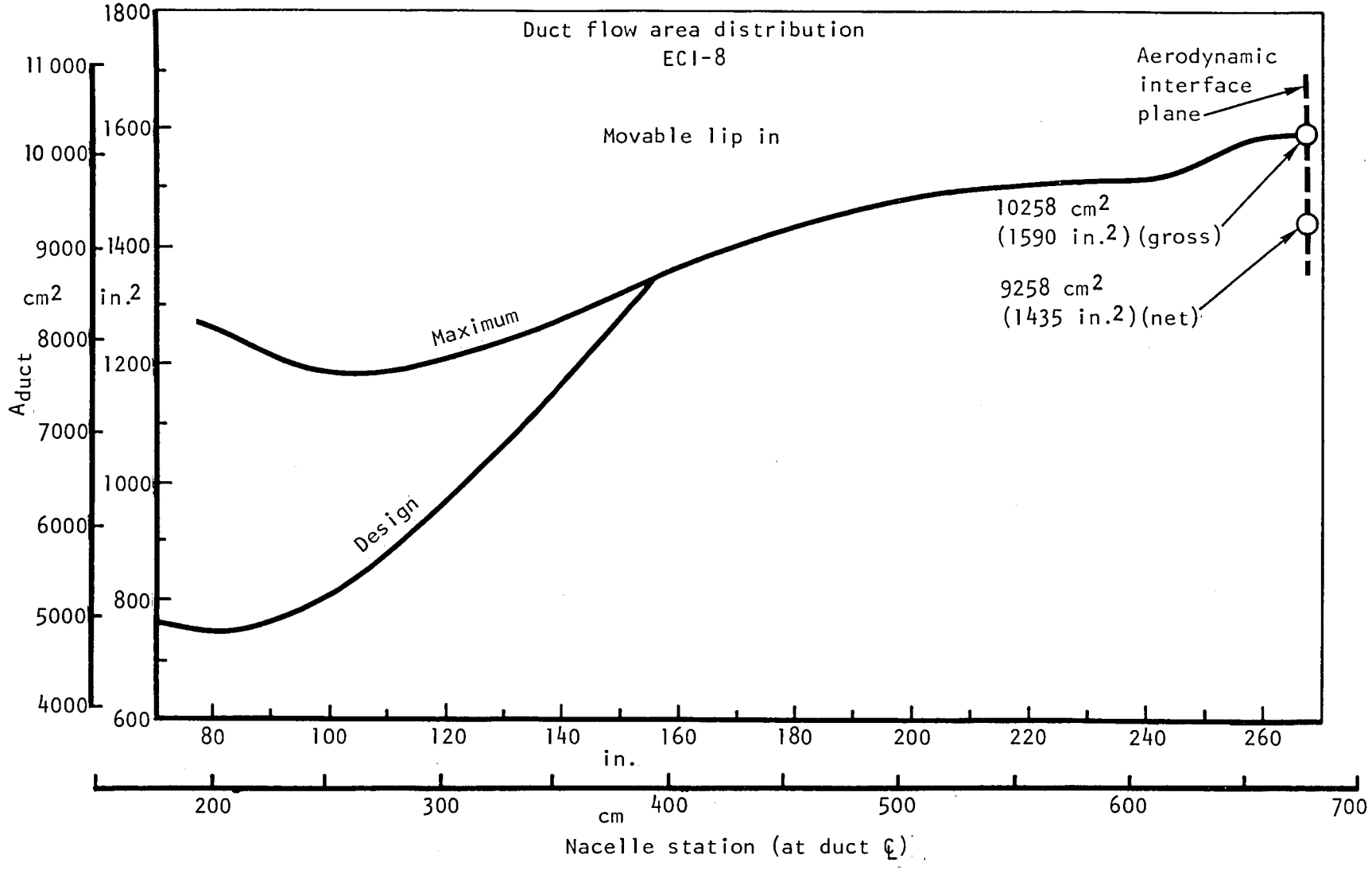

Figure 103. - B-1 inlet subsonic diffuser flow area distribution.

FLIGHT-TEST INSTRUMENTATION

B-1 flight-test aircraft were instrumented to measure more than 1600 parameters of which approximately 700 pertained to the propulsion system. Instrumentation at the inlet/engine AIP included 40 dual-purpose probes in both engines in the left-hand nacelle to measure both the steady-state and dynamic components of total pressure. Probes were installed integral with eight engine-inlet guide vanes, each with five probes located at the center of equal areas. (see figure 104.)

Computed distortion parameters are sensitive to errors in individual total-pressure measurements. Several techniques were employed during the flight-test program to minimize these errors. High-response, differential transducers manufactured by Kulite were referenced to a duct static pressure upstream of the inlet/engine AIP to maintain signal resolution over a wide range of operating conditions. The reference pressure was measured by an accurate, digital, absolute transducer installed in a conditioned compartment in the aircraft. The reference system was constructed with sufficient volume and orifices to restrict rapid changes during aircraft and/or inlet transients. Reference pressure was sampled four times per second.

An in-flight calibration system was developed to update individual probe calibrations once per minute throughout each flight. A schematic of this system, using a three-way pneumatic valve for each total-pressure probe, is shown in figure 105. The valve alternately sequences the back side of the transducer from the normal reference pressure (operate mode) first, to a calibrate pressure regulated to a pressure approximately 5 pounds per square inch above the reference pressure (calibrate mode), and then to the same pressure seen by the front side of the transducer (zero mode) (hence the name ZOC valves).

The calibrate and zero positions were each held for 2 seconds, and the operate position was held for the remaining 56 seconds. In the zero position, the total pressure being sensed is routed to the back side of the transducer through an infinite coil, approximated by a coiled line 20 feet in length. This provision was necessary to prevent reflecting waves affecting the frequency response of the probes and was determined empirically. Both coils and pneumatic valves, the latter grouped in gangs of five, are shown installed on the engine in figure 104.

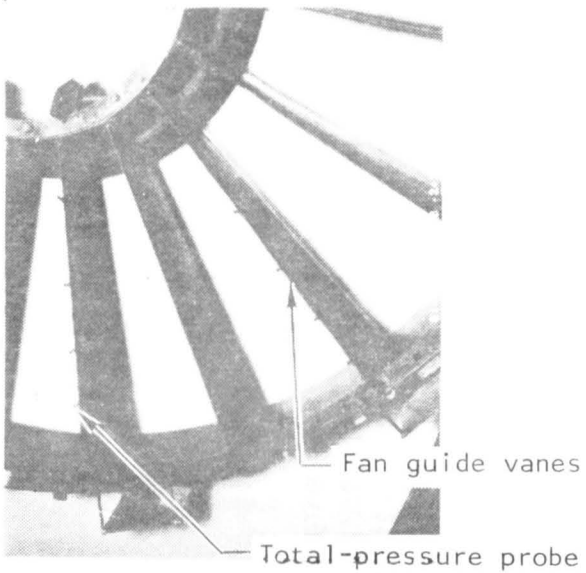

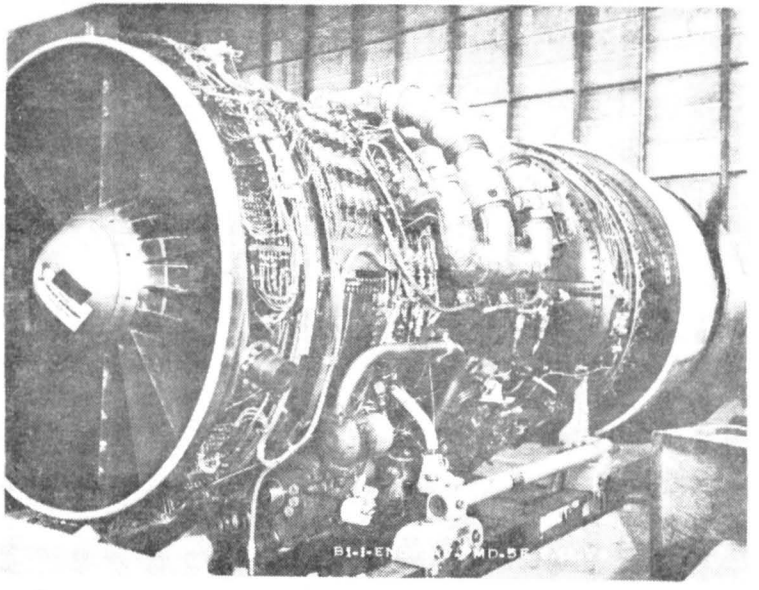

Kulite AIP probes

View looking aft

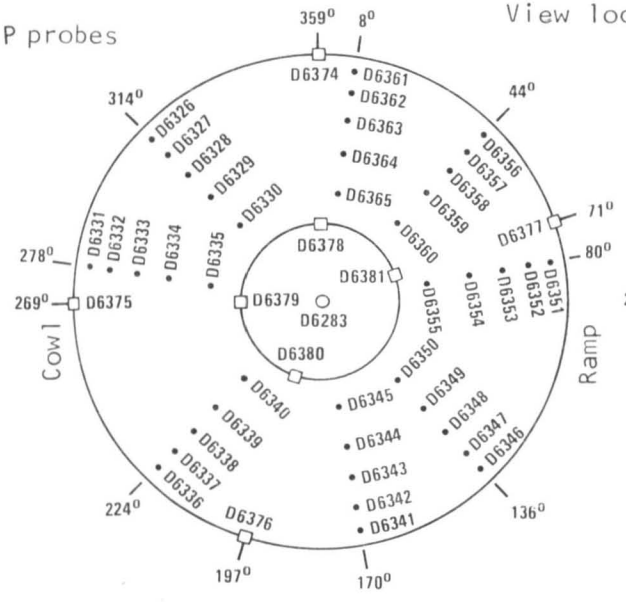

Engine 1

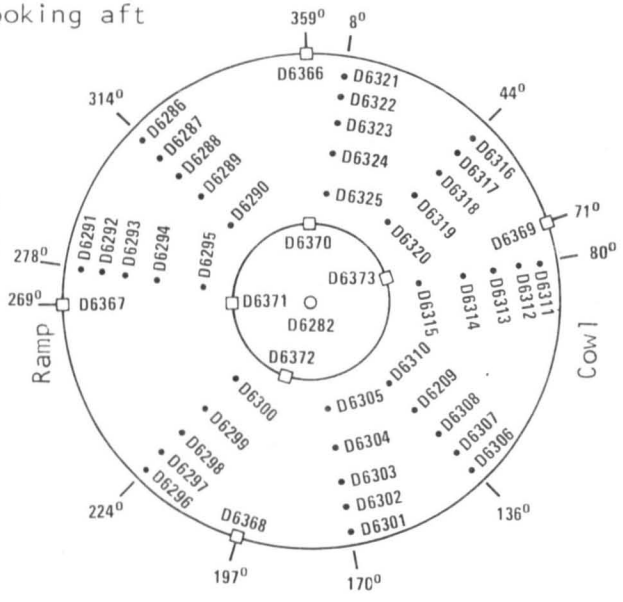

Engine 2

Figure 104. - B-1 inlet/engine aerodynamic interface plane instrumentation.

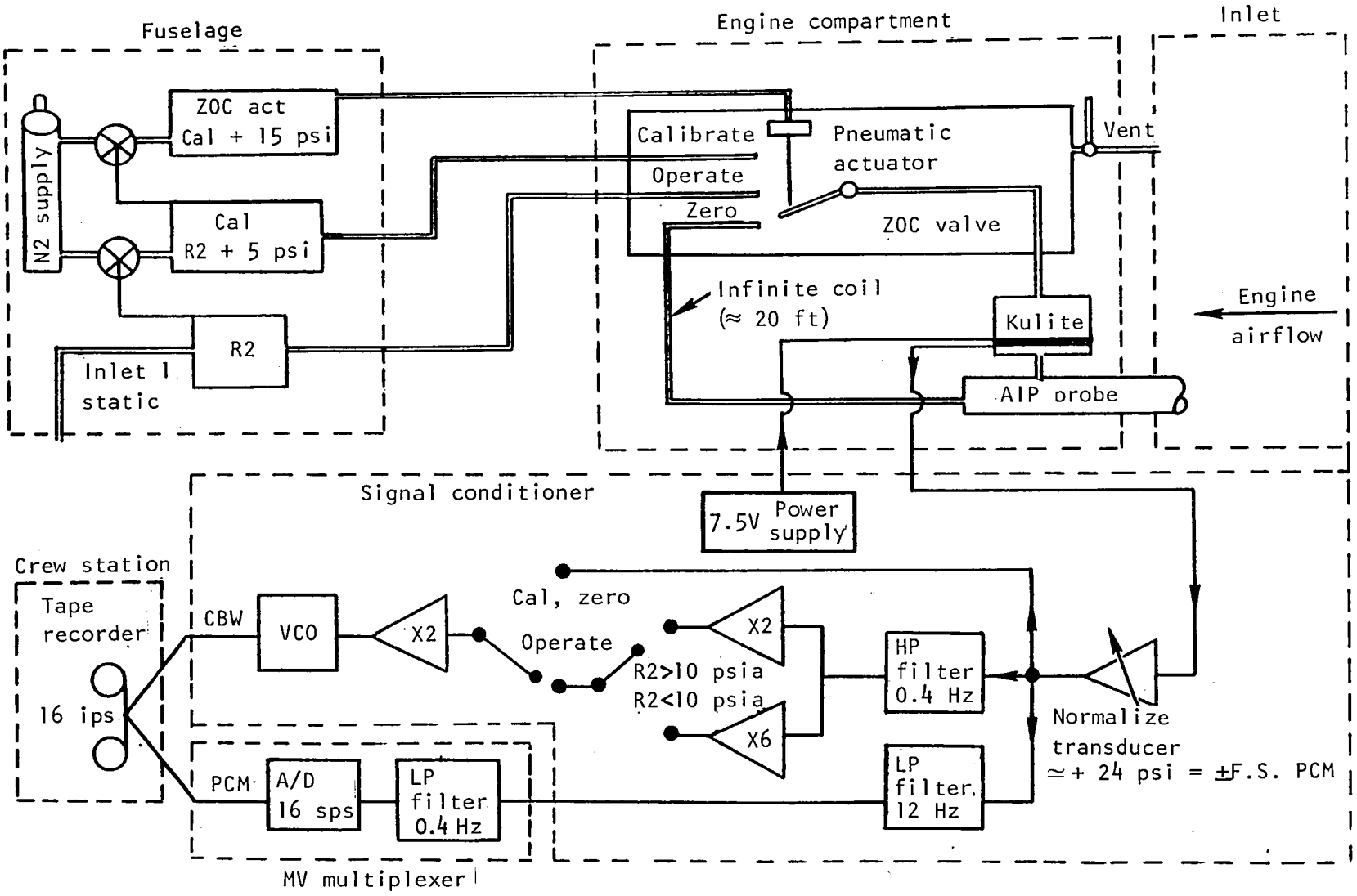

Figure 105. - B-1 flight-test AIP data acquisition and signal conditioning system.

Pneumatic valves were actuated by a pressure source regulated to 15 pounds per square inch above the calibrated pressure. Provisions were included to vent trapped pressures within the valve to either the engine compartment (ambient pressure) or an engine-face static pressure, depending on the operating condition. Vent pressures were required to be the lowest pressure in the system at all times. Selection of vent pressure was accomplished by a crew compartment switch. A pressurized nitrogen bottle was used as a pressure source for the actuate and calibrate tanks.

Signal conditioning for the transducer output is also shown in figure 105. Each signal is initially passed through a variable amplifier that is used to establish a full-scale range for the steady-state component at approximately 24 pounds per square inch. Zero output levels can also be biased to favor normal operation. Subsequently, signals are split to record low- and high-frequency components separately.

Low-frequency or quasi steady-state components are generated by low-pass filters that effectively eliminate frequency components above 0.4 Hz (3 decibel level). Signals are sampled by a sequential analog-to-digital converter onboard the aircraft and stored as digital words on a tape recorder located in the crew compartment.

High-frequency or dynamic components are generated by high-pass filters that effectively eliminate frequency components below 0.4 Hz (3-decibel level). Signals are further amplified before passing through voltage-controlled oscillators, multiplexed, and recorded on the same tape recorder (different tracks) used to record the low-frequency components. With 21 continuous bandwidth (CBW) signals multiplexed per track, four tracks were required to record the 80 high-frequency signals from both instrumented inlets.

During the zero and calibrate steps, all filters are bypassed, and the total signal (minus the reference pressure) is recorded both as pulse-code modulation (PCM) and CBW parameters. Calibration sequence is operate-calibrate-zero-operate. Transition between the zero and operate positions imposes a step change in pressure differential across the transducer diaphragm. This has no essential impact on the low-frequency component because of the low-pass filter. However, the high-pass filter responds to this step change and results in a damping characteristic with a period of approximately 10 seconds. As a consequence, dynamic data are invalid during this time, and data records for detailed dynamic analysis are selected to circumvent any problems. Typical output signals, including calibration cycles, are illustrated in figures 106 and 107.

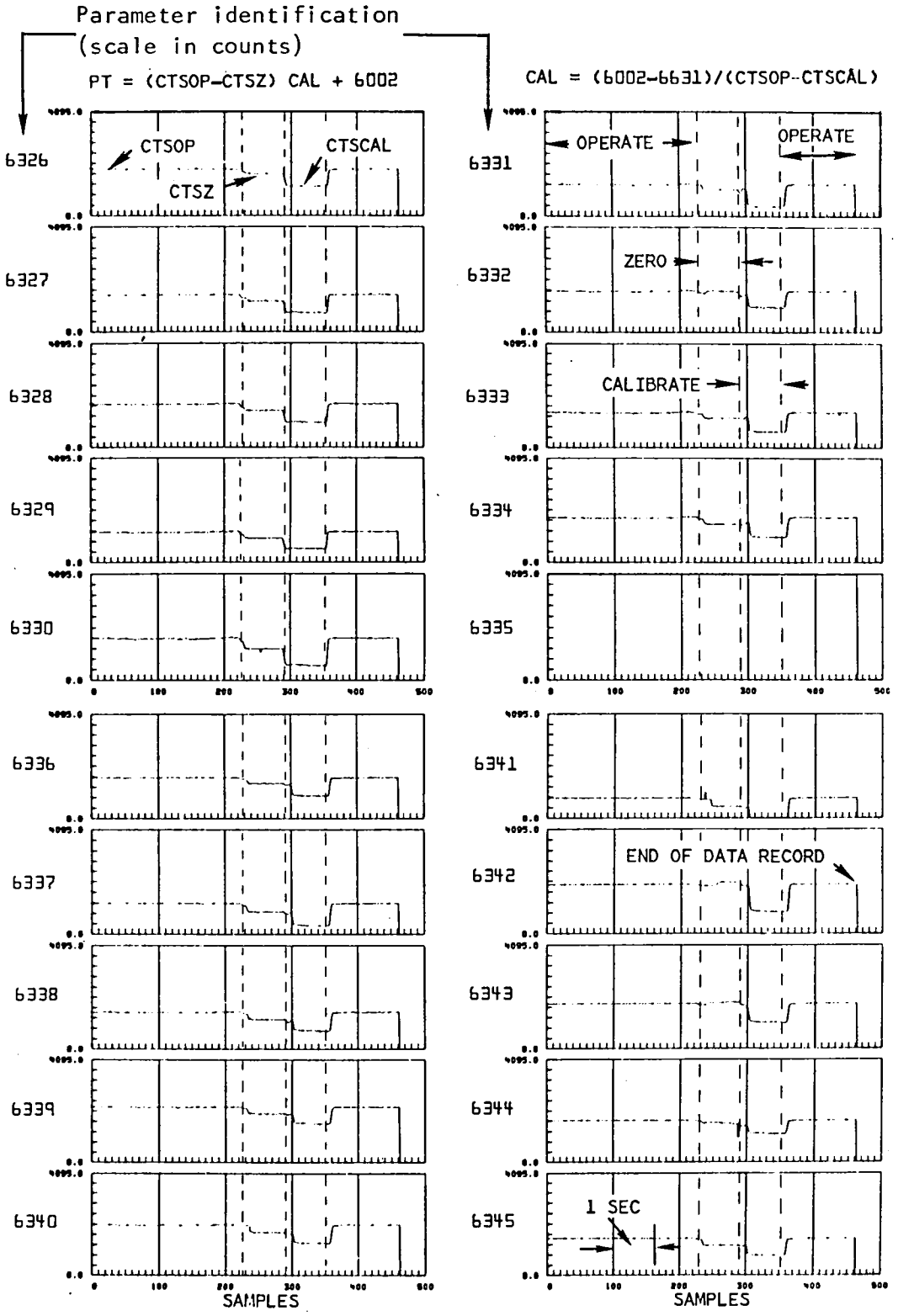

Figure 106. In-flight calibration cycle, total pressures at aerodynamic interface plane, flight 1-5, 64 sps.

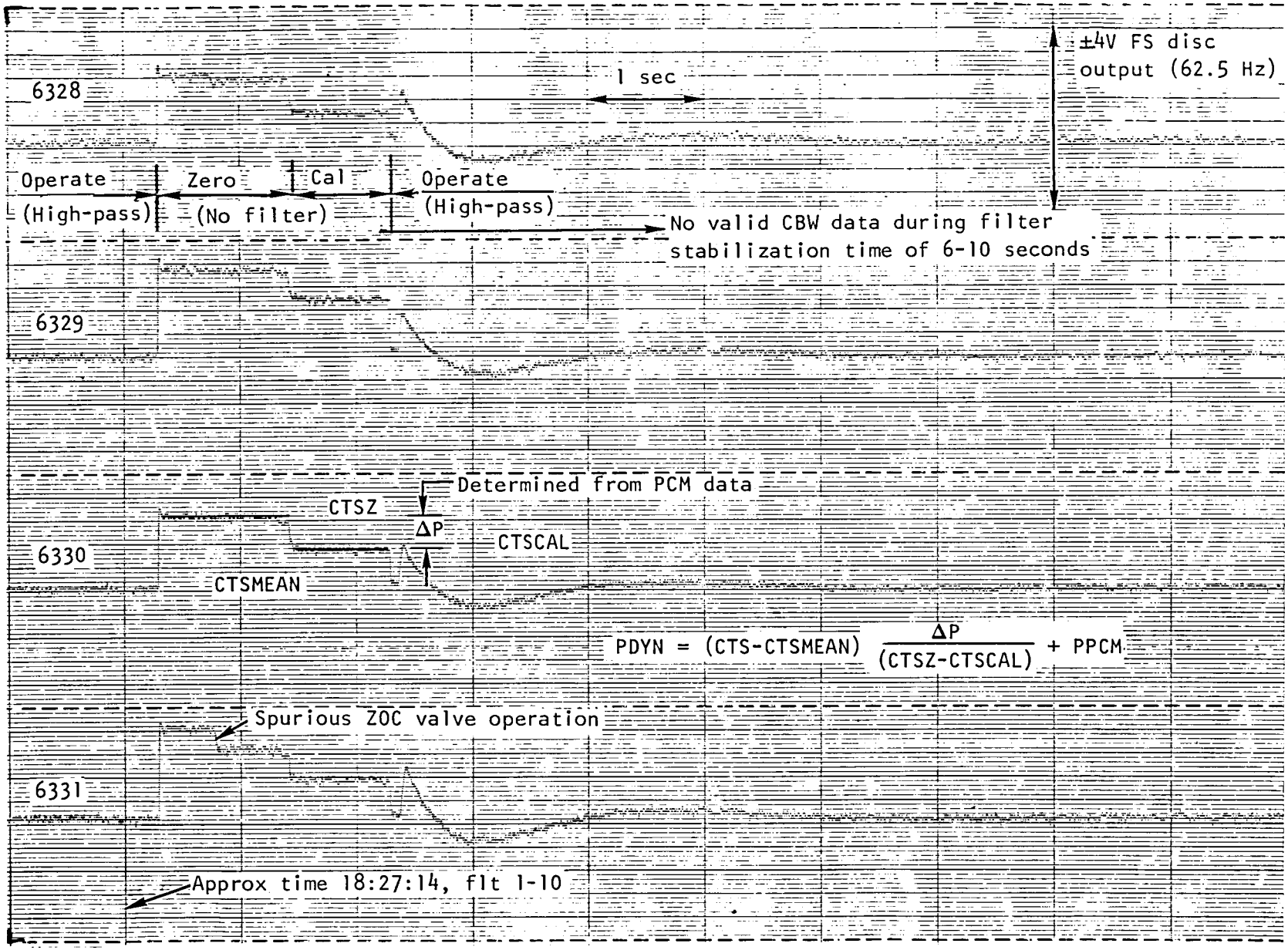

Figure 107. - Representative discriminator output, AIP total-pressure CBW data, flight 1-10.

In summary, particular emphasis during the flight-test program was placed on obtaining accurate, total-pressure surveys at the inlet/engine AIP. As described, these features included the following:

(1) Differential transducers with a floating reference pressure

(2) Accurately measured reference and calibrate pressures

(3) Automatic in-flight calibration procedures

(4) Signal conditioning to obtain good resolution of both high- and low-frequency components from the same transducer

Flight-test experience has shown that, as one might expect with all the pneumatic and electrical connections, the system required considerable maintenance. However, it is believed that system accuracy approached levels available with a well-constructed wind-tunnel program, and this seems to be confirmed by comparisons between wind-tunnel and flight-test results.

TEST RESULTS

A total of 5 flight-test hours were dedicated to exploring SMCS vane effects on inlet/engine characteristics. Flight conditions and operating variables are summarized in table IX.

Several computed parameters from the 40 total-pressure measurements at the inlet/engine AIP are used to present test results. Recovery (PT1/PT0) is the average of the 40 low-response signals referenced to free-stream, total pressure.

Several distortion indexes are used and were computed by digital techniques. High-response signals were filtered to 62.5 Hz and sampled at 360 samples per second to represent a one-per-revolution engine-frequency response (signals fully attenuated at 125 Hz). Circumferential (IDC) and radial (IDR) distortion components were computed for each ring (each group of eight AIP pressures at the same radii) and combined mathematically to form a fan stall-margin index (IDL). This latter index is normalized to stall-margin allocations, and thus, values of unity computed from the high-response signals identify distortion levels approaching design limits. Inlet distortion, (PTMAX - PTMIN)/PTAVG, was also computed. Record lengths were in the range between 5 and 20 seconds. Scans resulting in maximum values of stall-margin index are generally used to identify trends.

TABLE IX. - SMCS VANE EFFECTS ON INLET/ENGINE CHARACTERISTICS, FLIGHT TEST INVESTIGATION

Flt no.	Dedicated flt time[a] (min)	Objectives/accomplishments	AIP instrumentation status
2-19	65	Initial flight-test investigations with oscillating vanes at 1 Hz, vane angle ±10 degrees, α = 3-8 degrees, β = 0-3 degrees, initial throttle transients	Reference pressure transducer malfunction, no conversion to engineering units
2-33	45	Static vane deflection angles in 5 degree increments, ± full scale, α = 1, 3, 5 degrees, β = 0-4 degrees, no. 2 throttle transients	ZOC valves malfunctioned on no. 1 eng, data reduced only for no. 2 engine.
2-36	60	Repeat of flight 2-33	Leaks in reference system precluded AIP data reduction.
2-37	55	Repeat of flight 2-36	Satisfactory
2-38	60	Max rate throttle transients with vane deflected 20 degrees combined with nose left sideslip	Satisfactory
2-42	20	Conduct pushovers and pullups with vane deflected 20 degrees	Satisfactory

[a]Total ≈5 hours

Engine-face, total-pressure contours are used to illustrate variations in distortion patterns. High-pressure regions (pressures higher than average) are shaded on the contour plots. Low-pressure regions (pressures lower than average) are unshaded. The magnitude of the difference above or below the average pressure level is defined by the number on the contour. The annular region is formed by protrusion of the engine bullet nose at the AIP.

Envelopes encompassing all combinations of circumferential and radial distortion components are used to identify the magnitude of dynamic activity and to compare them to design goals. Two types of time histories have also been found useful in documenting inlet turbulence characteristics. Analog strip charts of the high-response AIP signals help to identify wake ingestion during transient maneuvers. Digital time histories help to define transient conditions based on computed parameters.

Oscillating Vanes

Initial tests with the SMCS operative were conducted with the vanes deflected symmetrically at nominal angles of ±10 degrees and then oscillated ±10 degrees about that mean at a frequency of 1 Hz. Vane deflection angle thus oscillated between 0 and ±20 degrees; the latter representing full-scale deflection. Note that with these procedures, the vane is being used as an excitor and induces some discomfort to the crew members. With the vane oscillating, aircraft maneuvers involving combined angles of attack and sideslip were performed.

Time histories of aircraft attitude and vane deflection angles recorded during a 30-minute segment of flight 2-19 are shown schematically in figure 108 during operation at Mach 0.83. Angle of attack was varied between 3 and 8 degrees; sideslip angle was varied between 0 and 3 degrees. Tests were conducted at positive sideslip angles only to ingest the wake in the instrumented nacelle.

Flight times where increased dynamic activity (identified from strip charts of the high-response AIP instrumentation) could be definitely attributed to SMCS vane deflection are indicated. Increased dynamic activity was also noted at other times; however, effects of sideslip and vane deflection angles could not be definitely separated. Ingestion is generally restricted to positive vane deflection angles (leading edge up) greater than 10 degrees in combination with aircraft sideslip operation.

One major advantage of oscillating the vanes is to produce recognizable wake ingestion effects in the data. The 1 Hz vane oscillation between 1.5 and 18.5 degrees during a sideslip maneuver is shown in figure 109. Time histories

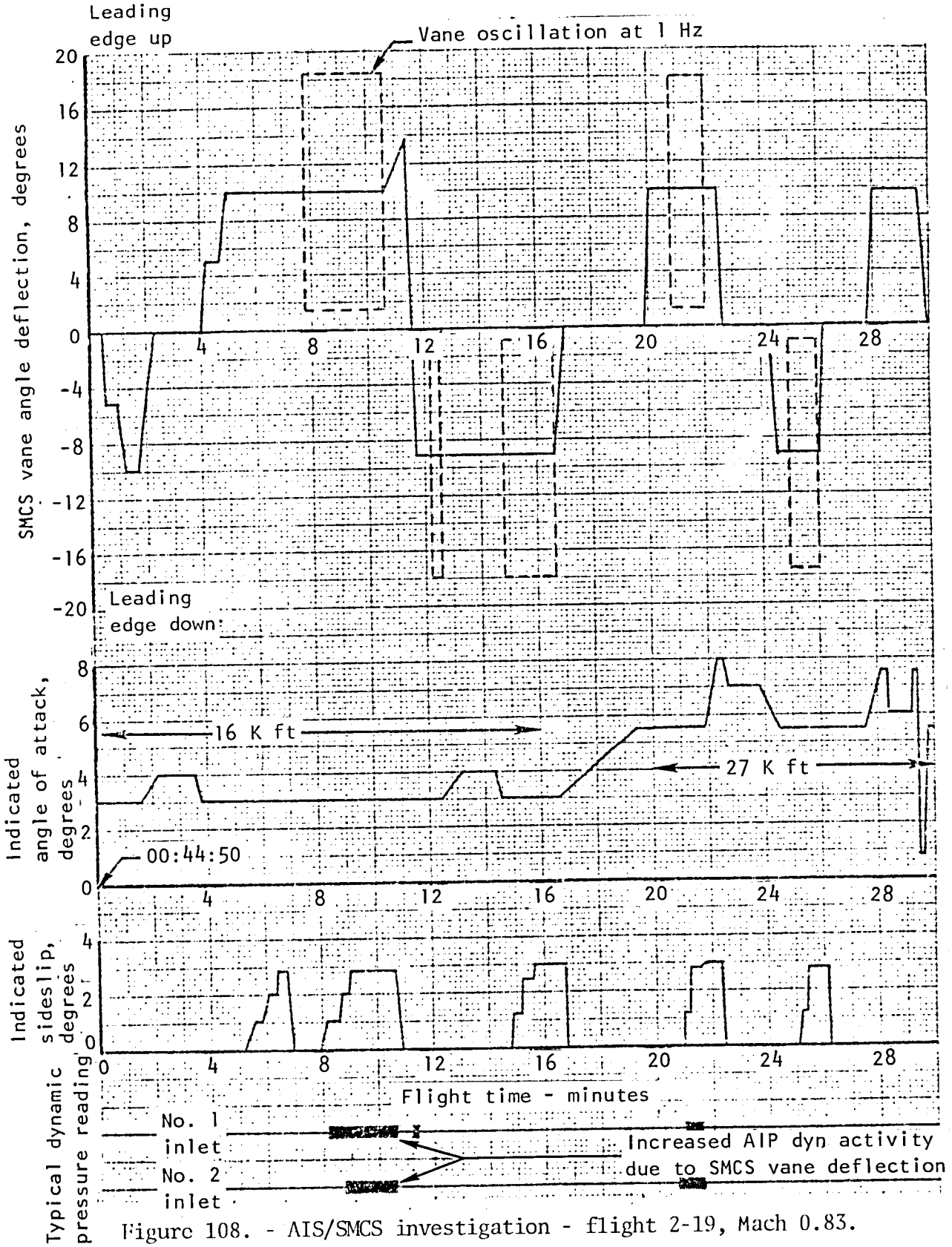

Figure 108. - AIS/SMCS investigation - flight 2-19, Mach 0.83.

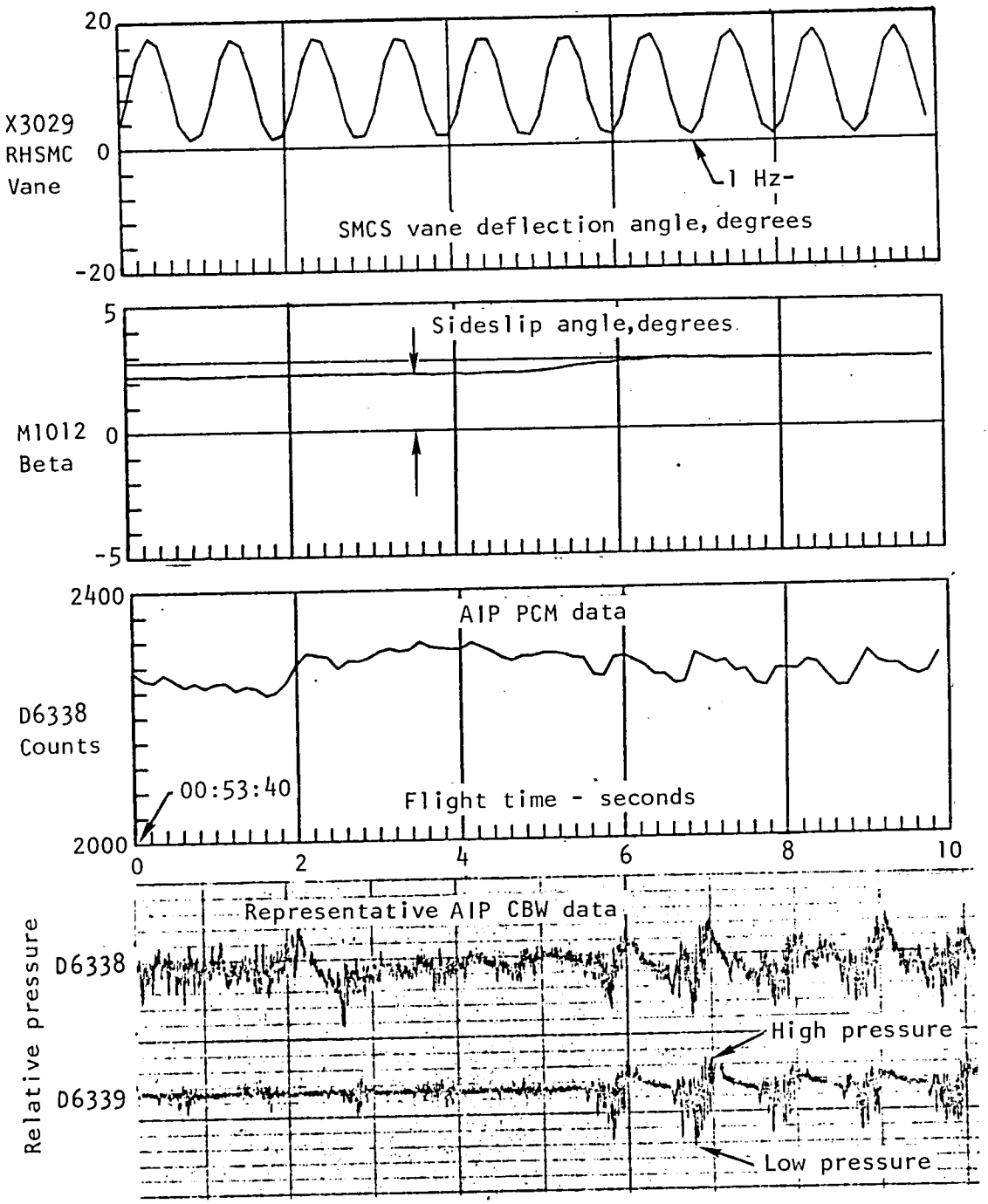

Figure 109. - AIS/SMCS investigation flight 2-19, Mach 0.83/16 000 feet, α = 3 degrees, vortex ingestion in no. 2 inlet during sideslip operation, PLA = max.

of both low- and high-response AIP signals are shown during an increase in sideslip from 2.2 to 2.7 degrees. Wake ingestion is evident throughout the transient, and turbulence levels increase significantly at the higher sideslip angle. Although the individual plots are not precisely aligned in time, low pressures generally coincide with positive vane deflection angles. Similar results were obtained with the no. 1 inlet. (See figure 110.) Smaller amplitudes are partially attributed to reduced engine airflow indicated by lower fan corrected speeds.

Engine airflow demand has a significant influence on peak-to-peak amplitudes. Representative AIP pressures are shown in figure 111 during a throttle burst from IDLE to INTERMEDIATE (maximum airflow) power settings. Peak-to-peak amplitudes at INTERMEDIATE power are greater by a factor of 1.7 than the amplitudes recorded during IDLE power. Again, the lower pressures in the cycle appear to coincide with maximum, positive, vane-deflection angles.

Static Vane Deflections

Comparison of results from tests described previously indicated that results similar to those obtained with oscillating vanes could be obtained with the vanes positioned at a constant deflection angle. Crew members found these procedures less objectionable, and their work load was slightly reduced. All subsequent flight tests exploring SMCS vane effects on inlet/engine characteristics during maneuvers and engine throttle transients were conducted in this manner.

Maneuvers.- Tests conditions investigated during flight 2-33 (with SMCS vanes deflected +20 degrees) are summarized in figure 112. Tests were conducted at Mach 0.85 and included maneuvers at combined angles of attack and sideslip where the maximum angle of attack was 6 degrees and maximum sideslip angle was 4 degrees. Representative AIP high-frequency, total-pressure signals are shown during maneuvers where vane vortex/wake ingestion was measured in the no. 2 inlet. Faulty ZOC operation precluded analyses of data recorded in the no. 1 inlet. A strip-chart trace, recorded during normal cruise attitudes, is shown for reference. Aircraft attitudes resulting in ingestion during flight test generally agree with those recorded previously during wind-tunnel tests.

Steady-state total-pressure recovery and distortion parameters are shown in figures 113 and 114 as functions of sideslip angle. Angle of attack is used as the independent variable in figure 113 with the vanes deflected 20 degrees. The largest defect in recovery (approximately 0.06) was measured at 6 degrees angle of attack and approximately 1.75 degrees of sideslip. Effects of the wake diminish as sideslip is further increased. At approximately 3 degrees

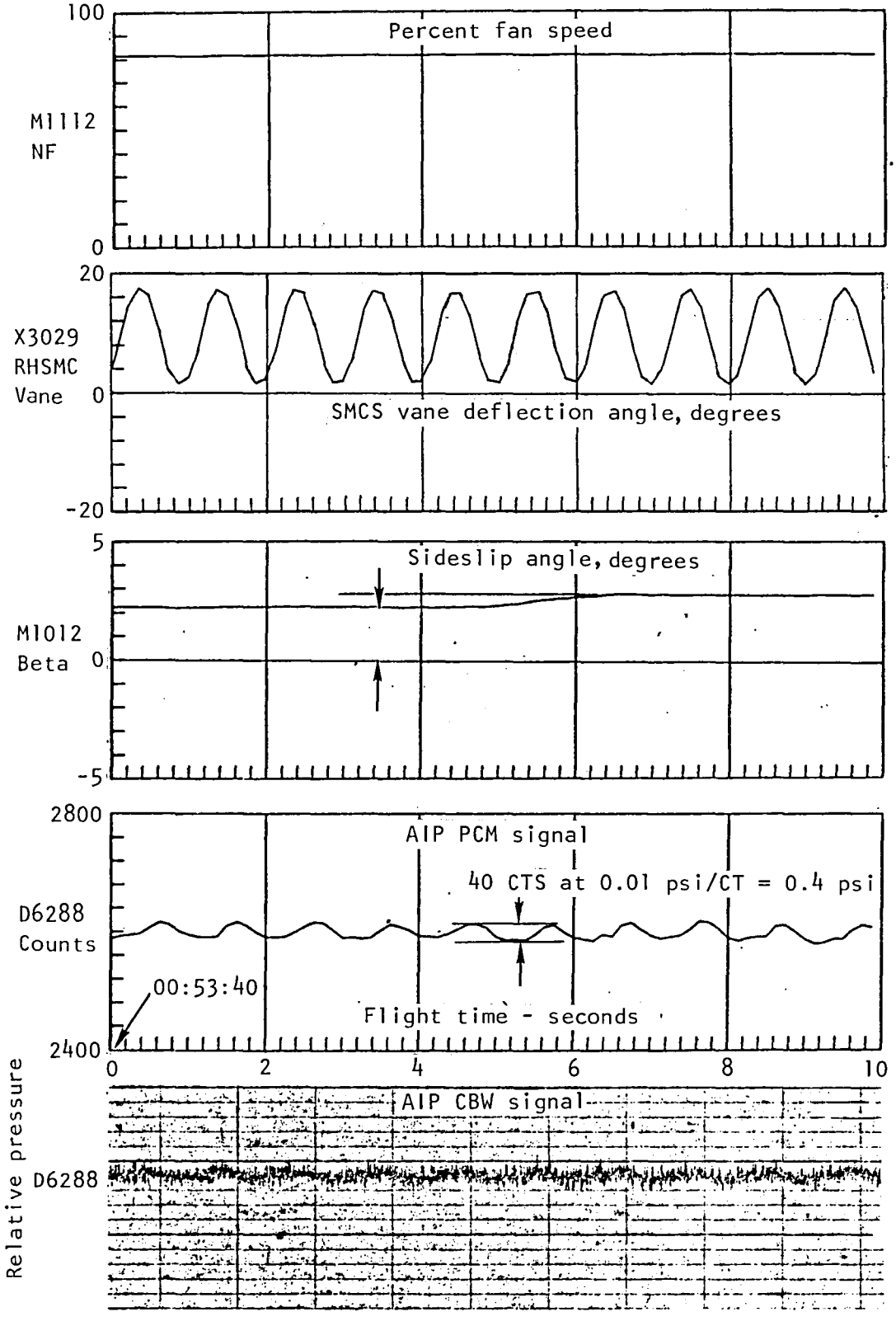

Figure 110. - AIS/SMCS investigation, flight 2-19, α = 3 degrees, vortex ingestion in no. 1 inlet during sideslip operation.

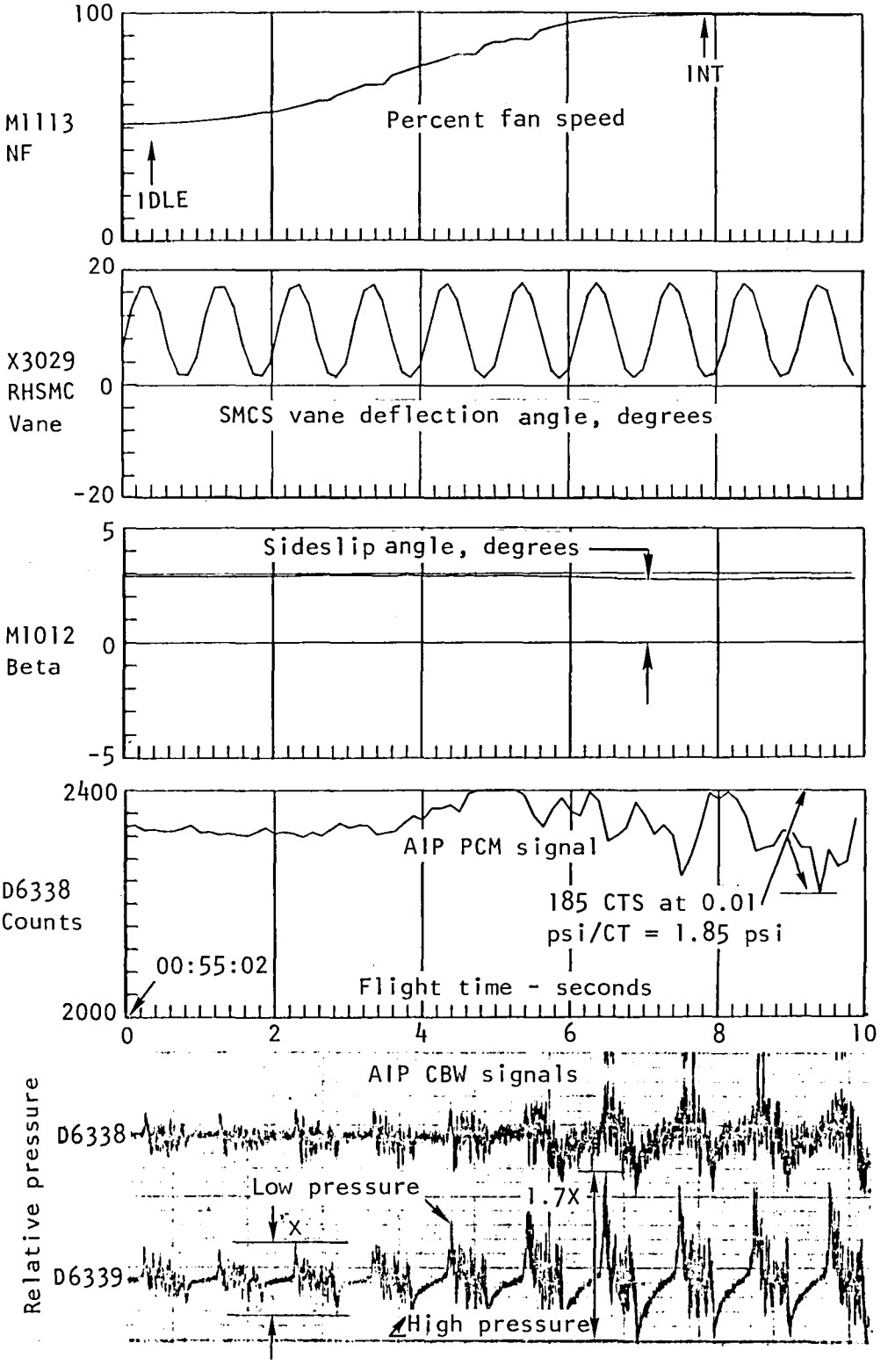

Figure 111. - AIS/SMCS investigation, flight 2-19, α = 3 degrees, vortex ingestion in no. 2 inlet during IDLE-INT throttle transient.

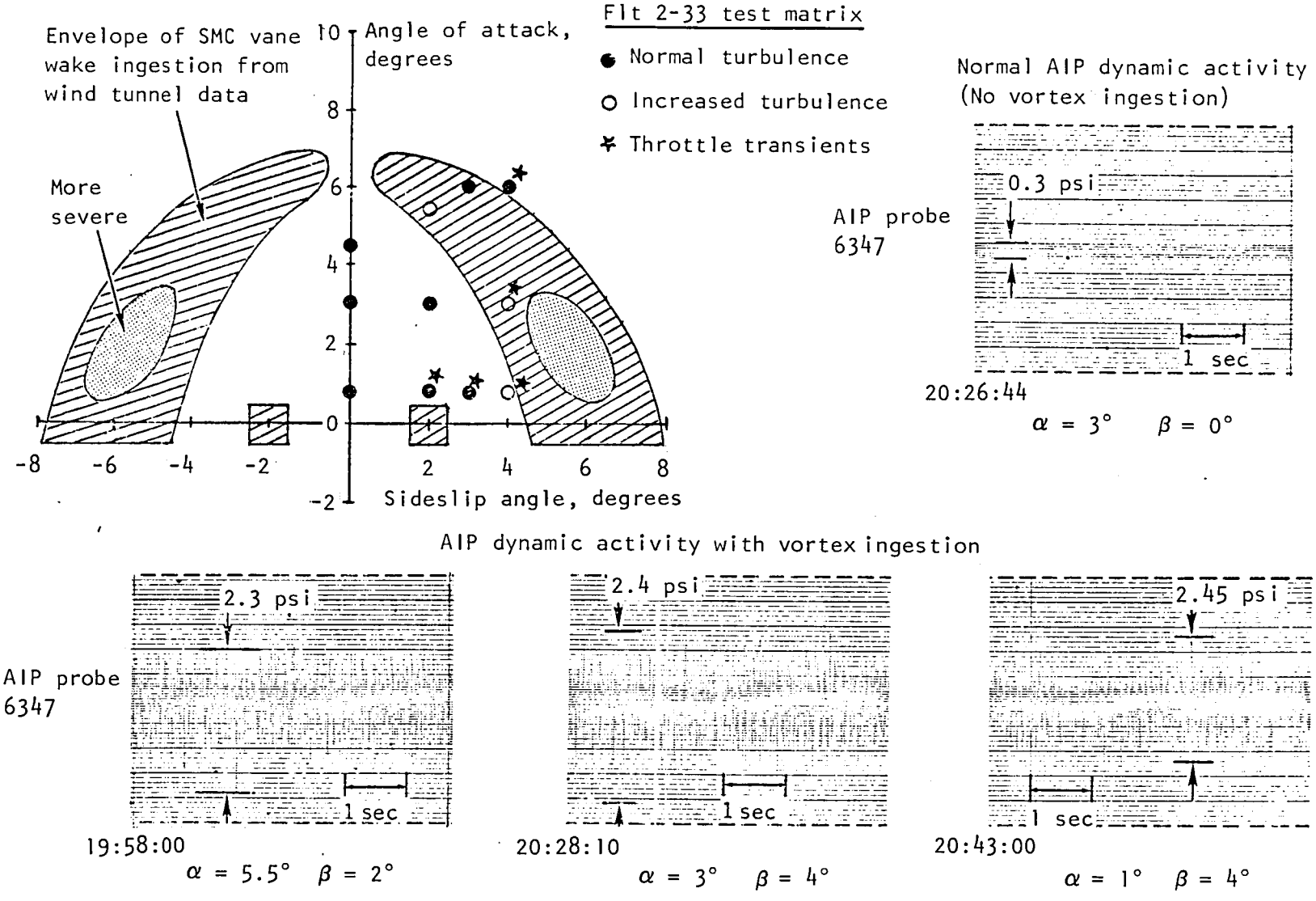

Figure 112. - Flight 2-33 test matrix and AIP signals during Mach 0.85 operation with SMCS vanes deflected 20 degrees, no. 2 inlet, RB = 7 degrees, RC = 5 degrees.

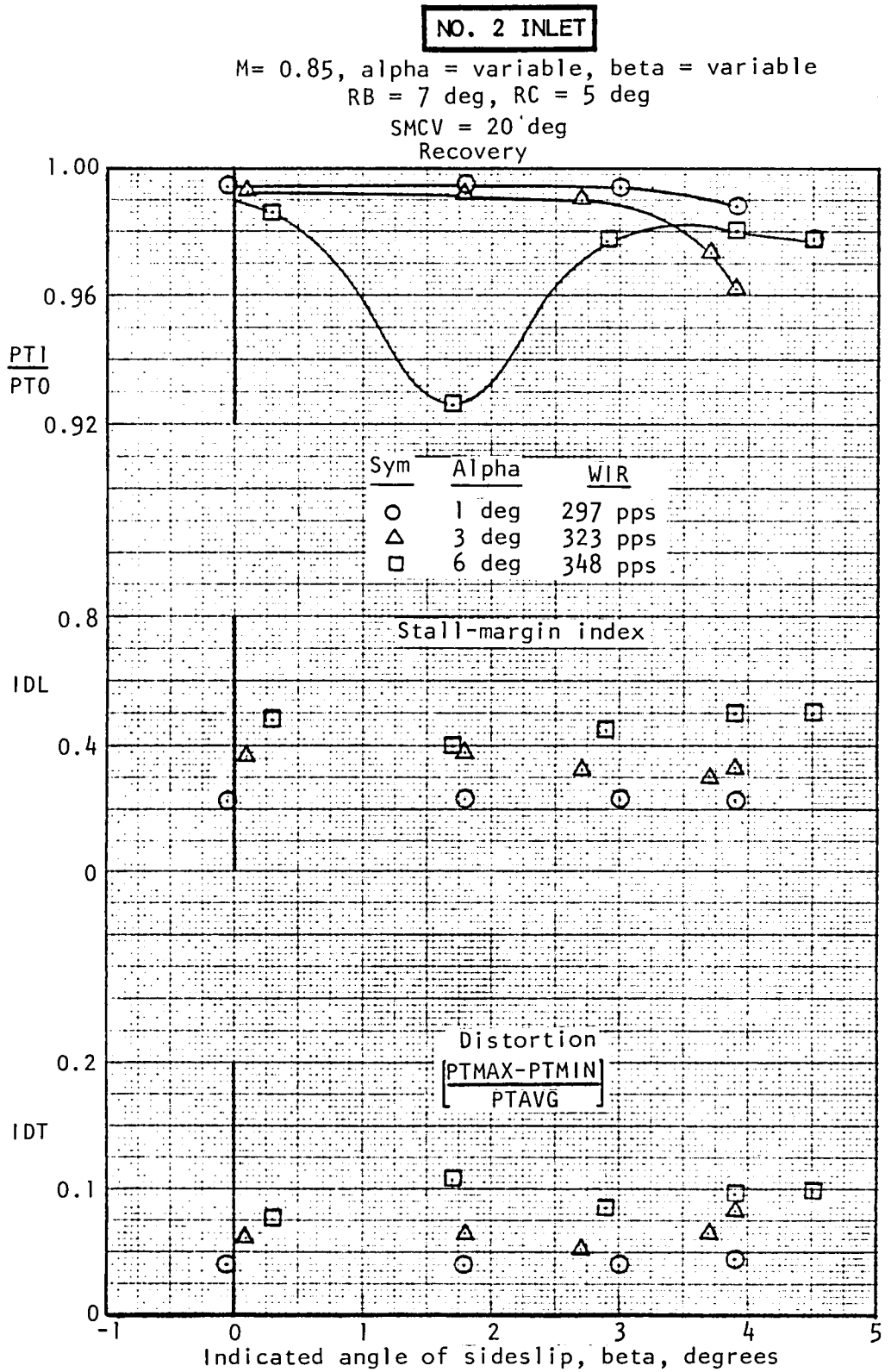

Figure 113. - No. 2 inlet, effect of sideslip angle on steady-state inlet characteristics at SMCV = 20 degrees, flight 2-33.

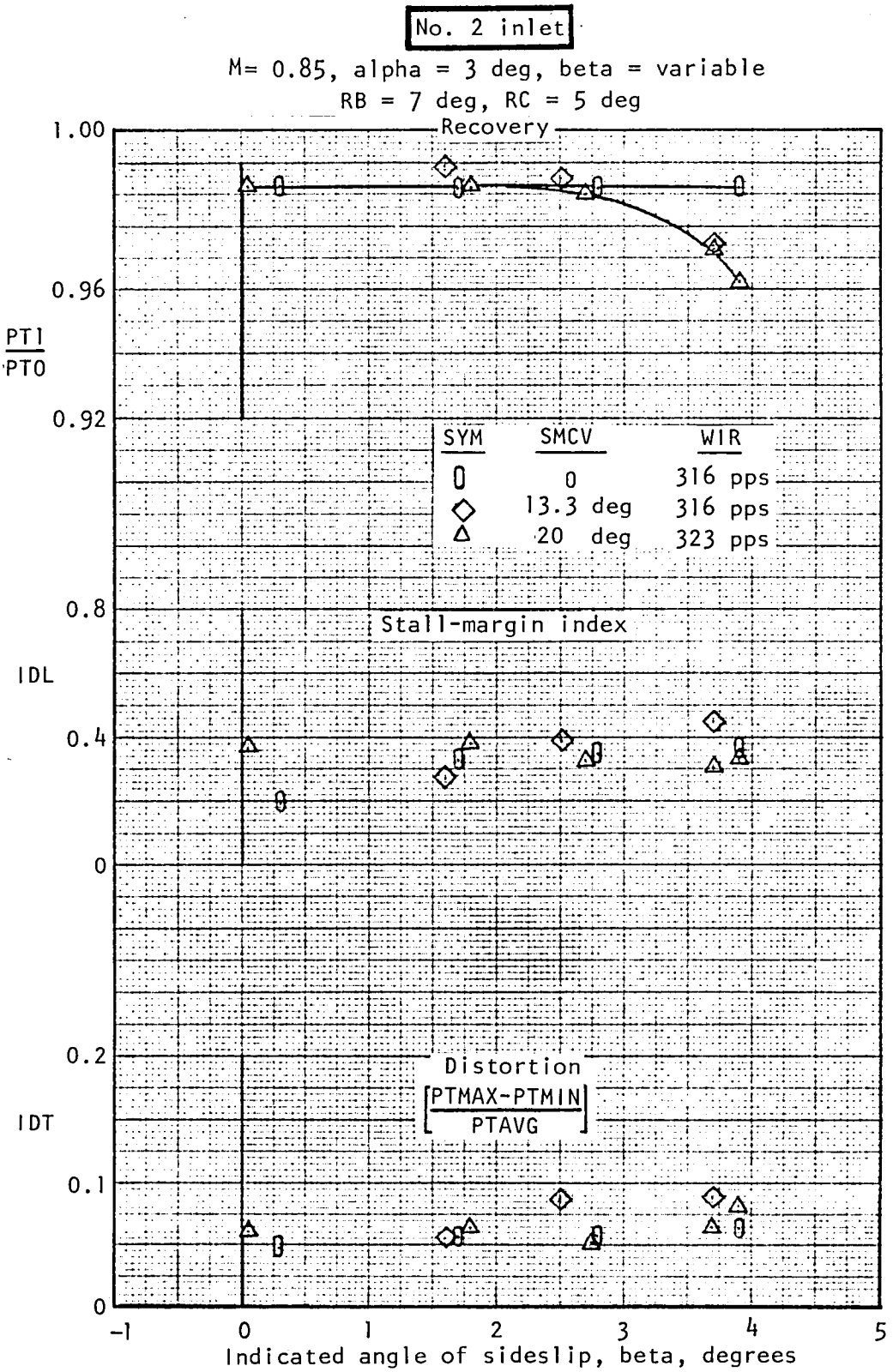

Figure 114. - No. 2 inlet, effect of sideslip angle on steady-state inlet characteristics at various SMC vane angles, flight 2-33.

sideslip wake effects are no longer present in the inboard inlet. At lower angles of attack, sideslip angles greater than 3 degrees are required before wake ingestion becomes evident.

Effect of vane deflection angle is shown in figure 114 during operation at 3 degrees angle of attack. Pressure recovery values from this figure indicate a similar loss during sideslip operation for both the 13- and 20-degree vane deflections. No losses in recovery are evident with the vane held in a neutral position.

No definitive trends are evident in the steady-state distortion indexes. However, with the measured increase in turbulence previously shown in figure 112, this is sometimes indicative of an in-phase component present in the flow as shown in the time histories of total-pressure recovery (figure 115) where SMCS wake ingestion was most evident. Time histories of stall-margin index are also shown. Similar traces during operation at normal attitudes with no vane deflection are shown for comparison.

Resulting envelopes of circumferential and radial distortion components are shown in figure 116. Total pressure contours representing maximum values of stall-margin index are shown in figure 117. Maximum dynamic effects correspond to operating conditions resulting in lowest total-pressure recovery at 6 degrees angle-of-attack and 2 degrees of sideslip. Maximum stall-margin index was 0.74, and the associated total-pressure contour shows a well-developed, low-pressure region in the hub.

An extensive series of tests with the SMCS vanes was also conducted during flight 2-37. Performance and distortion characteristics are summarized for the no. 2 inlet at normal aircraft attitudes (α = 2.7 degrees, β = 0 degrees) in figure 118 for the complete range of SMCS vane deflection angles from 20 to -20 degrees. No indications of wake ingestion are evident.

A series of tests investigating SMCS vane effects during sideslip operation were conducted over a range of angle of attacks. Results are generally shown for both inlets, and in each case, results are shown with the vane at a neutral position to help separate vane deflection effects from sideslip effects. Results at a nominal 1 degree angle-of-attack are shown in figures 119 through 123, 2.5 degrees angle-of-attack in figures 124 through 126, and 6.0 degrees angle-of-attack in figures 127 through 132.

Generally, these figures illustrate that the higher the angle-of-attack, the less sideslip required for the wake to enter the inlet and affect the distortion patterns. Data recorded during tests at 6 degrees angle of attack are also used to illustrate additional data analysis techniques besides the digital time histories of quasi steady-state measured and computed parameters.

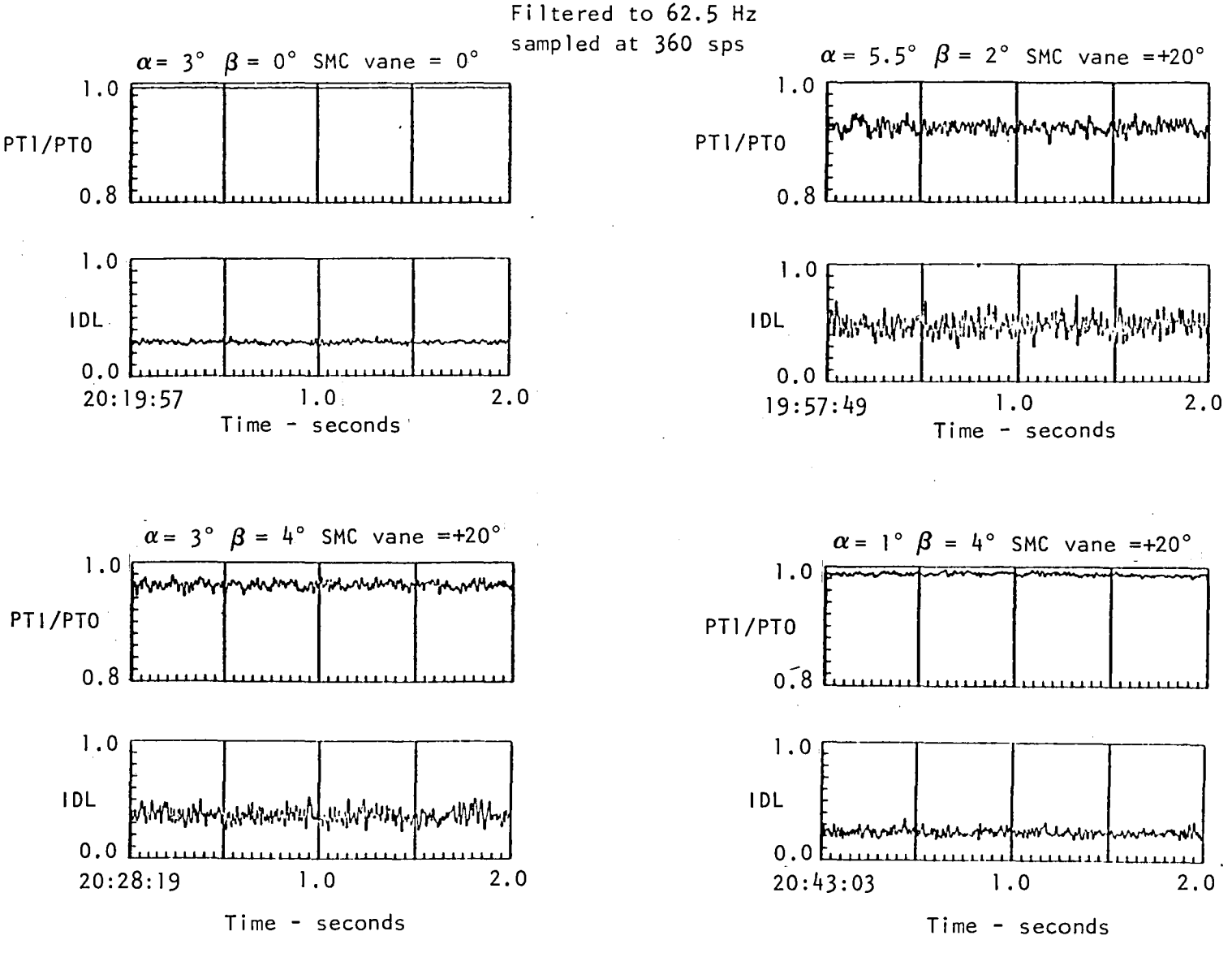

Figure 115. - Time histories of total-pressure recovery and stall-margin index, Mach 0.85, with SMCS vane deflected 0 and 20 degrees, no. 2 inlet, RB = 7 degrees, RC = 5 degrees, flight 2-33.

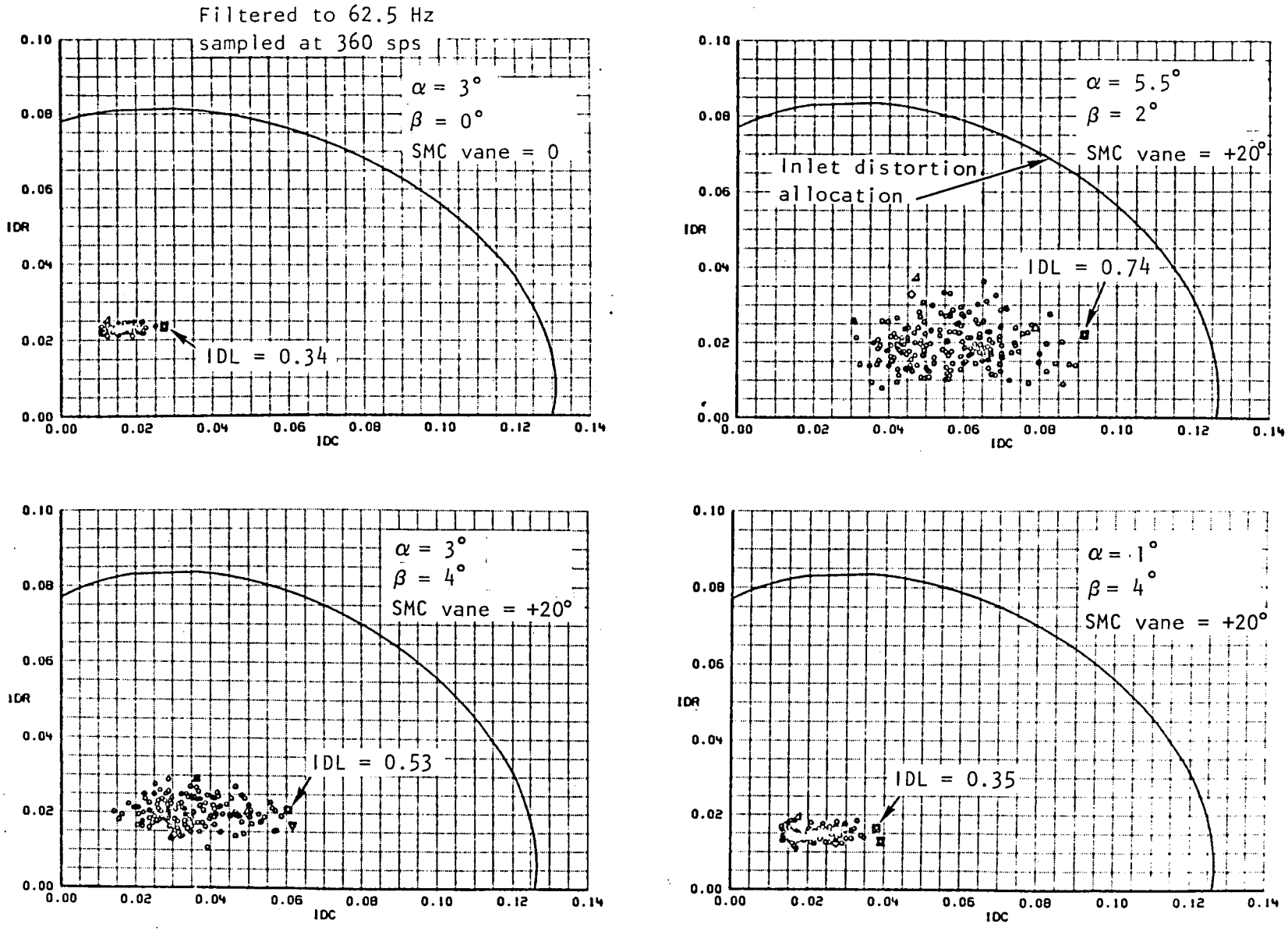

Figure 116. - Dynamic circumferential and radial distortion components, Mach 0.85, with SMCS vane deflected 0 and 20 degrees, no. 2 inlet, RB = 7 degrees, flight 2-33.

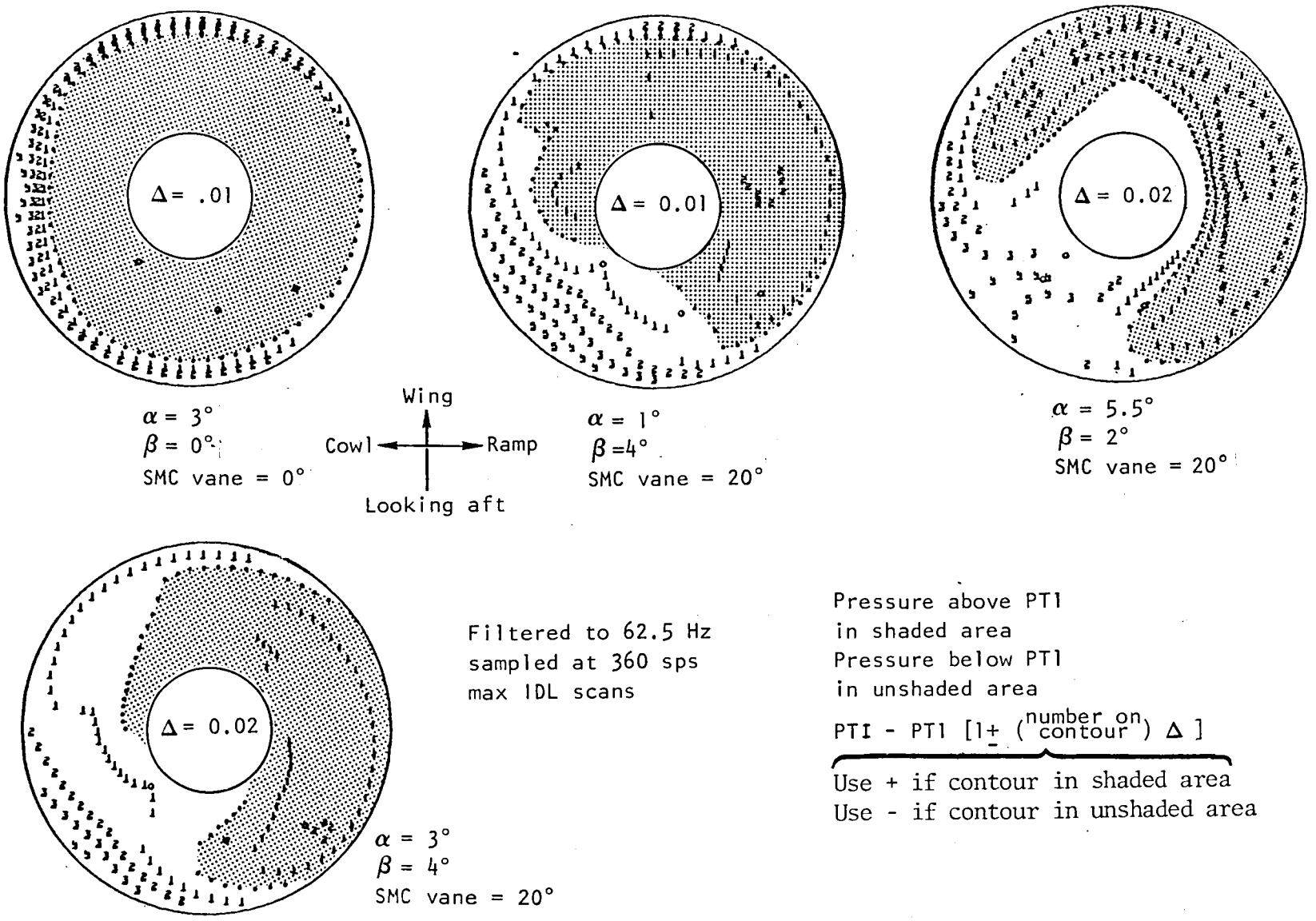

Figure 117. - Dynamic total pressure contours during Mach 0.85 operation with SMCS vane deflected deflected 0 and 20 degrees, no. 2 inlet, RB = 7 degrees, RC = 5 degrees, flight 2-33.

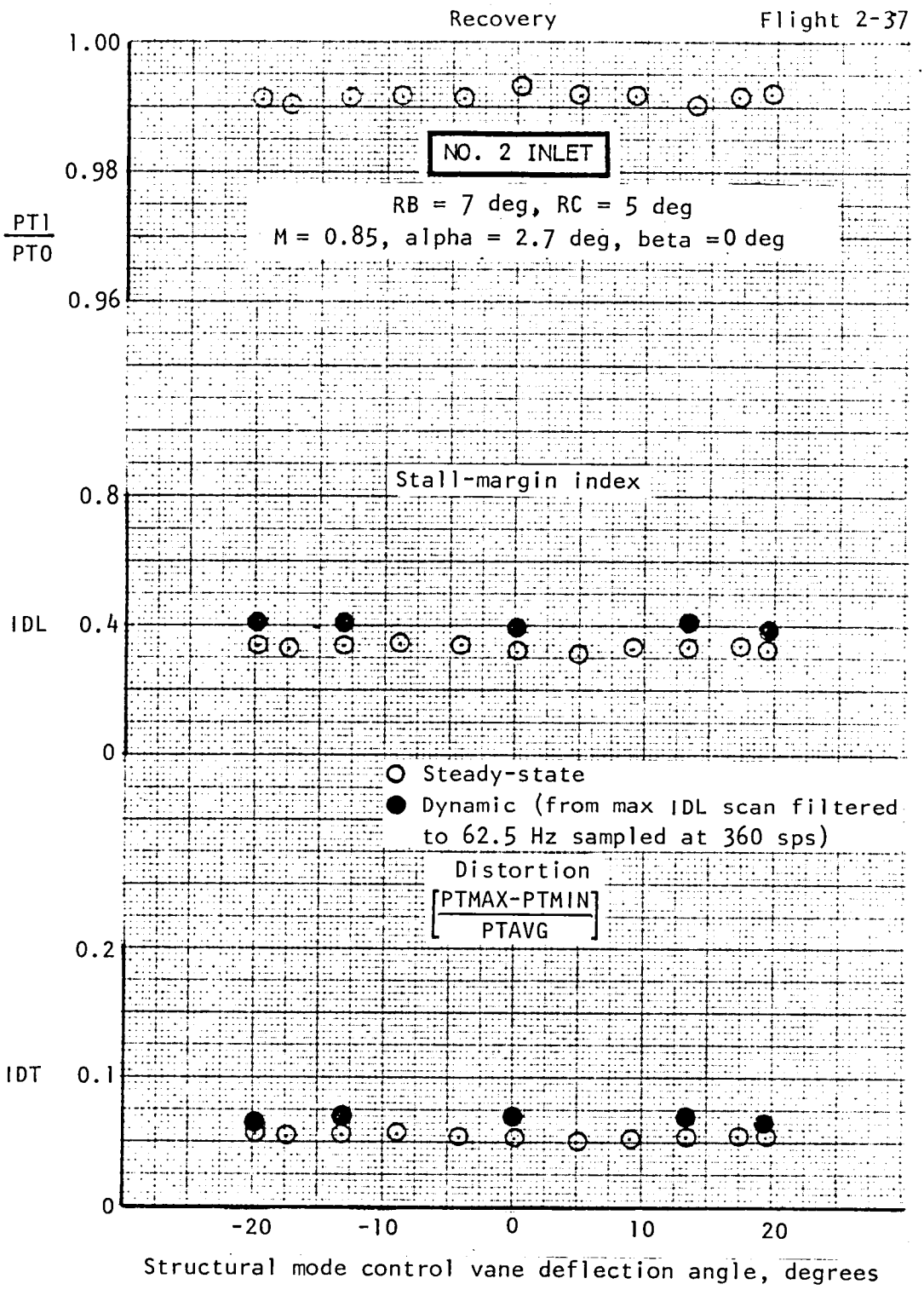

Figure 118. - Effects of SMC vane position on no. 2 inlet steady-state and dynamic characteristics, Mach = 0.85 and alpha = 2.7 degrees, flight 2-37.

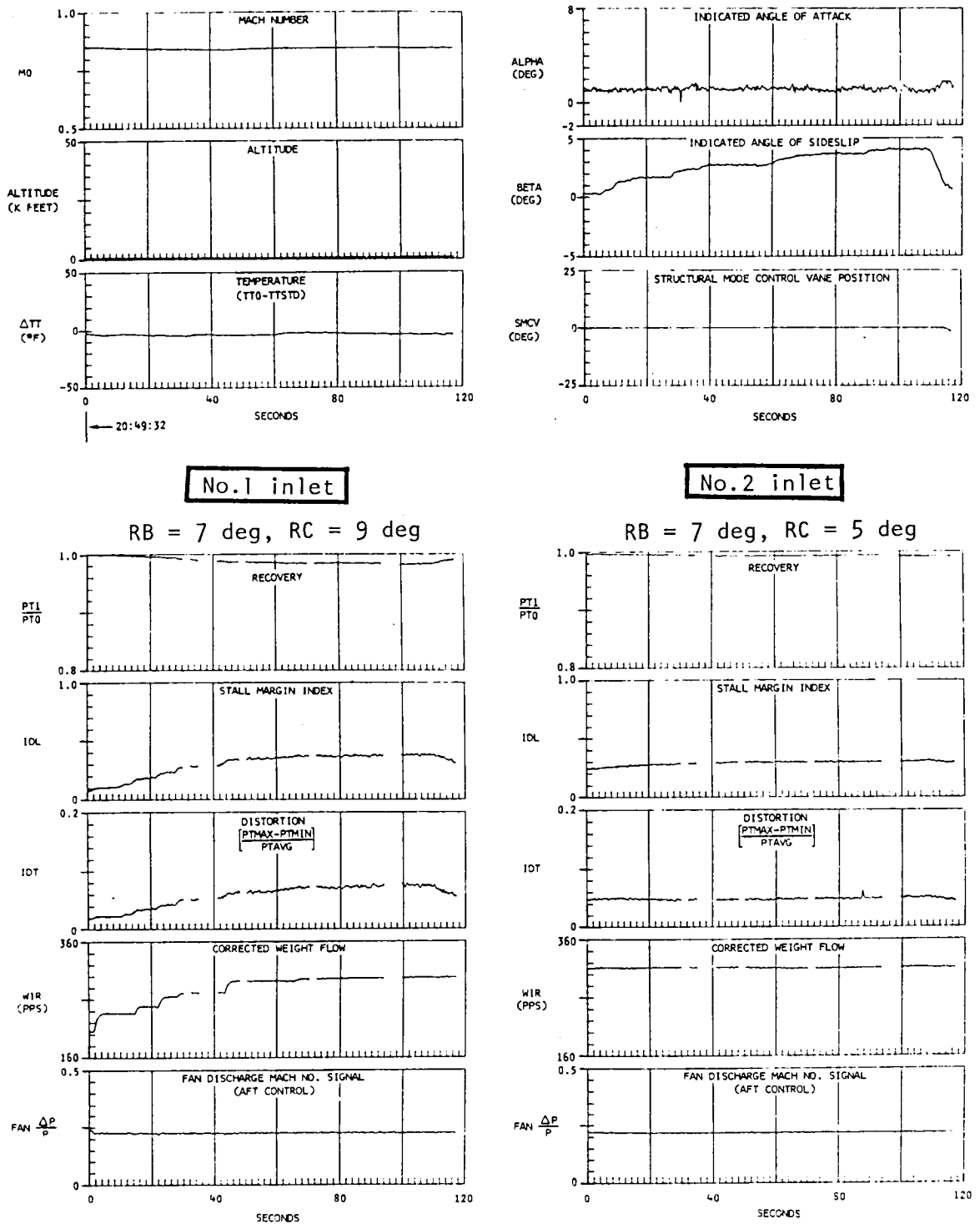

Figure 119. - Effects of sideslip angle on steady-state inlet characteristics with SMCV = 0 degrees and alpha = 1 degree, flight 2-37.

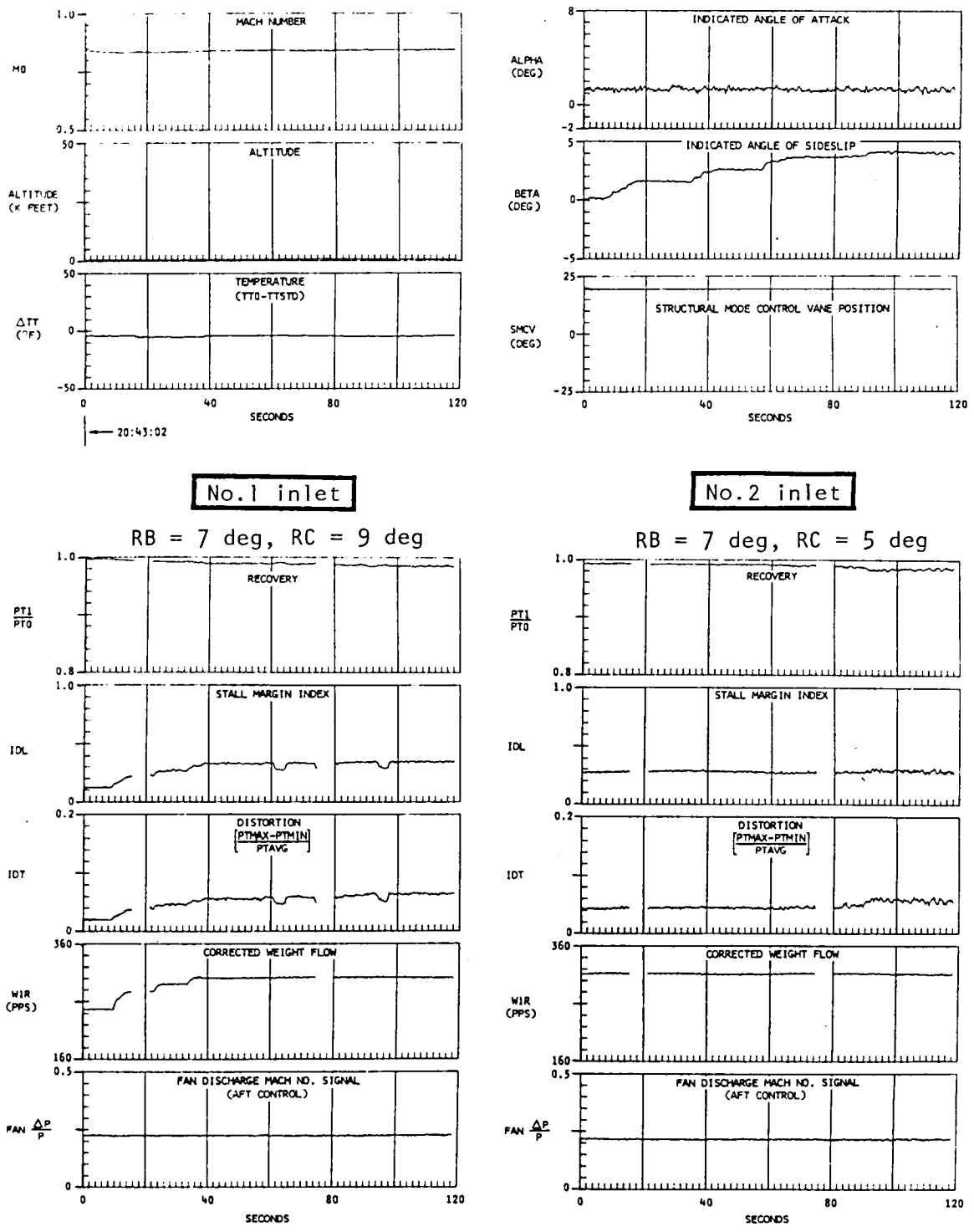

Figure 120. - Effects of sideslip angle on steady-state inlet characteristics with SMCV = 20 degrees and alpha = 1 degree, flight = 2-37.

Pressure above PTI
in shaded area
Pressure below PTI
in unshaded area

PTI - PTI [1± (number on contour) Δ]

Use + if contour in shaded area
Use - if contour in unshaded area

No. 2 inlet

M = 0.84, RB = 7 deg, RC = 5 deg
SMCV = 20 deg

Wing
Cowl ← → Ramp
Looking aft

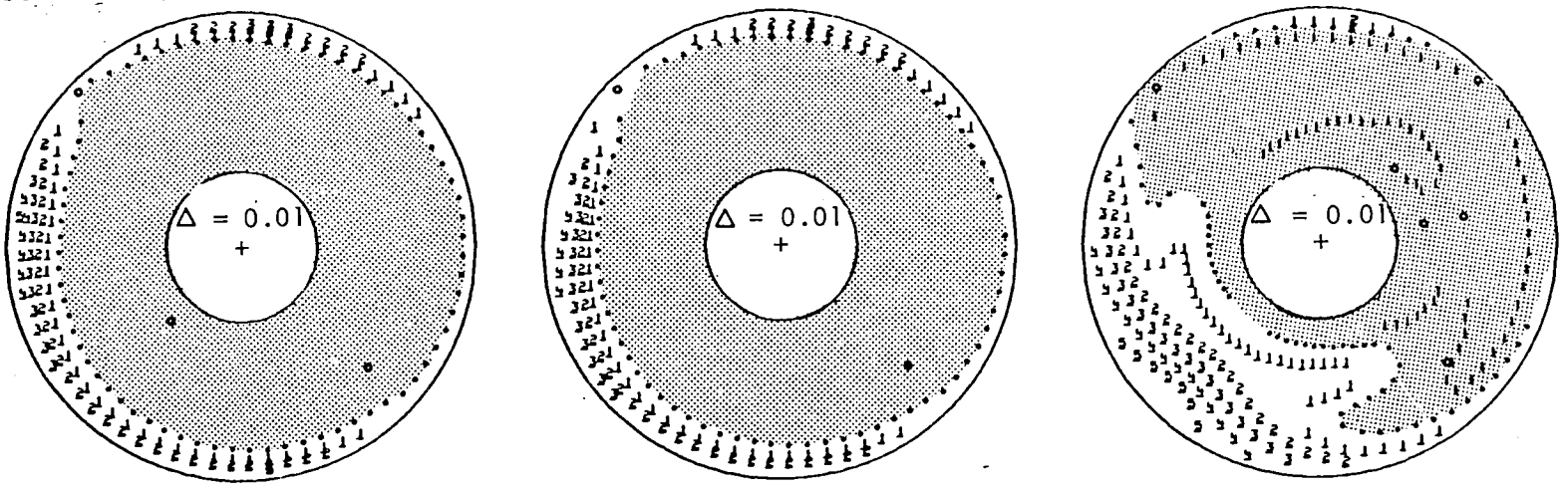

Beta = 0 deg.	Beta = 1.6 deg	Beta = 4.0 deg
Alpha = 1.4 deg	Alpha = 1.3 deg	Alpha = 1.4 deg
WIR = 312 pps	WIR = 313 pps	WIR = 311 pps
IDL = 0.296	IDL = 0.304	IDL = 0.420
IDT = 0.056	IDT = 0.055	IDT = 0.076

Dynamic total-pressure contours
(max IDL scans, filtered to 62.5 Hz, sampled at 360 sps)

Figure 121. - Effects of SMCV wake on no. 2 inlet dynamic total-pressure contours during sideslip, SMCV = 20 degrees and alpha = 1.4 degrees, flight 2-37.

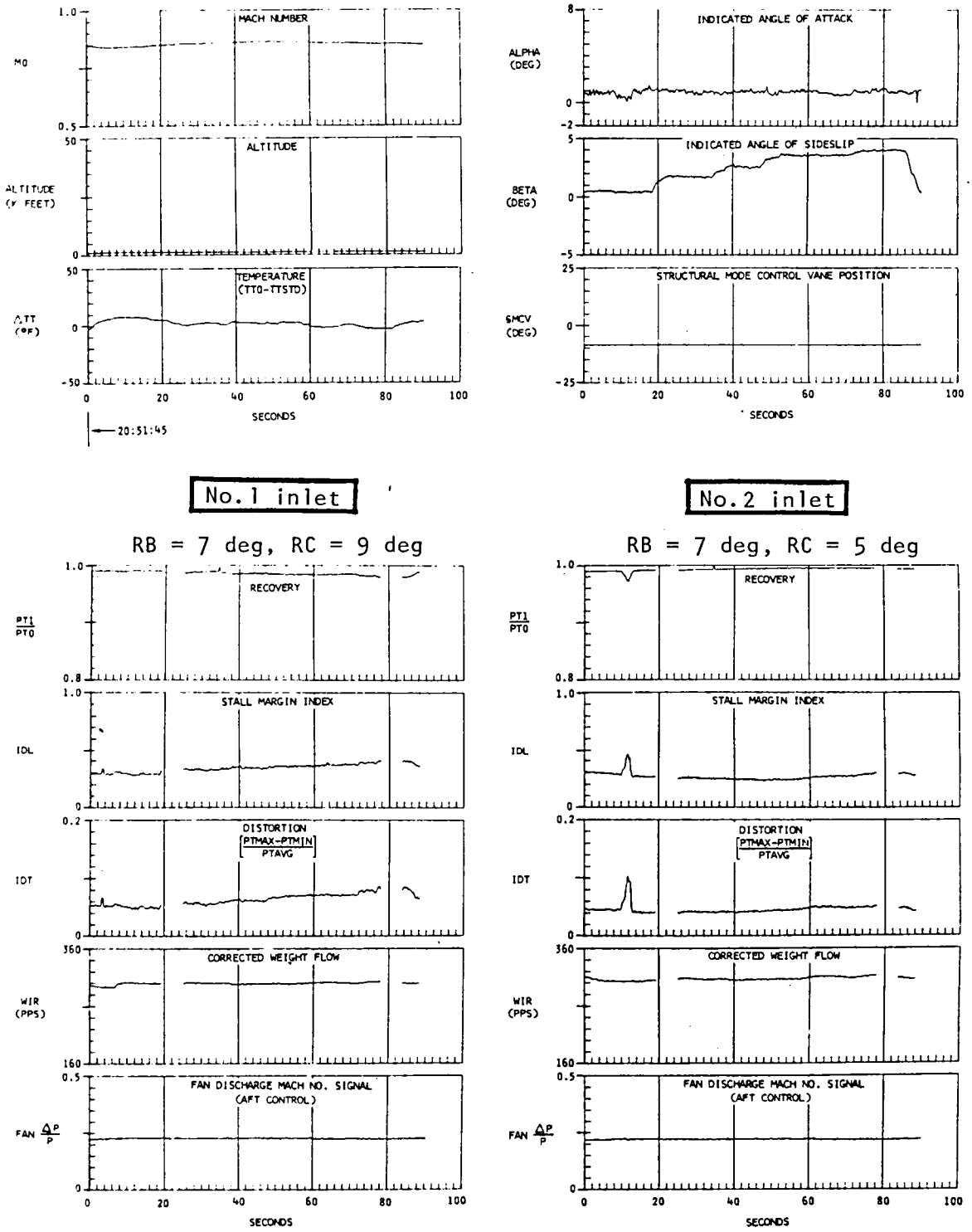

Figure 122. - Effects of sideslip angle on steady-state inlet characteristics with SMCV = -8 degrees and alpha = 1 degree, flight 2-37.

Pressure above PTI
in shaded area
Pressure below PTI
in unshaded area

$PTI - PTI\ [1 \pm (\text{number on contour})\ \Delta\ ]$

Use + if contour in shaded area
Use - if contour in unshaded area

No. 2 inlet

M= 0.85, RB = 7 deg, RC = 5 deg
SMCV = -8 deg

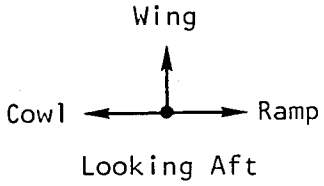

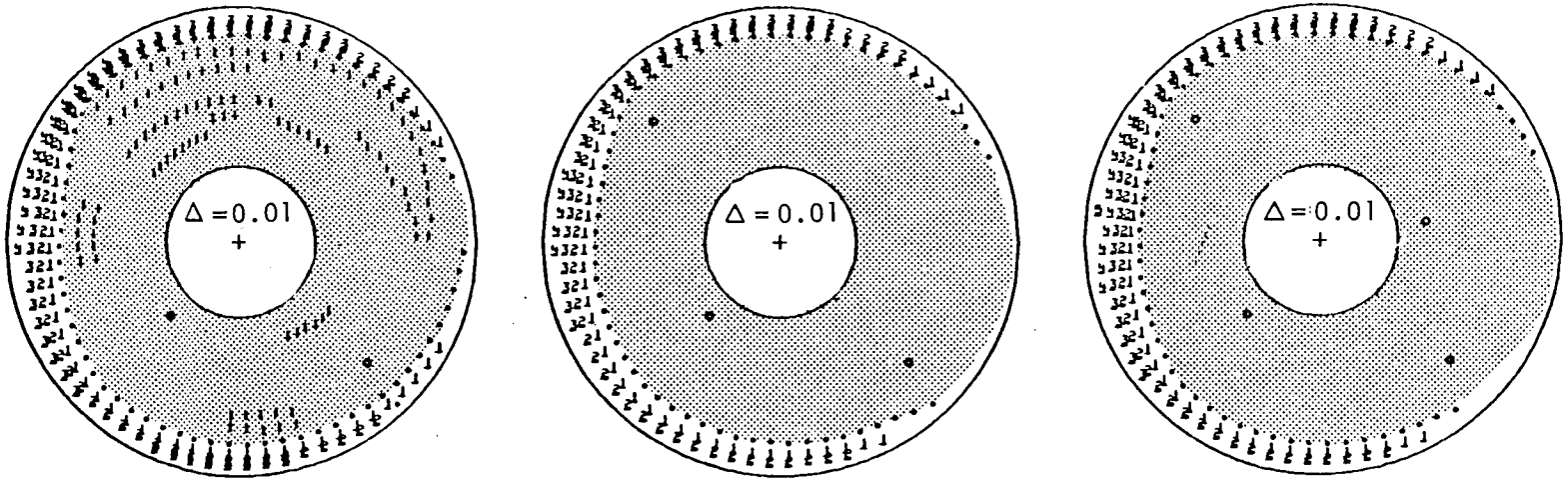

Beta = 0 deg	Beta = 2.6 deg	Beta = 4.0 deg
Alpha = 0.8 deg	Alpha = 1.0 deg	Alpha = 1.0 deg
WIR = 307 pps	WIR = 305 pps	WIR = 312 pps
IDL = 0.351	IDL = 0.291	IDL = 0.338
IDT = 0.055	IDT = 0.054	IDT = 0.059

Dynamic total-pressure contours
(max IDL scans, filtered to 62.5 Hz, sampled at 360 sps)

Figure 123. - Effects of SMCV wake on no. 2 inlet dynamic total-pressure contours during sideslip, SMCV = -8 degrees and alpha = 0.9 degrees, flight 2-37.

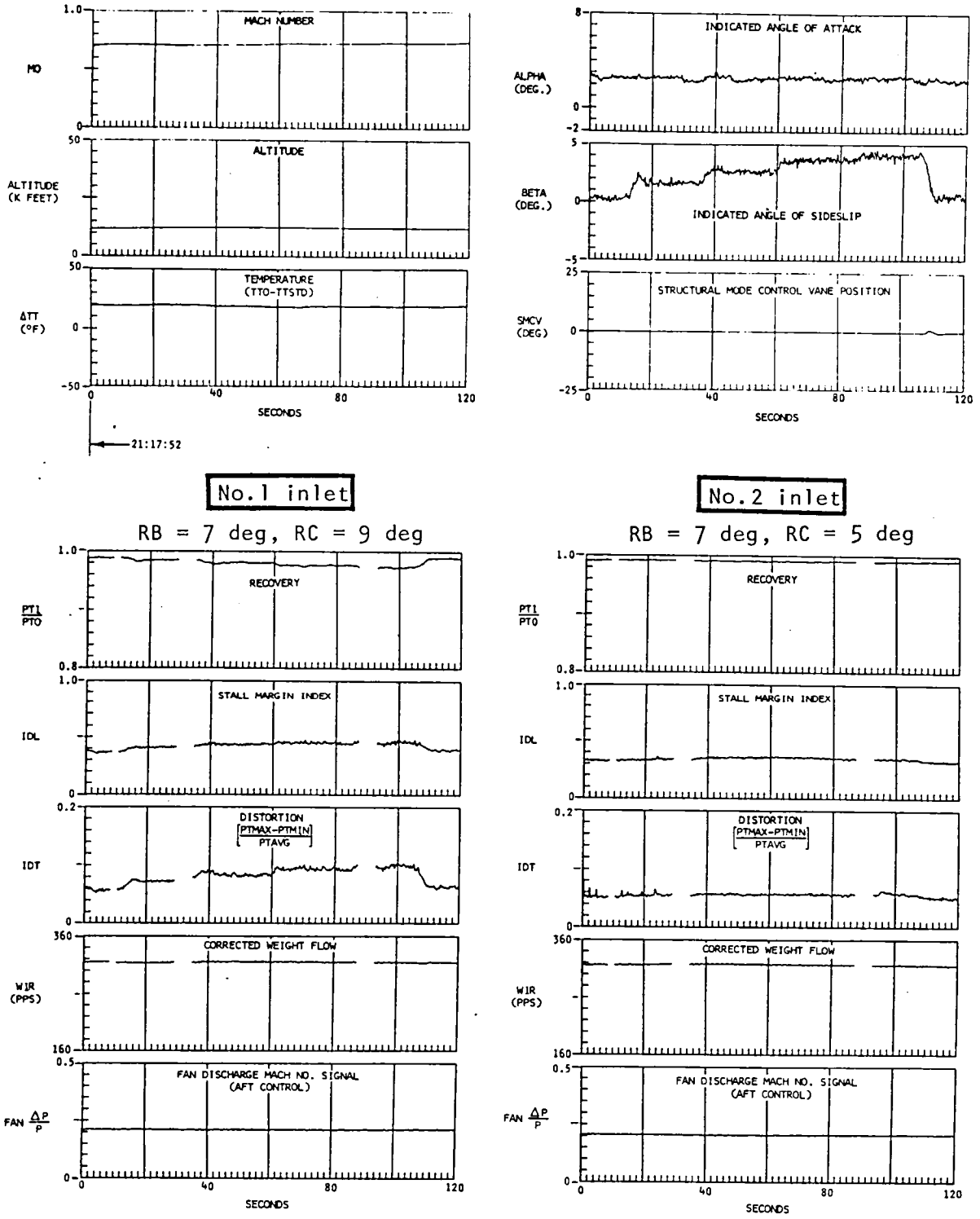

Figure 124. -Effects of sideslip angle on steady-state inlet characteristics with SMCV = 0 degrees and alpha = 2.6 degrees, flight 2-37.

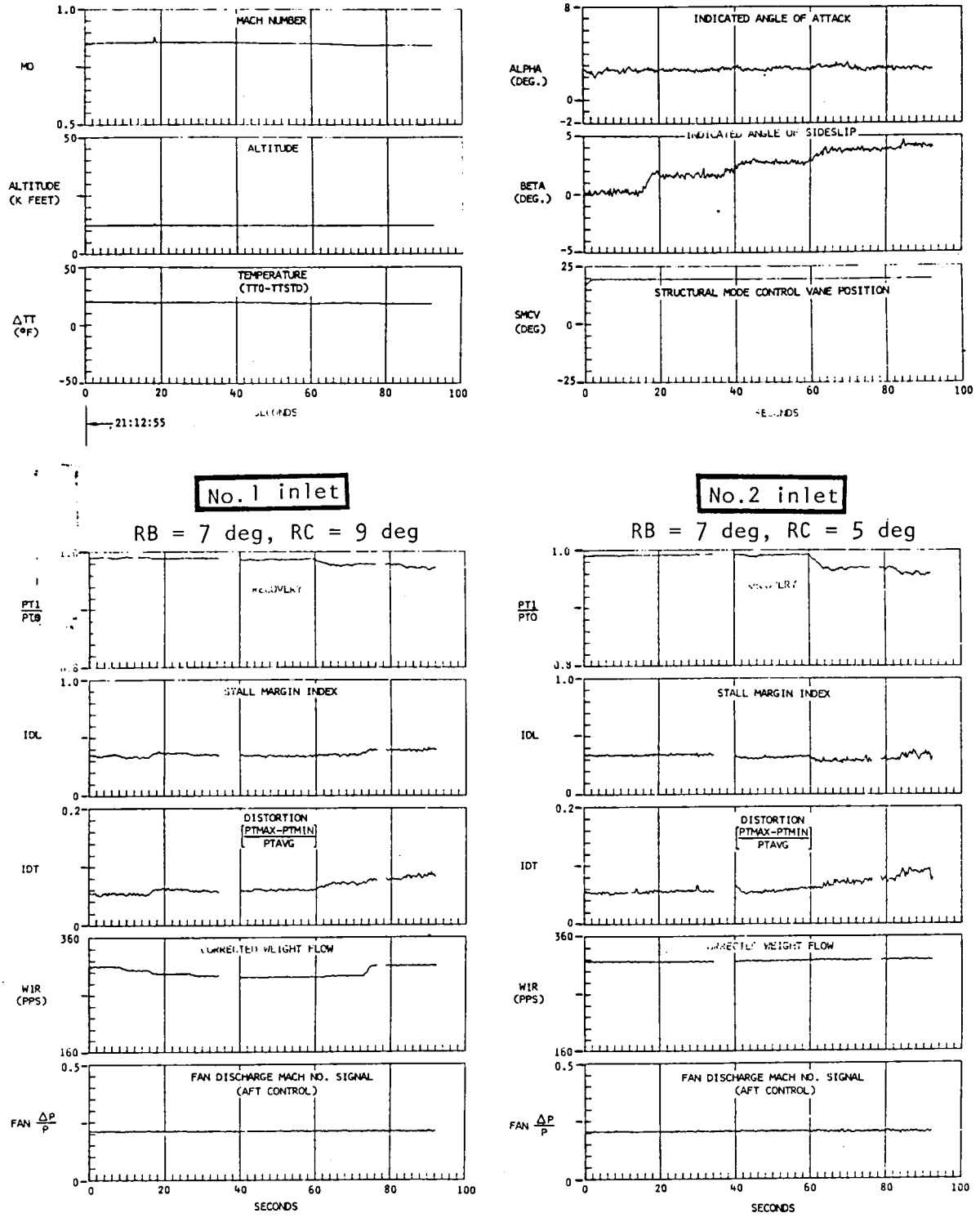

Figure 125. - Effects of sideslip angle on steady-state inlet characteristics with SMCV = 20 degrees and alpha = 2.6 degrees, flight 2-37.

Pressure above PTI
in shaded area
Pressure below PTI
in unshaded area

$PT_I - PT_I [1 \pm (\overset{\text{number on}}{\text{contour}}) \Delta]$

Use + if contour in shaded area
Use - if contour in unshaded area

No. 2 inlet

M = 0.85, RB = 7 deg, RC = 5 deg
SMCV = 20 deg

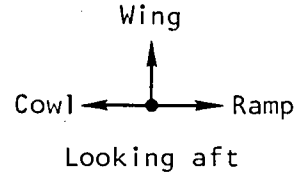

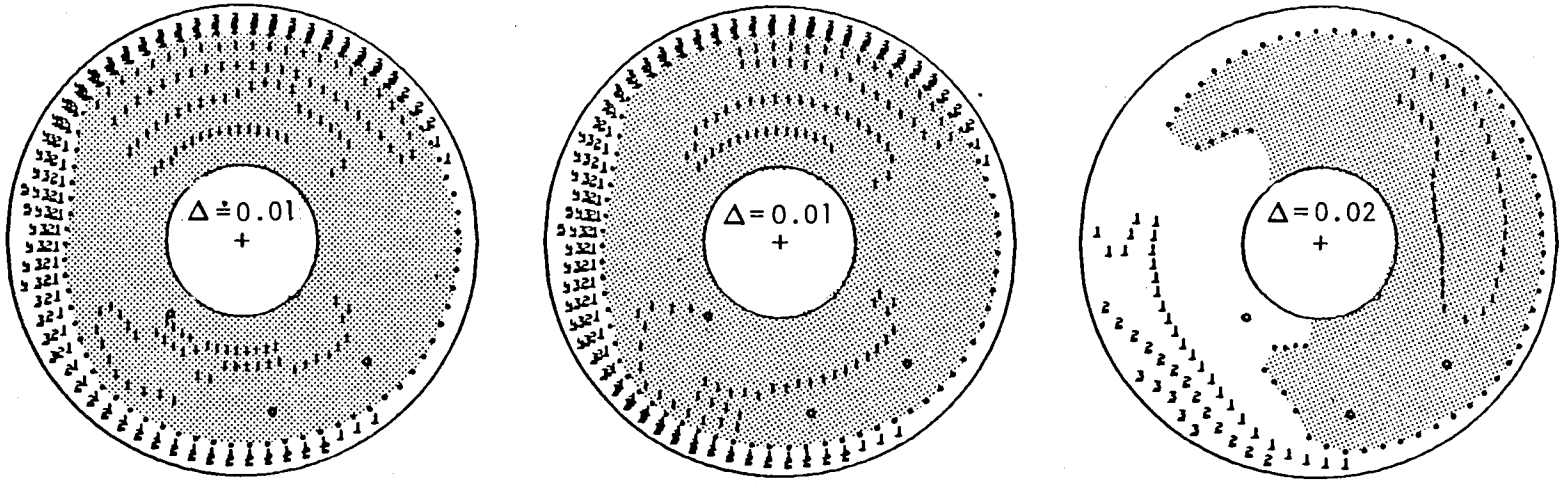

Beta = 0 deg	Beta = 1.7 deg	Beta = 3.8 deg
Alpha = 2.6 deg	Alpha = 2.6 deg	Alpha = 2.7 deg
WIR = 317 deg	WIR = 317 pps	WIR = 318 pps
IDL = 0.391	IDL = 0.397	IDL = 0.449
IDT = 0.064	IDT = 0.064	IDT = 0.104

Dynamic total-pressure contours
(max IDL scans, filtered to 62.5 Hz, sampled at 360 sps)

Figure 126. - Effects of SMCV wake on no. 2 inlet dynamic total-pressure contours during sideslip, SMCV = 20 degrees and alpha = 2.6 degrees, flight 2-37.

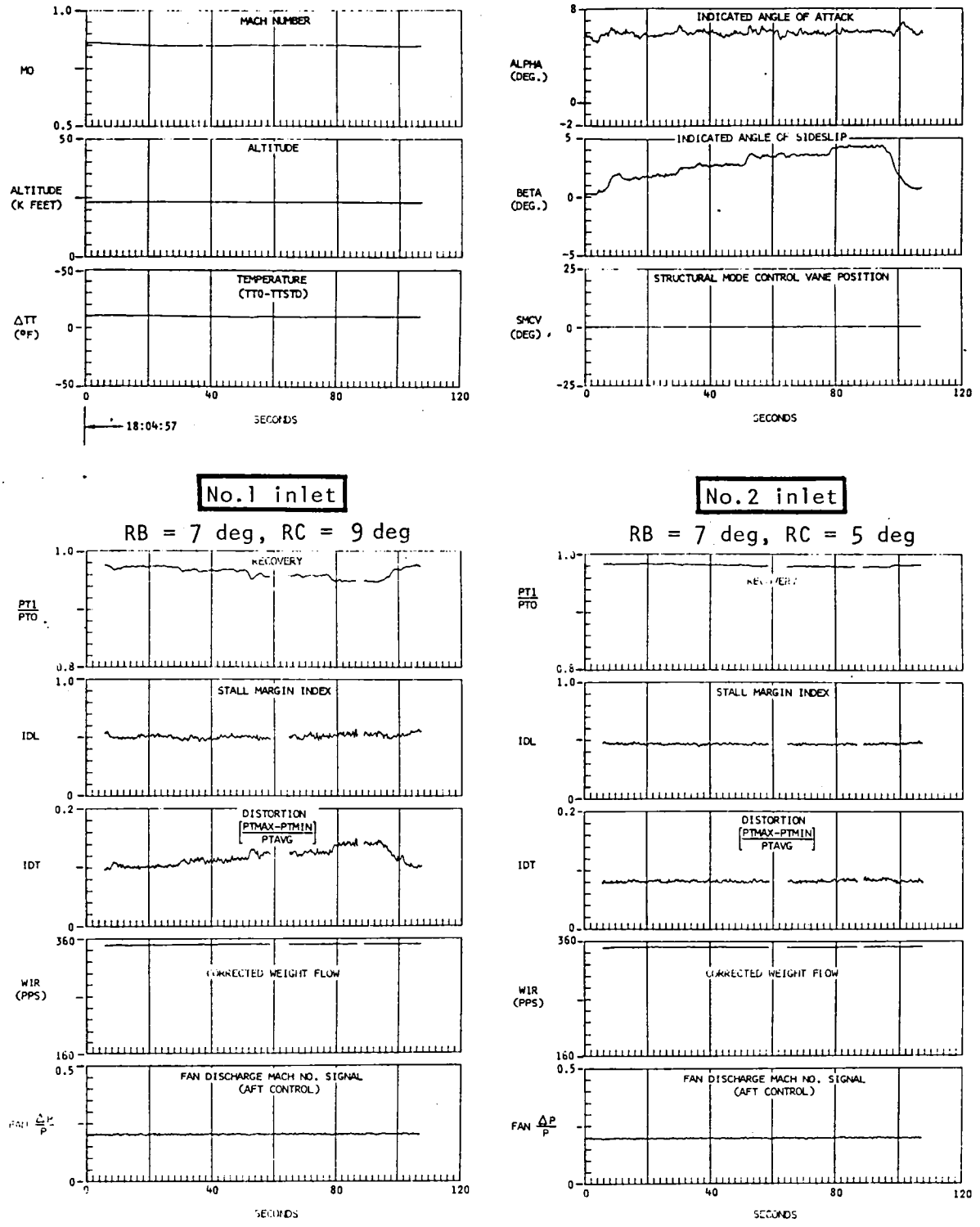

Figure 127. - Effects of sideslip angle on steady-state inlet characteristics with SMCV = 0 degrees and alpha = 5.8 degrees, flight 2-37.

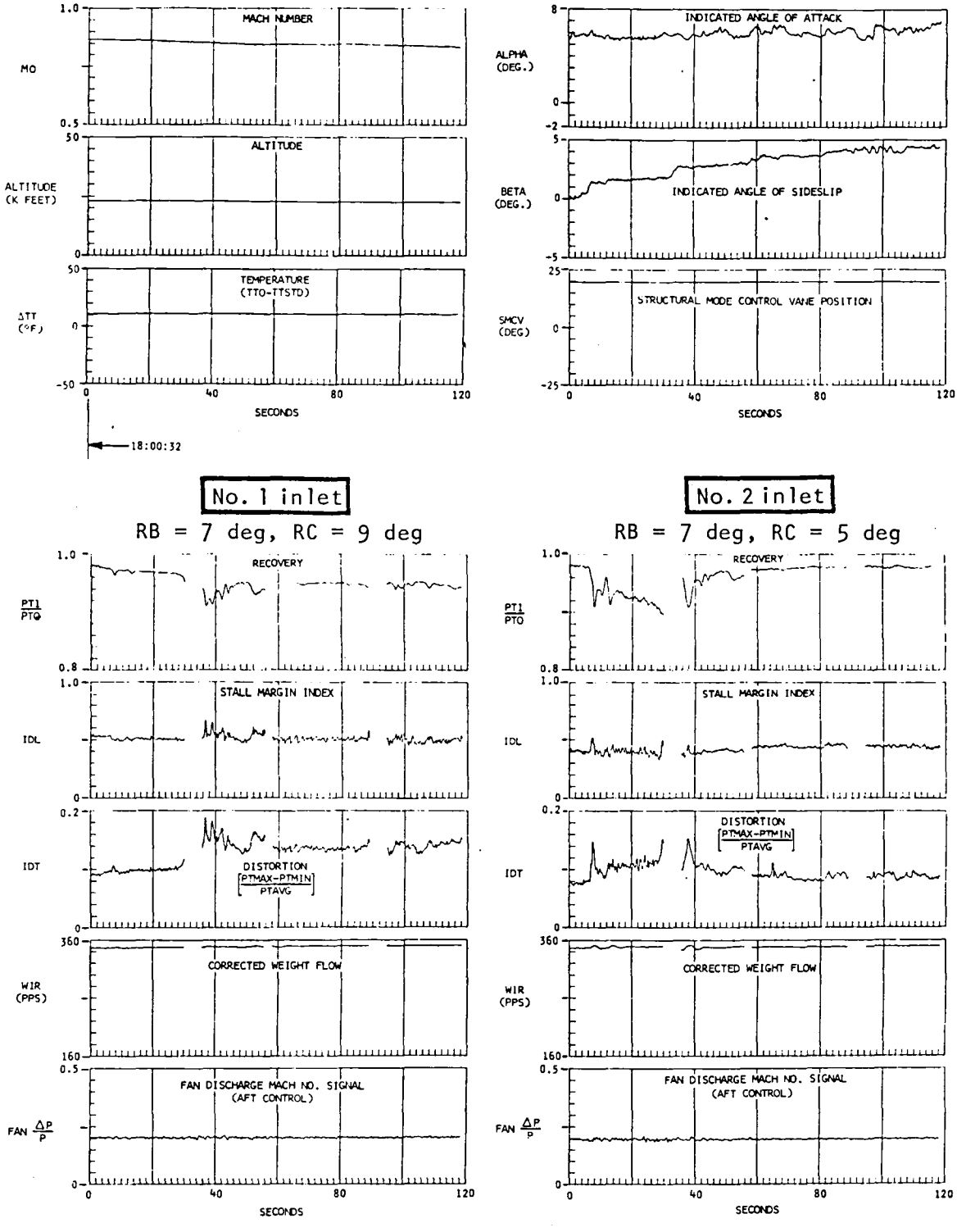

Figure 128. - Effects of sideslip angle on steady-state inlet characteristics with SMCV = 20 degrees and alpha = 5.8 degrees, flight 2-37.

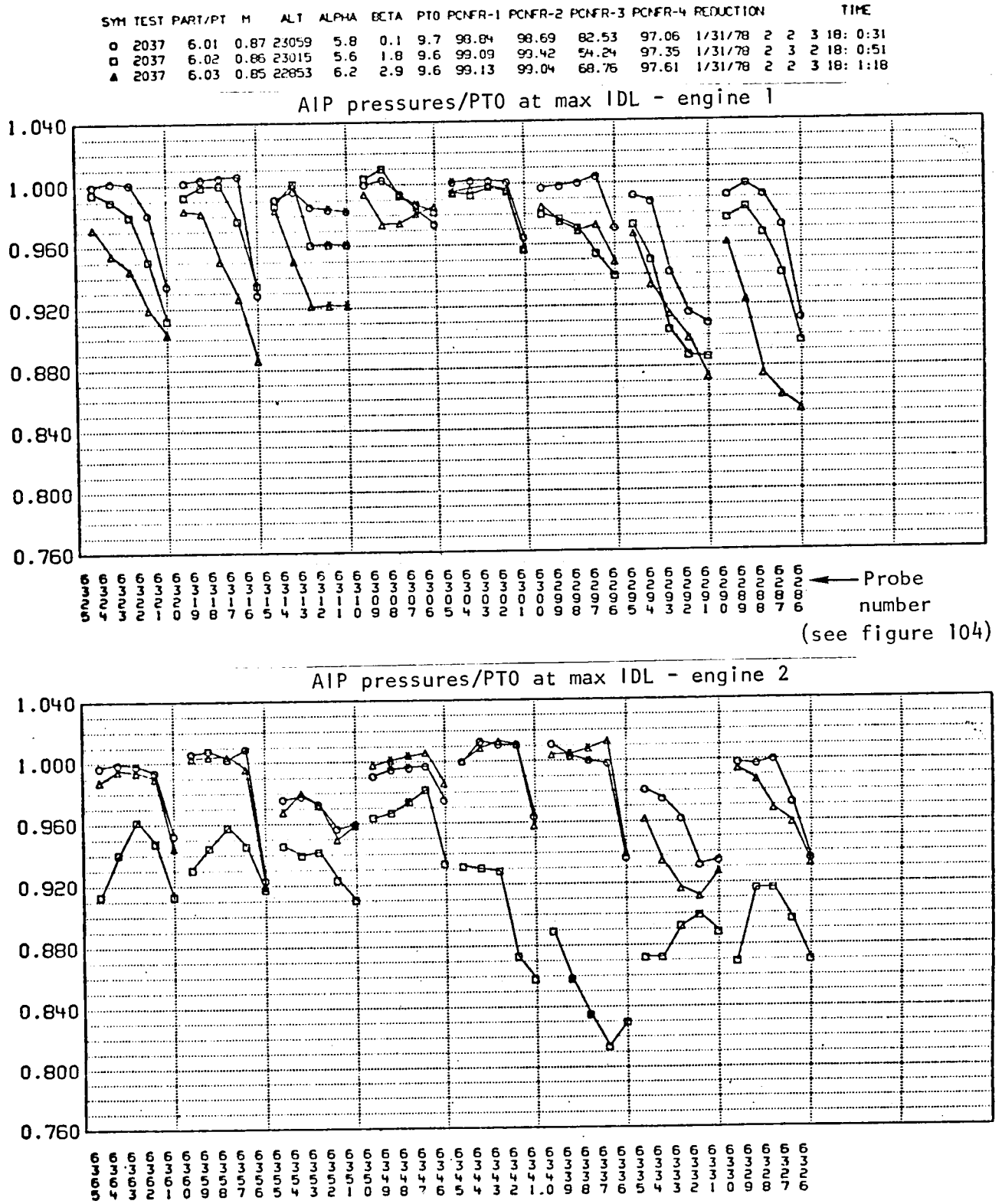

Figure 129. - Individual AIP probes, total-pressure recovery array, SMCS vane deflected 20 degrees, Mach 0.85, α = 6 degrees, flight 2-37.

Filtered to 62.5 Hz
sampled at 360 sps

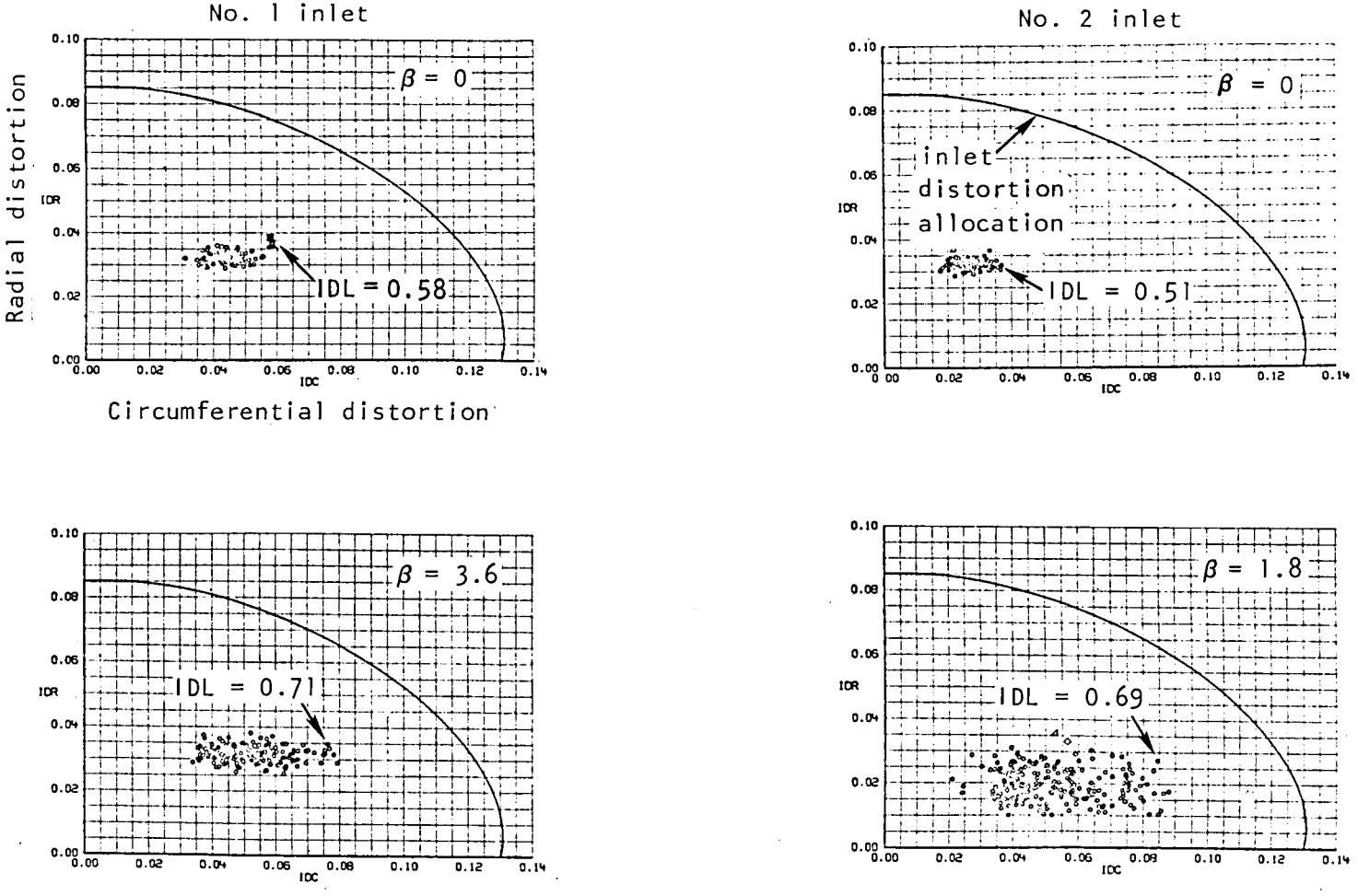

Figure 130. - Variations in circumferential and radial distortion components during sideslip operation with the SMCS vane deflected+20 degrees, Mach 0.85, α = 6 degrees, flight 2-37.

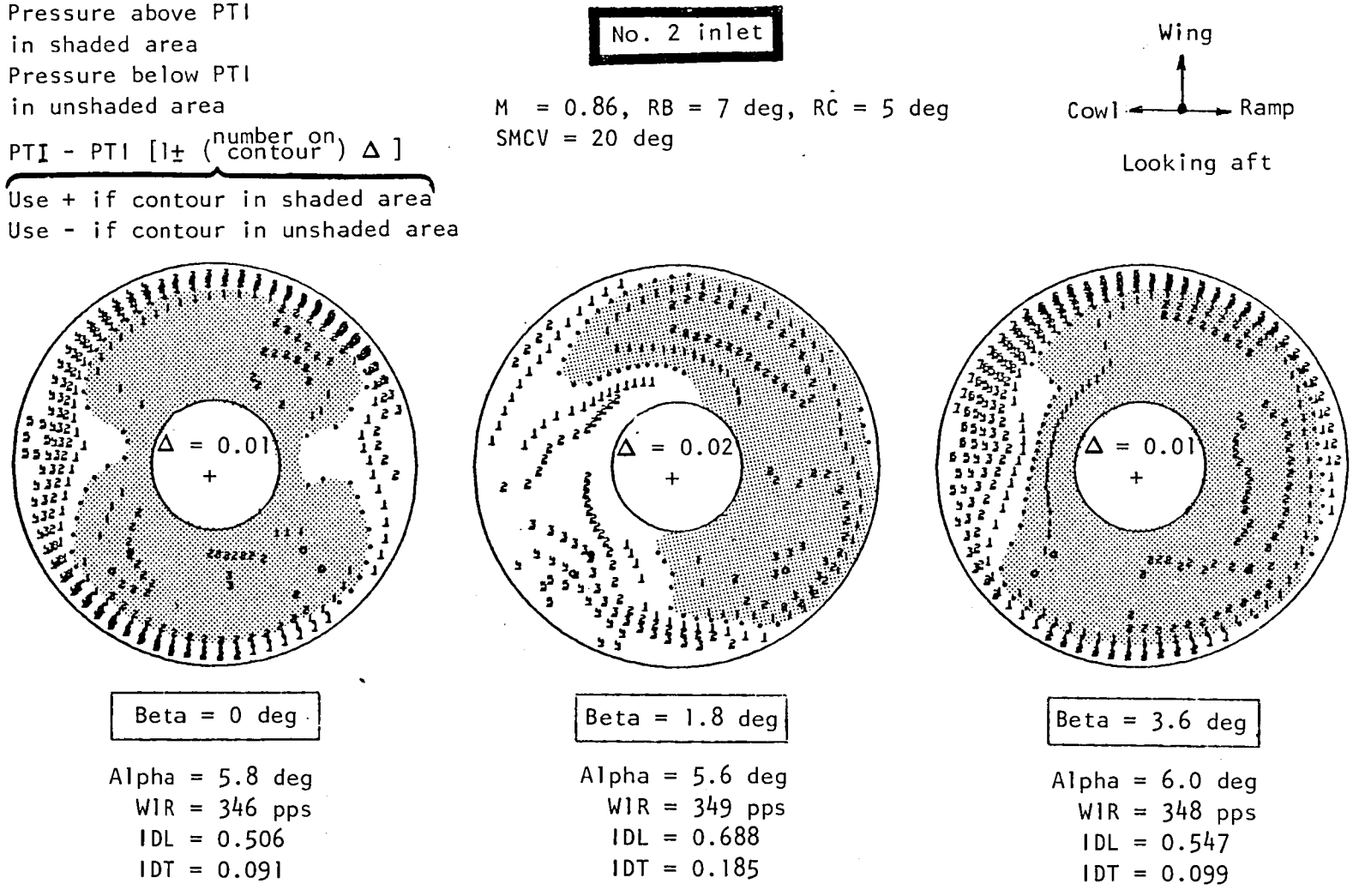

Figure 131. - Effects of SMCV wake on no. 2 inlet dynamic total-pressure contours during sideslip, SMCV = 20 degrees and alpha = 5.8 degrees, flight 2-37.

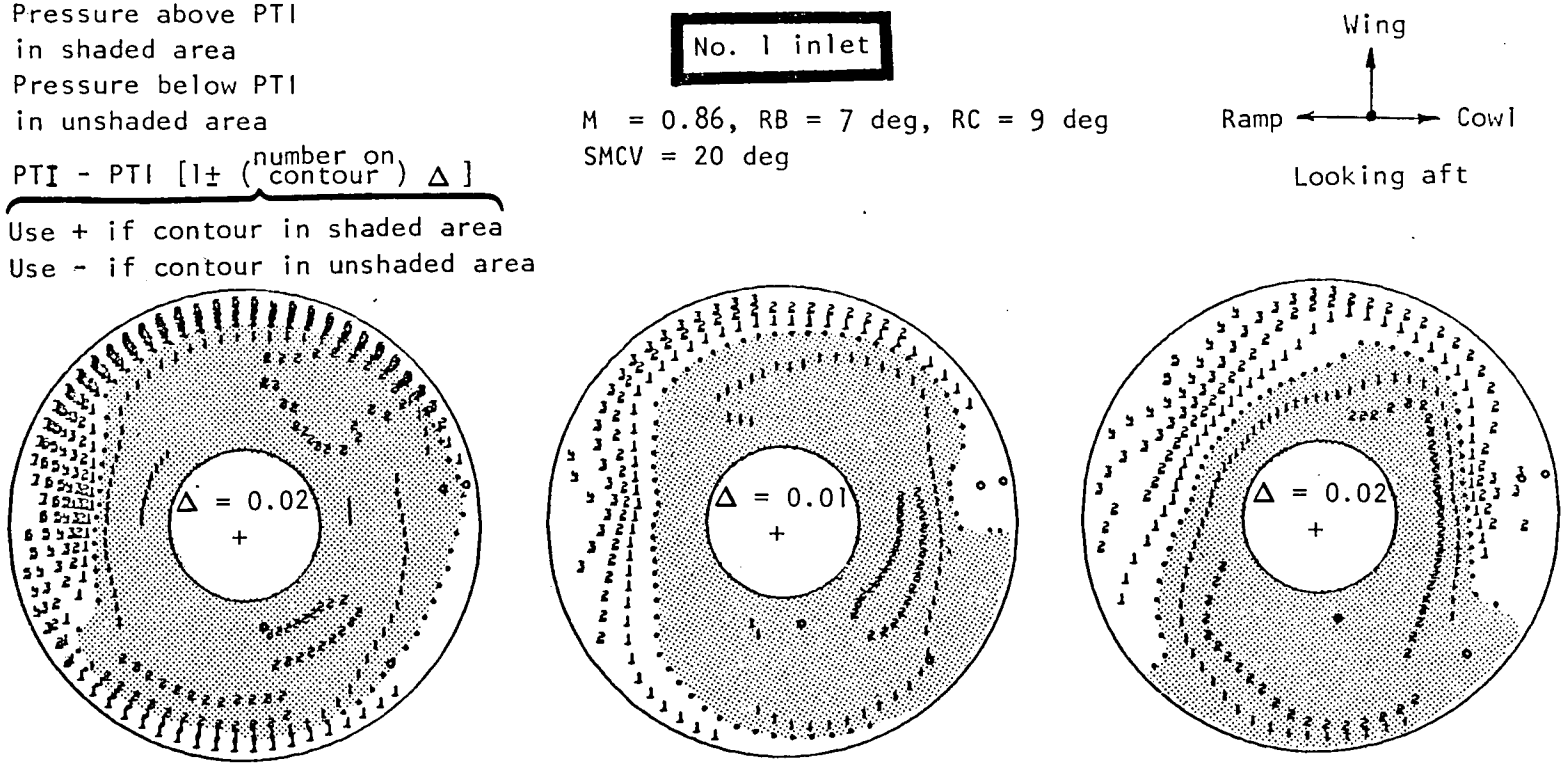

Dynamic total-pressure contours
(max IDL scans, filtered to 62.5 Hz, sampled at 360 sps)

Figure 132. - Effects of SMCV wake on no. 1 inlet dynamic total-pressure contours during sideslip, SMCV = 20 degrees and alpha = 5.8 degrees, flight 2-37.

For example, local recoveries on a probe-by-probe basis are illustrated in figure 129. Probes within a particular rake are connected by straight lines and are arranged in order from hub to tip. This particular plot uses sideslip as the independent parameter. SMCS vane wake ingestion is evident in the inboard inlet at 2 degrees of sideslip and is becoming evident in the outboard inlet as sideslip is increased to 3 degrees. Distortion characteristics resulting from scans that produced the maximum value of stall-margin index are illustrated in figure 130. Combinations of circumferential and radial distortion components computed at 360 samples per second are shown for selected aircraft attitudes with the SMCS vanes deflected 20 degrees. Maximum values of stall-margin index are identified and compared against inlet design goals (IDL = 1.0). Corresponding total-pressure contours are illustrated in figures 131 and 132.

Maneuvers with the SMCS vane deflected 20 degrees (figure 133) illustrate the sensitivity of vortex ingestion to angle of attack. At zero sideslip, vortex ingestion is evident in the no. 2 inlet between angles of attack of 7 and 8 degrees, consistent with the maneuver envelopes presented earlier. (See figure 112.) Similar angle-of-attack excursions with the vanes held in a neutral position are shown in figures 134 through 136 for comparison.

Steady-state inlet characteristics during sideslip maneuvers with the SMCS vanes deflected 13 degrees are shown in figure 137. Total-pressure recovery decreases approximately 5 percent when sideslip angle increases from 1.7 to 4.0 degrees. Recovery losses are accompanied by significant increases in distortion levels. Total-pressure contours representing maximum dynamic values of stall-margin index as a function of sideslip angle are shown in figure 138, and a well-developed, low-pressure region is evident in the hub. Stall-margin index increases from 0.5 to 0.75 as sideslip is increased from 1.7 to 4.0 degrees.

Engine Throttle Transients. Engine throttle transients were conducted at selected conditions to demonstrate engine stall-margin capability beyond that required by the inlet during SMCS vane wake ingestion. Initial tests were conducted during flight 2-19 and 2-33. Qualitative data and operating conditions are summarized in figures 111 and 112.

During flight 2-38, maximum rate throttle transients between IDLE and INTERMEDIATE power-lever settings were conducted on the no. 2 engine during sideslip maneuvers at different altitudes with the SMCS vanes deflected 20 and -8 degrees. Steady-state results at nominal angles of attack between 1 and 5 degrees with sideslip out to 4 degrees are shown in figures 139 through 141.

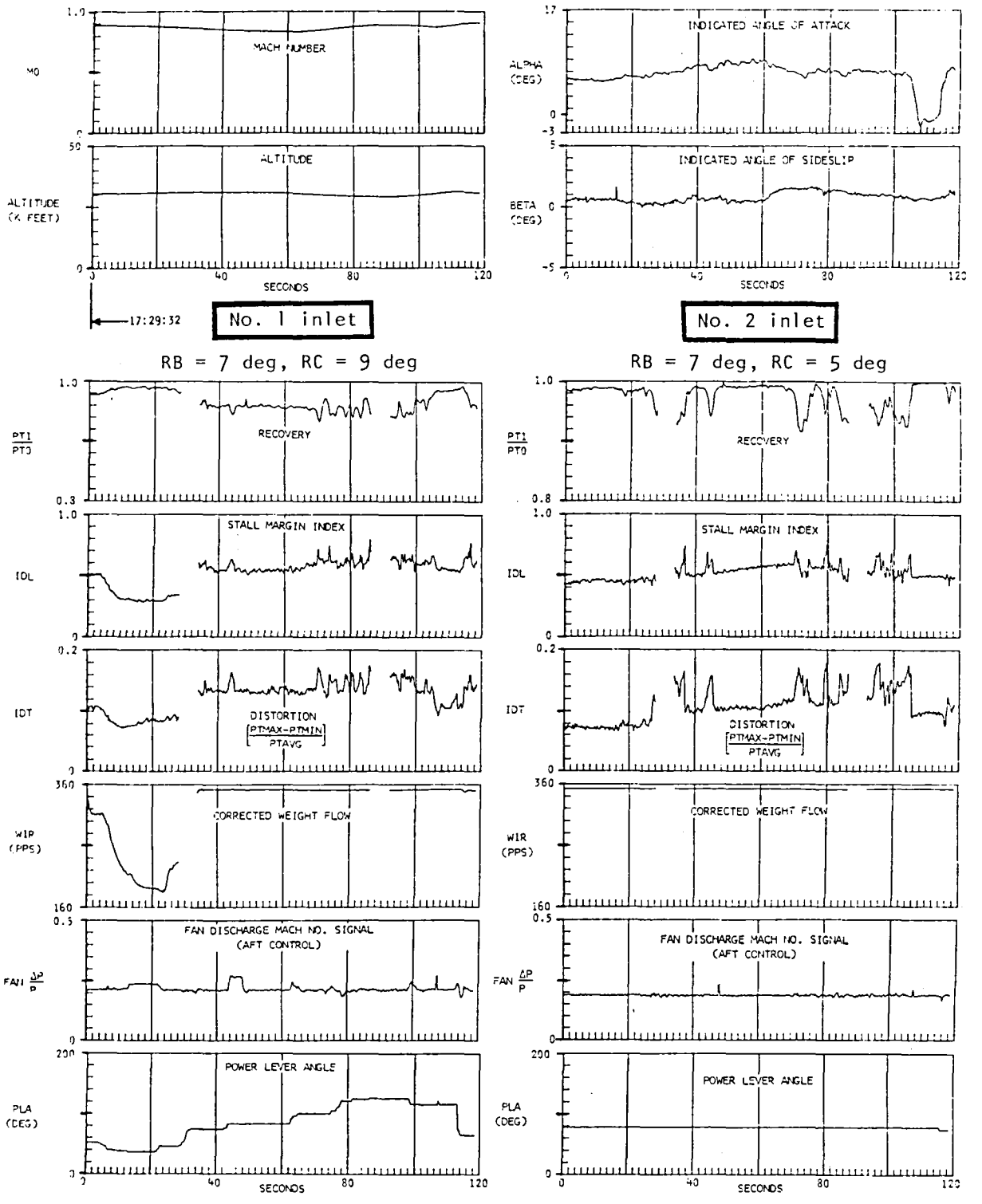

Figure 133. - Effects of angle-of-attack maneuvers on steady-state inlet characteristics with SMC vane at 20 degrees, flight 2-42.

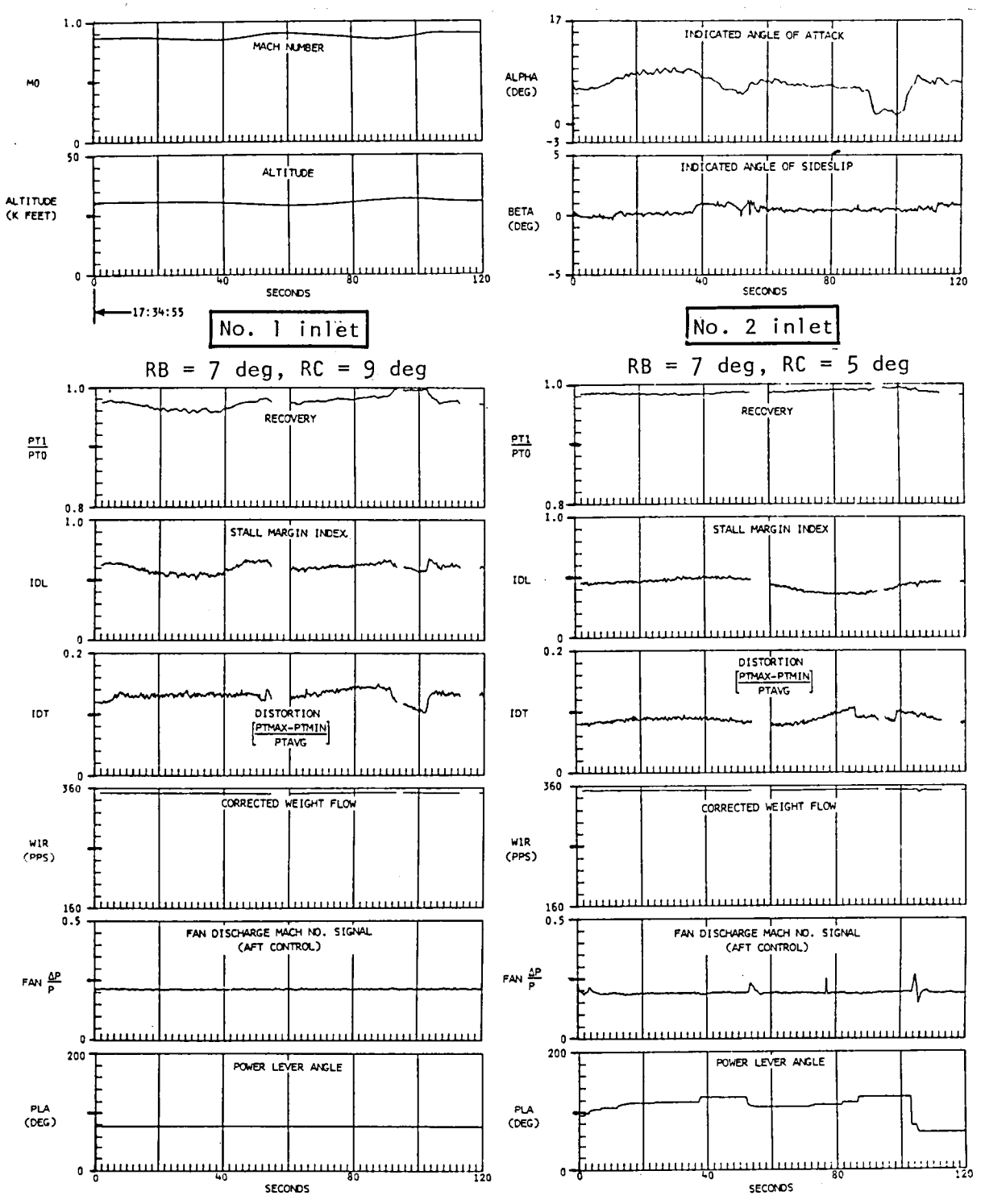

Figure 134. - Effects of an angle-of-attack maneuver on steady-state inlet characteristics with no. 1 engine at intermediate, flight 2-42, SMCS vane deflection angle = 0 degrees.

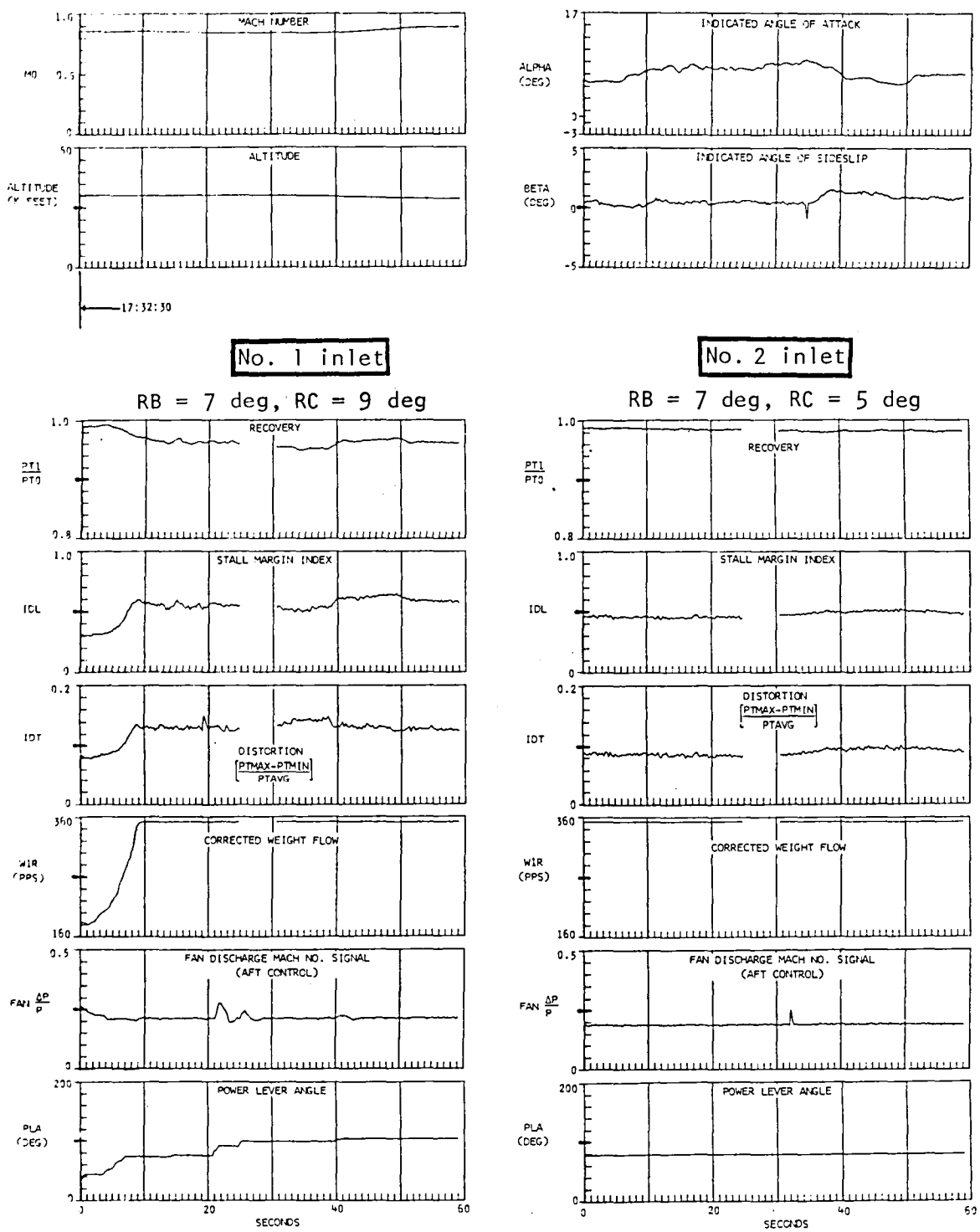

Figure 135. - Effects of an angle-of-attack maneuver on steady-state inlet characteristics with no. 2 engine at intermediate, flight 2-42, SMCS vane deflection angle = 0 degrees.

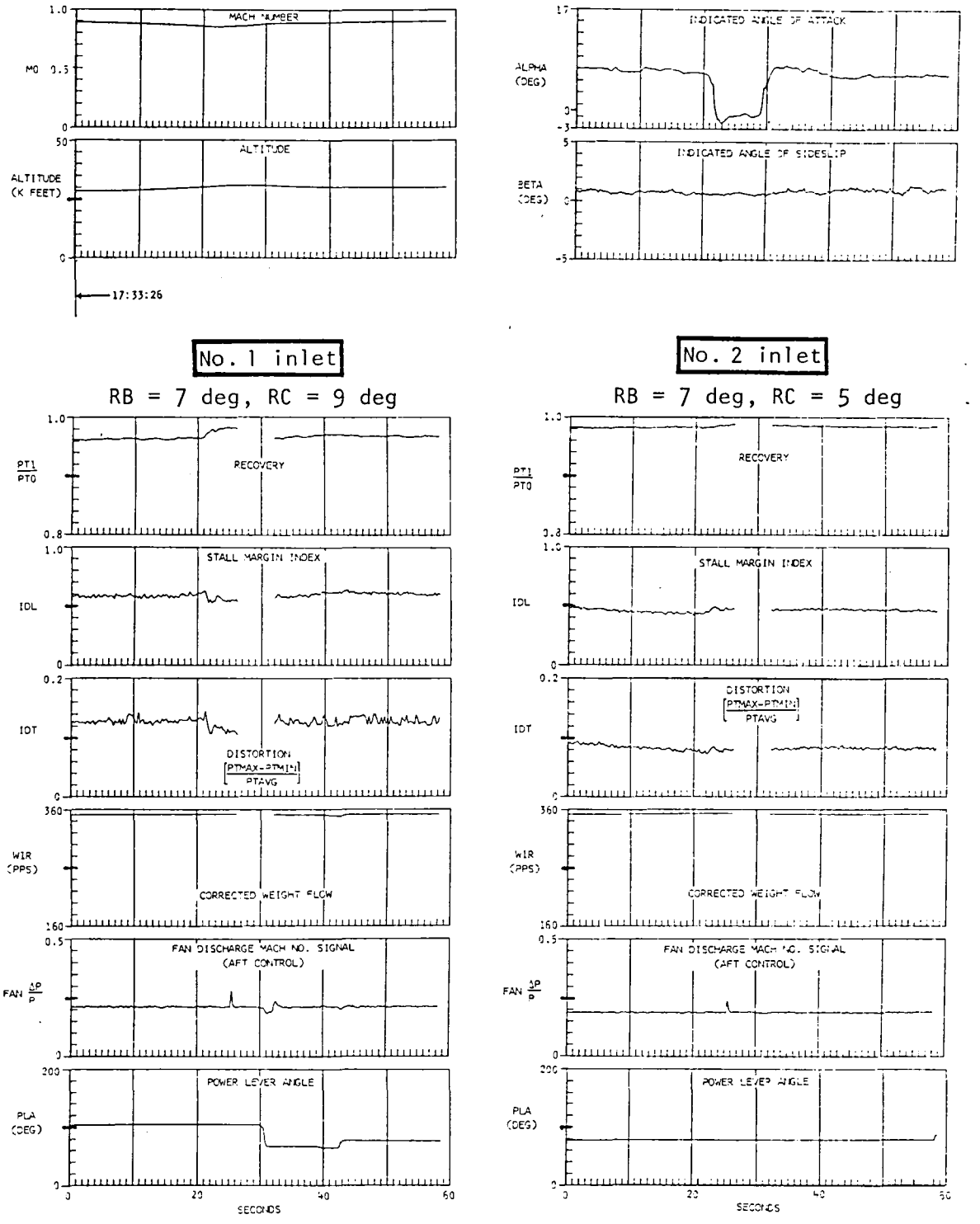

Figure 136. - Effects of an angle-of-attack maneuver on steady-state inlet characteristics with no. 2 engine at intermediate, flight 2-42, SMCS vane deflection angle = 0 degrees.

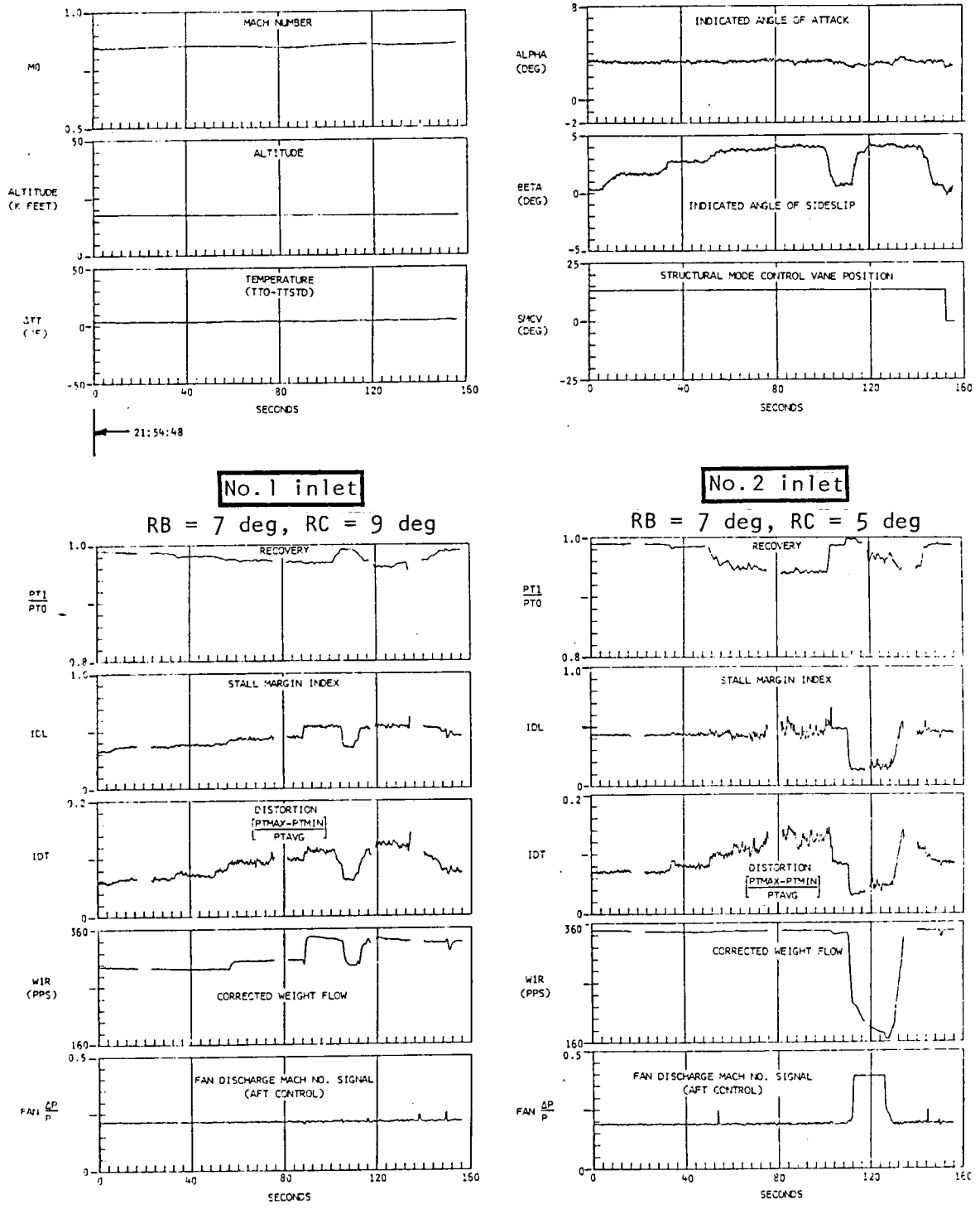

Figure 137. - Effects of sideslip angle on steady-state inlet characteristics with SMCV = 13 degrees and alpha = 3.3 degrees, flight 2-38.

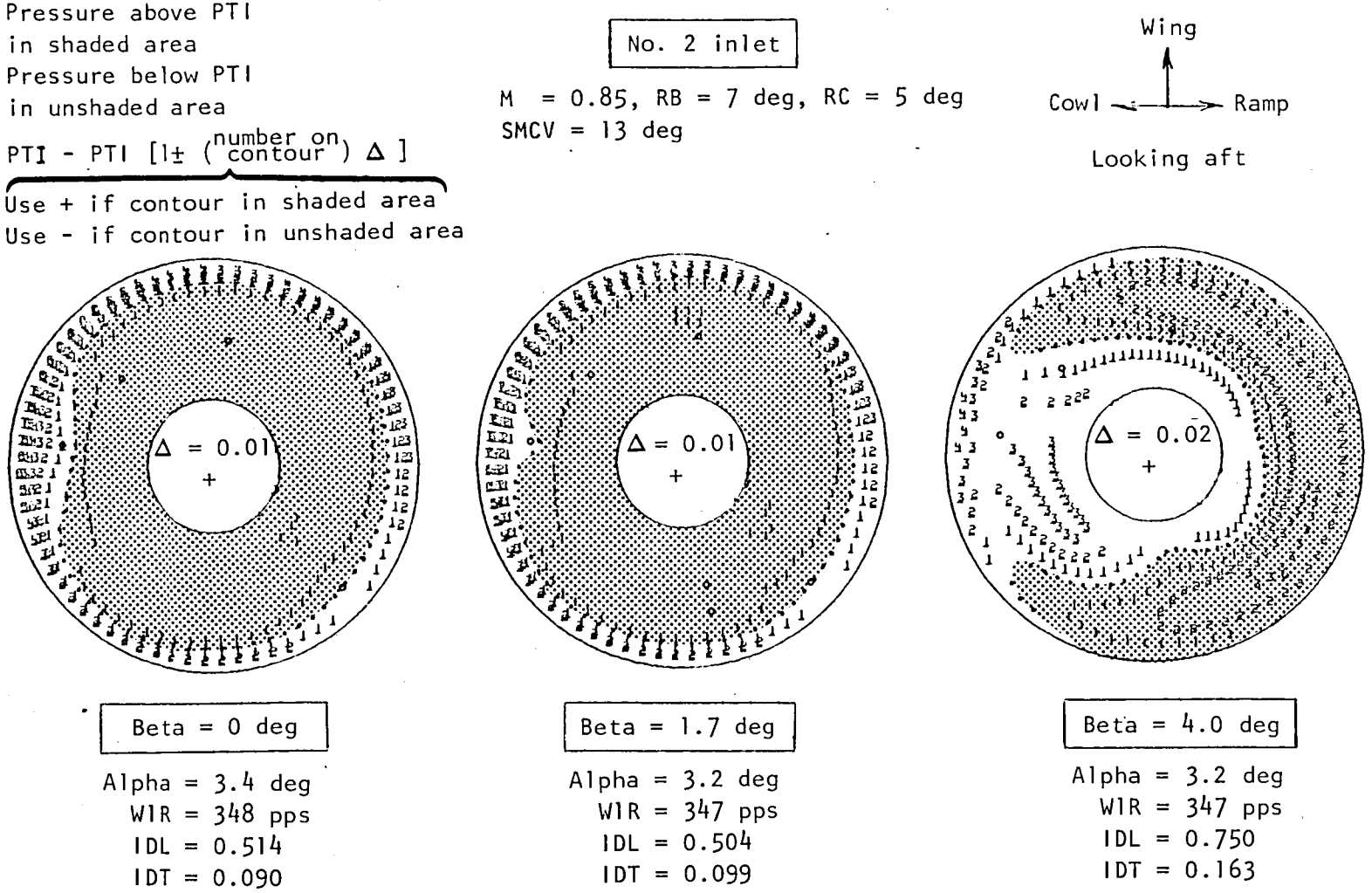

Figure 138. - Effects of SMCV wake on no. 2 inlet dynamic total-pressure contours during sideslip, SMCV = 13 degrees and alpha = 3.3 degrees, flight 2-38.

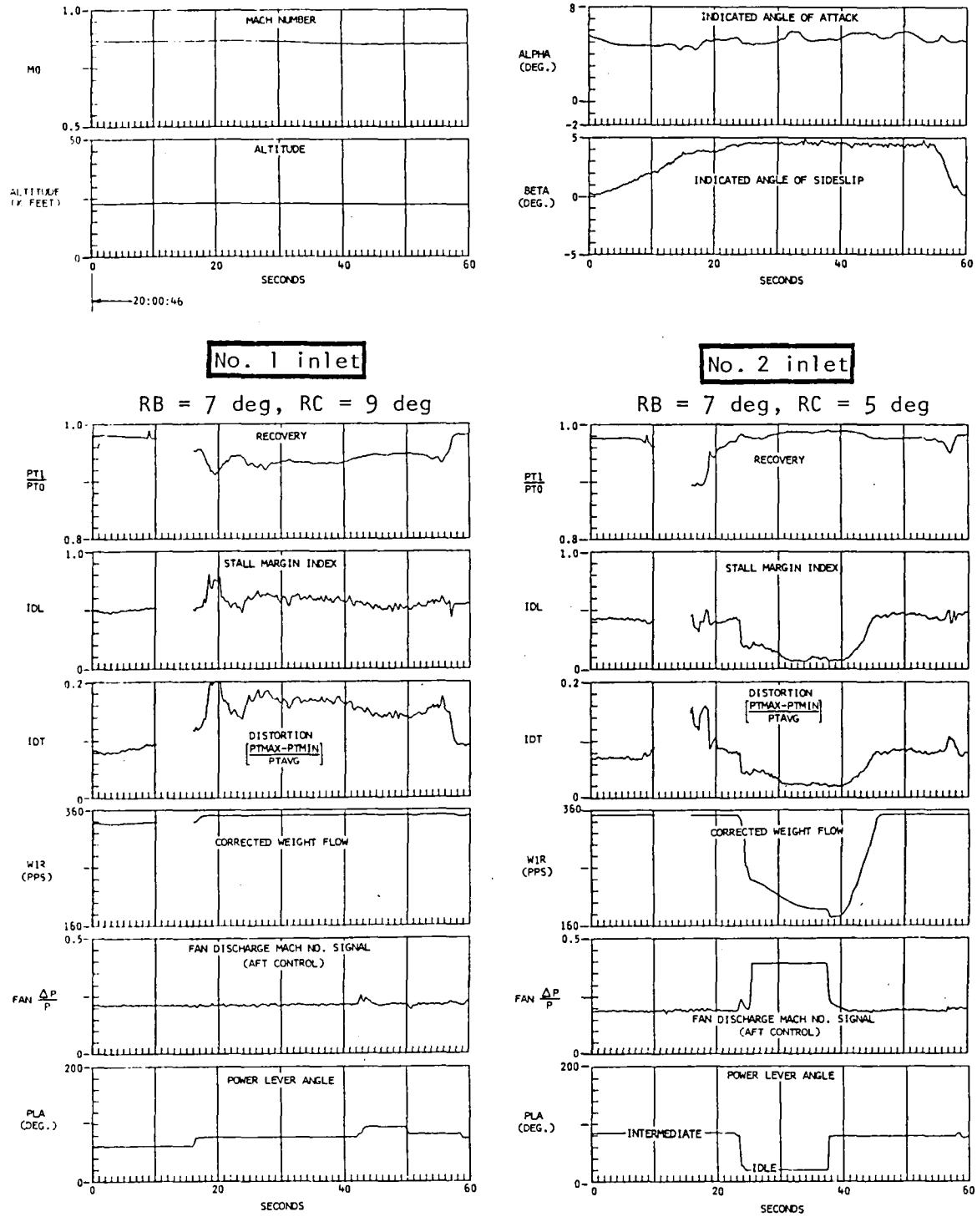

Figure 139. - Steady-state inlet characteristics during no. 2 engine transients, SMCV = 20 degrees, alpha = 5.5 degrees, and beta = +4 degrees, flight 2-38.

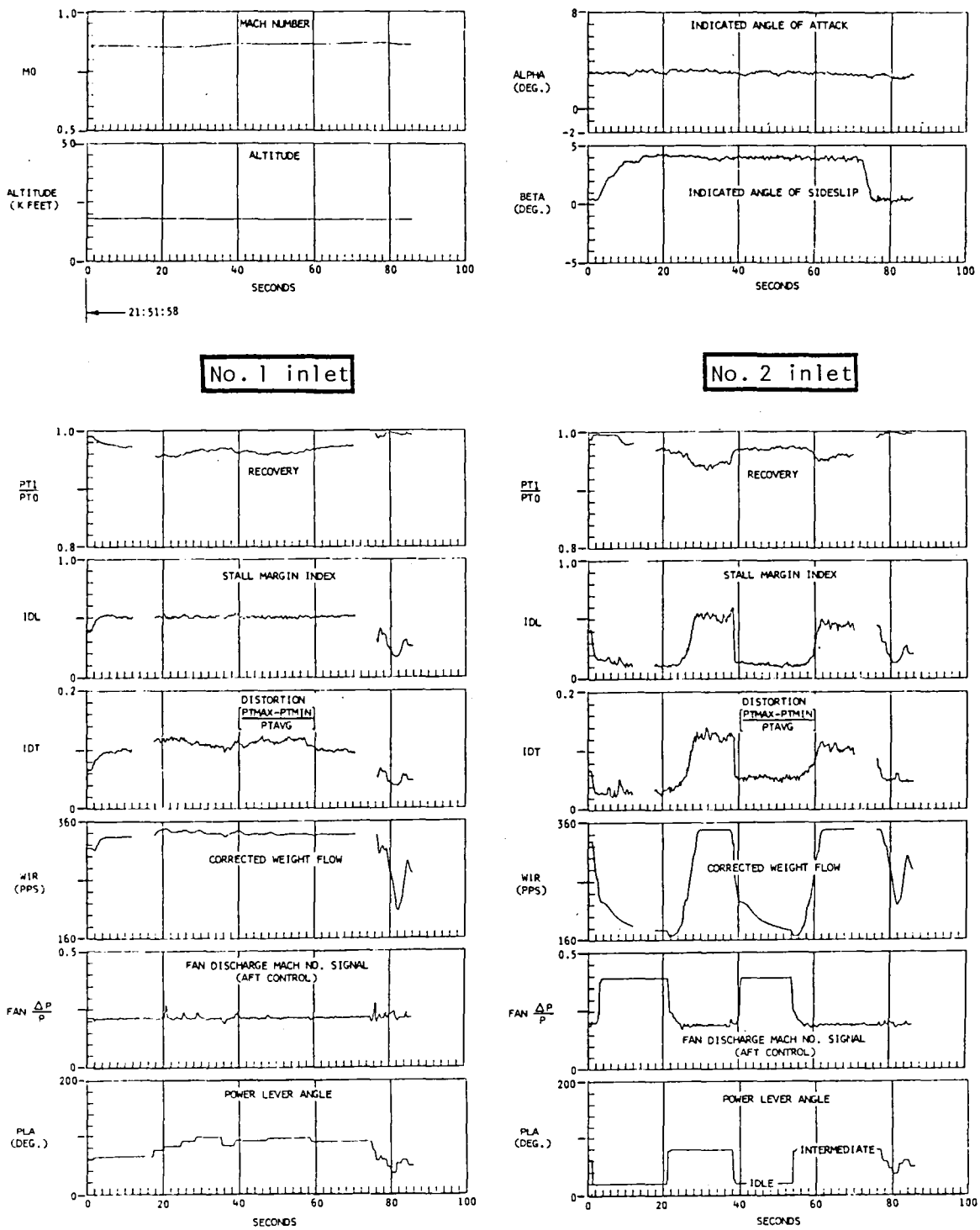

Figure 140. - Steady-state inlet characteristics during no. 2 engine transients, SMCV = 20 degrees, alpha = 3 degrees, and beta = +4 degrees, flight 2-38.

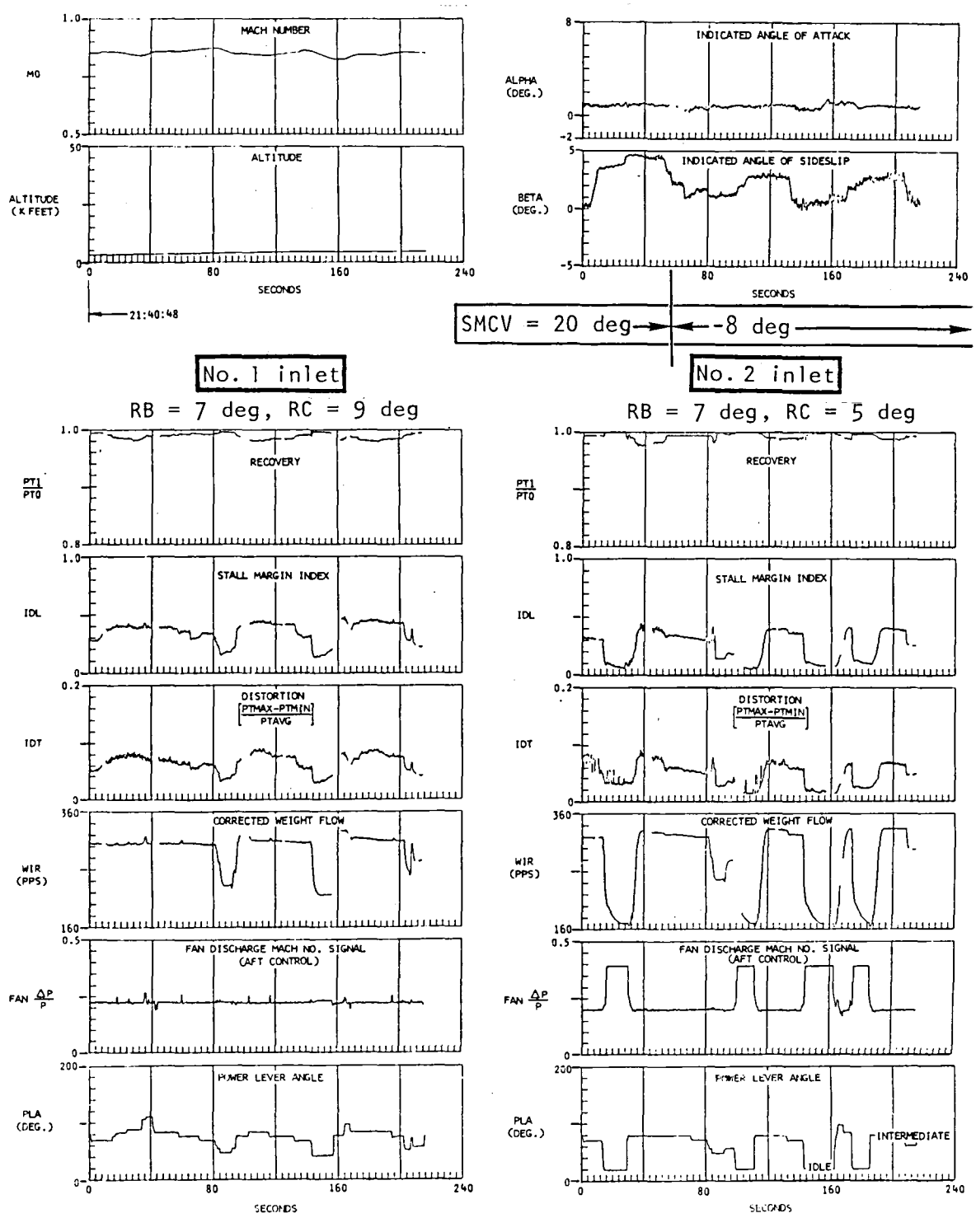

Figure 141. - Steady-state inlet characteristics during no. 2 engine transients, SMCV = 20 degrees and -8 degrees, alpha = 1 degree with positive sideslip, flight 2-38.

SUMMARY

B-1 experience from air-induction system flight tests with vortices generated by the SMCS vanes is summarized with the following observations:

(1) Agreement between flight-test and wind-tunnel test results was generally good. Small differences were noted in maneuvers (combinations of angles of attack and sideslip) that resulted in wake ingestion.

(2) Inlet total-pressure recovery and distortion characteristics can be adversely affected by wake ingestion, and consideration of these factors plays an important role in establishing good inlet/engine compatibility.

(3) Tests were conducted with the vanes deflected and held at a static condition and also with the vanes driven plus and minus full-scale deflection at a frequency of 1 Hz. Tests with oscillating vanes verified SMCS vane wake/vortex ingestion in flight. Tests with static vane deflections produced results consistent with oscillating vanes and were less objectionable to the crew.

(4) SMCS operation has not resulted in any flight restrictions. Dynamic values of stall-margin index remained well within allocations for all conditions investigated, and there were no flight incidents related to the conduct of the SMCS tests.

(5) Effects on total-pressure recovery and engine-face distortion were generally restricted to windward sideslip operation combined with leading-edge-up vane deflections. The 13-degree vane deflection angle produced effects similar to the 20-degree deflection angle on inlet performance.

(6) Sideslip angles resulting in wake ingestion are smaller during operation at higher angles of attack due to the increased outwash from the fuselage forebody. Also, the range of sideslip angles resulting in wake ingestion decreases as angle of attack increases. No wake ingestion was encountered above 7.5 degrees angle of attack.

SUMMARY OF SMCS FLIGHT TEST RESULTS

The objectives of the SMCS flight-test program were fourfold: (1) obtain specific dynamic response data to validate analytical models of the aircraft and control systems, (2) determine detail SMCS performance characteristics, (3) determine impact of SMCS on handling qualities, and (4) determine impact of SMCS on operational capabilities of the aircraft.

Four aircraft were built under the B-1 contract; A/C-1 and A/C-2 were used for detailed engineering and development tests while A/C-3 and A/C-4 were used for operational tests. As of 16 March 1979, B-1 SMCS-related test time was as follows:

A/C-1	13.6 hr
A/C-2	3.3
A/C-3	116.5
A/C-4	0.3
Total	133.7 hr

A considerable amount of the flight-test data has already been discussed in association with the topics of previous paragraphs of this report. It is the intent of this section to present flight-test data not touched upon by the specific topics covered earlier.

SMCS PERFORMANCE IN TIME-HISTORY-DATA FORMAT

Acceleration time histories are perhaps the most dramatic means of demonstrating the ride quality problem solved by the SMCS. In the vertical axis, the symmetric first-fuselage mode at approximately 3 Hz is the big motion producer at the nose of the aircraft due to turbulence. In the lateral axis, the antisymmetric (lateral) first-fuselage mode at approximately 5 Hz produces the largest response to turbulence. Figure 142 illustrates these motions with typical time-history plots of vertical and lateral acceleration at the nose of the aircraft at the SMCS vane location. The aircraft was flying through low-altitude turbulence at M = 0.75 with the SMCS off at the time that these records were taken.

Figure 143 shows data similar to that of figure 142; only during this flight test, the SMCS was operated to determine its effectiveness. The data shown were recorded on a-flight at M = 0.70 where the B-1 was flying at altitudes of 305 to 610 meters (1,000 to 2,000 feet) above the terrain in the local Edwards Air Force Base area. Considerable light to moderate turbulence was present nearly continuously. The SMCS was turned on with both the vertical and lateral cockpit gains set at 1.5. To demonstrate comparative aircraft performance with and without SMCS operating, several time periods with the SMCS on and off were recorded. Figure 143 is typical of these data. The pilot station vertical accelerometer was not operative during this flight, so the reading of the vertical accelerometer on the radome is shown.

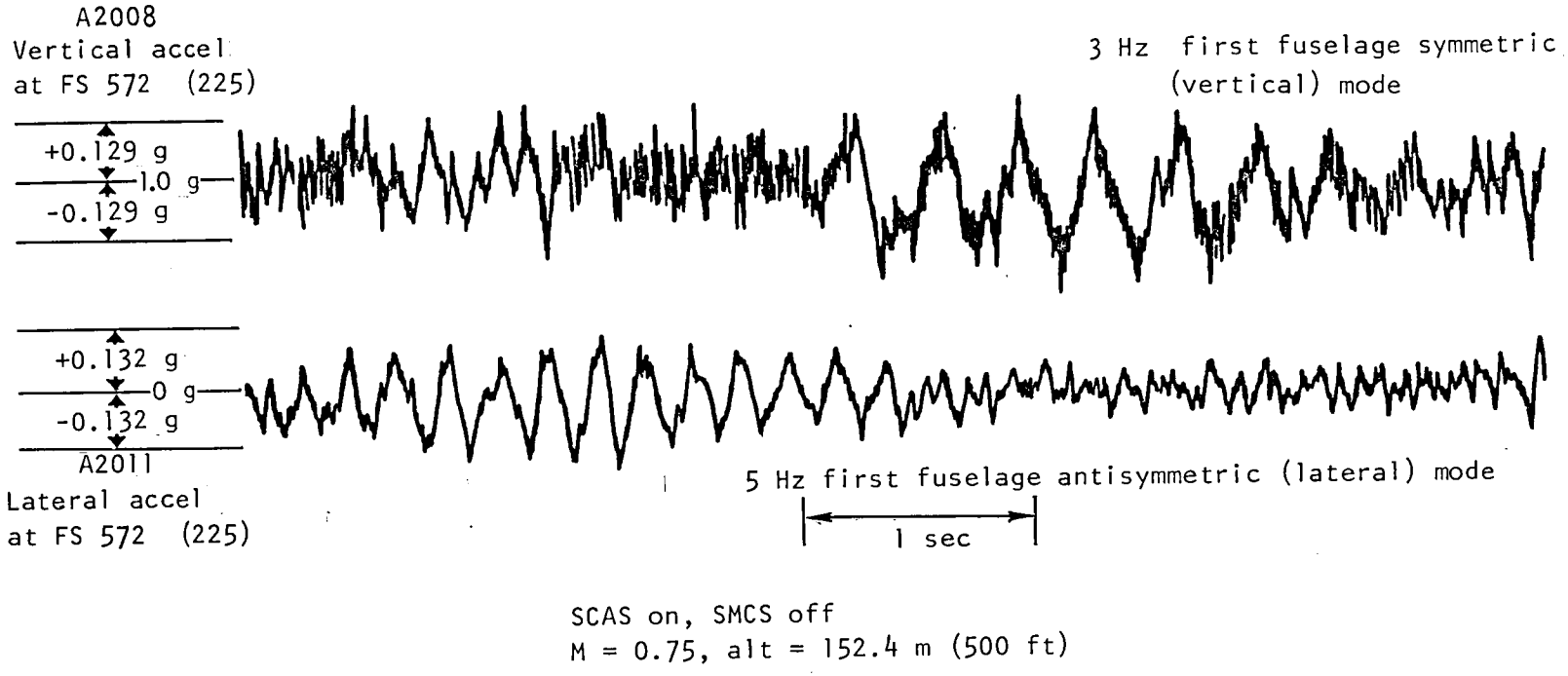

Figure 142. - Typical dynamic response near crew station due to turbulence during low-altitude, high-speed flight.

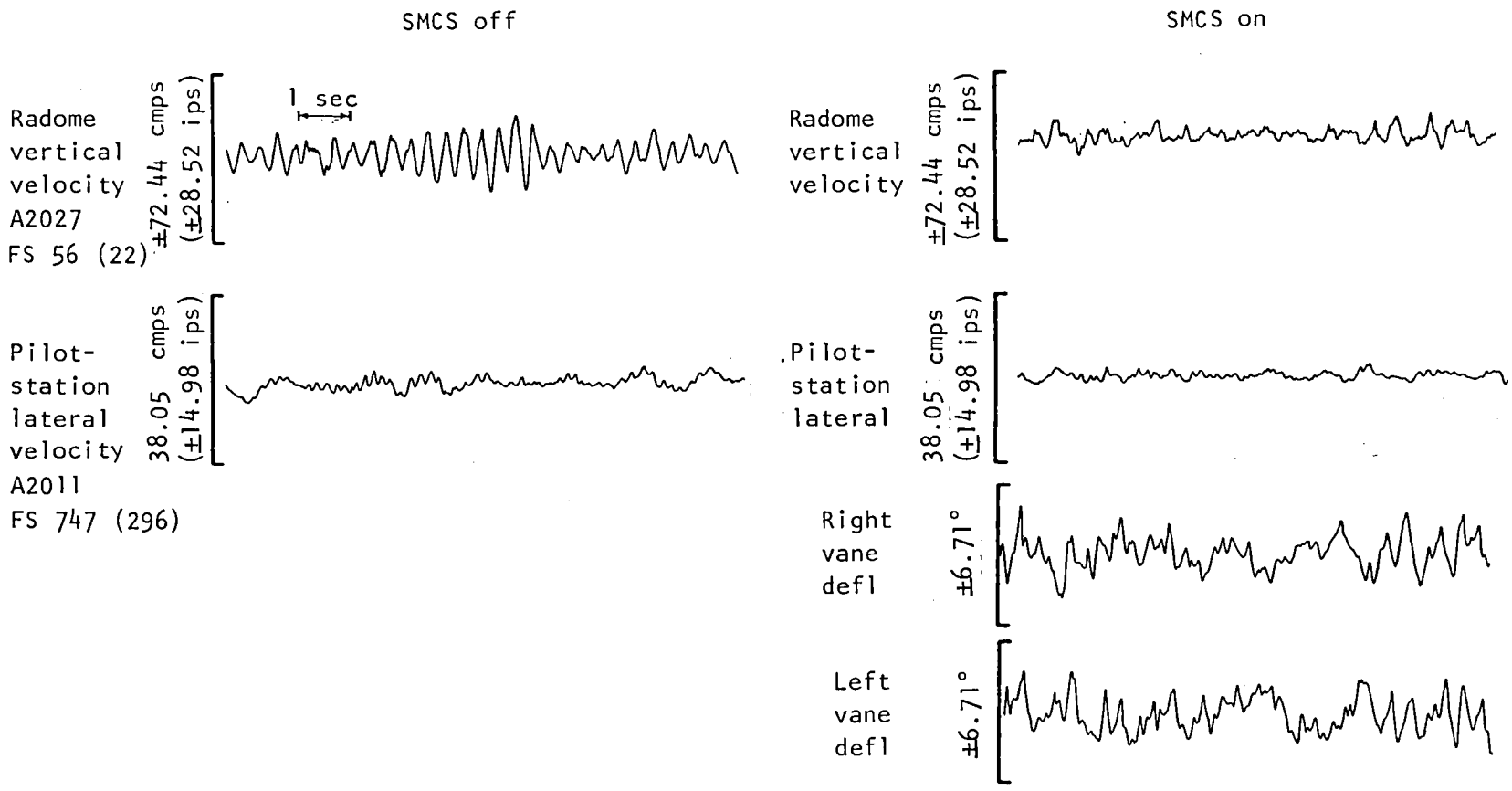

Figure 143. - SMCS performance in turbulence M = 0.70, alt = 305 m (1,000 ft) AGL $\Lambda = 65°$.

Vertical and lateral motion at the front end of the aircraft with the SMCS off are shown by the first two time histories of figure 143. As indicated, the primary motion in the vertical axis was the first fuselage bending mode at approximately 3 Hz. The lateral motion was composed of whole-vehicle motion near 1 Hz and the first-fuselage side-bending mode motion of approximately 5 Hz superimposed. When the SMCS was operated, as shown in the next two plots, considerable attenuation of the 3 Hz motion was achieved. Very little motion of the aircraft at lower frequencies appears to be present. The effect of the SMCS on the lateral axis motion was not as dramatic as on the vertical motion, but the 5 Hz motion was partially suppressed. The whole-vehicle lateral motion was not attenuated. It is to be recalled, however, that the SMCS is designed to attenuate structural mode response without adversely affecting whole-vehicle motion (handling qualities). The last two plots in figure 143 show the SMCS right and left vane motion during the time that the SMCS was operating. As shown, the maximum vane deflections seldom exceeded ±6 degrees, whereas, ±20 degrees were available. Both the 3 Hz vertical and 5 Hz lateral structural motion can be seen to drive the vane deflections; the largest component is due to the vertical motion.

Another measure of the SMCS effectiveness is the amount of structural damping the system is able to provide to the key fuselage response modes. The upper left-hand plot in figure 144 shows that it was possible to excite the symmetric first-fuselage bending mode with a sharp horizontal-tail input pulse. From the time history of the vertical load factor at the SMCS vane location (after the horizontal-tail pulse was removed), it was possible to extract the structural mode damping ratio, ζ. Figure 144 shows a plot of ζ obtained in this manner versus SMCS vertical gain setting (as set in the cockpit). A typical nominal gain setting of 1.5 is indicated. The upper right-hand plot shows the time-history response of the normal load factor with the vertical gain at this setting. Figure 145 demonstrates the vertical SMCS performance over a wide range of vehicle weights.

Attempts were made to excite the antisymmetric side-bending modes with sharp lower rudder pulses and to extract structural mode damping ratios. This did not prove to be a successful technique. A different excitation technique was used. As has been mentioned in an earlier section, A/C-1 and A/C-2 of the test B-1 aircraft have systems installed allowing the SMCS vanes to be oscillated at various amplitudes (A) across a range of frequencies up to 10 Hz. This capability was used in an attempt to extract structural mode damping for lateral side-bending modes. The technique was to select a resonant frequency and amplitude sufficiently large so as to provide transient data when the forcing motion was cut off. The data of figure 146 shows that it was possible to excite the 5 Hz first-fuselage lateral bending mode rather cleanly. Except for SMCS off response, the decay response could not be used to extract the structural mode-damping ratio because of high-frequency mode

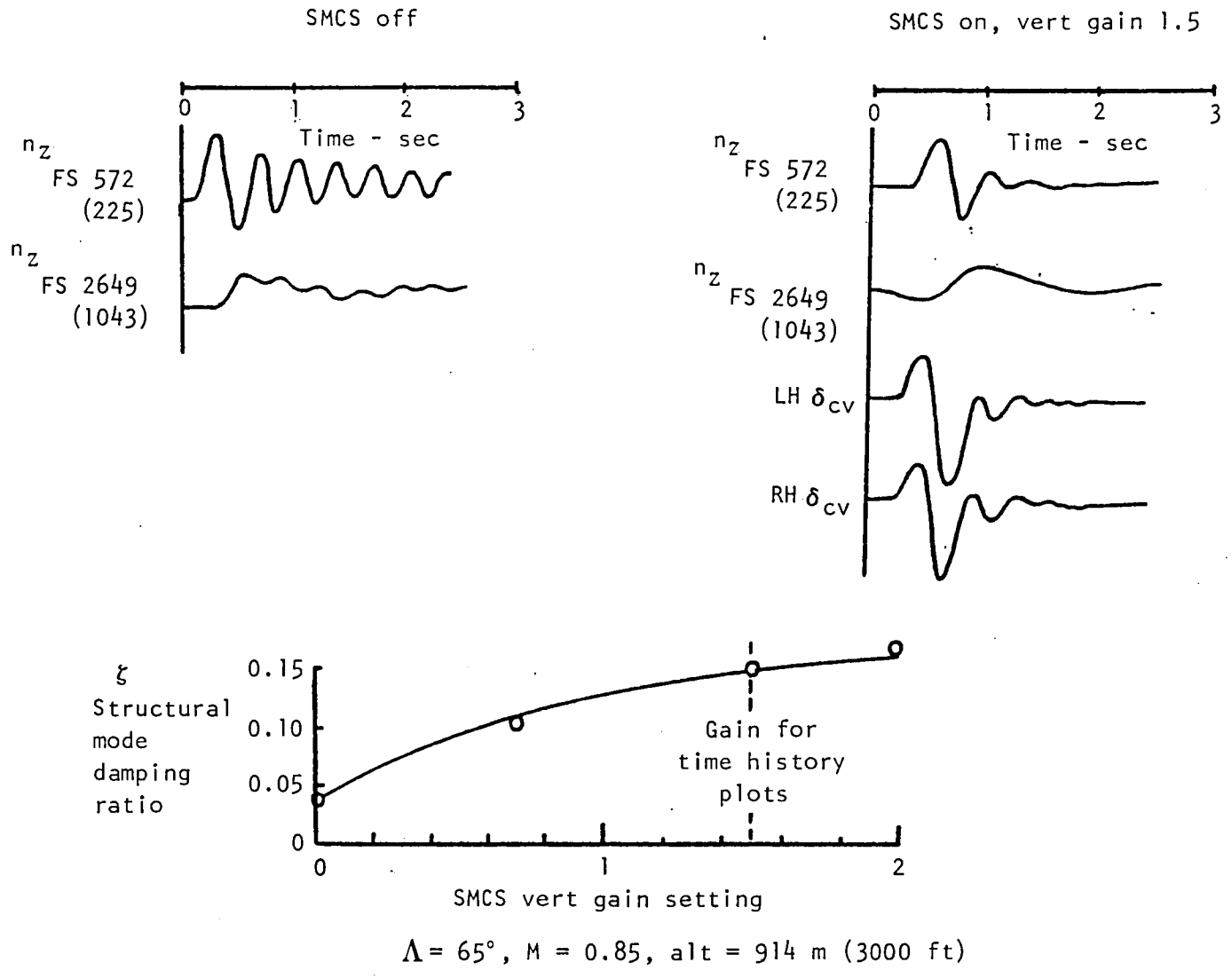

Figure 144. - First fuselage symmetric structural mode damping from horizontal tail pulse excitations.

○ M = 0.85, alt = 1829 m(6000 ft), wt = 131 544 kg (290 000 lb)

◇ M = 0.85, alt = 914 m (3000 ft), wt = 116,575 kg (257 000 lb)

○ M = 0.85, alt = 914 m (3000 ft), wt = 123 969 kg (273 300 lb)

□ M = 0.85, alt = 914 m (3000 ft), wt = 144 698 kg (319 000 lb)

△ M = 0.85, alt = 152 m (500 ft), wt = 127 008 kg (280 000 lb)

$\Lambda = 65°$

Structural mode frequency ≈ 3 H_z

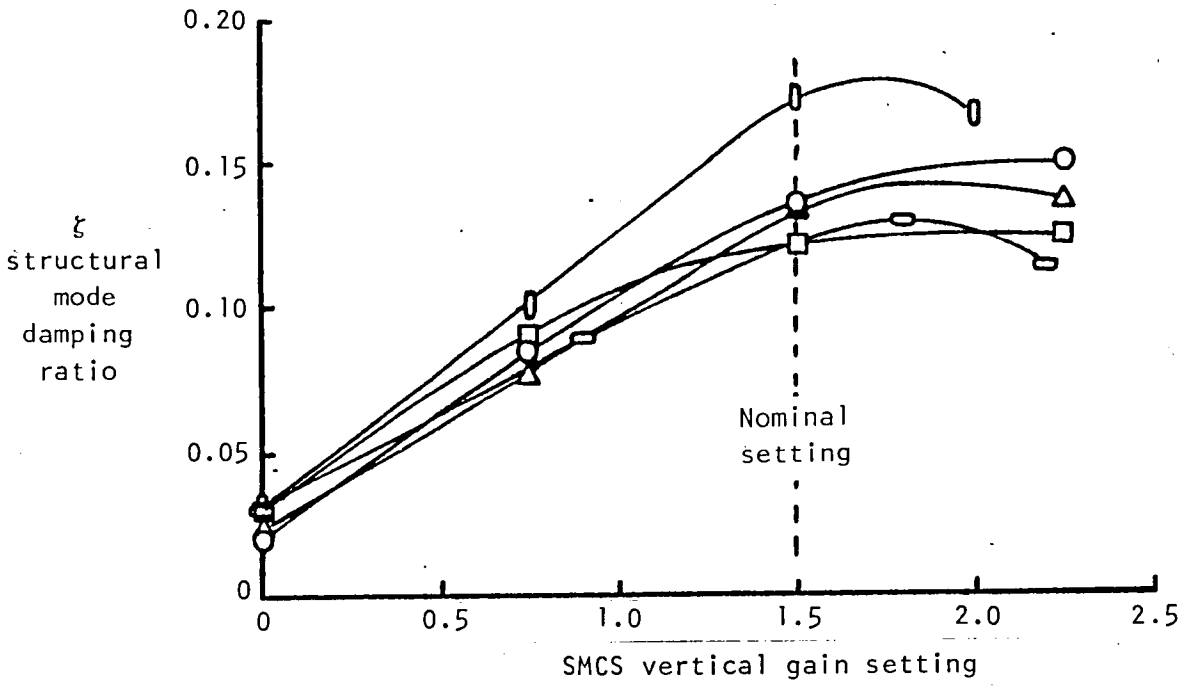

Figure 145. - Effect of SMCS vertical gain setting on first fuselage symmetric structural mode damping at various aircraft weights.

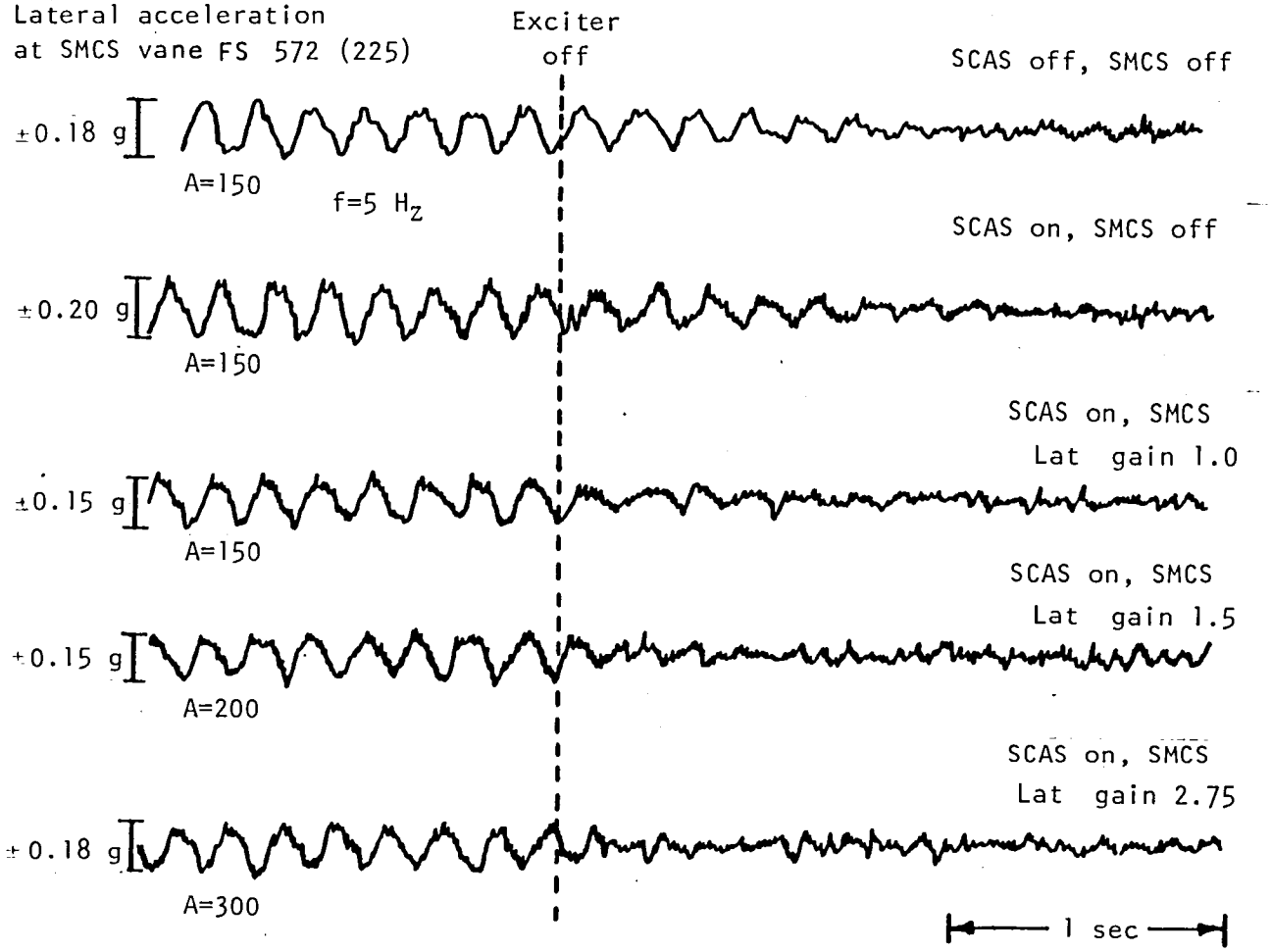

$\Lambda = 65°$, M = 0.85, Alt. = 762 m (2500 ft)

Figure 146. - First fuselage antisymmetric structural mode damping from forced SMCS vane oscillations.

contamination. The data do indicate that the SMCS is effective in eliminating structural response motions at the lateral system gains tested.

SMCS PERFORMANCE IN PSD-DATA FORMAT

In addition to time-history data, another conventional way of looking at ride quality performance and the effect of the SMCS on performance is in the form of PSD plots of load factors at the pilot station. Figures 147, 148, and 149 show typical data of this type for the vertical and lateral load factors with SMCS off and on. Because of other test requirements, none of the B-1 flight-test aircraft had a gust boom installed. Approximate vertical and lateral gust intensities were estimated using nose-boom angles of attack and sideslip angles in order to provide normalizing factors for the PSD data. Gust intensities for the data shown were estimated at 1.22 to 1.52 meters per second RMS (4 to 5 feet per second RMS).

Figure 147 shows that the approximately 3 Hz first-fuselage vertical bending mode, previously shown in the time-history plots of figures 142 and 143, is the main contributor to the vertical motion at the pilot station. As in figure 143, the data of figure 147 demonstrate that the SMCS is very effective in reducing the pilot vertical load factor.

PSD plots of the pilot station lateral load factor are shown in figures 148 and 149 for the SMCS off and on conditions. Instead of a consistent single-peak response as in the vertical case, the lateral response exhibits two different types of responses, depending on fuel loading. Figure 148 illustrates a single-peak response as seen in the time-history plot of figure 142. Figure 149 shows the other common response with two peaks between 4.5 to 6 Hz. In this latter instance, the time-history data appear more random than the lateral acceleration trace of figure 142. These data were taken with the SMCS forward sensor package in its original location. The SMCS is seen to significantly reduce the main response peaks but tends to excite some of the higher frequency modes in the immediate vicinity. It was this coupling that led to the sensor relocation study discussed in detail earlier.

SMCS AND HANDLING QUALITIES

One of the design goals for the SMCS was not to interfere significantly with basic handling qualities. The impact of SMCS operation on the B-1 handling qualities was determined from horizontal-tail and rudder-doublet transient responses. The results of these tests are shown in figure 150. The wings were at the 65-degree sweep position, Mach 0.85, and altitude 1524 meters (5000 feet). During these tests, the CG location was varied.

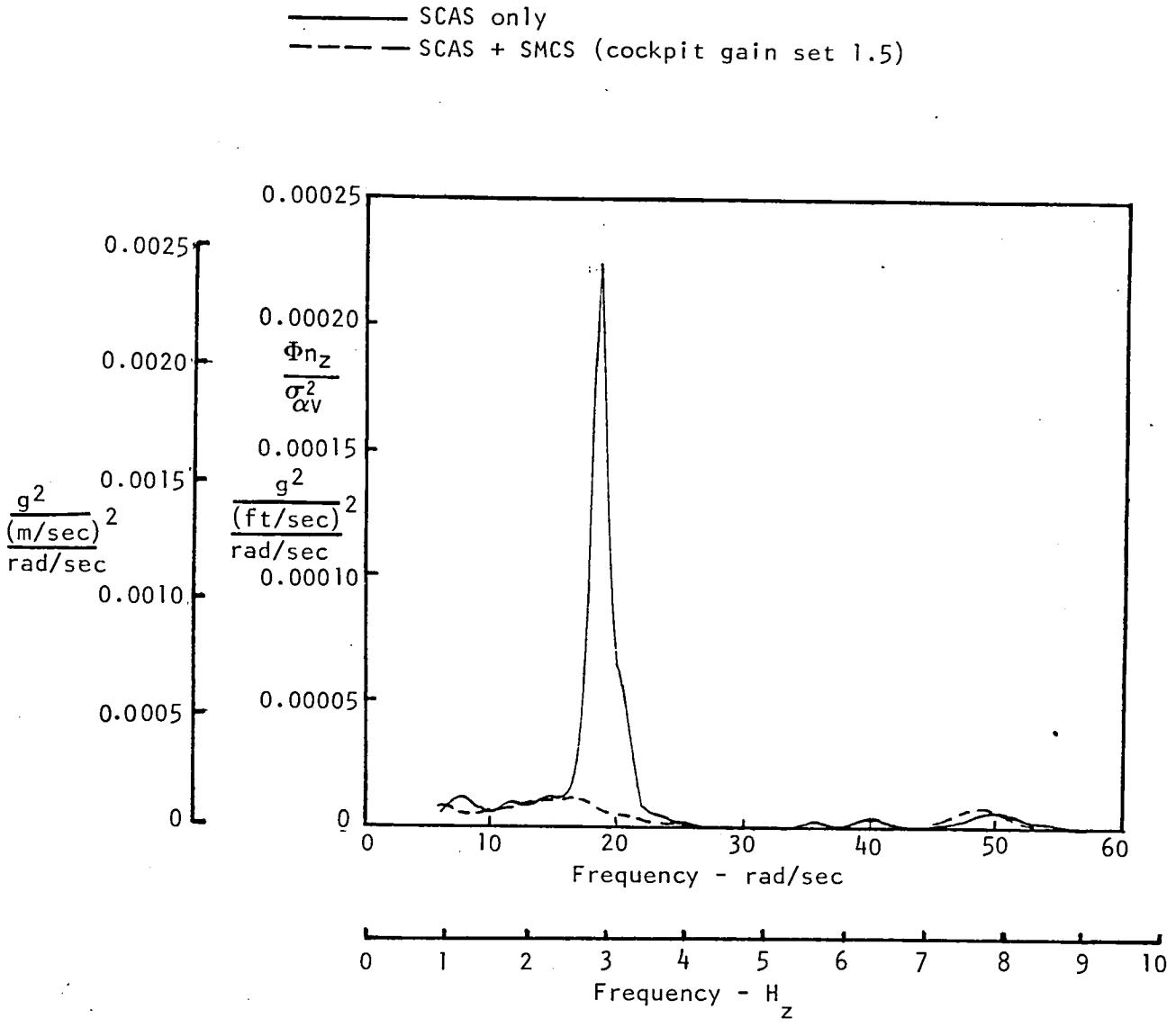

Wt = 125 194 kg (276 000 lb), CG at .35 $\bar{c}_w$

Λ = 65°, M = 0.85, alt ≈ 152 m (500 ft)AGL

Figure 147. - Vertical SMCS performance in turbulence as shown by power spectral density of vertical load factor at pilot station, FS 747 (294).

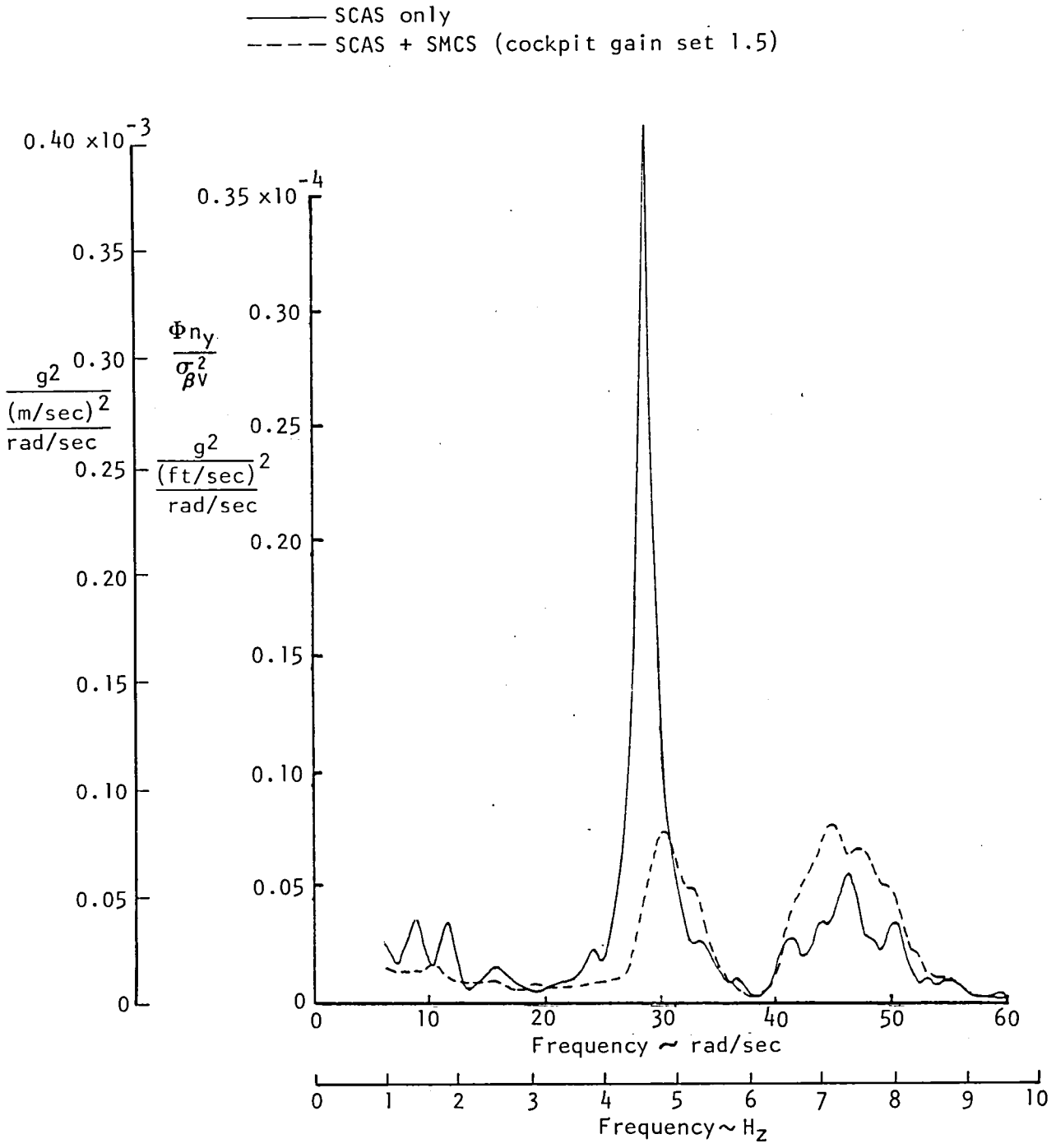

Wt = 125 194 kg (276 000 lb), CG at .35 $\bar{c}_w$

Λ = 65°, M = 0.85, alt ≈ 152 m (500 ft) AGL

Figure 148. - Lateral SMCS performance in turbulence as shown by power spectral density of lateral load factor at pilot station, FS 747 (294), single-peak response.

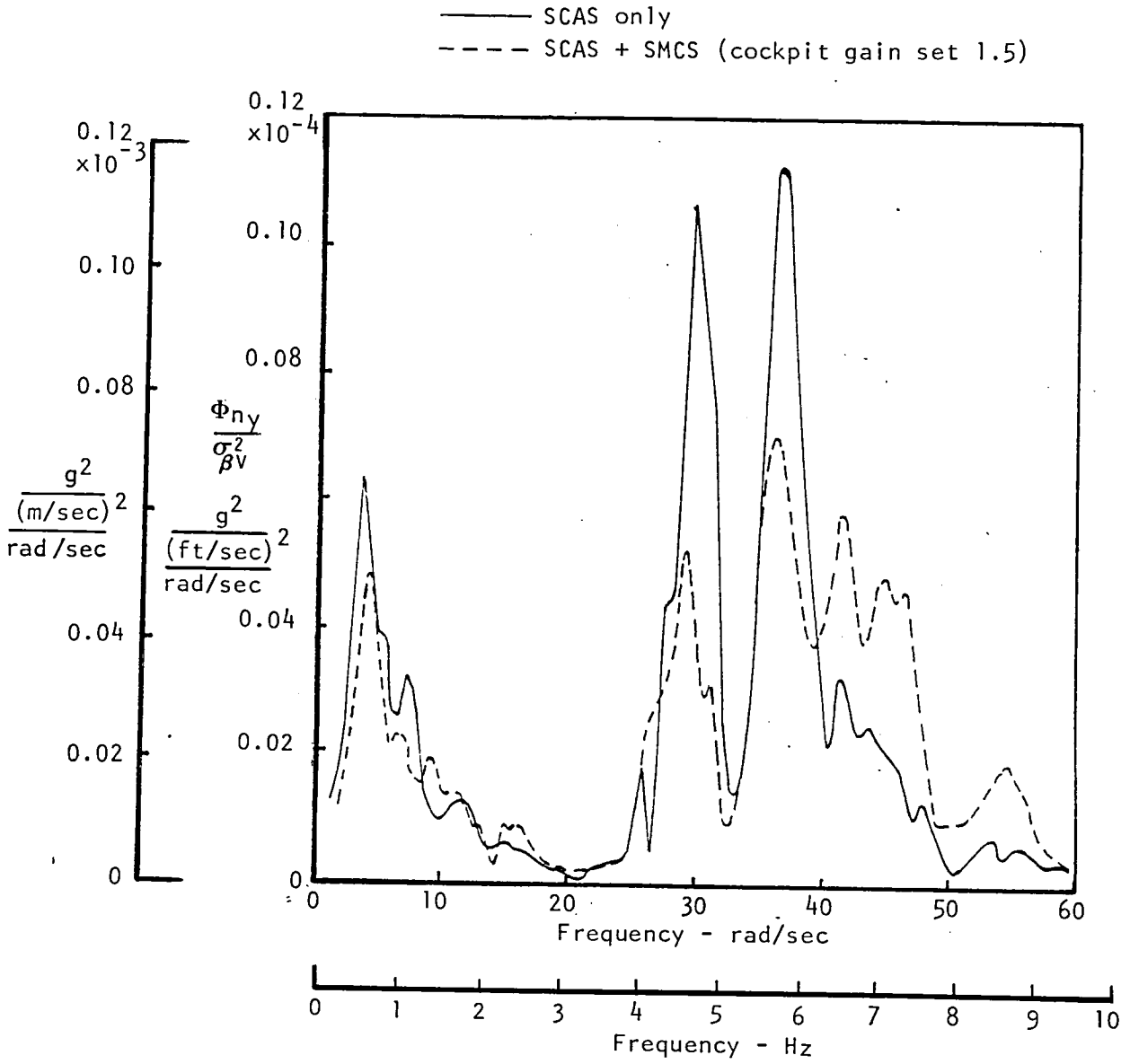

Wt = 128 369 kg (283 000 lb), C.G. at 0.46 $\bar{c}_w$

Λ = 65°, M = 0.70, alt ≈ 305 m (1000 ft) AGL

Figure 149. - Lateral SMCS performance in turbulence as shown by power spectral density of lateral load factor at pilot station, S 747 (294), double-peak response.

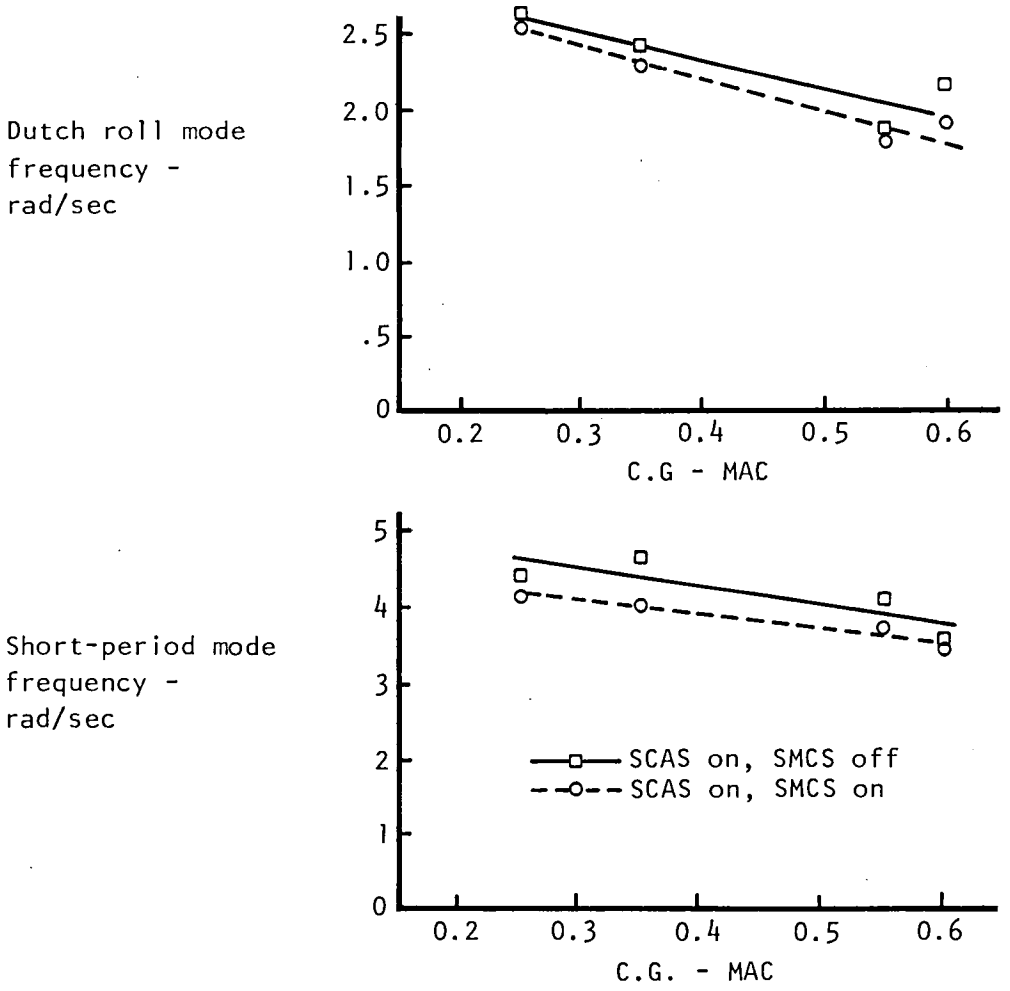

Wt = 117 482 kg(259 000lbs) to 128 822 kg(284 000lbs)

Λ = 65°, M = 0.85, alt = 1524 m (5000 ft)

Figure 150. - SMCS impact on short-period and dutch roll frequencies.

In the longitudinal mode, short-period mode frequency and damping ratio were extracted from the transient following the pitch doublets. A slight reduction in the short-period mode frequency was observed when operating with the SMCS on (figure 150) for all CG positions. No significant change in the short-period mode damping ratio was observed.

In the lateral-directional mode, the Dutch-roll mode frequency and damping ratio were extracted from the transient following rudder doublets. Results obtained for the lateral-directional handling qualities were similar to those for the longitudinal handling qualities. The Dutch-roll frequency is slightly reduced by the SMCS at all CG positions. (See figure 150.) Again, no significant effect of SMCS on Dutch-roll damping could be detected.

In order to determine whether SMCS would interfere with aircraft maneuvering, a roller-coaster maneuver was executed with the SMCS off and on. Evaluations of recorded data of the SMCS vane deflections showed no significant motion; maximum vane deflections recorded were less than 2 degrees. This was determined to have a negligible impact on the maneuvering of the aircraft. Subsequent to the previously described tests, pilots have reported a slight increase in stick force required in terrain following with the SMCS on over that with the SMCS off.

SMCS HIGH-GAIN TESTS

B-1 A/C-1 and A/C-2 were used in the high-gain tests to demonstrate system gain margins over the expected nominal gains. It had been initially planned to do all of the testing of the relocated forward SMCS sensor package on A/C-1 only, including the high-gain tests under discussion. However, after only a few of the tests associated with the relocated forward SMCS sensor package had been completed, A/C-1 went into layup for modifications. In order to continue with testing, the forward SMCS sensor package was relocated on A/C-2.

A summary of the high-gain tests on A/C-1 and A/C-2 is presented in table X. At nominal gains, there appears to be no difference in the SMCS performance on A/C-1 or A/C-2. At high gains, however, A/C-2 was limited by a 35 Hz limit cycle which was not evident in similar A/C-1 data. These data show that A/C-1 and A/C-2 have nearly a factor of two gain margins over expected nominal settings for the ride quality design point of Mach 0.85 at low altitudes. It is at Mach 0.55 at low altitudes on A/C-2 in a lightweight configuration that the 35 Hz limit cycle prevents obtaining the expected nominal gains. From the lightweight configuration data of flight 1-41 obtained at Mach 0.85 at high altitude where the dynamic pressure schedule gain in the

TABLE X. - SMCS HIGH-GAIN TESTS SUMMARY

Wing sweep (degrees)	Heavy weight M = .85, low alt			Light weight M = .85 low alt		
65	Vertical gain	Lateral gain	Flt no.	Vertical gain	Lateral gain	Flt no.
	1.9 expected nominal	2.2 expected nominal		1.9 expected nominal	2.2 expected nominal	
	4.8	3.9 35 Hz limit cycle	2-23	4.5	6.0 no 35 Hz	1-48
				3.0	6.0 35 Hz evident	[a]2-25
55	Heavy weight M = .55, low alt			Light weight M = .55, low alt		
	Vertical gain	Lateral gain	Flt no.	Vertical gain	Lateral gain	Flt no.
	3.0 expected nominal	3.7 expected nominal		3.0 expected nominal	3.7 expected nominal	
	4.5	4.7 35 Hz limit cycle	2-23	3.0	3.1 35 Hz limit cycle	2-23
				5.0	5.5 no 35 Hz	[b]1-50

[a]Repeat of 1-48 runs
[b]Repeat of 2-23 runs

SMCS is about the same as at the low-altitude mach 0.55 flight condition, it was expected that a vertical gain of six would be obtained. However, as the table shows, this value was not obtained.

These inconsistencies in A/C-1 and A/C-2 data led to repeating with A/C-2 a set of previously run A/C-1 tests and vice-versa. These tests were completed on flights 2-25 and 1-50. Analyses of these data indicate that the 35 Hz gain limitations are unique to A/C-2. Ground tests were conducted on both aircraft in an attempt to identify the causes of the 35 Hz limitations of A/C-2; these tests were unable to isolate the causes of the 35 Hz.

CREW EVALUATIONS OF SMCS EFFECTS

The bulk of the SMCS operational suitability tests were conducted on B-1 A/C-3. Ten B-1 flight crewmen participated in the tests: four pilots (PLT), three flight-test engineers (FTE), and three Offensive System Operators (OSO). The crews flew regularly scheduled manual terrain-following (MTF) and automatic terrain-following (ATF) flight-test missions with the SMCS on and off. Crewmembers were instructed to maintain awareness of comfort and personal performance during the various TF missions. Each crewmember was instructed to complete a test questionnaire to document his evaluation of the B-1 ride and effects of this ride on his performance.

The curves in figure 151 through 158 summarize the subjective responses to questions on overall ride quality and the effect of turbulence on: flight path/nonflight path control tasks; readability of instruments and displays; reaching/using controls; crew fatigue, motion sickness, and physical discomfort. These data are in the form of composite responses from all crewmembers.

Overall Ride Quality

Subjects were asked to rate ride quality during TF flight as a function of SMCS on and off for the following conditions of turbulence: smooth air and light, moderate, and heavy turbulence. The combined ratings for all subjects are shown in figure 151. The data reveal the following:

(1) Ride quality ratings decrease (ride quality worsens) as turbulence increases.

(2) In smooth air, use of the SMCS results in little improvement in ride quality.

(3) Use of the SMCS improves ride quality in light, moderate, and heavy turbulence.

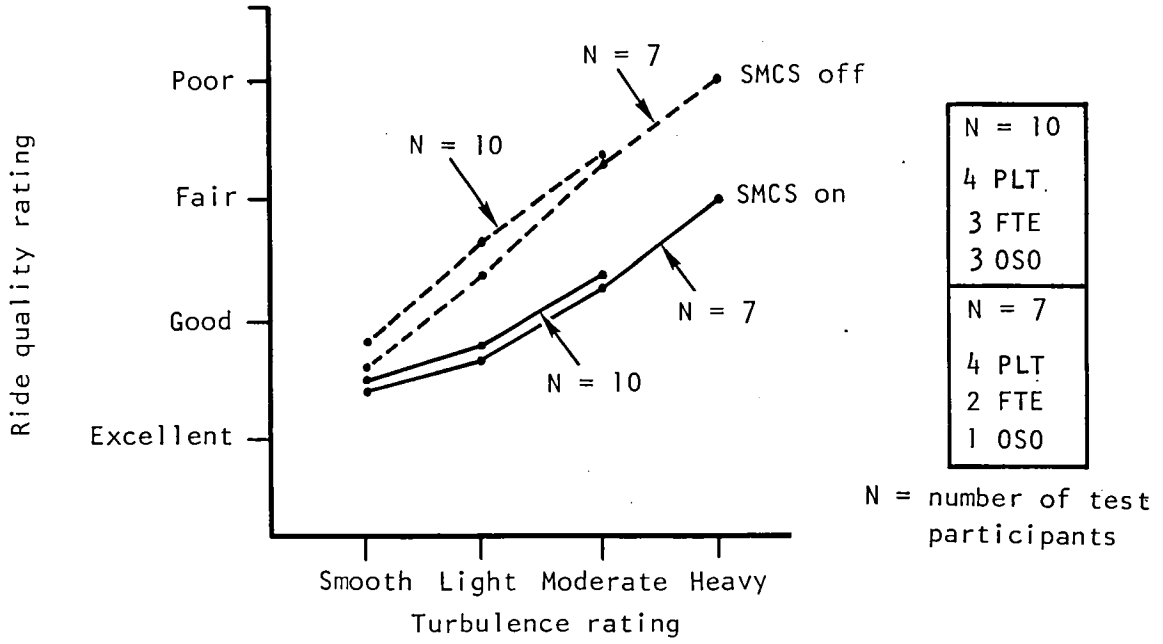

Figure 151. Ride quality ratings for varying degrees of turbulence.

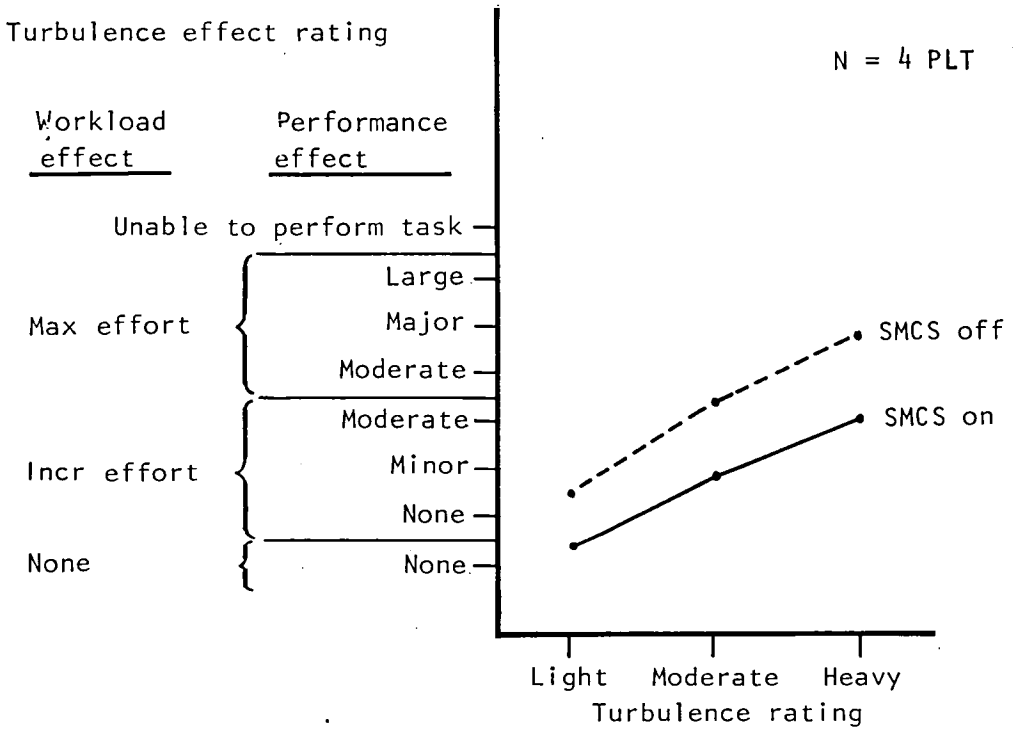

Figure 152. - Effects of turbulence on flight path control tasks.

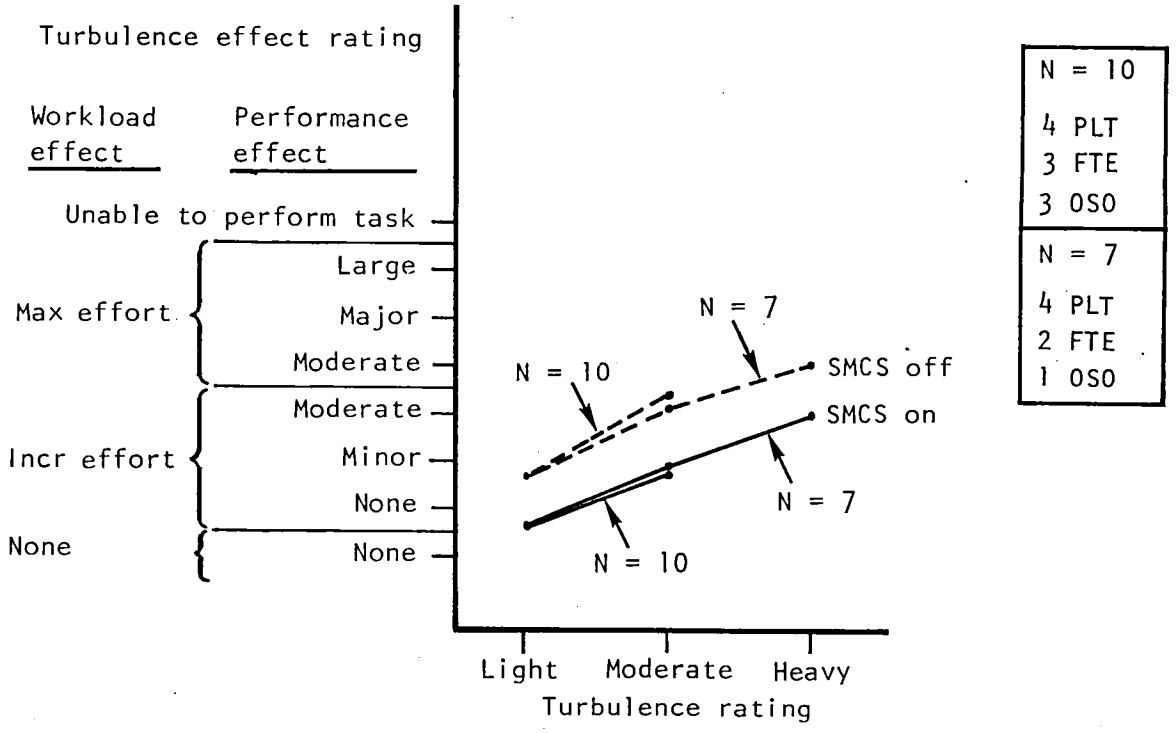

Figure 153. - Effects of turbulence on tasks other than flight path control.

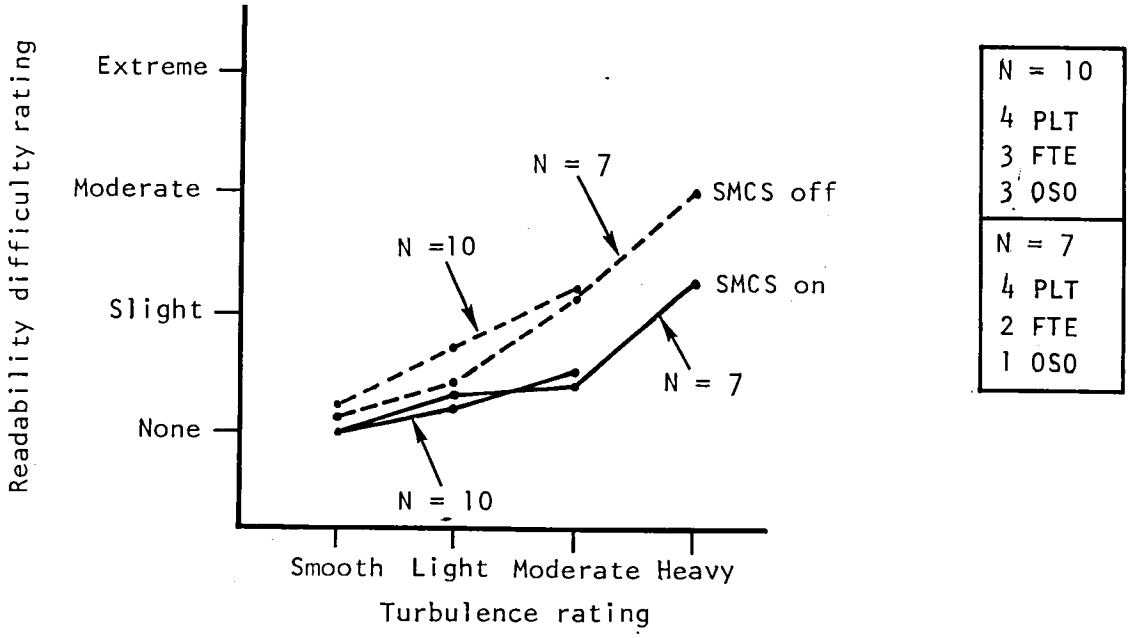

Figure 154. - Effects of turbulence on readability of instruments and displays.

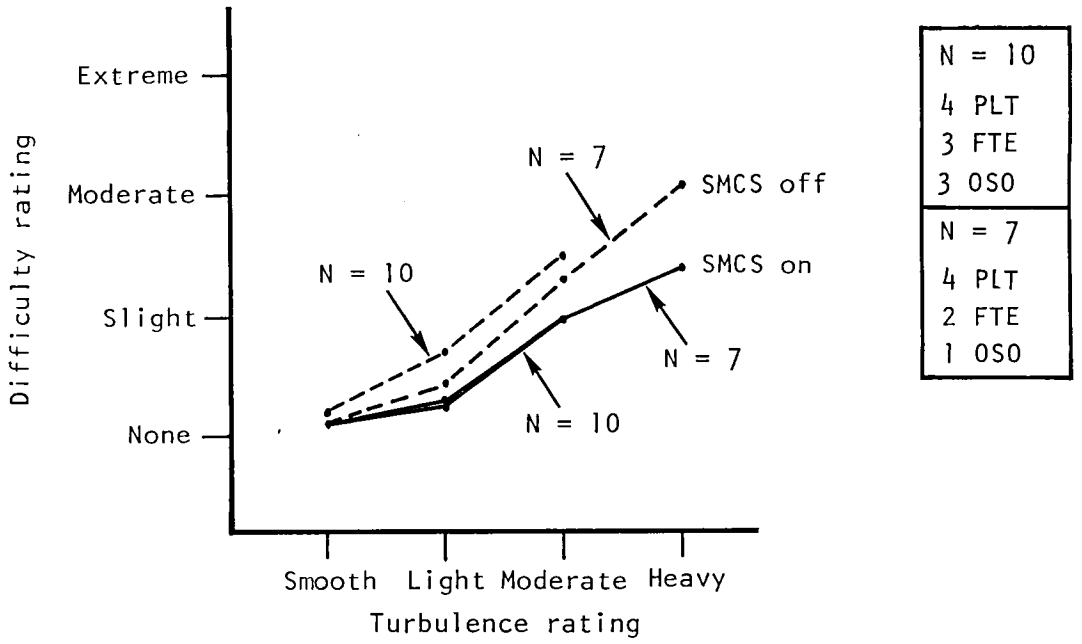

Figure 155. - Effects of turbulence on reaching/using controls.

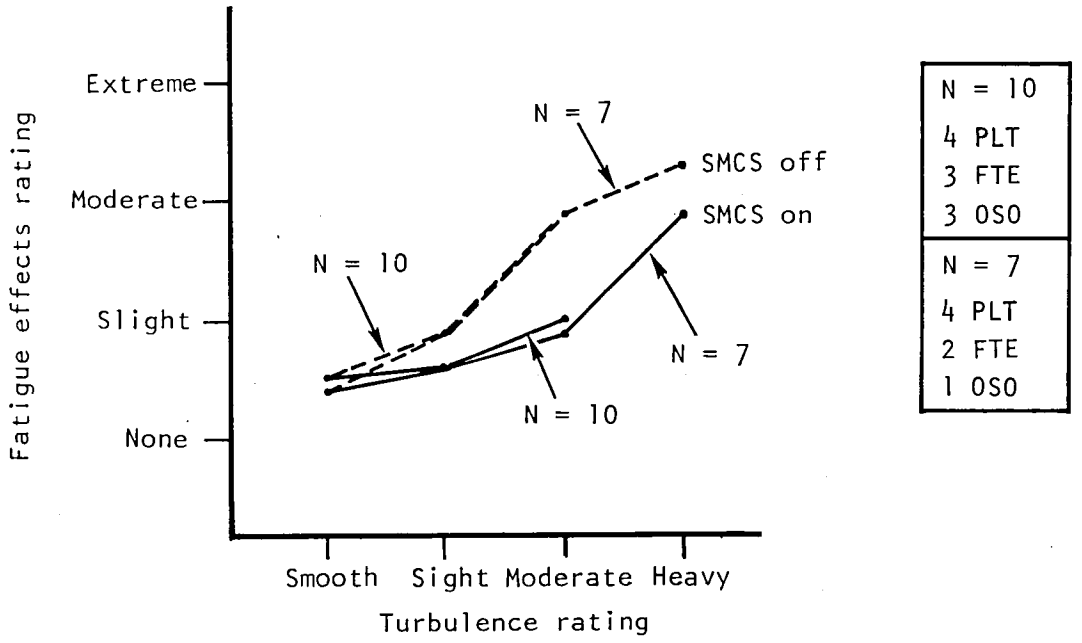

Figure 156. - Effects of turbulence on crew fatigue.

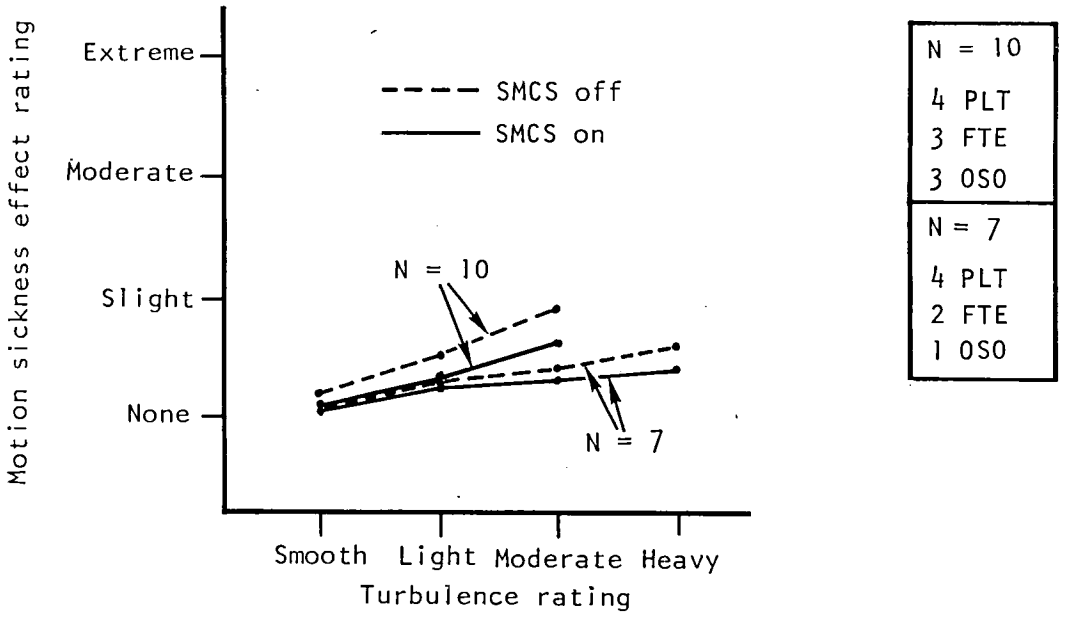

Figure 157. - Effects of turbulence on tendency for motion sickness.

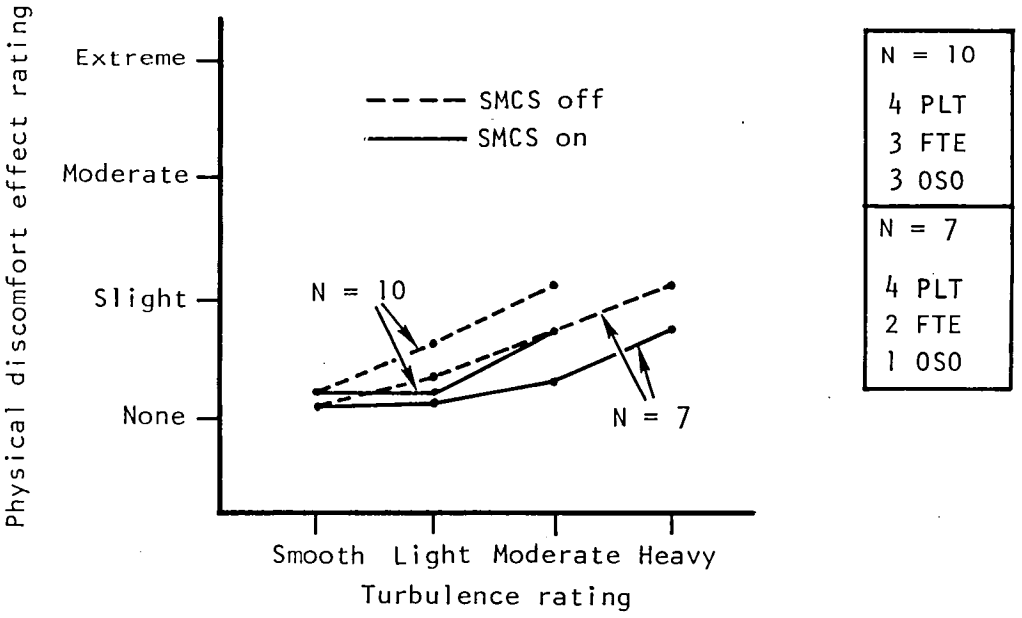

Figure 158. - Effects of turbulence on physical discomfort.

One subject added the following comment to his ratings: "In smooth air, SMCS is not needed. Standard of comparison is the F-111 which is excellent." (OSO A)

Flight-Path Control Tasks

Pilots were asked to rate the effects of turbulence on flight-path control tasks during TF with SMCS off and on. Ratings were to be made with reference to a turbulence-effect rating scale. The combined ratings for all subjects are shown in figure 152. The data reveal the following:

(1) The effort to perform flight-path control tasks and the negative effect on task performance increase as turbulence increases.

(2) Greater effort is required, and the negative effect on subject performance is greater with SMCS off than with SMCS on; i.e., workload is less when SMCS is being used.

Non-Flight-Path Control Tasks

All subjects were asked to rate the effects of turbulence on non-flight-path control tasks during TF with SMCS off and on. Ratings were made to a turbulence-effect rating scale. The combined ratings are shown in figure 153. The data reveal the following:

(1) The effort to perform non-flight-path control tasks and the negative effect on task performance increase as turbulence increases.

(2) Greater effort is required, and the negative effect on subject performance is greater with SMCS off than with SMCS on; i.e., workload is less when SMCS is being used.

One subject added the following comment, "Operation of equipment difficult - particularly CITS." (FTE C)

Readability of Instruments and Displays

All subjects were asked to rate the degree of difficulty they experienced in reading instruments and displays during TF flight as a function of SMCS off and on for four conditions of turbulence: smooth air and light, moderate, and

heavy turbulence. The combined ratings for all subjects are shown in figure 154. The data reveal the following:

(1) The difficulty to read instruments and displays increases as turbulence increases.

(2) Difficulty ratings are higher (readability less difficult) with SMCS on than with SMCS off.

One subject added the following comment: "'E' scope always extremely difficult to read because of location - turbulence no factor."

Reaching/Using Controls

All subjects were asked to rate the difficulty in reaching controls or in performing control actions during TF flight as a function of SMCS off and on for four conditions of turbulence: smooth air and light, moderate, and heavy turbulence. The combined ratings for all subjects are shown in figure 155. The data reveal the following:

(1) The difficulty to reach and use controls increases as turbulence increases.

(2) As turbulence increases, it is easier to reach and use controls with SMCS on than with SMCS off.

Five of the subjects added a comment, as follows:

(1) "In manual TF, pitch stick force too heavy." (PLT C)

(2) "Rating is based primarily on use of central integrated test system (CITS)." (FTE A)

(3) "CITS controls somewhat difficult in turbulence." (FTE B)

(4) "Operation of CITS is difficult at best. SMCS helps." (FTE C)

(5) "Some of the ratings are due to the locations of the controls." (OSO C)

Crew Fatigue

All subjects were asked to rate the degree to which TF flight introduced any special tendencies toward fatigue. Ratings were requested for the SMCS off and on modes for four conditions of turbulence: smooth air, and light, moderate, and heavy turbulence. The combined ratings for all subjects are shown in figure 156. The data reveal the following:

(1) Fatigue effects increase as turbulence increases.

(2) There is little difference in fatigue-effect ratings with SMCS off versus SMCS on except for the moderate turbulence condition. For moderate turbulence, the fatigue-effects rating for SMCS on is higher (less fatigue effect) than for SMCS off.

Three of the subjects added a comment, as follows:

(1) "Ratings made for AUTO TF." (PLT A)

(2) "Turbulence is not the primary factor in producing fatigue - TF itself produces a high level of fatigue." (FTE B)

(3) "Turbulence definitely increases fatigue." (FTE C)

Motion Sickness

All subjects were asked to rate the degree to which TF flight introduced any special tendency for motion sickness. Ratings were requested for the conditions of SMCS off and on for four levels of turbulence: smooth air and light, moderate, and heavy turbulence. The combined ratings for all crewmen are shown in figure 157. The data reveal the following:

(1) The composite data show little tendency for motion sickness for all turbulence conditions for both SMCS off and on modes. FTE were more affected than pilots.

One subject commented that: "Turbulence is not a major influence. The roughness of terrain has more impact when you are stuffed in that 'black hole' with no windows." (FTE C)

Physical Discomfort

All subjects were asked to rate the degree to which TF flight introduced any special tendencies toward physical discomfort. Ratings were requested for the conditions of SMCS off and on for four levels of turbulence: smooth air and light, moderate, and heavy turbulence. The combined ratings for all crewmen are shown in figure 158. The data reveal the following:

(1) Physical discomfort increases as turbulence increases; although at heavy turbulence, the effects are rated only as slight.

(2) Less physical discomfort is reported for light, moderate, and heavy turbulence with SMCS on than with SMCS off. For smooth air, there is no difference in physical discomfort ratings for the SMCS off versus SMCS on modes.

One subject commented that: "Physical discomfort results from feelings of irritation, aggravation, and anxiety produced by the rough ride and high workload, hard to pin down further." (PLT D)

Additional Ride Quality Observations

All subjects were asked to add any additional observations (not covered by the ride quality questions) concerning ride quality characteristics or SMCS effects during TF flight or any other characteristics realting to TF which have a bearing on crew comfort and efficiency. Comments included the following:

(1) "SMCS is very effective and required in the B-1 to aid the flight crew in performance of the TF task." (PLT A)

(2) "Essential for effective B-1 MTF, desired for effective B-1 ATF." (PLT C)

(3) "Turbulence makes this aircraft hard to stabilize on a bank angle, adds to an already high workload." (PLT D)

(4) "Ride qualities with SMCS are definitely better than without - the difference I don't think is really able to be seen in the layout of this questionnaire." (FTE A)

(5) "Lack of outside visual reference contributes significantly to disorientation and motion sickness. Movement about the crew compartment is hampered by TF, especially in turbulence. Any movement in the crew compartment

also contributes to disorientation and motion sickness. There is a significant improvement in the ride with SMCS on." (FTE B)

(6) "I consider SMCS essential for long term TF flight." (OSO A)

(7) "Due to part of the controls and displays location, it is difficult to accomplish some weapon-oriented tasks under turbulent conditions. The sensitivity of both the navigation (NAV) panel and Stores Management System (SMS) FWD/REV switch make it difficult to use under turbulent flight conditions." (OSO B)

(8) "The discomforts in the OSO station are more severe in light or moderate turbulence with SMCS off due to the fact that we have no outside reference." (OSO C)

Handling Qualities

Pilots were asked to describe the effects, if any, of SMCS activation on aircraft handling qualities during MTF. Comments included the following:

Pitch Control

(1) "A/C ride is smoother with SMCS on and therefore control is easier." (PLT A)

(2) "Assists by damping." (PLT B)

(3) "Could have some detrimental effect because rapid control inputs are apparently countered by SMCS -- not considered a problem to date, more evaluation required." (PLT C)

(4) "Increases pitch forces, seems to slow aircraft response." (PLT D)

Lateral/Directional Control

(1) "A/C ride is moother with SMCS on and therefore control is easier." (PLT A)

(2) "Assists by damping." (PLT B)

APPENDIX

NOMENCLATURE

This report was the result of the contributions of a number of authors and each has used nomenclature unique to his particular discipline. In order to help the reader to quickly locate a given symbol, this section has been organized so that a general section is presented first followed by nomenclature associated with three sections of this report which are especially heavy in specialized nomenclature. These sections are: "Flexible Aircraft Equations of Motion," "Impact of SMCS on Selected Loads," and "SMCS Vane Effect on Inlet/Engine Characteristics." Under this system, similar symbols often have different meanings; the reader is cautioned to identify symbols within the context of their use.

GENERAL

A	amplitude setting of B-1 oscillating system for the SMCS vanes
A/C	aircraft
alt	altitude
ATF	automatic terrain following
AUTO	automatic
BP	butt plane
b_{REF}	reference length
$\bar{c}$	mean aerodynamic chord
CITS	central integrated test system
CG	center of gravity
cm	centimeters
deg	degrees
EI	bending stiffness
f	frequency, cycles per second
F, Flex	subscript denoting flexible

Flt	flight
ft	feet
FTE	flight test engineer
F/R	flexible-to-rigid ratio
$\frac{[\ ]_F}{[\ ]_R}$	flexible-to-rigid ratio of bracketed parameter
FS	fuselage station
g	Acceleration of gravity
GJ	torsional stiffness
GVT	ground vibration test
$\overline{H}_{(\ )}$	crew sensitivity index; subscript Z denotes vertical axis, Y denotes lateral axis
Hz	hertz (cycles per second)
hr	hours
in.	inches
k	reduced frequency, $\frac{\omega\bar{c}}{2V_o}$, $\frac{\omega b_{REF}}{V_o}$
K	SMCS gain
K_{h_p}	SCAS gain scheduled with altitude
kg	kilogram
$K_{MN_{n_y}}$	yaw SCAS lateral accelerometer gain
k_q	pitch SCAS gyro gain
$k_{\bar{q}}$	SMCS gain scheduled with dynamic pressure

K_{MN_r}	yaw SCAS gyro gain
K_{n_z}	pitch SCAS normal acceleration gain
lb	pounds
L-gain	lateral SMCS gain
L_h	dimensional force along Z-axis due to plunging motion h, + down
L_θ	dimensional force along Z-axis due to pitching motion θ, + down
$\left[\Delta L_\theta\right]_{Real}$	$\left[L_\theta\right]_{Real} - \frac{V_o}{\omega}\left[L_h\right]_{Imag}$
L_{η_i}	dimensional force along Z-axis due to structural mode generalized coordinate motion η_i, + down
L_{w_g}	dimensional force along Z-axis due to vertical gust velocity w_g, + down
L_δ	dimensional force along Z-axis due to control surface motion δ, + down
m	meter
M	Mach number
MTF	manual terrain following
M_h	dimensional moment about Y-axis due to plunging motion h, + nose up
M_θ	dimensional moment about Y-axis due to pitching motion θ, + nose up
$\left[\Delta M_\theta\right]_{Real}$	$\left[M_\theta\right]_{Real} - \left(\frac{V_o}{\omega}\right)\left[M_h\right]_{Imag}$
M_{η_i}	dimensional moment about Y-axis due to structural mode generalized coordinate motion η_i, + nose up

M_{w_g}	dimensional moment about Y-axis due to vertical gust velocity w_g, + down
N	newton
N	number of test participants
Qi_h	dimensional generalized force in structural mode i due to plunging motion h, + for η_i increased
Qi_θ	dimensional generalized force in structural mode i due to pitching motion θ, + for η_i increased
$\left[\Delta Qi_\theta\right]_{Real}$	$\left[Qi_\theta\right]_{Real} - \left(\frac{V_o}{\omega}\right)\left[Qi_h\right]_{Imag}$
Qi_{η_i}	dimensional generalized force in structural mode i due to structural mode generalized coordinate motion ηi, + for η_i increased
Qi_{w_g}	dimensional generalized force in structural mode i due to vertical gust velocity w_g, + for η_i increased
Qi_δ	dimensional generalized force in structural mode i due to control-surface motion δ, + for η_i increased
SL	sea level
V-gain	vertical SMCS gain
WL	waterline
ζ	damping ratio
θ	pitch angle about elastic axis
Λ	sweep angle of leading edge of lifting surface
$\sigma_{\alpha V}$	Vertical gust intensity derived from angle-of-attack vane measurements
$\sigma_{\beta V}$	lateral gust intensity derived from sideslip angle vane measurements
ϕ	elastic axis-bending slope

$\Phi_{(\ )}$	power spectral density of subscript parameter
ω	frequency, radians per second

RIDE QUALITY EQUATIONS OF MOTION RELATED

q_o	$1/2\ \rho V_o^2$, dynamic pressure
ρ	density of air
$\frac{\Delta P}{q_o}$	pressure coefficient
V_o	resultant velocity of the CG
$V_{(\ )}$	component of resultant velocity; subscript denotes axis along which component acts
w_g	vertical component of gust velocity
v_g	lateral component of gust velocity
S_w	wing area
b_w	wing span
$\bar{c}_w$	wing mean aerodynamic chord
Z	vertical deflection
Y	side deflection
ℓ_x, ℓ_y, ℓ_z	distance along the x, y, and z-axis, respectively
$\bar{\ell}$, $\bar{\ell}_{(\ )}$	distance from vehicle CG to control surface k hingeline (+ aft), subscript identifies surface
ℓ, $\ell_{(\ )}$	distance from control surface hingeline to surface CG (+ aft), subscript identifies surface
$\ell^T_{(\ )}$	distance from X-axis to surface CG in-plane perpendicular to plane of symmetry (always +), subscript identifies surface.
ℓ_Γ	perpendicular distance from CG to thrust axis; + down

W	airplane weight
m	airplane mass
m, $m_{(\ )}$	mass of control surface, subscript identifies surface
M_i	the ith mode generalized mass, $\iiint \phi^2_{i(x,y,z)} \ \Delta m_{(x,y,z)} dxdydz$
I_x, I_y, I_z	moment of inertia about the X-, Y-, and Z-body axis, respectively
I_{xz}	product of inertia; positive when the principal X-axis is below the body axis at the nose of the vehicle
I_R	engine rotor moment of inertia
$I_{(\ )HL}$	moment of inertia about hingeline; ( ) subscript identifies surface
$n_{(\ )}$	load factor; subscript denotes axis along which component acts
Ψ	Euler azimuth angle
Θ	Euler pitch angle
Φ	Euler roll angle
X, Y, Z	body-axis coordinates
X_e, Y_e, Z_e	earth-axis coordinates

} see figure 6

h	altitude (+ up from sea level)

p	rolling rate about X-body axis	see figure 2
$\dot{p}$	rolling acceleration about X-body axis	
q	pitching rate about Y-body axis	
$\dot{q}$	pitching acceleration about Y-body axis	
r	yawing rate about Z-body axis	
$\dot{r}$	yawing acceleration about Z-body axis	
ω_R	rotational rate of engine rotor relative to airframe	
ω_i	natural frequency of ith mode	
ω	forcing frequency	
α	angle of attack; angle between the projection of the resultant velocity vector on the XZ-plane and the X-body (reference axis)	see figure 5
β	sideslip angle; angle between the resultant velocity vector and the plane of symmetry XZ	
Γ	control-vane dihedral angle	
$\delta_{(\ )}$	control-surface deflection; positive deflection produces positive force ($+C_N$, $+C_Y$)(see figure 3); subscript identifies surface	
$\ddot{\delta}_{(\ )}$	control-surface acceleration; positive in the sense that $\delta_{(\ )}$ is positive; subscript identifies surface	
δ'_H	rolling tail control differential deflection, + deflection produces $+C_\ell$	
g	acceleration of gravity	
g_{s_i}	structural damping constant, mode i	

η_i	deflection of the ith normalized structural mode at normalization point	see figure 4
$\dot{\eta}_i$	rate of change of the ith mode at point of normalization	
$\ddot{\eta}_i$	acceleration of the ith mode at point of normalization	
$\phi_i^{(\ )}$	the i normalized mode shape; i.e., ratio of local deflection to deflection at normalizing point (nondimensional); ( ) superscript denotes location	
$\phi_i^{(\ )'}$	slope of the ith normalized mode; ( ) superscript denotes location	
$\phi_i^{(\ )^T}$	fuselage torsional angle, ( ) superscript denotes location	
F	force	
Z	aerodynamic force in Z-direction	see figure 3
N	aerodynamic normal force (N = -Z)	
L	aerodynamic lift force ($L \approx N$ for small α)	
C	aerodynamic chord force (C = -X)	
D	aerodynamic drag force ($D \approx C$ for small α)	
X	aerodynamic force in X-direction	
Y	aerodynamic force in Y-direction	
T	thrust (T = X)	
L	aerodynamic rolling moment about X-axis	
M	aerodynamic pitching moment about Y-axis	
N	aerodynamic yawing moment about Z-axis	

N_{w_g} normal force due to unit vertical gust velocity

M_{w_g} pitching moment due to unit vertical gust velocity

Q_i generalized force in ith mode $\iiint F_{(x,y,z)} \phi_{i(x,y,z)} dxdydz$

Qi_{w_g} generalized force in structural mode i due unit vertical gust velocity

Y_{v_g} side force due to a unit lateral gust velocity

L_{v_g} rolling moment due to a unit lateral gust velocity

N_{v_g} yawing moment due to a unit lateral gust velocity

N_{η_i} yawing moment due to mode i deflection

Y_{η_i} side force due to mode i deflection

M_{η_i} pitching moment due to mode i deflection

N_{η_i} yawing moment due to mode i deflection

L_{η_i} rolling moment due to mode i deflection

Q_{ij} generalized force in mode i due to mode deflection j

$C_C = \frac{C}{S_w q_o}$ chord-force coefficient

$C_{C_{\delta_{(\ )}}} = \frac{\partial C_C}{\partial \delta_{(\ )}}$ chord-force coefficient due to control-surface deflection, subscript identifies surface

$C_N = \frac{N}{S_w q_o}$ normal-force coefficient

$C_{N_\alpha} = \frac{\partial C_N}{\partial \alpha}$ normal-force curve slope

$C_{N_{\dot{\alpha}}} = \dfrac{\partial C_N}{\partial\left(\dfrac{\dot{\alpha}\bar{c}_w}{2V_o}\right)}$ normal-force coefficient due to downwash lag and vertical acceleration

$C_{N_q} = \dfrac{\partial C_N}{\partial\left(\dfrac{q\ \bar{c}_w}{2\ V_o}\right)}$ normal-force coefficient due to pitch rate

$C_{N_{\dot{q}}} = \dfrac{\partial C_N}{\partial\left(\dfrac{\dot{q}\bar{c}_w^{\,2}}{4V_o^{\,2}}\right)}$ normal-force coefficient due to pitch acceleration

$C_{N_{\eta_i}} = \dfrac{\partial C_N}{\partial \eta_i}$ normal-force coefficient due to structural mode deflection

$C_{N_{\dot{\eta}_i}} = \dfrac{\partial C_N}{\partial\left(\dfrac{\dot{\eta}}{V_o}\right)}$ normal-force coefficient due to structral mode deflection rate

$C_{N_{\delta_{(\ )}}} = \dfrac{\partial C_N}{\partial \delta_{(\ )}}$ normal-force coefficient due to control surface deflection, subscript identifies surface

$C_{N_{\dot{\delta}_{(\ )}}} = \dfrac{\partial C_N}{\partial \dot{\delta}_{(\ )}}$ normal-force coefficient due to control surface deflection rate, subscript identifies surface

$C_m = \dfrac{M}{S_w \bar{c}_w q_o}$ pitching-moment coefficient

$C_{m_\alpha} = \dfrac{\partial C_m}{\partial \alpha}$ pitching-moment curve slope

$C_{m_{\dot{\alpha}}} = \dfrac{\partial C_m}{\partial\left(\dfrac{\dot{\alpha}\bar{c}_w}{2V_o}\right)}$ pitching-moment coefficient due to downwash lag and vertical acceleration

$C_{m_q} = \dfrac{\partial C_m}{\partial\left(\dfrac{q\bar{c}_w}{2V_o}\right)}$ pitching-moment coefficient due to pitch rate

$C_{m_{\dot{q}}} = \dfrac{\partial C_m}{\partial\left(\dfrac{\dot{q}\bar{c}_w^2}{4V_o^2}\right)}$ pitching-moment coefficient due to pitch acceleration

$C_{m_{\eta_i}} = \dfrac{\partial C_m}{\partial \eta_i}$ pitching-moment coefficient due to structural mode deflection

$C_{m_{\dot{\eta}_i}} = \dfrac{\partial C_m}{\partial\left(\dfrac{\dot{\eta}_i}{V_o}\right)}$ pitching-moment coefficient due to structural mode deflection rate

$C_{m_{\delta_{(\ )}}} = \dfrac{\partial C_m}{\partial \delta_{(\ )}}$ pitching-moment coefficient due to control surface deflection, subscript identifies surface

$C_{m_{\dot{\delta}_{(\ )}}} = \dfrac{\partial C_m}{\partial \dot{\delta}_{(\ )}}$ pitching moment due to control surface deflection rate, subscript identifies surface

$(\ )_{(\alpha)}$ = a subscript α, β, etc, as shown indicates that bracketed parameter is a nonlinear function of the subscript variable

$C_{n_i} = \dfrac{Q_i}{s_w q_o}$ generalized-force coefficient in the ith mode

$C_{\eta i_\alpha}$ = $\frac{\partial C_{\eta_i}}{\partial \alpha}$ generalized-force coefficient due to angle of attack in ith mode

$C_{\eta i_{\dot{\alpha}}}$ = $\frac{\partial C_{\eta_i}}{\partial\left(\frac{\dot{\alpha}\bar{c}_w}{2V_o}\right)}$ generalized-force coefficient due to downwash lag and vertical acceleration

$C_{\eta i_q}$ = $\frac{\partial C_{\eta_i}}{\partial\left(\frac{q\bar{c}_w}{2V_o}\right)}$ generalized-force coefficient due to pitch rate in ith mode

$C_{\eta i_{\dot{q}}}$ = $\frac{\partial C_{\eta_i}}{\partial\left(\frac{\dot{q}\bar{c}_w^2}{4V_o^2}\right)}$ generalized-force coefficient due to pitch acceleration in the ith mode

$C_{\eta i_{\eta j}}$ = $\frac{\partial C_{\eta_i}}{\partial \eta_j}$ generalized-force coefficient due to the jth mode shape in the ith mode

$C_{\eta i_{\dot{\eta} j}}$ = $\frac{\partial C_{\eta_i}}{\partial\left(\frac{\dot{\eta}_i}{V_o}\right)}$ generalized-force coefficient due to rate of change of jth mode in ith mode

$C_{\eta i_{\delta(\ )}}$ = $\frac{\partial C_{\eta_i}}{\partial \delta(\ )}$ generalized-force coefficient due to control-surface deflection in ith mode, subscript identifies control surface

$C_{\eta i_{\dot{\delta}(\ )}}$ = $\frac{\partial C_{\eta_i}}{\partial \dot{\delta}(\ )}$ generalized-force coefficient due to control-surface k deflection rate in ith mode, subscript identifies control force

C_Y = $\frac{Y}{q_o S_w}$ side-force coefficient

C_{Y_β} = $\frac{\partial C_Y}{\partial \beta}$ side-force coefficient due to angle of sideslip

$C_{Y_{\dot{\beta}}} = \dfrac{\partial C_Y}{\partial\left(\dfrac{\dot{\beta} b_w}{2V_o}\right)}$ side-force coefficient due to rate of change of sideslip angle (lateral acceleration)

$C_{Y_{\beta_{\eta_i}}} = \dfrac{\partial C_{Y_\beta}}{\partial \eta_i}$ side-force coefficient due to sideslip angle caused by symmetric structural bending (dihedral)

$C_{Y_r} = \dfrac{\partial C_Y}{\partial\left(\dfrac{r b_w}{2V_o}\right)}$ side-force coefficient due to yaw rate

$C_{Y_{\dot{r}}} = \dfrac{\partial C_Y}{\partial\left(\dfrac{\dot{r} b_w^2}{4V_o^2}\right)}$ side-force coefficient due to yaw acceleration

$C_{Y_p} = \dfrac{\partial C_Y}{\partial\left(\dfrac{P b_w}{2V_o}\right)}$ side-force coefficient due to roll rate

$C_{Y_{\dot{p}}} = \dfrac{\partial C_Y}{\partial\left(\dfrac{\dot{P} b_w^2}{4V_o^2}\right)}$ side-force coefficient due to roll acceleration

$C_{Y_{\delta_{(\ )}}} = \dfrac{\partial C_Y}{\partial \delta_{(\ )}}$ side-force coefficient due to control-surface deflection, subscript identifies surface

$C_{Y_{\dot{\delta}_{(\ )}}} = \dfrac{\partial C_Y}{\partial \dot{\delta}_{(\ )}}$ side-force coefficient due to control-surface deflection rate, subscript identifies surface

$C_n = \dfrac{N}{S_w b_w q_o}$ yawing-moment coefficient

$C_{n_\beta} = \dfrac{\partial C_n}{\partial \beta}$ yawing-moment coefficient due to sideslip angle

$C_{n_{\dot\beta}} = \dfrac{\partial C_n}{\partial\left(\dfrac{\dot\beta b_w}{2V_o}\right)}$ yawing-moment coefficient due to rate of change of sideslip angle (lateral acceleration)

$C_{n_{\beta_{n_i}}} = \dfrac{\partial C_{n_\beta}}{\partial \eta_i}$ yawing-moment coefficient due to sideslip angle caused by symmetric structural bending (dihedral)

$C_{n_r} = \dfrac{\partial C_n}{\partial\left(\dfrac{r b_w}{2V_o}\right)}$ yawing-moment coefficient due to yaw rate

$C_{n_{\dot r}} = \dfrac{\partial C_n}{\partial\left(\dfrac{\dot r b_w^{\,2}}{4V_o^{\,2}}\right)}$ yawing-moment coefficient due to yaw acceleration

$C_{n_p} = \dfrac{\partial C_n}{\partial\left(\dfrac{p b_w}{2V_o}\right)}$ yawing-moment coefficient due to roll rate

$C_{n_{\dot p}} = \dfrac{\partial C_n}{\partial\left(\dfrac{p b_w^{\,2}}{4V_o^{\,2}}\right)}$ yawing-moment coefficient due to roll acceleration

$C_{n_{\delta_{(\ )}}} = \dfrac{\partial C_n}{\partial \delta_{(\ )}}$ yawing-moment coefficient due to control surface deflection, subscript identifies surface

$C_{n_{\dot{\delta}_{(\ )}}}$	=	$\dfrac{\partial C_n}{\partial \dot{\delta}_{(\ )}}$	yawing-moment coefficient due to control surface deflection rate, subscript identifies surface
C_{ℓ}	=	$\dfrac{L}{S_w b_w q_o}$	rolling moment
C_{ℓ_β}	=	$\dfrac{\partial C_{\ell}}{\partial \beta}$	rolling-moment coefficient due to sideslip angle
$C_{\ell_{\dot{\beta}}}$	=	$\dfrac{\partial C_{\ell}}{\partial\left(\dfrac{\dot{\beta} b_w}{2V_o}\right)}$	rolling-moment coefficient due to rate of change of sideslip angle (lateral acceleration)
$C_{\ell_{\beta_{n_i}}}$	=	$\dfrac{\partial C_{\ell_\beta}}{\partial \eta_i}$	rolling-moment coefficient due to sideslip angle caused by symmetric structural bending (dihedral)
C_{ℓ_r}	=	$\dfrac{\partial C_{\ell}}{\partial\left(\dfrac{r b_w}{2V_o}\right)}$	rolling-moment coefficient due to yaw rate
$C_{\ell_{\dot{r}}}$	=	$\dfrac{\partial C_{\ell}}{\partial\left(\dfrac{\dot{r} b_w^{\,2}}{4V_o^{\,2}}\right)}$	rolling-moment coefficient due to yaw acceleration
C_{ℓ_p}	=	$\dfrac{\partial C_{\ell}}{\partial\left(\dfrac{p b_w}{2V_o}\right)}$	rolling-moment coefficient due to roll rate
$C_{\ell_{\dot{p}}}$	=	$\dfrac{\partial C_{\ell}}{\partial\left(\dfrac{\dot{p} b_w^{\,2}}{4V_o^{\,2}}\right)}$	rolling-moment coefficient due to roll acceleration

$C_{\ell_{\delta_{(\ )}}} = \dfrac{\partial C_{\ell}}{\partial \delta_{(\ )}}$ rolling-moment coefficient due to control surface deflection, subscript identifies surface

$C_{\ell_{\dot{\delta}_{(\ )}}} = \dfrac{\partial C_{\ell}}{\partial \dot{\delta}_{(\ )}}$ rolling-moment coefficient due to control surface deflection rate, subscript identifies surface

$C_{\eta_{i_{\beta}}} = \dfrac{\partial C_{\eta_i}}{\partial \beta}$ generalized-force coefficient due to sideslip angle in ith mode

$C_{\eta_{i_{\dot{\beta}}}} = \dfrac{\partial C_{\eta_i}}{\partial \left(\dfrac{\dot{\beta} b_w}{2V_o}\right)}$ generalized-force coefficient due to sideslip angle rate of change in ith mode

$C_{\eta_{i_{\beta_{\eta_j}}}} = \dfrac{\partial C_{\eta_{i_{\beta}}}}{\partial \eta_j}$ generalized-force coefficient due to sideslip in the ith antisymmetric mode due to bending in the jth symmetric mode

$C_{\eta_{i_r}} = \dfrac{\partial C_{\eta_i}}{\partial \left(\dfrac{r b_w}{2V_o}\right)}$ generalized-force coefficient due to yaw rate in ith mode

$C_{\eta_{i_{\dot{r}}}} = \dfrac{\partial C_{\eta_i}}{\partial \left(\dfrac{\dot{r} b_w^2}{4V_o^2}\right)}$ generalized-force coefficient due to yaw acceleration in the ith mode

$C_{\eta_{i_p}} = \dfrac{\partial C_{\eta_i}}{\partial \left(\dfrac{p b_w}{2V_o}\right)}$ generalized-force coefficient due to roll rate in ith mode

$C_{\eta_{i_{\dot{p}}}} = \dfrac{\partial C_{\eta_i}}{\partial \left(\dfrac{\dot{p} b_w^2}{4V_o^2}\right)}$ generalized-force coefficient due to roll acceleration in the ith mode

$K_\alpha = \dfrac{q_o S_w}{mV_o}$

$K_q = \dfrac{q_o S_w \bar{c}_w}{I_y}$

$K_\beta = \dfrac{q_o S_w}{mV_o}$

$K_r = \dfrac{q_o S_w b_w}{I_z}$

$K_p = \dfrac{q_o S_w b_w}{I_x}$

$K_{\eta_i} = \dfrac{q_o S_w}{M_i}$

i	$\sqrt{-1}$
i, j	used as subscript to identify structural mode
k	subscript identifying control surface
H	subscript identifying horizontal-tail control surface
r	subscript identifying rudder
cv	subscript identifying structural mode control vane
R	subscript indicating real part
I	subscript indicating imaginary part
o	subscript indicating trim value
HL	hingeline
FRL	fuselage reference line

MAC	mean aerodynamic chord
$( )^{TF}$	aerodynamic transfer function

LOAD EQUATIONS OF MOTION RELATED

a	acceleration
$\bar{A}$	gust response factor σ_o/σ_w
b	turbulence field parameter denoting gust intensity
$[B]$	phased loading conditions, one column per condition, each element proportional to $\rho_{ij}\ \sigma_i\ \sigma_j$
$[E]$	expected load values for each load item
$\{F\}$	forces at each SIC point: real or in the frequency domain, complex
g	structural damping parameter
$\{h\}$	real generalized coordinates
$H(\omega)$	frequency response function for a load item
$H^*(\omega)$	denotes complex conjugate of $H(\omega)$
$[H(\omega)]$	frequency response functions of load items, one row per item for 101 frequencies
j	$\sqrt{-1}$
$\{LOADS\}$	loads; shears, moments, and torques; real or in the frequency domain, complex
$\begin{bmatrix} LOAD \\ GEOM \end{bmatrix}$	geometry to compute shears, moments, and torques, one row per load item, one column for each SIC load point
$\begin{bmatrix} LOAD \\ GEN \end{bmatrix}$	load generation matrix, one row per load item, one column for each normal elastic mode
$[M]$	mass matrix

$[\overline{M}_{RBM}]$	generalized mass matrix for rigid-body motions
$[\overline{M}]$	generalized mass matrix = $[\phi]^T [M][\phi]$, rigid and elastic modes
N_o	number of crossings of zero per hour with a positive slope
N(y)	average number of level crossings with a positive slope equally or exceeding y per hour
P	turbulence field parameter denoting proportion of time in turbulence
$\{q\}$	complex generalized coordinates
$[Q_M]$	generalized aerodynamic forces due to modal motion
$[Q_C]$	generalized aerodynamic forces due to unit deflections of control surface, column 1 for horizontal tail and column 2 for the mode control vane
$\{Q_G\}$	generalized forces due to a unit sinusoidal gust
$[R]$	rigid-body mode-modifying matrix
S	Laplace operator
$[S]$	phased loading conditions, one column per condition, each column scaled so that the diagonal element equals the corresponding expected load value
$[SIC]$	structural flexibility influence coefficients
$\{SLOADS\}$	phased loading column from [S], shears, moments, and torques
$[T]$	transformation matrix, for control system feedback, relating control-surface deflections to the generalized coordinates
V	velocity

δ_H, δ_{cv}	control-surface deflections; subscript H for horizontal stabilizer, subscript V for mode control vane
ϕ	mode deflection
$\left[\phi^{\quad}\right]$	mode shapes by columns. superscript denotes type of modes; RBM for rigid-body, and E for normal elastic
σ_w, σ_o	root mean-square values of gust velocity and output item response, respectively
σ_i, σ_j	root mean square value of response items i and j
$\Phi_w(\omega)$	gust power spectrum, normalized on unit gust intensity, σ_w^2
$\Phi_o(\omega)$	load item output response power spectrum
$\dot{\theta}$	pitch rate
ρ_{ij}	correlation coefficient expressing the degree of statistical linear dependence between load item i and load item j
ω	frequency
Ω	structural normal elastic-mode frequency
$\left[\ \right]_{i,j}$	square or rectangular matrix; where i = number of rows, and j = number of columns
$\left[\ \right]$	diagonal matrix
$\left\|\ \right\|$	column matrix
$\lfloor\ \rfloor$	row matrix
$\left[\ \right]^T$	matrix transpose
$\left[\ \right]^{-1}$	matrix inverse

ENGINE/INLET RELATED

A/D	analog to digital
AIP	inlet/engine aerodynamic interface plane
AIS	air induction system
A_{duct}	duct area, psi/count
CAL	calibration
CBW	constant bandwidth
CTS	counts
CTSCAL	counts output during calibration step
CTSMEAN	mean value in counts during operate step
CTSOP	counts output during operate step
CTSZ	counts output during zero step
db	decibels
ECI-8	inlet configuration identification
FS	full scale
HP	high pass
IDC	circumferential distortion component
IDL	engine stall-margin ratio (function of IDC and IDR)
IDR	radial distortion component
ips	inches per second
K	1000 feet
LP	low pass

NF	engine fan speed
N2	nitrogen
P	pressure
ΔP	pressure difference
PCM	pulse-code modulation
PDYN	Instantaneous pressure (dynamic)
PLA	engine power lever angle
PPCM	time-averaged pressure (steady state)
pps	pounds per second
psi	pound per square inch
PT	total pressure
PT1	average total pressure at inlet/engine AIP
PTI	local total pressure at inlet/engine AIP
PTO	free-stream total pressure
PTMAX	maximum total pressure at inlet/engine AIP
PTMIN	minimum total pressure at inlet/engine AIP
RB	first movable inlet ramp angle
RC	second movable inlet ramp angle
R2	reference pressure
SMCV	structural mode control system vane
sps	sample per second
VCO	voltage controlled oscillator
WIR	corrected engine airflow

X2	amplifier (times 2)
X6	amplifier (times 6)
ZOC	a three-way value (refer to page 161)
Δ	fractional increment on total pressure contour, AIP
6002	reference pressure, absolute units
6631	calibration pressure, absolute units

REFERENCES

1. Wykes, John H.; Borland, Christopher J.; Klepl, Martin J.; and MacMiller, Cary, J.: Design and Development of a Structural Mode Control System, NASA CR-143846, October 1977.

2. Etkin, Bernard: Dynamics of Flight. John Wiley and Sons, Inc., New York.

3. Bisplinghoff, Raymond L.; Ashley, Holt; Halfman, Robert L.: Aeroelasticity. Addison-Wesley Publishing Company, Inc., Reading, Massachusetts.

4. Landahl, M. T.: Graphical Techniques for Analyzing Marginally Stable Systems. Journal of Aircraft, September-October 1964.

5. Rustenburg, John W.: Development of Tracking Error Frequency Response Functions and Aircraft Ride Quality Design Criteria for Vertical and Lateral Vibration. ASD-TR-70-18, January 1971.

6. Stenton, Thomas E.: Theoretical Frequency Response Functions and Power Spectra of the XB-70 Response to Atmospheric Turbulence. NASA CR-1621, August 1970.

7. Dugundji, John: On the Calculation of Natural Modes of Free Free Structure. Journal of the Aeronautical Sciences, February 1961.

8. Flight Control System Description, Rockwell International, North American Aircraft Division, El Segundo, TFD-71-807, June 1971 (Revision August 1975).

9. Austin, William H., Jr.: Development of Improved Gust Load Criteria for United States Air Force Aircraft. SEG-TR-67-28, September 1967.

10. Fuller, J. R.; Richmond, L. D.; Larkins, C. D.; and Russell, S. W.: Contributions to the Development of a Power Spectral Gust Design Procedure for Civil Aircraft. FAA-ADS-54, January 1966.

1. Report No.	2. Government Accession No.	3. Recipient's Catalog No.
NASA CR-144887		

4. Title and Subtitle	5. Report Date
ANALYSES AND TESTS OF THE B-1 AIRCRAFT STRUCTURAL MODE CONTROL SYSTEM	January 1980
	6. Performing Organization Code
7. Author(s) John H. Wykes, Thomas R. Byar, Cary J. MacMiller, and David C. Greek	8. Performing Organization Report No. NA-79-405
	10. Work Unit No.
9. Performing Organization Name and Address Rockwell International North American Aircraft Division 815 Lapham Street El Segundo, CA 90245	11. Contract or Grant No. NAS4-2519
	13. Type of Report and Period Covered Contractor Report - Final
12. Sponsoring Agency Name and Address National Aeronautics and Space Administration Washington, D. C. 20546	14. Sponsoring Agency Code H-1109

15. Supplementary Notes

NASA Technical Monitors: Jim McKay and Larry Felt, Dryden Flight Research Center
NASA Program Manager: Jack Nugent, Dryden Flight Research Center

16. Abstract

An 18-month program was conducted to compile and document for publication information pertaining to analyses and flight tests of the B-1 Structural Mode Control System (SMCS). This is the second phase of a continuing effort; results from the first phase study are documented in Design and Development of a Structural Mode Control System, by John H. Wykes, Christopher J. Borland, Martin J. Klepl, and Cary J. MacMiller (NASA CR-143846, October 1977). This report covers the following topics:

(1) Flexible aircraft equations of motion

(2) Description of flexible aircraft analyses model

(3) Comparison of analyses and flight-test performance results of the SMCS

(4) A summary of the study of the forward SMCS sensor package relocation

(5) Truncated analytical models used in simulation effort

(6) An analysis of the SMCS vane interference effects

(7) Impact of SMCS on selected loads

(8) Flight-test results of the SMCS vane effects on inlet/engine characteristics

(9) Summary of SMCS flight-test results

17. Key Words (Suggested by Author(s))	18. Distribution Statement
Structural mode control system Large flexible aircraft Analyses and tests	STAR category: 05

19. Security Classif. (of this report)	20. Security Classif. (of this page)	21. No. of Pages	22. Price*
Unclassified	Unclassified	268	

*For sale by the National Technical Information Service, Springfield, Virginia 22151